



Thesis submitted for the degree of  
Doctor of Philosophy

DUST-AFFECTED MODELS OF  
CHARACTERISTIC LINE EMISSION  
IN SUPERNOVAE

Antonia Bevan

---

Department of Physics & Astronomy  
UNIVERSITY COLLEGE LONDON

---

November 20, 2015

*In loving memory of Molly and Bill Siddle.*

I, Antonia Bevan, confirm that the work presented in this thesis is my own. Where information has been derived from other sources, I confirm that this has been indicated in the thesis.

## **Abstract**

---

FIRST PARAGRAPH MUST BE IN HERE.

OTHER PARAGRAPHS FOLLOW.

## Acknowledgements

---

FIRST PARAGRAPH MUST BE IN HERE.

OTHER PARAGRAPHS FOLLOW.

*Gather out of star-dust  
Earth-dust,  
Cloud-dust,  
Storm-dust,  
And splinters of hail,  
One handful of dream-dust  
Not for sale.*

- Langston Hughes  
*Dream Dust*

# Contents

---

<b>Table of Contents</b>	<b>5</b>
<b>List of Figures</b>	<b>9</b>
<b>List of Tables</b>	<b>15</b>
<b>List of Acronyms</b>	<b>18</b>
<b>1 Introduction</b>	<b>21</b>
1.1 A Handful of Dust . . . . .	22
1.1.1 A Brief History . . . . .	22
1.1.2 The Roles of Dust in the Universe . . . . .	23
1.1.3 The Medium of Dust . . . . .	24
1.1.4 Optical Properties of Dust . . . . .	25
1.1.5 Mie Theory . . . . .	26
1.1.6 Dust in Absorption . . . . .	29
1.1.7 Dust in Emission . . . . .	30
1.1.8 Dust as a Scatterer . . . . .	31
1.1.9 Radiative Transfer in Dusty Media . . . . .	31
1.2 Core-Collapse Supernovae as Dust Factories . . . . .	32
1.2.1 Origins of Dust in the Universe . . . . .	33
1.2.2 Types of Supernovae . . . . .	34
1.2.3 From Massive Stars to Remnants . . . . .	35
1.2.4 Energetics in Core-Collapse Supernovae . . . . .	36
1.2.5 Dust Formation and Destruction in CCSNe . . . . .	38

1.2.6	The Four Signatures of Dust . . . . .	39
1.2.7	The Dust Mass Debate . . . . .	40
1.2.8	Observations of Dust-Affected Asymmetric Line Profiles . . . . .	44
1.3	Content Of This Thesis . . . . .	47
<b>2</b>	<b>A Description of DAMOCLES</b>	<b>48</b>
2.1	Monte Carlo Methods . . . . .	48
2.2	Radiative Transfer and the Monte Carlo Method . . . . .	50
2.2.1	Energy Packets . . . . .	51
2.2.2	Initialisation and the Grid . . . . .	53
2.2.3	Properties of the Dusty Medium . . . . .	55
2.2.4	Emission and Propagation . . . . .	57
2.2.5	The Velocity Field and Doppler shifting . . . . .	60
2.2.6	Electron Scattering . . . . .	62
2.2.7	Doublets . . . . .	65
2.2.8	Comparing a Model with Observations . . . . .	65
2.3	The Structure of DAMOCLES . . . . .	66
2.3.1	Computational Architecture and Processes . . . . .	67
2.3.2	OpenMP Parallelisation . . . . .	76
2.3.3	Input Variables . . . . .	77
2.3.4	Output, Post-Processing and Visualisation . . . . .	85
2.4	Further Developments . . . . .	87
<b>3</b>	<b>Probing DAMOCLES: Testing and a Parameter Sensitivity Analysis</b>	<b>89</b>
3.1	Testing and benchmarking the code . . . . .	89
3.1.1	Theoretical line profiles from first principles . . . . .	90
3.1.2	Benchmarking against numerical models . . . . .	96
3.2	A Parameter Sensitivity Analysis . . . . .	97
3.2.1	The maximum line velocity, $V_{max}$ . . . . .	99
3.2.2	The ejecta radius ratio, $R_{in}/R_{out}$ . . . . .	99
3.2.3	The dust optical depth, $\tau$ . . . . .	100
3.2.4	The dust albedo, $\omega$ . . . . .	102
3.2.5	The dust density profile, $\rho \propto r^{-2\beta}$ . . . . .	103
3.2.6	Inferring properties of the dust from the models . . . . .	106

3.2.7	The wavelength dependence of dust absorption . . . . .	109
3.2.8	The effect of a grain radius distribution . . . . .	110
3.2.9	The effect of different species . . . . .	111
3.2.10	The velocity distribution . . . . .	112
3.3	Conclusions . . . . .	112
<b>4</b>	<b>The Evolution of Dust Formation in SN 1987A</b>	<b>114</b>
4.1	10,000 Days of Dust . . . . .	118
4.2	Spectral Observations of SN 1987A . . . . .	122
4.2.1	Contamination of the H $\alpha$ profiles . . . . .	124
4.2.2	The evolution of the maximum and minimum velocities . . . . .	125
4.3	Modelling SN 1987A . . . . .	126
4.3.1	Smooth Density Models for SN 1987A . . . . .	131
4.3.2	Clumped Dust Models for SN 1987A . . . . .	136
4.3.3	Goodness of fit . . . . .	138
4.3.4	The effects of clumping . . . . .	141
4.3.5	More complex models . . . . .	141
4.3.6	The effect of a grain radius distribution . . . . .	148
4.3.7	The effect of different grain species . . . . .	148
4.3.8	Modelling large masses of dust at early epochs: comparison with the results of Dwek & Arendt (2015) . . . . .	151
4.3.9	Unattenuated line fluxes . . . . .	156
4.4	Discussion . . . . .	157
4.5	Conclusions . . . . .	161
<b>5</b>	<b>Dust Masses in Other Supernova Remnants</b>	<b>163</b>
5.1	Introduction . . . . .	163
5.2	Cassiopeia A . . . . .	165
5.2.1	Integrated Spectrum of Cas A . . . . .	165
5.2.2	Smooth Models . . . . .	165
5.2.3	Clumped Models of Cas A . . . . .	170
5.2.4	The Geometry of Cas A . . . . .	172
5.2.5	The Chemistry of Cas A . . . . .	172
5.2.6	The Dust Mass in Cas A . . . . .	172

5.3	SN 1980K . . . . .	173
5.3.1	Smooth Models . . . . .	173
5.4	SN 1993J . . . . .	175
5.5	Discussion . . . . .	175
5.6	Conclusions . . . . .	175
<b>6</b>	<b>Conclusions and Future Work</b>	<b>177</b>
<b>A</b>	<b>Mie Theory</b>	<b>178</b>
A.1	Formulating the Problem . . . . .	178
A.2	Solving the Vector Wave Equations . . . . .	179
A.3	Calculating the Incident and Scattered Fields . . . . .	181
A.4	Determining the Scattering Coefficients . . . . .	182
A.5	The Scattering and Extinction Cross-Sections . . . . .	183
	<b>Bibliography</b>	<b>185</b>

# List of Figures

---

1.1	The dark globule Barnard 68, LDN 57. ESO press release 30 April 1999. . .	23
1.2	Extinction curves for different values of $R_V$ across the UV, optical and IR based on the parametrisation by Cardelli et al. (1989) . The bump at 2175Å can be clearly seen in all curves. . . . .	30
1.3	A flowchart summarising the supernova classification scheme . . . . .	34
1.4	Illustration of the different shapes of light curves for Type IIP and Type IIL supernovae. . . . .	35
1.5	Illustration of the Lyman, Balmer and Paschen series of transitions in hydrogen. . . . .	37
1.6	Images of Cas A at IR, sub-mm and radio wavelengths. The top six images are 7' on a side and the bottom three are 10' on a side. The inner and outer circles in the middle-right image correspond to the reverse and forward shocks respectively according to (Gotthelf et al. 2001). Image taken from Barlow et al. (2010). . . . .	41
1.7	Composite image of the Crab nebula using Hubble Space Telescope (HST) optical line emission data (blue-white) and <i>Herschel</i> 70μm dust emission (red) illustrating the close alignment between the optical knots and filaments. Credits: Oli Usher (UCL); <i>Herschel Space Observatory, Hubble Space Telescope</i> : ESA, NASA. Image taken from Owen & Barlow (2015). .	43
1.8	The emission profile of [O I] $\lambda\lambda$ 6300,6363 Å from SN 1987A on 5 August 1988 (day 529) and 3 March 1989 (day 739) showing the strong blue-shift by $\sim 600 \text{ km s}^{-1}$ of the latter profile. The profiles are scaled to the same peak intensity for the violet component. The image is taken from Lucy et al. (1989). . . . .	45

---

1.9	Figure taken from Gall et al. (2014) illustrating the progressive blue-shifting of line profiles from SN 2010jl. <i>a.</i> Evolution of the H $\beta$ line profile ( <i>left</i> ) and Lorentzian line fits to this line ( <i>right</i> ). <i>b.</i> Evolution of the H $\alpha$ line ( <i>left</i> ) and the HeI $\lambda 5876\text{\AA}$ line ( <i>right</i> ). . . . .	46
2.1	A flowchart representing the sequence of processes that take place in the DAMOCLES code. The modules involved at each stage are given in parentheses. . . . .	52
2.2	3D representations of the grid generated by DAMOCLES. A smooth distribution is shown on the left and a clumped distribution on the right. . . . .	56
2.3	A flowchart representing the hierarchy of modules and subroutines in the DAMOCLES code. Ellipses represent modules and rectangles represent subroutines (the red rectangle is a recursive subroutine). Green arrows indicate the dependence of a module or subroutine on previous modules or subroutines. Purple arrows indicate the flow of the code. . . . .	69
2.4	A flowchart representing the processes that occur in the <i>propagate</i> subroutine	74
2.5	Schematic representing which packets are collected when the line of sight environment is switched on. Packets that contribute to the emergent line profile are those that escape the nebula within a cone with vertical angle $\pi/6$ . . . . .	83
3.1	Diagrams illustrating the dust-free model and some of the relevant variables used in the derivation of the equations of analytical line profiles. On the left is the general case with curves of constant $u$ labelled. On the right is the special case of an orthogonal $(u, s)$ net when $\alpha = 1$ and therefore $v(r) \propto r$ . . . . .	91
3.2	<i>Red:</i> Benchmark models for optically thin ( $\tau = 0$ ) line profiles with fractional velocity $v(r) \propto r$ . Top to bottom: initial emissivity profiles $i(r) \propto r^{-2\beta}$ with $\beta = 0.0$ , $\beta = 1.0$ and $\beta = 2.0$ . Cases with $R_{in}/R_{out} = 0.2$ are on the left and $R_{in}/R_{out} = 0.0$ on the right. The presence of a plateau in the upper plots is due to the finite inner radius (detached shell). <i>Blue:</i> The analytical case with $i(u) \sim 1 - u^{2(1-\beta)}$ except in the case of $\beta = 1$ where $i(u) \sim -\log u$ . . . . .	94
3.3	The analytically derived line profiles of Lucy et al. (1989) corresponding to their Model II scenario with zero albedo dust, for a variety of total dust optical depths. . . . .	95

---

3.4	The numerically modelled line profiles of Lucy et al. (1989) corresponding to their Model III scenario with dust of albedo $\omega = 0.6$ , for a variety of total dust optical depths. . . . .	96
3.5	Benchmark models for line profiles with $v \propto r$ , $i(r) \propto$ constant and a filled sphere with $R_{in}/R_{out} = 0$ . Pure dust absorption models ( $\omega = 0$ ) are presented in the top plot, whilst partially scattering models are presented at the bottom ( $\omega = 0.6$ ) as per Lucy et al. (1989) Models II and III. All resulting profiles have been scaled to unity flux at their peaks. . . . .	98
3.6	Set of models with $i(r) \propto r^{-2\beta}$ for $\beta = 1.0$ (left), $\beta = 1.5$ (middle) or $\beta = 2.0$ (right), $\omega = 0$ , $R_{in}/R_{out} = 0.2$ , $v(r) \propto r$ and $v_{max} = 1$ illustrating the effects of varying $\tau$ . Peak fluxes are scaled to unity. . . . .	101
3.7	Set of models with $i(r) \propto r^{-4}$ (i.e. $\beta = 2.0$ ), $R_{in}/R_{out} = 0.2$ , $v(r) \propto r$ and $v_{max} = 1$ illustrating the effects of varying $\tau$ and $\omega$ . Peak fluxes are scaled to unity. . . . .	102
3.8	The variation of extinction efficiency ( $Q_{ext}$ ) with grain radius at $\lambda = 656$ nm for Zubko et al. (1996) BE amorphous carbon, Draine & Lee (1984) astronomical silicate and the MgSiO <sub>3</sub> and MgFeSiO <sub>4</sub> samples of Jäger et al. (2003) and Dorschner et al. (1995) respectively. A linear scale is presented on the top and a log scale on the bottom. . . . .	104
3.9	The variation of albedo with grain radius at $\lambda = 656$ nm for Zubko et al. (1996) BE amorphous carbon, Draine & Lee (1984) astronomical silicate and the MgSiO <sub>3</sub> and MgFeSiO <sub>4</sub> samples of Jäger et al. (2003) and Dorschner et al. (1995) respectively. A linear scale is presented on the top and a log scale on the bottom. . . . .	105
3.10	Model line profiles for H $\alpha$ (6563Å in red), H $\beta$ (4861Å in yellow) and Pa $\delta$ (10049Å in blue) for optically thin and optically thick cases on the left-hand side and right-hand side respectively. All models adopted density profile $\rho(r) \propto r^{-4}$ (i.e. $\beta = 2$ ), velocity profiles $v(r) \propto r$ and radii ratio $R_{in}/R_{out} = 0.2$ . The grain radii used were $a = 0.001 \mu\text{m}$ (top), $a = 0.1 \mu\text{m}$ (middle) and $a = 1.0 \mu\text{m}$ (bottom). All the above models used amorphous carbon. . . . .	107

3.11	The variation of amorphous carbon dust absorption efficiency with grain radius. The grain radii plotted are $a = 0.001 \mu\text{m}$ (top), $a = 0.1 \mu\text{m}$ (middle) and $a = 1.0 \mu\text{m}$ (bottom). The vertical lines mark the wavelengths of H $\alpha$ (6563Å in red), H $\beta$ (4861Å in yellow) and Pa $\delta$ (10049Å in blue).	108
4.1	SN 1987A in the Large Magellanic Cloud. The three-colour image is composed of several pictures of the region taken with the Wide Field and Planetary Cameras on the Hubble Space Telescope between September 1994 and July 1997. Image courtesy of NASA, ESA, and The Hubble Heritage Team (STScI/AURA).	115
4.2	Evolution of the ring collision from 1994 to 2014 from a combination of HST B- and R- band images. The brightness of the ring has been reduced by a factor of 20 by applying a mask to the images making it possible to see the morphology of the ring at the same time as the faint ejecta. The image is taken from (Fransson et al. 2015).	116
4.3	<i>Herschel</i> images of SN 1987A. Image taken from Matsuura et al. (2011).	118
4.4	ALMA, ATCA, HST and Chandra images of SN 1987A showing the location of the dust in the inner ejecta at 450 $\mu\text{m}$ . The image is taken from (Indebetouw et al. 2014). Inset HST image courtesy of R. Kirshner and the SAINTS collaboration (also see Larsson et al. (2013)) and the inset Chandra X-ray image is from Helder et al. (2013).	119
4.5	Archival data showing the evolution of the H $\alpha$ and [O I] line profiles from SN 1987A at the earlier of the epochs considered. The spectral gaps at the last two epochs correspond to where narrow line emission from the equatorial ring has been removed. The spectra have been continuum-subtracted and offsets have been applied for display purposes.	121
4.6	Archival data showing the evolution of the H $\alpha$ line profile from SN 1987A at the later epochs. The spectral gaps correspond to where narrow line emission from the ER has been removed. The spectra have been continuum-subtracted and offsets applied for display purposes.	122

---

4.7	The low resolution H $\alpha$ line profile from SN 1987A observed at the CTIO on day 1054. The unresolved narrow nebular [N II] lines at $\lambda = 6583 \text{ \AA}$ and $\lambda = 6548 \text{ \AA}$ and the narrow nebular H $\alpha$ line at $\lambda = 6563 \text{ \AA}$ can be clearly seen. . . . .	125
4.8	Amorphous carbon smooth dust fit to the day 714 H $\alpha$ line of SN 1987A using an MRN size distribution, illustrating the underestimation of the red scattering wing for small grain radii. Model parameters are the same as the smooth dust fit for day 714 (Table 4.4) except for the grain radius distribution and dust mass: $M_{dust} = 8.0 \times 10^{-6} M_{\odot}$ , $a_{min} = 0.005 \mu\text{m}$ , $a_{max} = 0.25 \mu\text{m}$ and $n(a) \propto a^{-3.5}$ . . . . .	129
4.9	Best model fits to the SN 1987A H $\alpha$ line at day 714 and day 806 for the parameters detailed in Tables 4.4 and 4.5. The two fits on the top are smooth dust models using amorphous carbon grains of radius $a = 0.35 \mu\text{m}$ and the two fits on the bottom are clumped dust models using amorphous carbon grains of radius $a = 0.6 \mu\text{m}$ . . . . .	130
4.10	Best model fits to the SN 1987A H $\alpha$ line at days 1862, 2875 and 3604 for the parameters detailed in Tables 4.4. Smooth model fits with amorphous carbon grains of radius $a = 0.35 \mu\text{m}$ are presented. . . . .	131
4.11	Best smooth dust fits to the SN 1987A [O I] $\lambda 6300, 6363 \text{ \AA}$ doublet at days 714, 806, 1054 and 1478 for the parameters detailed in Tables 4.4. Smooth dust fits with amorphous carbon grains of radius $a = 0.35 \mu\text{m}$ are presented.	132
4.12	Best model fits to the SN 1987A H $\alpha$ line at days 1862, 2875 and 3604 for the parameters detailed in Tables 4.5 and 4.6. On the left are clumped model fits with amorphous carbon grains of radius $a = 0.6 \mu\text{m}$ and on the right are clumped model fits with amorphous carbon grains of radius $a = 3.5 \mu\text{m}$ .	137
4.13	Best clumped model fits to the SN 1987A [O I] $\lambda 6300, 6363 \text{ \AA}$ doublet at days 714, 806, 1054 and 1478 for the parameters detailed in Tables 4.5 and 4.6. On the left are clumped dust fits with amorphous carbon grains of radius $a = 0.6 \mu\text{m}$ and on the right are clumped dust fits with amorphous carbon grains of radius $a = 3.5 \mu\text{m}$ . . . . .	139

4.14 Fits to the H $\alpha$ line profile for day 714 for a variety of dust masses. All other parameters are given as per Table 4.5. Dust masses are given as a multiple of the best fitting dust mass ( $M_{bf}$ ) and the mean squared error is presented for each plot. . . . .	142
4.15 Fits to the H $\alpha$ line profile for day 2875 for a variety of dust masses. All other parameters are given as per Table 4.5. Dust masses are given as a multiple of the best fitting dust mass ( $M_{bf}$ ) and the mean squared error is presented for each plot. . . . .	143
4.16 Fits to the H $\alpha$ line profile for day 714 for a variety of density distributions with the $\beta = 1.4$ case representing the best fit. All other parameters are given as per Table 4.5. The mean squared error is presented for each plot. . .	144
4.17 Fits to the H $\alpha$ line profile for day 2875 for a variety of density distributions with the $\beta = 2.0$ case representing the best fit. All other parameters are given as per Table 4.5. The mean squared error is presented for each plot. .	145
4.18 Fits to the H $\alpha$ and [O I] $\lambda\lambda 6300,6363$ Å lines at day 714 using the more complex dust model described in Section 4.3.5 with a dust mass of $2.3 \times 10^{-4} M_{\odot}$ . . . . .	147
4.19 H $\alpha$ models using different grain species and dust masses. Models for the dust masses presented by Dwek & Arendt (2015) are on the top and models using my minimum required dust masses are on the bottom. From left to right the dust species are composite grains (82% MgSiO <sub>3</sub> and 18% amorphous carbon by volume), pure MgSiO <sub>3</sub> , pure amorphous carbon and pure MgFeSiO <sub>4</sub> . A density distribution with $\beta = 2.3$ was adopted with a filling factor $f = 0.09$ and an effective clump radius $R_{eff}/R_{out} = 0.044$ . All other parameters are the same as in Table 4.5. . . . .	150

---

4.20 [O I] $\lambda$ 6300,6363 Å models using different grain species and dust masses. Models using the dust masses presented by DA15 are on the top and models using my minimum required dust masses are on the bottom. From left to right the species are composite grains (82% MgSiO <sub>3</sub> and 18% amorphous carbon by volume), pure MgSiO <sub>3</sub> , pure amorphous carbon and pure MgFeSiO <sub>4</sub> . A density distribution with $\beta = 1.3$ was adopted with a filling factor $f = 0.09$ and an effective clump radius $R_{eff}/R_{out} = 0.044$ . The ratio between the doublet components was 2.2. All other parameters are the same as in Table 4.5. . . . .	152
4.21 Predicted undepleted luminosities for the H $\alpha$ line ( <i>above</i> ) and [O I] $\lambda$ 6300,6363 Å doublet ( <i>below</i> ) presented with the best power-law fit to the data. . . . .	155
4.22 Derived dust masses for SN 1987A as a function of epoch. <i>Red squares</i> - dust masses derived by W15 from their photometric SED modelling of SN 1987A. <i>Yellow line</i> - W15's sigmoid fit to their values. <i>Dark and light blue asterisks</i> - maximum ( $a = 3.5 \mu\text{m}$ ) and minimum ( $a = 0.6 \mu\text{m}$ ) dust masses respectively for the [O I] models for $t \leq 1478$ days and for the H $\alpha$ models for $t \geq 1862$ days. <i>Purple stars</i> - predicted dust masses calculated as the mean of the maximum and minimum dust masses. <i>Green line</i> - sigmoid fit to my predicted dust masses. . . . .	158
5.1 The integrated spectrum of Cas A (Milisavljevic & Fesen 2013). . . . .	164
5.2 Finding charts of the long-slit positions used to compose the integrated spectrum of the main shell of Cas A. The background image is a mosaic created from 2004 HST/ACS observations (Fesen et al. 2006). Image is taken from Milisavljevic & Fesen (2013). . . . .	166
5.3 smooth fits to Cas A OIII shifted and unshifted . . . . .	166
5.4 Cas A OI and OII . . . . .	168
5.5 Cas A clumped . . . . .	171
5.6 Smooth fits to SN 1980K . . . . .	173
5.7 clumped fits to SN 1980K . . . . .	174
5.8 smooth fits to SN 1993J . . . . .	175
5.9 dust masses . . . . .	176

## List of Tables

---

2.1	Values of $q_{H\alpha}(T)$ at three different temperatures as used by DAMOCLES.	62
2.2	The input variables read in from the input file and example values	78
2.3	List of all outputs and example values produced by the DAMOCLES code.	86
4.1	Details of the archival data for SN 1987A.	123
4.2	$H\alpha$ full-width half-maxima (FWHM) and the half-width zero intensities (HWZI) in $\text{km s}^{-1}$ determined by the zero intensity velocity on the blue side of the line. The tabulated line widths have been corrected for the relevant instrumental resolution.	126
4.3	Observed luminosities of the $H\alpha$ line and estimated electron scattering optical depths from $R_{in}$ to $R_{out}$ for the radii detailed in Tables 4.4 to 4.5 based on an assumed gas temperature of 10,000 K.	127
4.4	The parameters used for the best fitting smooth models of SN 1987A with amorphous carbon grains of radius $a = 0.35 \mu\text{m}$ . Optical depths are given from $R_{in}$ to $R_{out}$ at $\lambda = 6563 \text{\AA}$ for $H\alpha$ and $\lambda = 6300 \text{\AA}$ for [O I]. Values of $\tau_V$ are very close to the quoted values of $\tau_{H\alpha}$ .	133
4.5	The parameters used for the best fitting clumped models of SN 1987A with amorphous carbon grains of radius $a = 0.6 \mu\text{m}$ . Optical depths are given from $R_{in}$ to $R_{out}$ at $\lambda = 6563 \text{\AA}$ for $H\alpha$ and $\lambda = 6300 \text{\AA}$ for [O I]. Values of $\tau_V$ are very close to the quoted values of $\tau_{H\alpha}$ .	134
4.6	The parameters used for the best fitting clumped models of SN 1987A with amorphous carbon grains of radius $a = 3.5 \mu\text{m}$ . Optical depths are given from $R_{in}$ to $R_{out}$ at $\lambda = 6563 \text{\AA}$ for $H\alpha$ and $\lambda = 6300 \text{\AA}$ for [O I]. Values of $\tau_V$ are very close to the quoted values of $\tau_{H\alpha}$ .	135

4.7	Mean square errors illustrating the variation in goodness of fit for the H $\alpha$ line profile for a range of dust masses with other parameters fixed at their best-fitting values for the clumped model with $a = 0.6\mu\text{m}$ as detailed in Table 4.5. The MSE is calculated between $-5000 \text{ km s}^{-1}$ and $+7000 \text{ km s}^{-1}$ for the day 714 H $\alpha$ profile and between $-8000 \text{ km s}^{-1}$ and $+8000 \text{ km s}^{-1}$ for the day 2875 H $\alpha$ profile. A factor of zero represents the dust-free model. The best-fitting model is italicised.	140
4.8	Mean square errors illustrating the variation in goodness of fit for the H $\alpha$ line profile for a range of density profiles with other parameters fixed at their best-fitting values for the clumped model with $a = 0.6\mu\text{m}$ as detailed in Table 4.5. The MSE is calculated between $-5000 \text{ km s}^{-1}$ and $+7000 \text{ km s}^{-1}$ for the day 714 H $\alpha$ profile and between $-8000 \text{ km s}^{-1}$ and $+8000 \text{ km s}^{-1}$ for the day 2875 H $\alpha$ profile. The best-fitting model is italicised.	140
4.9	Dust masses for day 714 clumped models of the H $\alpha$ line using different grain radius distributions and 100% amorphous carbon. The final column shows the factor of increase over the dust mass for the single size model ( $M = 7 \times 10^{-5} M_{\odot}$ with $a = 0.6 \mu\text{m}$ ) and $p$ is the exponent of the grain radius distribution $n(a) \propto a^{-p}$ .	149
4.10	Dust mass conversion factors for single size models using grains of 100% Zubko BE amorphous carbon or 100% Draine & Lee silicate at $\lambda \sim 656 \text{ nm}$ . $f$ is the factor by which the dust mass changes on going from amorphous carbon to silicates.	151
5.1	The variation in dust mass for a fixed optical depth $\tau_{5007\text{\AA}} = 0.49$ for the parameters listed in Table 5.2.	168
5.2	The parameters used for the smooth models of Cas A with a medium composed of 50% amorphous carbon and 50% silicate grains of radius $a = 0.05 \mu\text{m}$ . Optical depths are given from $R_{in}$ to $R_{out}$ at $\lambda = 5007 \text{ \AA}$ for [O III], $\lambda = 7319 \text{ \AA}$ for [O II] and $\lambda = 6300 \text{ \AA}$ for [O I]. The doublet ratio is always the ratio of the stronger line to the weaker line. The asterisk indicates that the parameters listed describe the gas density distribution. The dust density distribution is the same in all cases (as detailed for the shifted [O II] doublet in the second row).	169

- 5.3 The fraction of increase in dust mass over the smooth model with parameters as given in Table 5.2 for clumped models with different clump widths and different clump volume filling factors. The other parameters in the models were fixed at the values given in Table 5.2. . . . . 172

## List of Acronyms

---

- AAT - Anglo-Australian Telescope  
AGB - Asymptotic Giant Branch  
ALMA - Atacama Large Millimetre Array  
API - Application Program Interface  
CCSN(e) - Core-Collapse Supernova(e)  
CDE - Continuous Distribution of Ellipsoids  
CTIO - Cerro Tololo Inter-American Observatory  
ER - Equatorial Ring  
ESO - European Southern Observatory  
FWHM - Full-Width Half Maximum  
HST - Hubble Space Telescope  
HWZI - Half-Width Zero Intensity  
IR - Infra-Red  
ISM - Inter-Stellar Medium  
LMC - Large Magellanic Cloud  
MC - Monte Carlo  
MCMC - Markov Chain Monte Carlo  
MIR - Mid Infra-Red  
MRN - The Mathis, Rumpl & Nordsieck (1977) grain distribution  
MSE - Mean Squared Error  
NASA - National Aeronautics and Space Administration  
NIR - Near Infra-Red  
QSO - Quasi-Stellar Object (Quasar)

SCUBA - Sub-millimetre Common-User Bolometer Array

SED - Spectral Energy Distribution

SN(e) - Supernova(e)

UV - Ultra-Violet

VLT - Very Large Telescope

# Chapter 1

---

## Introduction

Should you choose to seek out one of my friends and ask them about my whereabouts in recent months, they would probably yield the information that I had been noticeable by my absence because I was preoccupied writing about dust, a fact which I imagine they find bemusing and possibly somewhat concerning. Blissful as they are in their ignorance of dust (astronomers find no such peace), they do not know the importance of this all-pervading substance.

The universe is an extremely dusty place. The ubiquity of dust throughout almost all epochs and environments demands a comprehensive understanding of its formation and evolution, properties and effects. It plays numerous roles in a variety of scenes; it is a building block of all solid bodies, a birthing place for molecules, a crucial ingredient in star formation and an extreme annoyance for cosmologists. It is both a product of physical processes and an agent of chemical ones.

It is perhaps confusing therefore that there is comparatively little consensus regarding the formation processes and natal environments that result in the evolution of certain atoms and molecules into the grains we call dust. Over the years since the first discovery of dust in the very early universe, a growing population of astronomers and astrophysicists have turned their attention to the study of dust formation in core-collapse supernovae (CCSNe), in the hope that these objects might prove to be the missing piece of the puzzle. Recent observations of a number of CCSNe and supernova remnants (SNRs) have lent weight to this theory, with models and analyses of spectral energy distributions (SEDs)

suggesting the presence of large reservoirs of cool, ejecta-condensed dust in these objects.

I have sought to make my own small contribution to this field by exploiting a different observational signature, that of blue-shifted line profile asymmetries observed in the spectra of many CCSNe and attributed to the formation of dust in the ejecta. By quantitatively modelling characteristically asymmetric spectral line profiles using a new code, DAMOCLES, I have attempted to determine the rate of dust formation in CCSNe and the expected order of magnitude of the eventual dust masses produced.

Throughout the remainder of this chapter I will attempt to elucidate the above synopsis in more detail. In Section 1.1, a brief description of the roles that dust plays in the universe will be followed by a discussion of the physical properties of dust that allow for its detection in emission and absorption. In Section 1.2, I will give a summary of our current understanding of dust formation, with particular attention paid to dust formation in CCSNe. At the end of this section, I will describe the current state of the field before concluding this chapter with an outline of the structure of this thesis.

## 1.1 A Handful of Dust

### 1.1.1 A Brief History

The presence of dust in the universe was first theorised when astronomers observed dark patches of sky in the Milky Way where all of the stars had been “erased” (see Figure 1.1). Whilst some claimed that these black regions were in fact a true absence of stars resulting from some anomaly in the stellar distribution, others felt that it was more likely that an obscuring cloud of material was blocking the light from the stars behind. In 1930, Donald Trumpler confirmed this latter theory by considering the apparent magnitudes and colours of stars located at different angles to the galactic plane, discovering that those closer to the plane appeared redder than their more distant counterparts. This was the first evidence of interstellar reddening and the beginnings of our understanding of dust as a scatterer, absorber and emitter of radiation.

For the next few decades, dust was largely thought to be an irritating obstacle to observing and comprehending more interesting facets of the universe. We now have a much fuller understanding of the variety and importance of the roles that dust plays throughout astrophysics.

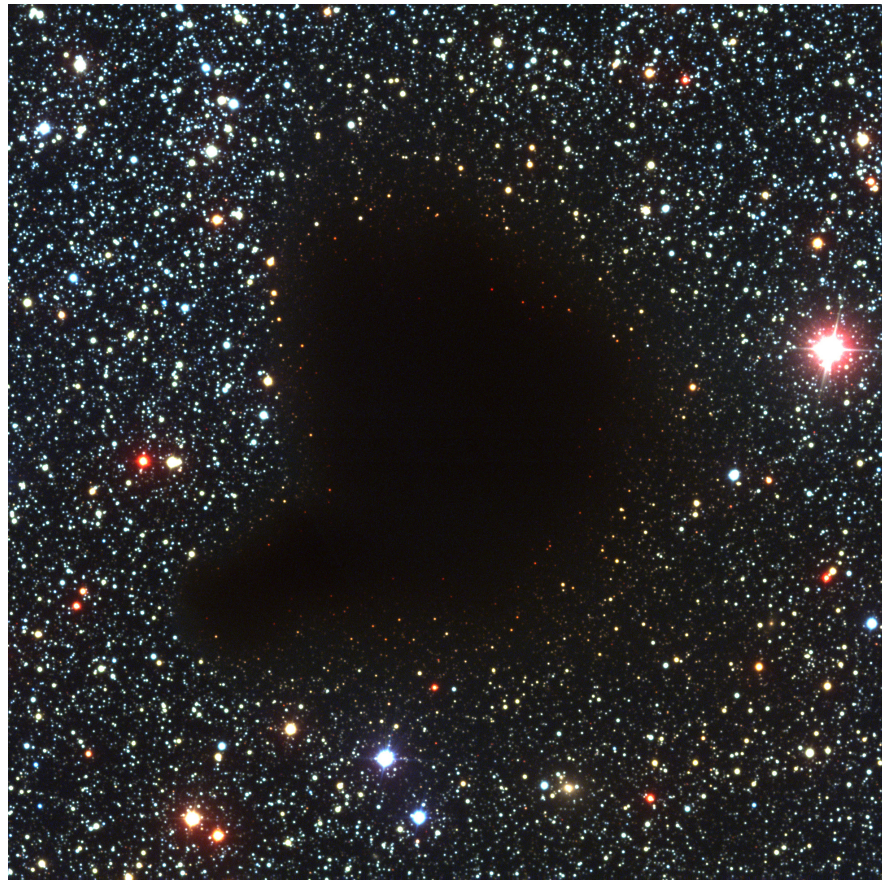


**Figure 1.1.** The dark globule Barnard 68, LDN 57. ESO press release 30 April 1999.

### 1.1.2 The Roles of Dust in the Universe

Despite comprising only  $\sim 1\%$  of the mass of the interstellar medium (ISM), dust grains account for as much as 30% of the total galactic luminosity via their emission in the infrared (IR) (Li & Greenberg 2003). In the cycle of matter from the ISM to condensing clouds to stars and back again, dust is far more than a passive passenger along for the ride. Whilst residing in the ISM, dust is important in determining its thermodynamics. It acts both as a heating agent via the emission of photoelectrons in regions of strong ultra-violet (UV) radiation and a coolant in dense regions via the emission of IR radiation. In this role as a coolant, dust is also crucial to the process of star-formation, helping to remove gravitational energy and allowing the natal cloud to collapse. Dust also contributes to the star formation process by shielding the gas from ionising radiation, helping to speed up the growth of the protostellar core.

In addition to the above physical functions, dust plays an essential part in chemical

processes. Heavy elements in the local medium are depleted through their inclusion in dust grains. These grains then attract gaseous atoms to their surfaces and catalyse the formation of molecules which are then released back into the surrounding medium.

Dust does not reside solely in the ISM however. It is present in large quantities in the circumnuclear tori found around active galactic nuclei. Dust is also found between planets, around stars and in protoplanetary discs, where dust grains constitute the smallest unit of the building blocks that will go on to form planetesimals and planets. These grains may even be responsible for the origins of life.

The more detailed our understanding of dust as an astrophysical community, the more accurate we can make our inferences across an entire range of fields. There is arguably no other topic in astronomy that has such wide-ranging effects.

### 1.1.3 The Medium of Dust

An increasingly detailed knowledge of the nature and properties of dust has developed over the last few decades. Dust grains have their terrestrial analogue in soot or very fine sand rather than in the dust bunnies that one may find behind the sofa. When found in the ISM they are generally small, between  $0.05\mu\text{m}$  and  $0.25\mu\text{m}$  in radius, and are normally predominantly composed of carbon or silicates. Carbonaceous grains may take many forms ranging from structured solids such as diamond and graphite to amorphous molecules and aromatics. They are generally found to be strongly attenuating. Silicates tend to be more glassy and contain silicon and oxygen potentially with the dirtying addition of magnesium, iron or other heavier elements. Condensates of more complex molecules such as olivine ( $\text{MgFeSiO}_4$ ) and pyroxene ( $\text{MgSiO}_3$ ) make up these grains.

Dust grains are generally assumed to be spherical in order to make their simulative treatment more straightforward but in reality dust grain shapes are actually much more complex. Sophisticated models of dust grains sometimes adopt a continuous distribution of ellipsoids to represent dust grain shape (Bohren & Huffman 1983). This allows grains to take any ellipsoidal form ranging from flat discs to needles to perfect spheres. However, even this more detailed consideration omits structures that are akin to long strings or to fluffy particles (not dissimilar to a tumble dryer ball in shape). Heretofore, the vast majority of models, including DAMOCLES, have only considered spherical grains and this wide variety of shapes therefore represents a significant modelling challenge to be addressed in the future.

### 1.1.4 Optical Properties of Dust

Whilst an increasingly strong picture of the composition and properties of dust is becoming apparent, there are still a number of largely unresolved issues regarding the makeup of a dusty medium. Different species and composites thereof have different optical properties. In order to model the absorption and scattering of radiation off dust grains it is necessary to first know the complex refractive indices of a given species over the relevant wavelength range (see Section 1.1.5). Laboratory measurements have produced a number of different sets of optical constants for a variety of carbonaceous and silicate species and these are well-utilised throughout the field. It is noted at this early juncture however that in many cases there are numerous, somewhat contradictory, sets of optical constants for a given species and that these variations can potentially cause a degree of confusion regarding the results of models that use them (e.g. Owen & Barlow (2015)).

In order to quantitatively model the effects of dust on line emission in an expanding atmosphere, the physics of how dust particles scatter, absorb and re-emit radiation must be understood. In the next few sections, I will review the physical facets of dust grains that allow for their detection via emission in the IR and absorption and scattering in the UV and optical.

We must first be able to describe the manner in which a single grain scatters an incident photon and with what probability it will absorb rather than scatter that photon. These properties are defined via the scattering and absorption cross-sections of interaction ( $C_{sca}$  and  $C_{abs}$  respectively). In combination with the scattering anisotropy parameter  $g$ , they are used to define the angular distribution and amount of light that is scattered by the grain. The aim is to calculate these quantities for a beam of radiation of given wavelength, incident on a particle of given size and shape, and composed of a given material.

Calculation of these quantities is not straightforward. In order to determine the above properties, we must take a step back to first principles, away from dust, and consider what is meant by ‘scattering’ and ‘absorption’. Matter, regardless of its superficial composition, is intrinsically composed of fundamental, charged particles: electrons and protons. When an electromagnetic field is induced in the presence of these particles, such as when a beam of radiation illuminates an obstacle, which could be a liquid or an atom or a dust grain or a solid, the fundamental particles that make up that object are set into oscillatory motion. These motions cause the radiation of electromagnetic energy and it is this secondary

radiation that we refer to as scattered light. Similarly, the excited charges may transform some of the incident energy into other forms such as thermal energy. This is the process that is referred to as absorption.

Returning now to the concept of scattering and absorption by a single particle, derivation of the quantities of interest, namely  $C_{sca}$  and  $C_{abs}$ , therefore requires us to be able to describe the electromagnetic field at all points interior to and exterior to the particle. In order to perform this calculation, we imagine that the particle is made up of infinitesimally small regions each of which is approximated as a dipole in the presence of an applied oscillating field (i.e. an incident electromagnetic photon). The strength of the applied electromagnetic field affects that strength of the response by each of the dipoles and thus of the dust grain as a whole. The relationship between this response and the induced field is determined by the material, which is described for this purpose by the complex refractive index

$$m(\lambda) = n(\lambda) + ik(\lambda) \quad (1.1)$$

where  $n(\lambda)$  and  $k(\lambda)$  are the real and the imaginary parts of the complex refractive index. Broadly speaking,  $n$  may be considered to describe the scattering component of the complex refractive index and  $k$  the absorptive component. These optical properties are the starting point to solving Maxwell's equations inside and outside of the particle and thus calculating the scattering and absorption cross-sections.

### 1.1.5 Mie Theory

Whilst relatively simple approximations to this calculation exist in the regime where the scattering particle is substantially smaller than the wavelength (the Rayleigh regime), for particles which are of a similar size to the wavelength of the incident radiation, the calculation is a complex one. The full solution to Maxwell's equations in this case was first described by Gustav Mie in 1908 (Mie 1908). The Mie solution has wide application to a number of fields ranging from the study of interstellar dust to plasmonics. Mie himself developed his approach in order to better understand the colourful effects of a colloidal gold solution. The nature of Mie's solution meant that it was not widely used until many years after its initial publication, when computing power had reached a stage capable of computing the infinite series expansions on which the solution depends.

In this section, I will discuss the key results that allow for the calculation of the scattering and absorption efficiencies that are crucial for modelling the effects of dust on electromagnetic radiation. Much of this mathematics is somewhat dense and I will therefore restrict my discussion to the most relevant points. An outline of the derivation of the Mie solution to Maxwell's equations is given in Appendix A. For further details and an unusually lyrical description of the relevant physics and mathematics please see Bohren & Huffman (1983), on which the majority of this section is based.

The Mie solution to Maxwell's equations applies only to spherical particles although there are extensions to more complex morphological distributions such as the “T-matrix method” and the “Discrete Dipole Approximation” (Mishchenko et al. 2002; Draine & Flatau 2004)). For my models, the wavelength of the monochromatic line to be modelled is very often of a similar order of magnitude to the grain radius and as such the full Mie solution must be implemented.

For a single spherical particle, the scattering cross-section of interaction is defined to be the net rate at which electromagnetic energy is scattered across the surface of the particle divided by the total irradiance of the incident beam (i.e. the rate at which energy falls onto the surface). The extinction cross-section is similarly defined.

For a spherical particle of radius  $a$  and an incident beam of wavelength  $\lambda$ , we may define the size parameter

$$x = \frac{2\pi Na}{\lambda} \quad (1.2)$$

where  $N$  is the complex refractive index of the surrounding medium. Assuming the particle to be surrounded by a vacuum such that  $N = 1$ , we can show that the scattering coefficients are given by

$$a_n = \frac{m\psi_n(mx)\psi'_n(x) - \psi_n(x)\psi'_n(mx)}{m\psi_n(mx)\xi'_n(x) - \xi_n(x)\psi'_n(mx)} \quad (1.3)$$

$$b_n = \frac{\psi_n(mx)\psi'_n(x) - m\psi_n(x)\psi'_n(mx)}{\psi_n(mx)\xi'_n(x) - m\xi_n(x)\psi'_n(mx)} \quad (1.4)$$

where  $m$  is the complex refractive index of the particle and a prime denotes differentiation with respect to the argument in parentheses. The scalar functions  $\psi_n$  and  $\xi_n$  are the

Riccati-Bessel functions and are given by

$$\psi_n(\rho) = \rho j_n(\rho), \quad \xi_n(\rho) = \rho h_n^{(1)}(\rho) \quad (1.5)$$

where  $j_n$  and  $h_n^{(1)}$  are the spherical Bessel functions of the first and second kind. The scattering coefficients can then be used to calculate the scattering and extinction cross-sections of interaction:

$$C_{sca} = \frac{2\pi}{k^2} \sum_{n=1}^{\infty} (2n+1)(|a_n|^2 + |b_n|^2) \quad (1.6)$$

$$C_{ext} = \frac{2\pi}{k^2} \sum_{n=1}^{\infty} (2n+1)\text{Re}\{a_n + b_n\} \quad (1.7)$$

For a single spherical particle of radius  $a$ , the scattering and extinction efficiencies are related to the above quantities via

$$Q_{ext} = \frac{C_{ext}}{\pi a^2}, \quad Q_{sca} = \frac{C_{sca}}{\pi a^2} \quad (1.8)$$

The above solution has the primary drawback of only being applicable to spherical particles. Obviously, the adoption of this solution presents a potential issue for a medium of dust grains that may well be crystalline, fluffy or extremely amorphous. However, despite its limitations, Mie theory does provide a first-order description of the optical effects of non-spherical particles. DAMOCLES adopts the Mie theory solution to Maxwell's equations in order to calculate scattering and absorption efficiencies. In the future, when alternative morphologies may be considered, the algorithm may be extended to alternative solutions in order to address this limitation (e.g. the Discrete Dipole Approximation and the T-matrix method mentioned above). Similarly, the above solution applies only to a single particle. Various weighted summations must be performed over the scattering and extinction cross-sections in order to treat a medium of multiple different grain sizes and species. This is discussed in further depth in Sections 2.2.3 and 4.3.6.

### 1.1.6 Dust in Absorption

We may relate the frequency-dependent extinction cross-section to the opacity  $\kappa_\nu$  of the dusty medium via

$$\kappa_\nu \rho = C_{ext,\nu} n_d \quad (1.9)$$

where  $n_d$  is the number density of the dust,  $\rho$  is the mass density and  $\nu$  is the frequency. The opacity determines the fraction of radiation that is absorbed when a beam of given frequency travels through the medium. The intensity of the beam after having travelled a distance  $x$  is given by

$$I(x) = I_0 e^{-\kappa_\nu \rho x} \quad (1.10)$$

for a medium with constant density  $\rho$  and initial intensity  $I_0$ . This relationship is clearly central to understanding the effects of dust absorption on line profiles emitted in the ejecta of CCSNe. However, it applies to any dusty environment. The key to our current understanding of the properties of dust was the investigation of its attenuating effects in the ISM.

By considering the reddening and attenuation of starlight from background stars, Bless & Savage (1972) determined the first section of the interstellar extinction curve from  $0.11\mu\text{m}$  to  $2.15\mu\text{m}$ . Eventually, further observations would allow for the variation of interstellar extinction to be determined across the full wavelength range (Rieke & Lebofsky 1985). It was found that dust in the ISM is most strongly attenuating at shorter wavelengths and its extinction efficiency decreases towards the IR, with a noticeable bump at around  $2175\text{\AA}$  (see Figure 1.2). In 1989, Cardelli, Clayton & Mathis postulated that not only was the total interstellar extinction (from the UV to the NIR) independent of the line-of-sight to the background stars, but that it could be entirely characterised by the quantity

$$R_V = \frac{A_V}{A_B - A_V} = \frac{A_V}{E(B - V)} \quad (1.11)$$

$A_V$  and  $A_B$  represent the extinction in the V- and B-bands respectively. The quantity  $R_V$  is known as the *total-to-selective* extinction. The extinction in the ISM can generally be described by  $R_V \approx 3.1$  whilst denser regions such as some molecular clouds are described by

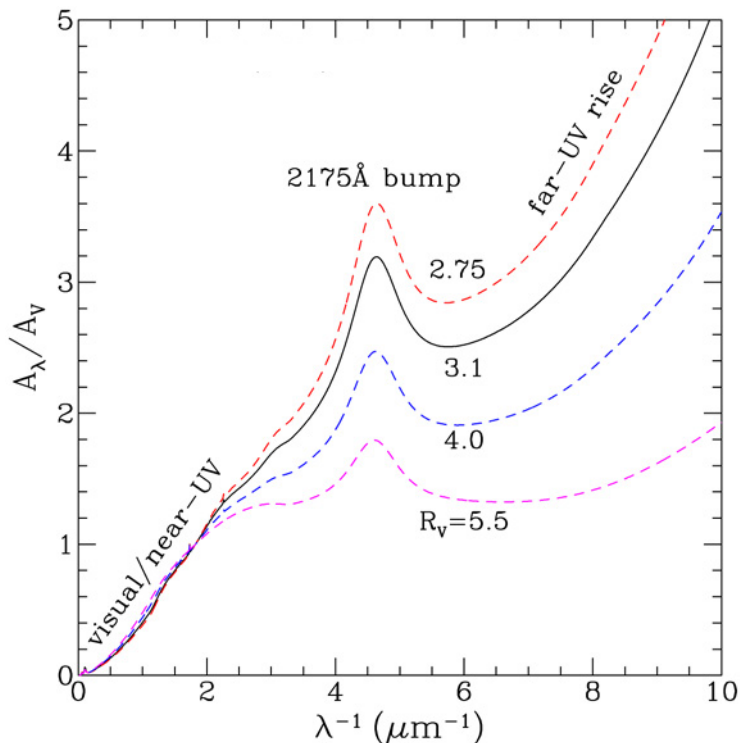


**Figure 1.2.** Extinction curves for different values of  $R_V$  across the UV, optical and IR based on the parametrisation by Cardelli et al. (1989) . The bump at 2175Å can be clearly seen in all curves.

$R_V \approx 5$ . Properties of the ISM extinction curve, such as the strong absorption feature seen at around  $10\mu\text{m}$ , allowed Mathis, Rumpl & Nordsieck (1977) to determine the composition and grain size distribution of dust in the ISM. They attributed the  $10\mu\text{m}$  absorption feature to silicates and found that a grain size distribution  $n(a) \propto a^{-3.5}$ , with graphite grains distributed between  $0.001 < a < 1\mu\text{m}$  and silicate grains distributed between  $0.025 < a < 0.25\mu\text{m}$ , would reproduce the extinction curve. This grain size distribution has become known as the “MRN” distribution as a result.

### 1.1.7 Dust in Emission

Energy absorbed by dust grains in the optical and UV causes the dust to be heated. Warm dust emits continuum radiation in the near- to mid-IR and cool dust emits in the far-IR and sub-millimetre (sub-mm). For dust that is in local thermodynamic equilibrium in an optically thin environment, the continuum emission from the dust,  $F_\nu$ , is proportional to

---

the temperature-dependent blackbody spectrum,  $B_\nu(T)$  (Hildebrand 1983):

$$F_\nu \propto \kappa_\nu B_\nu(T) \quad (1.12)$$

This expression determines the temperature dependence of dust grains with a given opacity. Using this dependence, it is possible to fit theoretical SEDs to observed photometric data in the IR and sub-mm in order to derive various properties of the emitting dust, such as the dust mass and composition.

In addition to its continuum emission, dust also has a number of spectroscopic emission features. These features allow the composition of dust in a given region to be probed more directly than is possible using SED fitting. A detailed discussion of the spectroscopic features of a variety of dust species ranging from silicates to ices is given by Draine (2003).

### 1.1.8 Dust as a Scatterer

Dust's role as a scatterer is rarely considered and has few observable signatures. However, it gives rise to some particularly unusual and interesting features in the fast moving environments of supernovae. As shall be discussed in detail throughout this thesis, dust scattering can result in significant, possibly asymmetrical broadening of emission lines. It can cause an effect known as a “light echo”. This is when light emitted from an object is reflected off a surrounding dusty region, such as a dense circumstellar shell, back towards the observer. Observing light echoes allows astronomers to see the state of an object in the past and therefore to understand its evolution. Analysis of light echoes from Cassiopeia A (Cas A) allowed its age and type to be determined (Krause et al. 2008) and the circumstellar environment of SN 1987A was investigated using light echoes as well (Sugerman et al. 2005). Whilst light echoes can provide much insight into the past, they can also present a problem for current observations. When observing supernovae, it is important to determine whether observations are of the current state of the object or a previous one.

### 1.1.9 Radiative Transfer in Dusty Media

In Section 1.1.6, I discuss the effect of dust absorption on an incident beam of radiation. In general, the calculation of the emergent radiation field given an incident field on a dusty medium is not a straightforward one. This calculation is dependent on the *equation of radiation transfer*. This equation defines the relationship between an incident beam of

radiation and the emergent beam dependent on the properties of the medium through which it is passing. Mathematically, it is given by

$$\frac{dI_\nu}{ds} = \rho\kappa_\nu I_\nu + \rho j_\nu \quad (1.13)$$

where  $\nu$  is the frequency of the beam and  $I_\nu$  is the intensity of the beam. The quantity  $j_\nu$  is the emission coefficient per unit mass and determines the radiated emission. The quantity  $s$  represents distance and as such  $\frac{dI_\nu}{ds}$  is the rate of change of the intensity of the beam with distance. All other quantities are as previously defined. The first term in Equation 1.13 represent the absorption by the dust and the second term represents emission along the line  $ds$ , as well as light that is scattered into the path of the beam.

In certain cases, this equation can be solved analytically. However, for general cases and particularly for complex 3-dimensional geometries, it is best solved using numerical codes that model the transfer of radiation. There exist a great many radiative transfer codes written using Monte Carlo methods and I will discuss this approach in detail at the start of the next chapter.

Whilst DAMOCLES does indeed model the transfer of radiation, certain facets of the models, namely the narrow wavelength range that is considered and the assumption of the temperature-independence of dust extinction, simplify the problem greatly and therefore detailed consideration of the processes involved in solving Equation 1.13 are omitted.

## 1.2 Core-Collapse Supernovae as Dust Factories

In an effort to explicate the motivations behind studying dust, I have so far mostly limited my discussion to the evolution, properties and physics of dust after the initial stages of its formation. The most current and contentious debate, however, is over the natal environment of dust grains.

Supernovae are the violent explosions that are the death of stars. They evolve very quickly and create extreme conditions. Focus on supernovae as a possible source of dust in the universe has been motivated by the physical conditions that they produce shortly after their outbreak and by the presence of large quantities of heavy elements that constitute the integrant ingredients of dust grains.

### 1.2.1 Origins of Dust in the Universe

Over the past two decades, several high redshift galaxies and quasars (QSOs) have been found to contain significant masses of dust as evidenced by the detection of red-shifted dust emission at sub-millimetre wavelengths (Carilli et al. 2001; Omont et al. 2001; Bertoldi & Cox 2002; Bertoldi et al. 2003; Watson et al. 2015). Warm dust masses ( $T \sim 50K$ ) inferred from these observations are of the order of  $10^8 M_\odot$  at very early epochs  $z \gtrsim 6$  (Robson et al. 2004; Beelen et al. 2006; Dwek et al. 2007). A dusty, evolved galaxy has even been found to have existed during the epoch of reionization at  $z = 7.5$  when the universe was only about 500 Myr old (Watson et al. 2015). The presence of such large quantities of dust at such an early stage of the universe's evolution presents a significant challenge to astronomers to find a source.

Until these recent observations, Asymptotic Giant Branch (AGB) stars were thought to be the dominant source of dust in the universe. AGB stars are evolved stars with stellar masses in the range  $0.85M_\odot \lesssim M_* \lesssim 8M_\odot$ . These stars have reached a stage of evolution that is characterised by separate shells of hydrogen and helium burning surrounding a dense carbon-oxygen core. They are extremely luminous ( $> 10^3 L_\odot$ ) and have strong winds that can cause the star to lose up to 70% of its mass resulting in the formation of an extended circumstellar envelope (Wood et al. 2004b). It is in these regions that conditions are thought to be appropriate for dust formation and this process has been studied in the environment of AGB stars by many authors (e.g. Gail & Sedlmayr (1999); Cherchneff (2000); Ferrarotti & Gail (2005)). The theory has been confirmed on numerous occasions by observations of dust in these objects (Meixner et al. 2006; Matsuura et al. 2009; Sloan et al. 2009; Boyer et al. 2011, 2012; Riebel et al. 2012; Matsuura et al. 2013)). Theoretically, AGB stars may be capable of producing as much as  $0.04M_\odot$  of dust for a narrow range of stellar masses around  $4M_\odot$  (Ferrarotti & Gail 2006). For a wider range of progenitor masses they are predicted to produce a typical dust mass of  $0.001M_\odot$ . However, it is unlikely that enough low-intermediate mass stars, which take around 0.1-10Gyr to reach the AGB (Salaris et al. 2014) and likely formed around  $z \lesssim 20$  with the star formation rate (SFR) peaking at  $z \sim 5$  (Greif & Bromm 2006), had enough time to reach the AGB stage of their evolution. The few higher mass stars that may have done likely cannot have contributed significantly to the large dust masses seen at very early epochs. In addition to this, local metal-poor galaxies contain more dust than can

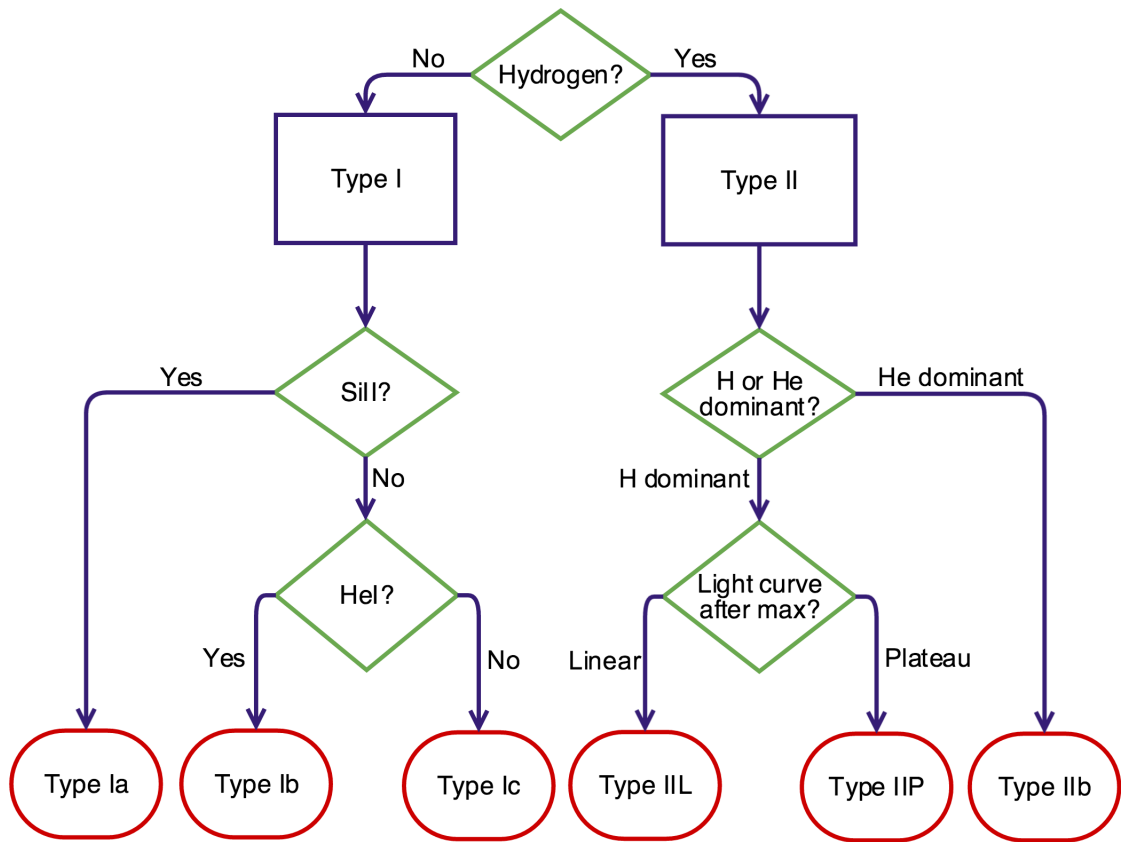


**Figure 1.3.** A flowchart summarising the supernova classification scheme

be accounted for by dust formation in AGB stars alone. In fact, it has been shown that AGB stars are likely to contribute only about 1.6% of the  $2 \times 10^8 M_{\odot}$  of dust observed in the galaxy J114816.64+5251 at  $z = 6.4$  (Dwek et al. 2007; Matsuura et al. 2009, 2013). Such evidence has been used to rule out the possibility that AGB stars could account for the dust masses observed in the early universe (Michałowski 2015).

CCSNe are one of the few potential sources that could contribute large quantities of dust at early epochs. With the probable elimination of the theory that AGB stars were a significant source of dust at high redshifts, attention is now strongly focussed on determining whether dust formation in CCSNe could resolve the dust mass dilemma at high redshifts.

### 1.2.2 Types of Supernovae

Supernovae may be classified into a number of different types. They are bisected initially into Types I and II according respectively to the absence or presence of hydrogen in their

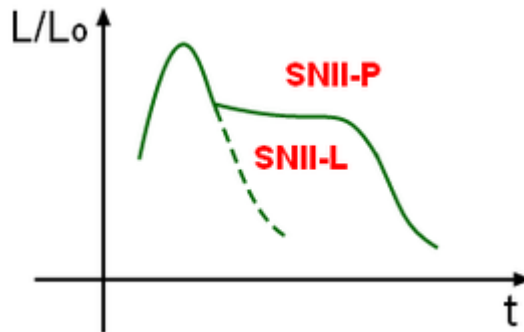


**Figure 1.4.** Illustration of the different shapes of light curves for Type IIP and Type IIL supernovae.

early spectra. Further sub-classifications depend on other features in the early spectra, properties of later spectra and the evolution of the light curve after maximum light. A summary of the supernova classification scheme is presented in Figure 1.3.

If the initial classification is Type I then all further sub-classifications depend solely on the properties of the early spectra (a few days after explosion) as detailed in Figure 1.3. Type II supernovae are somewhat more complex in their categorisation. After classification as a Type II, further subdivisions depend on the dominance of hydrogen or helium in *later* spectra. Helium dominant supernovae are classified as Type I Ib and hydrogen dominant supernovae are classified as either Type IIL (those which have a linearly decaying light curve after maximum light) or Type IIP (those that exhibit a plateauing light curve after maximum light) as illustrated in Figure 1.4. Type IIn supernovae are omitted from the summary presented in Figure 1.3 as they cannot be classified straightforwardly via a bifurcating process. Type IIn supernovae will generally have strong emission lines, particularly hydrogen lines, often with complex profiles. Crucially, the spectra of Type IIn supernovae do not exhibit the broad absorption features frequently seen in other types and instead contain narrow lines (hence Type IIn).

### 1.2.3 From Massive Stars to Remnants

It is generally accepted that the progenitors of Type Ia supernovae are white dwarfs that exist in a binary system with another star (Wang & Han 2012). The accretion of material from one star to another results in a thermonuclear explosion, a mechanism that is unique to Type Ia supernovae. There have not been any observations suggestive of ejecta-condensed dust forming in the aftermath of a Type Ia supernova and I therefore do

not consider these objects any further, focusing my attention solely on supernovae that explode via the core-collapse mechanism.

Broadly, this process is initiated when a massive star ( $\geq 8M_{\odot}$ ) starts to fuse heavier elements. The fusion of ever heavier elements generates increasingly less energy whilst also causing the mass of the core to increase. Eventually, radiation pressure drops sufficiently that the core can no longer support itself against its own self-gravity and begins to collapse rapidly. Within milliseconds, the core reaches extremely high densities and, when it can no longer condense further, “bounces” off itself causing an immense shockwave to propagate outwards and a vast quantity of energy to be released via the expulsion of neutrinos. Much of this complex process is still poorly understood and interesting models are currently being produced recreating these very early stages using a numerical approach (Hammer et al. 2010; Takiwaki et al. 2014; Wongwathanarat et al. 2015). Though the explosion mechanisms of CCSNe are largely beyond the scope of my work, some attention will be paid to these models later in this thesis since instabilities that arise in these early stages can influence the structure of the ejecta at later stages of its evolution.

For many years after the explosion, the supernova (now a remnant) is in the free-expansion phase (Landau & Lifshitz 1959; Ostriker & McKee 1988). During this phase, the mass and velocity of the expanding supernova massively exceed those of the surrounding medium, fortuitously allowing the behaviour of the SNR to be analysed as if it were expanding into a vacuum. The shock radius during this phase may therefore be calculated simply as  $R_s = v_s t$ . As the shockwave propagates through the ISM, interstellar material that has been compressed by the forward shock begins to accumulate. At the same time a reverse shock wave begins to propagate back through the ejecta. It is during this phase, which arises very soon after the initial explosion and typically lasts for a few hundred years, that the physical conditions in the ejecta are thought to be optimal for dust formation. The phase ends when the mass of material ahead of the forward shock is of a similar magnitude to that behind and the mathematical treatment of its behaviour must be altered as it enters the Sedov-Taylor phase.

#### 1.2.4 Energetics in Core-Collapse Supernovae

There are three different sources of energy in most supernovae. Each of these emerges from the supernova in different forms over different timescales. Initially, the most obvious energy source is that of the initial gravitational collapse which results in a huge emission

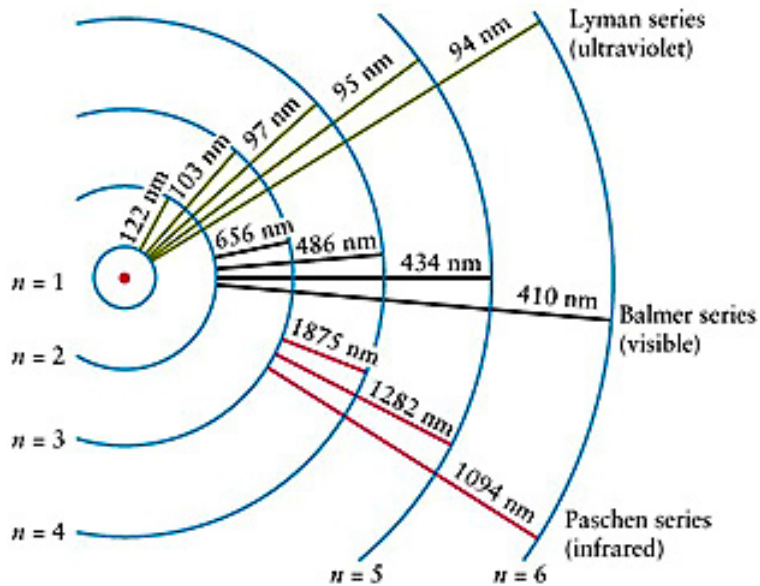


**Figure 1.5.** Illustration of the Lyman, Balmer and Paschen series of transitions in hydrogen.

of energy in the form of neutrinos and lasts for just a few seconds.

The next source of energy to become apparent is that of the radioactive decay of unstable isotopes in the debris. As these isotopes decay they produce gamma rays that Compton scatter off bound electrons. This produces a population of fast, primary photoelectrons that cause further ionisations and excitations and produces a family of slower secondary electrons. As these electrons recombine with ions and atoms become de-excited they emit monochromatic photons that we observe as line emission largely in the optical and IR. For example, the Balmer and Paschen series of hydrogen lines is often prominent in the spectra of CCSNe (see Figure 1.5).

Finally, over much longer timescales, the kinetic energy of the expanding debris will emerge as radiation when it impacts the surrounding material. This impact will propagate a reverse shock inwards through the ejecta and gas between the forward and reverse shocks will be heated and will therefore radiate its thermal energy as X-rays. This stage of the energetics is likely coincident with the supernova remnant entering the Sedov-Taylor phase and so will usually only occur after several centuries.

### 1.2.5 Dust Formation and Destruction in CCSNe

The initial formation of dust grains requires high densities and low temperatures. Although dust grains can grow via the accretion of individual atoms in the interstellar medium, various theoretical and experimental models indicate that dust grains cannot initially form via this process due to the low densities present (Osterbrock & Ferland 2006). There are two primary theories for the formation of dust grains. It was originally thought that the formation of dust grains resulted from the stochastic process of classical nucleation whereby particles coalesce to form the seeds of dust grains. These seeds become the nucleation sites from which grains are ultimately born through the aggregation of further particles. Various models of dust formation in the ejecta of CCSNe have used this approach (Kozasa et al. 1989; Todini & Ferrara 2001; Nozawa et al. 2003; Schneider et al. 2004).

More recently, several models of dust formation in CCSNe that consider the effects of chemistry on the growth of dust grains have been published. These models consider the chemical composition of the gas and include chemical reaction rates thereby considering the manner in which molecular evolution influences dust grain formation and growth rates (Cherchneff & Dwek 2009, 2010; Sarangi & Cherchneff 2013; Sarangi & Cherchneff 2015).

Models using both methods have predicted dust masses of the order of  $0.1\text{-}1M_{\odot}$  of dust forming within the ejecta of CCSNe of progenitor masses between  $12\text{-}40M_{\odot}$  within the first few years after the initial explosion. Regardless of the quantities of dust that are initially produced in the ejecta of SNe, the key question is what fraction of the dust that forms survives to enter the interstellar medium at later times. Dust grains can be destroyed by a number of different processes. Of primary interest is a process known as “sputtering”: collisions between dust grains and ions in a nebula can result in atoms or molecules being ‘knocked off’ the surface of the grain. Conditions for sputtering to occur are ideal near a shock-front (Barlow & Silk 1977) and it is therefore predicted that the passage of the reverse-shock back through the ejecta of a CCSN results in dust grains becoming fragmented into smaller grains or being destroyed entirely. Understanding the initial grain size distribution and mass of the newly-formed dust in the ejecta is therefore extremely important to determining whether CCSNe are in fact a significant source of dust in the universe.

### 1.2.6 The Four Signatures of Dust

The presence of dust in the ejecta of CCSNe can be indicated by four main signatures:

#### A decrease in the light curve

As the dust begins to form in the ejecta, UV and optical light is absorbed by the dust causing a decrease in the light curve at these wavelengths.

#### Excess IR emission

An increase in emission in the IR occurs contemporaneously with the decrease in the UV-optical light curve. A thermal MIR excess is caused by warm dust and an excess in the far-IR and sub-mm is the result of cold dust. The increase in emission in these wavelength can be caused by newly-formed dust condensing in the ejecta but can also be a result of the illumination of pre-existing dust

#### Blue-shifted line profiles

The onset of the formation of dust can cause an asymmetry in line profiles in the optical and IR. The absorption and scattering of optical or near-IR radiation by newly-formed dust within the ejecta can result in an asymmetry between the red and blue shifted components, with redwards emission from the far side of the ejecta undergoing greater absorption and resulting in an overall shift of the profile to the blue.

#### Polarised dust emission

The expansion of a CCSNe is often somewhat asympmetrical and dust grain shapes are likely not spherical in shape. Both of these factors can cause the emission from dust grains in the ejecta of supernovae to be highly polarised. Analysis of the degree and orientation of the polarised emission can provide insight into the distribution and mass of the emitting dust.

All four of these signatures have been discussed in detail over the timeline of this subject (e.g. Gomez (2013)) but the focus has largely been on using the excess IR emission seen in the SED of CCSNe to determine quantitatively dust masses in these objects.

### 1.2.7 The Dust Mass Debate

The formation of dust grains requires densities high enough for interaction between particles to take place, but temperatures that are cool enough to allow the grains to form and survive. The theory that the ejecta of a CCSN in its free-expansion phase could provide these conditions was first hypothesised by Cernuschi et al. in 1967 and they have now long been thought to be potential dust factories (Hoyle & Wickramasinghe 1970; Kozasa et al. 1991; Todini & Ferrara 2001; Nozawa et al. 2003). The ejecta cools rapidly as it expands and there is an abundance of heavy elements. In order to account for the large masses of dust seen in the early universe, it is estimated that CCSNe would need to produce 0.1-1.0  $M_{\odot}$  of dust per CCSN (Morgan & Edmunds 2003; Dwek et al. 2007)

Until recently, supernovae had been largely dismissed as a significant source of dust. Observations over the last decade at mid-infrared (MIR) wavelengths of warm dust (200 - 450K) emission from CCSNe had suggested that the quantities of ejecta-condensed dust produced during the first 1000 days were typically  $\leq 10^{-3} M_{\odot}$  (Sugerman et al. 2006; Meikle et al. 2007; Kotak et al. 2009; Andrews et al. 2010; Fabbri et al. 2011). This is much less than theoretical models predict (see Section 1.2.5) and would not account for the dust masses observed in the early universe. These observations indicated the need to find another early-time source of dust.

#### Cassiopeia A

In 2003, however, the field was shaken by the report that  $2-4 M_{\odot}$  of cold dust (20K) had been detected via sub-mm emission in the 300-year old SNR Cassiopeia A (Cas A) using the Sub-millimetre Common-User Bolometer Array (SCUBA) (Dunne et al. 2003). A heated debate followed as astronomers contested the source of the observed dust. Dunne et al. (2003) had concluded that the dust was associated with the remnant based on the high spatial correlation of the sub-mm emission from the cold dust and the forward and reverse shocks that were traced via X-rays. Krause et al. (2004) refuted this suggestion using analyses of the line emission and absorption to conclude that the dust was in fact located in clouds along the line of sight to the remnant. A determination was sought by considering the polarisation of the dust emission. As discussed in the previous section, the asymmetric nature of expansion likely results in a degree of polarisation relative to stationary dust located in the ISM. Observations of Cas A in the sub-mm were made

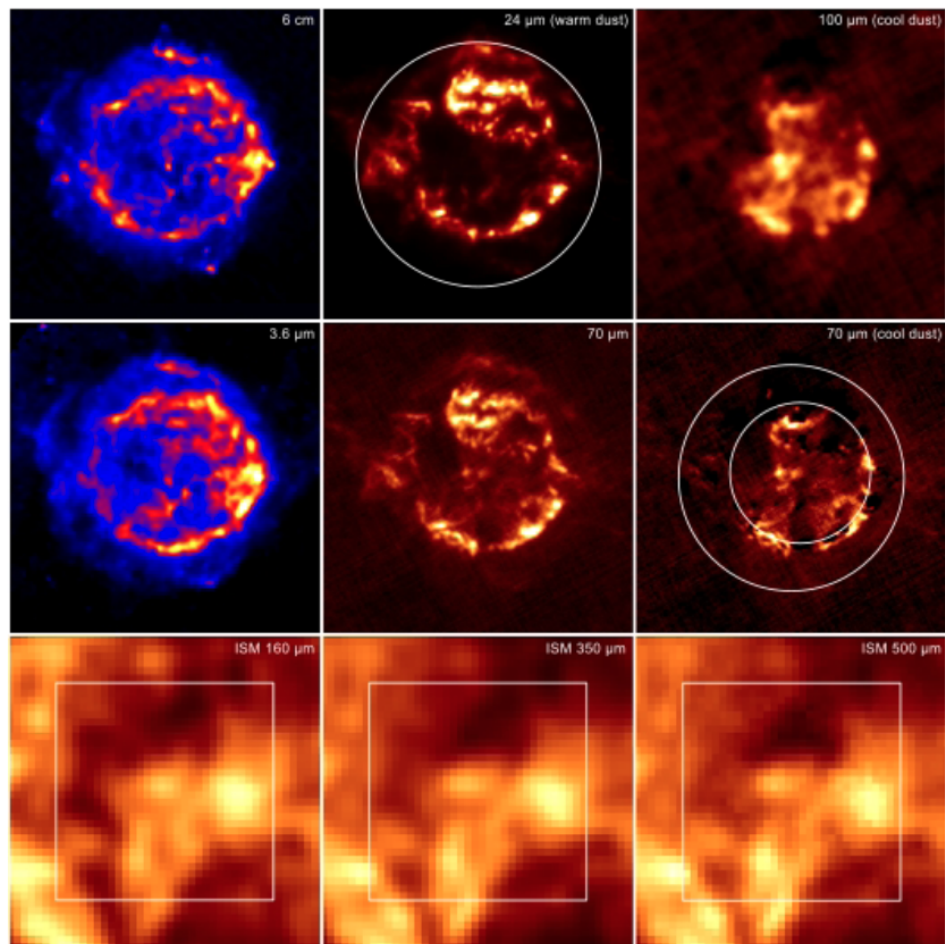


**Figure 1.6.** Images of Cas A at IR, sub-mm and radio wavelengths. The top six images are 7' on a side and the bottom three are 10' on a side. The inner and outer circles in the middle-right image correspond to the reverse and forward shocks respectively according to (Gotthelf et al. 2001). Image taken from Barlow et al. (2010).

using the SCUBA polarimeter and the emission was found to be extremely polarised to a fraction of 30% (compared to typical ISM fractions of 2-7%). A reevaluation of the dust mass based only on the polarised emission still estimated the mass of dust in Cas A to be  $1M_{\odot}$  (Dunne et al. 2009).

Even this revised estimate was still uncomfortably large compared to previous estimates. Sadly, SCUBA was taken offline shortly after this observation and so follow-up observations of Cas A and other remnants using SCUBA were not possible. It was only with the advent of the *Herschel* mission that the presence of cold dust in SNRs could again be investigated via emission in the sub-mm. These *Herschel* observations have, somewhat surprisingly for many in the field, consistently revealed dust masses of the order of 0.1-

$1.0M_{\odot}$  in a number of SNRs.

As the first result of its kind, and with a great many questions left unanswered, it was crucial to establish the dust mass in Cas A as conclusively as possible. Observations of Cas A using *Spitzer* detected emission from warm dust between  $24\mu\text{m}$  -  $70\mu\text{m}$ , analysis of which established a dust temperature of 60 - 120K and a dust mass of  $0.02$  -  $0.054M_{\odot}$  (Rho et al. 2008). Subsequent observations using *Herschel* detected a cool dust component of  $0.075M_{\odot}$  giving a total dust mass in Cas A of  $0.1M_{\odot}$  (Barlow et al. 2010). Like many *Herschel* observations, it is difficult to conclusively determine the location of the dust as within the remnant rather than in clouds in the foreground or background. Images of Cas A across a range of wavelengths are presented in Figure 1.6.

### The Crab Nebula

The Crab nebula was first detected by Chinese astronomers in 1054. A pulsar at the heart of the nebula illuminates the surrounding gas and dust and provides a rare opportunity to probe dust masses in a centuries old remnant. Unlike Cas A, the Crab does not have contaminating clouds of dust in its foreground and background ensuring that any detections of dust from this location are likely to be associated with the remnant.

*Spitzer* and *Herschel* observations have been made of this remnant and both have detected dust in the ejecta. *Spitzer*, however, only detected  $2.4 \times 10^{-3}M_{\odot}$ . Further spectroscopic and photometric observations with *Spitzer*, *Herschel* and Planck allowed the full range of the SED to be investigated and allowed for synchrotron and line emission to be well-characterised. Subtracting this from the continuum observations yielded two dust components, a warm component at 63K estimated to have a mass of  $\sim 10^{-3}$  and a cool component at 34K with an estimated mass of  $0.1$  -  $0.2M_{\odot}$  (Gomez et al. 2012; Temim et al. 2012). As might be expected, the dust is predominantly co-located with the gas in dense filaments (see Figure 1.7).

These dust masses were based on a two-component dust fitting. Further analyses and models of these results have resulted in revised estimates of the mass of dust in the Crab nebula. Multi-component fitting with multiple grain sizes by Temim & Dwek (2013) gave rise to a dust mass estimate of  $0.02$ - $0.13M_{\odot}$ , consistent with the lower end of the previous estimate. However, recent radiative transfer models by Owen & Barlow (2015) that account for varying grain size distributions, gas geometries and a more realistic heating source derive dust masses consistent with the estimated  $0.1$  –  $0.2M_{\odot}$  of Gomez

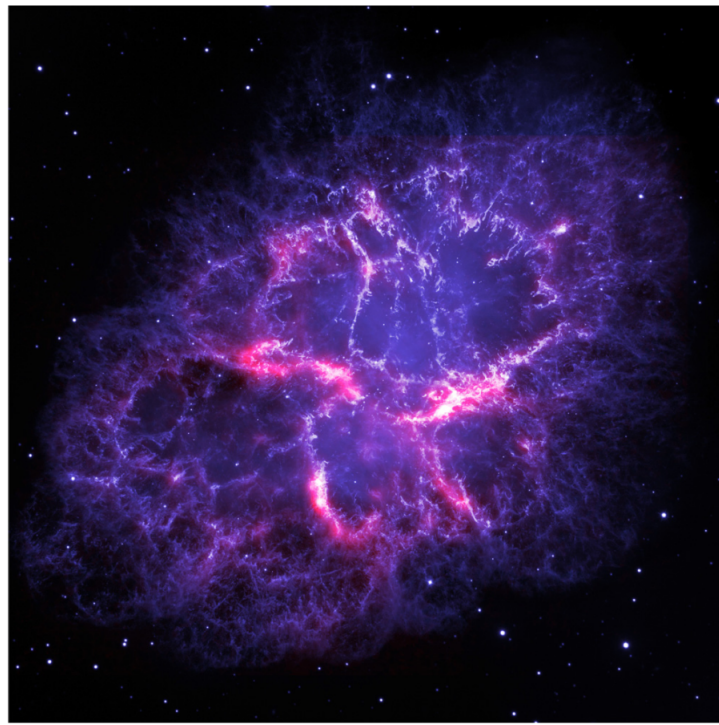


**Figure 1.7.** Composite image of the Crab nebula using Hubble Space Telescope (HST) optical line emission data (blue-white) and *Herschel* 70 $\mu\text{m}$  dust emission (red) illustrating the close alignment between the optical knots and filaments. Credits: Oli Usher (UCL); *Herschel Space Observatory*, *Hubble Space Telescope*: ESA, NASA. Image taken from Owen & Barlow (2015).

et al. (2012). If the dust in the ejecta is assumed to be clumped however, as is likely more realistic, then  $0.4 - 0.6 M_{\odot}$  of amorphous carbon grains are required to fit the SED. At this time, the Crab nebula was the only object to have provided a clean view of large masses of dust ( $> 10^{-3} M_{\odot}$ ) in a SNR .

### SN 1987A

Perhaps the most critical discovery however, was that of dust in the ejecta of SN 1987A. This object is uniquely helpful in the study of supernovae due its location only  $\tilde{50}\text{kpc}$  away. Dust had long been theorised in the ejecta of SN 1987A but only in comparatively small quantities. Observations of blue-shifted line profiles in the optical and of warm dust emission in the MIR confirmed this hypothesis with dust mass estimates of  $5 - 20 \times 10^{-4} M_{\odot}$  forming in the first 1000 days(Lucy et al. 1989; Roche et al. 1989; Bouchet et al. 1991; Wooden et al. 1993; Ercolano et al. 2007). In 2010, this view was fundamentally altered by observations by *Herschel* that indicated the presence of  $0.4 - 0.7 M_{\odot}$  of cold dust. Further

observations with *Herschel* and the Atacama Large Millimetre Array (ALMA) not only confirmed this dust mass estimate but also had sufficient spatial resolution to conclusively determine the origin of the cold dust emission as from within the ejecta (Matsuura et al. 2011; Indebetouw et al. 2014; Matsuura et al. 2015). Recent modelling of the evolution of the SED has estimated similar masses of cold dust to form in the ejecta of SN 1987A with the majority of the dust forming after 1000 days (Wesson et al. 2015).

This object is crucial to the field and is a central focus of this thesis. I have therefore only elucidated the key points above and will give a considerably more detailed synopsis of the story of SN 1987A at the start of Chapter 4.

These recent *Herschel* far-IR and sub-mm observations of several SNRs have revealed cold dust masses as high as  $0.2 - 0.8M_{\odot}$ . These discoveries have resulted in a re-evaluation of the rate of dust production by CCSNe and a renewed focus on these objects as sources of dust.

However, there remain a large number of outstanding challenges to consider. Firstly, there are still only a very small number of supernovae that have been observed to have sizeable masses of dust present in their ejecta. If further CCSNe were also shown to have formed large quantities of dust then the already shifting opinion might start to become consensus. Other points to consider regarding dust formation and evolution in CCSNe include the nature of the dust (composition, grain size, grain shape etc.) which is still largely unclear, as is the extent to which it is destroyed or sputtered after its initial formation. Related to these issues is the uncertainty of the dust formation rate in the ejecta and the issue of where this formation takes place. These are all interesting questions that call out for answers.

### 1.2.8 Observations of Dust-Affected Asymmetric Line Profiles

The *Hershel* dust mass estimates were based on fitting dust SEDs that peaked at far-IR wavelengths. Unfortunately, following the end of the *Herschel* mission in 2013, there is likely to be a long wait for far-IR facilities with comparable or better sensitivities than *Herschel* to become available. Without data, this methodology is temporarily ineffectual. This has provided an incentive to make use of alternative methods to estimate the dust masses that form in supernova ejecta.

As discussed in Section 1.2.6, there is more than one way of tracing dust formation

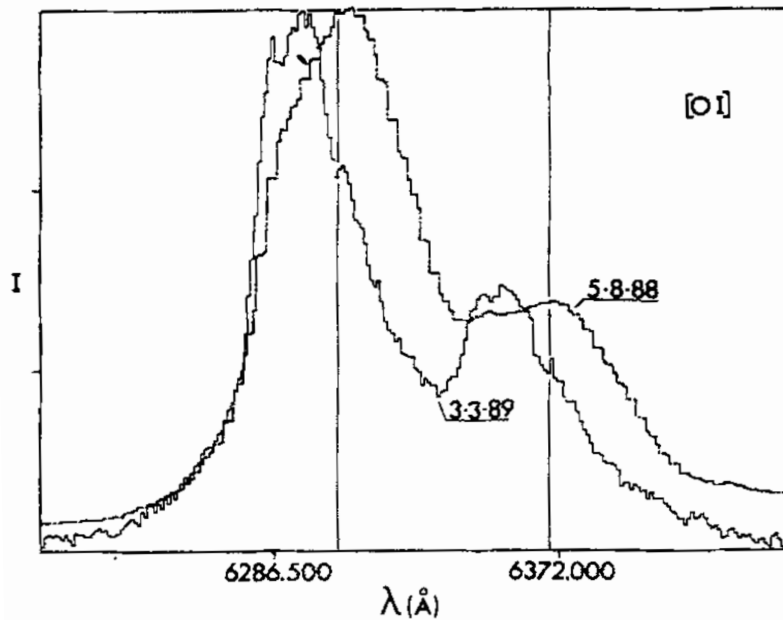


**Figure 1.8.** The emission profile of  $[O\text{ I}]\lambda 6300,6363\text{ \AA}$  from SN 1987A on 5 August 1988 (day 529) and 3 March 1989 (day 739) showing the strong blue-shift by  $\sim 600\text{ km s}^{-1}$  of the latter profile. The profiles are scaled to the same peak intensity for the violet component. The image is taken from Lucy et al. (1989).

in the ejecta of supernovae. In 1989, Lucy et al. identified a progressive blue-shifting of the  $[O\text{ I}]\lambda 6300,6363\text{ \AA}$  doublet from SN 1987A between days 529 and 739 after outburst, with the doublet in the later spectrum being blue-shifted by  $\sim 600\text{ km s}^{-1}$  (see Figure 3.5). Since then, such red-blue asymmetries have been frequently observed in the late-time ( $> 400$  days) spectra of supernova ejecta .

Numerous telescopes have recorded spectra of CCSNe in the optical and IR, some with extremely high resolution. The Anglo-Australian Telescope (AAT), the Cerro Tololo Inter-American Observatory (CTIO), the Hubble Space Telescope (HST) and the Very Large Telescope (VLT) have all observed several supernovae in the optical including SN 1987A. Other telescopes such as the two Gemini Multi-Object Spectrographs (GMOS) have also taken spectra of numerous CCSNe. As a result of observations with these telescopes, numerous CCSNe have been observed to exhibit the blue-shifted line profiles indicative of dust formation in the ejecta (e.g. Lucy et al. (1989); Fabbri et al. (2011); Mauerhan & Smith (2012); Milisavljevic et al. (2012)). An example of such is given in Figure 1.9 which illustrates the progressive blue-shifting of the line profiles of  $H\alpha$ ,  $H\beta$  and  $HeI\lambda 5876\text{\AA}$  from SN 2010jl (Gall et al. 2014).

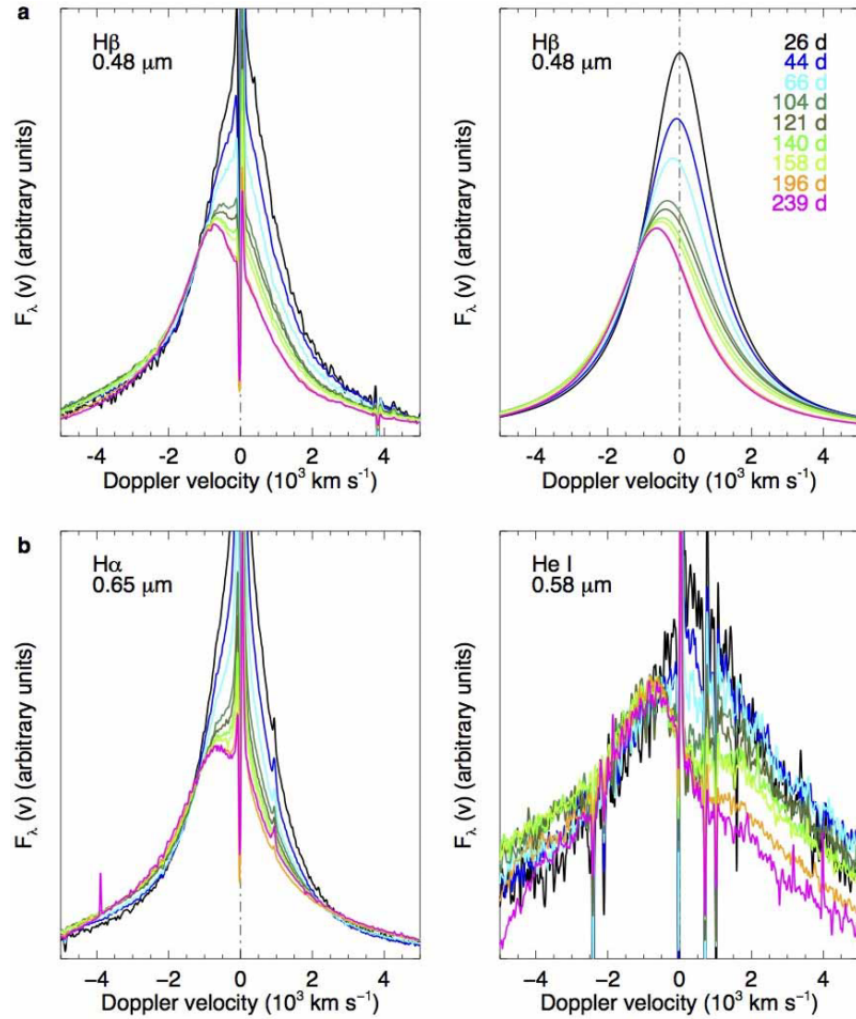


**Figure 1.9.** Figure taken from Gall et al. (2014) illustrating the progressive blue-shifting of line profiles from SN 2010jl. *a.* Evolution of the H $\beta$  line profile (*left*) and Lorentzian line fits to this line (*right*). *b.* Evolution of the H $\alpha$  line (*left*) and the HeI  $\lambda 5876\text{\AA}$  line (*right*).

Advances in digital storage have allowed for spectral and photometric observations to be made easily available online. Many observatories now publish their recent observations online in archives and are working to upload observations that pre-date file sharing services and so there is now a growing database of dust-affected asymmetric line profiles easily available. Much of the data used in this thesis was obtained from these archives.

Quantitative modelling of the extent of this asymmetry and other aspects of the shape of the line profile allow for dust in the ejecta of supernovae to be traced via an alternative method to SED-fitting.

### 1.3 Content Of This Thesis

The purpose of my work has been to develop a new approach to determining dust masses in supernovae, with the aim of providing an alternative to SED fitting for the future and of corroborating or contradicting past results. I looked to exploit the dust-forming signature of characteristically asymmetric line profiles. Though this feature has been discussed at length by numerous authors, it has very rarely been quantitatively measured or modelled.

To this end, I have developed a Monte Carlo code that numerically models this signature in the spectra of CCSNe in order to quantitatively determine dust masses formed at a variety of epochs post-explosion, additionally seeking to place constraints on the composition and grain size distributions of the newly-formed dust.

In Chapter 2, I will detail the physics that is included in DAMOCLES and the mechanisms and algorithms behind the functioning of the code. I will also discuss technical details and the motivations behind various choices such as the use of the Monte Carlo methodology and the use of the Fortran 95 programming language. In Chapter 3, I will describe the process of testing the code. I will detail the algebraic derivation of analytical line profiles in optically thin regimes and consider previous work published on line profiles in optically thick environments. I will demonstrate that DAMOCLES is capable of reproducing these results before moving on to present an investigation of the variable parameter space from a theoretical perspective. By probing the effects on the line profile of varying a single parameter, I discovered a number of interesting features that are caused by dust scattering and absorption. These are also discussed in Chapter 3.

I used DAMOCLES to number a model of CCSNe with a particular focus on SN 1987A. For many reasons this object became the central focus of this thesis. The detailed models of the H $\alpha$  and [O I] $\lambda 6300, 6363$  Å from SN 1987A over a wide range of epochs and a discussion of the implications of my results are presented in Chapter 4. Chapter 5 contains models of some late-time line profiles from a number of other CCSNe, namely SN 1980K, SN 1993J and Cas A. Finally, I will discuss my findings and conclude this thesis in Chapter 5.

# Chapter 2

---

## A Description of DAMOCLES

### 2.1 Monte Carlo Methods

The name “Monte Carlo” describes a class of modelling techniques that employ a stochastic approach to simulating mathematical and physical situations that are otherwise difficult or impossible to solve. By repeatedly sampling random numbers from a probability distribution, numerical results to non-analytic problems may be obtained. The approach was first used by researchers at Los Alamos in the late 1940s who adopted the method to model the transport of neutrons (Metropolis & Ulam 1949). It is from the code name for this project, “Monte Carlo”, that the methods derive their name.

As the available computing power increased over the following decades, Monte Carlo methods became more and more useful as a means of solving complex problems and are now used widely across numerous fields including mathematics, statistics, engineering, finance, the physical sciences and many others. The nature of the approach means that they are particularly well-suited to problems with multiple degrees of freedom, and especially when any of these degrees are coupled. By using random numbers to represent quantities that parametrise a physical problem, a solution to the problem may be sought using a pseudo-random number generator. It must be the case that the quantities that characterise the problem may be represented by a continuous distribution in the range [0,1] in order that the randomly generated numbers may be translated into physical properties (Buslenko et al. 1966).

---

Having thus obtained a random set of physical parameters, a model is constructed and an output - a “possible outcome” - is obtained. By repeatedly iterating this process with new randomly-generated inputs each time, many possible outcomes are produced and a probability distribution is built up. The interpretation of the outputted probability distribution is dependent on the manner of utilisation of the Monte Carlo method. For example, the procedure may be used to find the mean-free paths of millions of energy packets where the resulting probability distribution of the final frequencies of the packets is equivalent to an energy distribution. This is the process that I make use of and I will discuss it in more detail throughout this chapter.

More recently Monte Carlo methods have been applied to Bayesian statistical analyses that seek to uncover a complete multidimensional probability distribution describing the parameter space of a particular model. The intention is to derive not just a well-fitting model but to understand how variations in a given parameter affect the likelihood that the model is representative of the data. These investigations of parameter space generally adopt a Markov Chain Monte Carlo (MCMC) approach. Where a Monte Carlo method generates a sample from a required distribution, a MCMC technique draws samples according to a predefined set of rules that result in a sequence of samples called a Markov Chain. These methods allow for a more intelligent and efficient sampling of parameter space (Metropolis et al. 1953; Hastings 1970; Gilks et al. 1996).

Clearly, Monte Carlo simulations are limited by their finite nature and will never produce a perfect solution. However, this does not mean that Monte Carlo simulations are lacking in rigour. It may be shown that the error in a Monte Carlo model is approximately  $\sim \frac{1}{\sqrt{n}}$  for large  $n$ , where  $n$  is the number of quanta used in the simulation (Press et al. 2007). The error may therefore be made as small as required by increasing the number of quanta used in the simulation subject to the restrictions of computing time and expense.

In the next section, I discuss the use of Monte Carlo methods as applied to radiative transfer problems and specifically to DAMOCLES. I discuss the computational aspects of my work and the architecture of the code in section 2.3 before finally discussing the limitations of the code and its potential for future developments in section 2.4.

## 2.2 Radiative Transfer and the Monte Carlo Method

The application of Monte Carlo codes to radiative transfer problems in astrophysics has a strong history. Numerous codes that utilise this stochastic methodology have been written in the past few decades in order to model the transport of energy packets through various media, for example Cloudy (Ferland et al. 2013), Hyperion (Robitaille 2011), LIME (Brinch & Hogerheijde 2010), Mocassin (Ercolano et al. 2003, 2005), RATRAN (Hogerheijde & van der Tak 2000), SKIRT (Baes et al. 2003), TORUS (Harries 2000) and many others. The energy to be transported throughout the region of interest is discretised into packets and the path of each packet is calculated according to the properties of the environments that it passes through during its lifetime. Collating the escaped packets at the end of the simulation produces an energy distribution that may be compared to observed photometric or spectral data.

In addition to numerous codes that treat the continuous emission and absorption of energy in dusty environments in order to produce and fit spectral energy distributions (SEDs), there also exist several Monte Carlo radiative transfer codes that model the transfer and interaction of line emission through a 3D nebula in order to produce a synthetic spectrum (e.g. Brute (Thomas et al. 2003) and ARTIS (Kromer & Sim 2009)). These models frequently employ an approximation known as the Sobolev approximation (Sobolev 1957) to treat the absorption and scattering of photons. This method allows spectral lines in media moving with high velocity gradients to be treated more simply by solving the radiative transfer equation locally under the assumption that the macroscopic velocity gradient is more important than the thermal line width. Models of supernovae have been produced using both approaches and well-fitting spectra and SEDs have been generated but never, according to the best of my knowledge, has the Monte Carlo methodology been employed to produce sophisticated models of individual line profiles in expanding dusty regions. In this new code, DAMOCLES, we seek to apply the technique to an expanding dusty medium in order to consider the effects of dust on a single emitted line profile.

Previous work by Leon Lucy has considered the problem of computing the spectra of supernovae using Monte Carlo techniques (Lucy 1987, 1999, 2002, 2003; Lucy 2005a; Lucy 2005b). In particular Lucy and colleagues consider dust-induced asymmetric line profiles in the ejecta of CCSNe and they have published results derived both analytically and using simple Monte Carlo simulations (Lucy et al. 1989, 1991). These simulations appear to be

the only published instances of a numerical approach to studying this type of spectral feature. The DAMOCLES code adopts the same technique as the original modelling by Lucy et al. but allows for a considerably more complex treatment of the composition, geometry and motion of the dusty medium.

Radiative transfer methods as applied to supernovae generally treat a wide wavelength range and seek to conserve the total energy. In the case of SED modelling, this is often achieved by dividing the total energy into packets of equal weight and energy, and iteratively determining the temperature and ionisation structure. In this work, the approach we adopt is somewhat simpler as only a very narrow wavelength range need be considered. Rather than seeking to conserve the total energy, we assume that any packet absorbed by dust would be re-emitted outside the wavelength range of interest and thus no longer contributes to the resulting line profile. Any absorbed packet is therefore removed. In addition to this, the absorption and scattering of radiation by dust is assumed to be independent of temperature and there is therefore no need to calculate grain temperatures throughout the nebula. Similarly, the use of the Sobolev approximation (described above) is unnecessary here as the lines treated are assumed to be optically thin.

The subtleties of the problem we consider here lie in the treatment of an atmosphere expanding as fast as 10% of the speed of light, and in the complexities of the dusty medium itself. Lorentz transforms must be carefully applied in order that packets experience the appropriate degree of frequency shifting on their original emission and at each subsequent scattering event. In this respect, the code is analogous to Monte Carlo radiative transfer models of electron scattering published by Auer & van Blerkom (1972) and Hillier (1991). Indeed, similar features are observed in the outputs of both.

Throughout this section, I will describe the principles, assumptions and techniques adopted in the production of DAMOCLES (see Figure 2.1) before I move on to address the mechanics and architecture of the code itself. DAMOCLES stands for **D**ust-**A**ffected **M**odels **O**f **C**haracteristic **L**ine **E**mission in **S**upernovae.

### 2.2.1 Energy Packets

The fundamental principle underlying the Monte Carlo approach to the transport of radiation throughout a dusty nebula is that the radiation is discretised into packets. Each of these packets is then propagated throughout the nebula and ultimately contributes a fraction of the final energy distribution. At the start of the simulation, each packet is

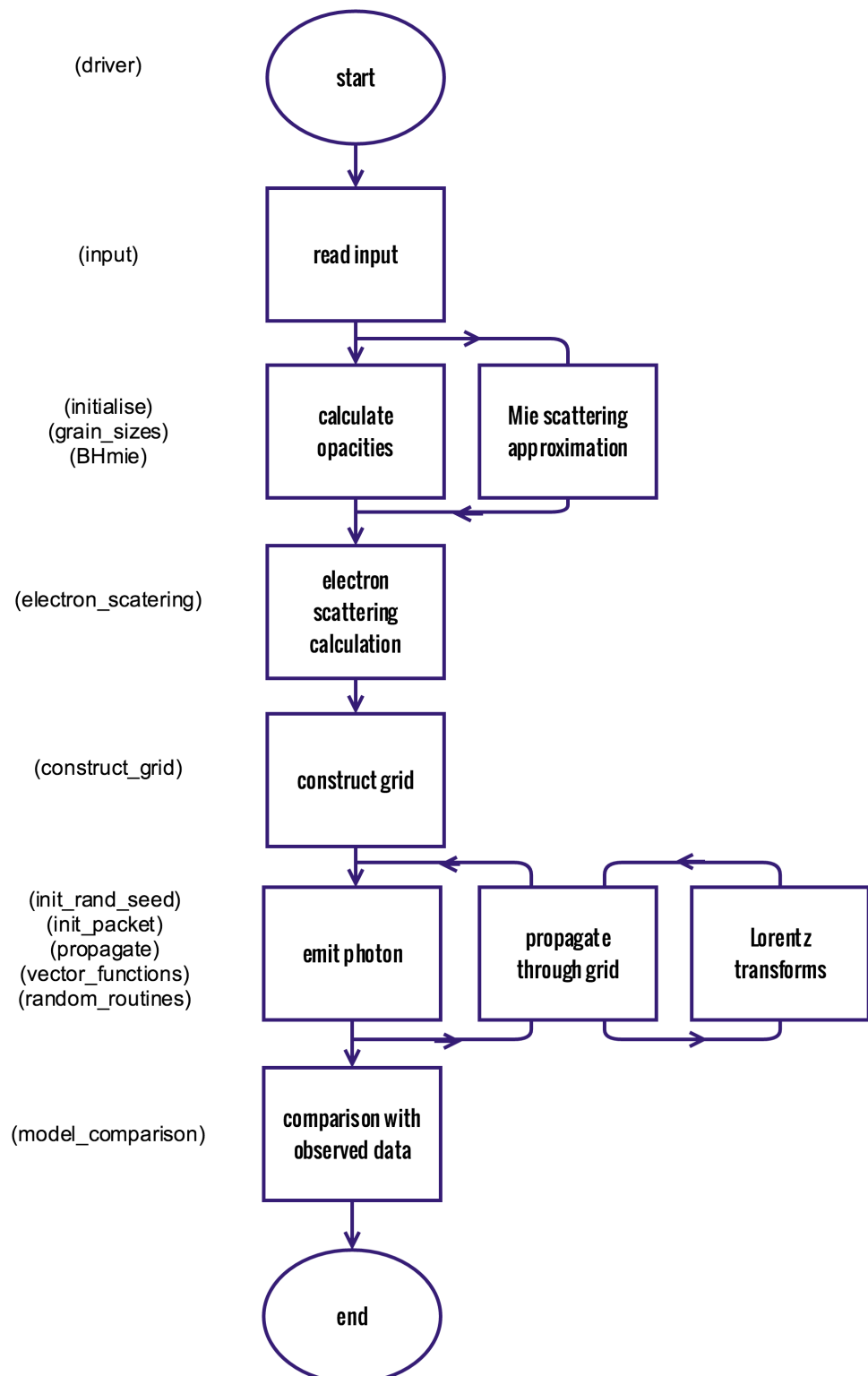


**Figure 2.1.** A flowchart representing the sequence of processes that take place in the DAMOCLES code. The modules involved at each stage are given in parentheses.

assumed to consist of  $n$  photons of frequency  $\nu_0$ , the rest frequency of the monochromatic emission line to be modelled. All packets therefore begin life with initial energy

$$E_0 = nh\nu_0 \quad (2.1)$$

where  $h$  is Planck's constant. As the packets move through the ejecta, they are scattered off high-velocity dust grains and after each scattering event the frequency of the packet is altered. In Monte Carlo simulations that model non-moving atmospheres, packets are usually taken to be of constant energy. When the frequency of a packet is altered after an event, the energy of that packet is kept constant and the number of real photons contained within it assumed to change. However, in the case of dust scattering, the number of real photons is conserved and thus the energy of the packet is altered. This is most easily achieved by weighting each packet over all scattering events as

$$w_p = \prod_{scat} \frac{\nu'}{\nu} \quad (2.2)$$

where  $w_p$  is the weight of the packet and  $\nu$  and  $\nu'$  are the frequencies of the packet before and after the scattering event respectively. The final energy of each packet is then  $E = wE_0$ , where  $E_0$  is the initial energy of the packet. The final dust-affected line profile is compiled by adding the total energy of all packets in a specific frequency bin in order to produce a histogram.

In these models, unlike fully self-consistent SED radiative transfer models, there is no requirement that the total energy be conserved. We drop this traditional requirement since radiation that is absorbed by dust is re-emitted outside of the wavelength range of interest and thus no longer contributes any flux to the resulting line profile. Packets that are absorbed may be safely removed from the simulation.

### 2.2.2 Initialisation and the Grid

The supernova ejecta is approximated by a three-dimensional cartesian grid, each cell of which is assumed to have uniform density and composition. By default, the ejecta occupies a shell between inner radius  $R_{in}$  and outer radius  $R_{out}$ . The grid extends from  $-R_{out}$  to  $+R_{out}$  in each of the three axes. Each side is split into the same number of divisions and thus each cell is a cube of volume  $R_{out}^3/n_{div}^3$  where  $n_{div}$  is the number of divisions

along each axis and is specified by the user. For the remainder of this thesis, a spherically symmetric situation is assumed and in all modelling and testing the grid is constructed in this manner. However, there are no assumptions of symmetry in the code and a cartesian grid was adopted in order to allow for arbitrary geometries to be modelled in the future e.g. ellipsoidal or toroidal ejecta distributions.

### Smooth power-law density distributions

Both gas and dust are by default assumed to have a power-law distribution declared as  $\rho(r) \propto r^{-\beta}$  between  $R_{in}$  and  $R_{out}$ . The distribution of gas determines the emissivity distribution and thus the starting positions of the packets in the simulation (see section 2.2.4). However, after the initial emission of energy packets, the gas plays no further role in the simulation as only interactions with dust grains are of interest here. By default, the dust is coupled to the gas and thus follows the same smooth power-law distribution previously described with exponent  $-\beta$ . The dust density in each cell is therefore calculated as

$$\rho(r) = \frac{(3 - \beta)M_{tot}}{4\pi(R_{out}^{3-\beta} - R_{in}^{3-\beta})}r^{-\beta} \quad (2.3)$$

if  $\beta \neq 3$ , where  $r$  is the radial distance from the centre of the cell to the origin and  $M_{tot}$  is the total desired dust mass to model. For the standard model with  $\beta = 2$  this becomes

$$\rho(r) = \frac{M_{tot}}{4\pi(R_{out} - R_{in})r^2} \quad (2.4)$$

If  $\beta = 3$  then the dust density in each cell is alternatively calculated as

$$\rho(r) = \frac{M_{tot}}{4\pi \log(R_{out} - R_{in})r^3} \quad (2.5)$$

Any cell whose centre falls outside of the bounds of the supernova ejecta has dust density set to zero. If the dust and gas are decoupled then the user must specify distinct profiles for the gas and the dust; that is, separate power laws must be declared and independent inner and outer radii specified. The same process is followed but with separate power-laws for each component. Including the capacity to specify the gas and dust distributions separately allows for more sophisticated modelling of, for example, circumstellar shells or dense cores of dust formation surrounded by more diffuse gas.

### Clumped geometries

It is known from SED modelling that models of clumped environments produce very different results to environments assumed to have a smooth distribution of dust and gas (e.g. Bianchi et al. (2000); Ercolano et al. (2007); Owen & Barlow (2015)). The capacity for modelling a clumped dusty medium is therefore included in the code. The fraction of the dust mass that is in clumps is declared ( $m_{frac}$ ) and the total volume filling factor of the clumps ( $f$ ) is also specified. Dust that is not located in clumps is distributed according to a smooth radial power-law. The clumps occupy a single grid cell and their size can therefore be varied by altering the number of divisions in the grid. They are distributed stochastically with probability of a given cell being a clump proportional to the smooth density profile (i.e.  $p(r) \propto r^{-\beta}$ ). The density of all clumps is constant and is calculated as

$$\rho_{clump} = \frac{M_{clumps}}{V_{clumps}} = \frac{m_{frac} M_{tot}}{\frac{4}{3} f \pi (R_{out}^3 - R_{in}^3)} \quad (2.6)$$

where  $M_{tot}$  is the total dust mass,  $M_{clumps}$  is the total dust mass in clumps and  $V_{clumps}$  is the total volume occupied by clumps.  $m_{frac}$  and  $f$  are defined as above.

A grid of cubic cells of varying dust and gas densities is thus produced in readiness for packets to be transported through it. Examples of smooth and clumped distributions of dust generated by DAMOCLES are presented in Figure 2.2. A frequency grid is also established centred on the rest-frame frequency of the line to be modelled.

#### 2.2.3 Properties of the Dusty Medium

Dust of any composition may be used for which optical data are available. The relative abundances of the species must be declared in an input file accompanied by a grain radius distribution (specified as a grain radius range and power-law) for each species. Files detailing the optical data ( $n$  and  $k$  values) for the chosen dust species are also declared at the start of the code. For each pairing of wavelength  $\lambda$  and grain radius  $a$ , a Mie scattering routine is employed to calculate  $Q_{abs}(\lambda, a)$  and  $Q_{sca}(\lambda, a)$  from the refractive index  $n + ik$ . These values are calculated for every species across the wavelength and grain radius ranges of interest. I have described the mathematics of converting the refractive index into scattering and absorption efficiencies using Mie theory in detail in the introduction to this thesis (see Section 1.1.5).

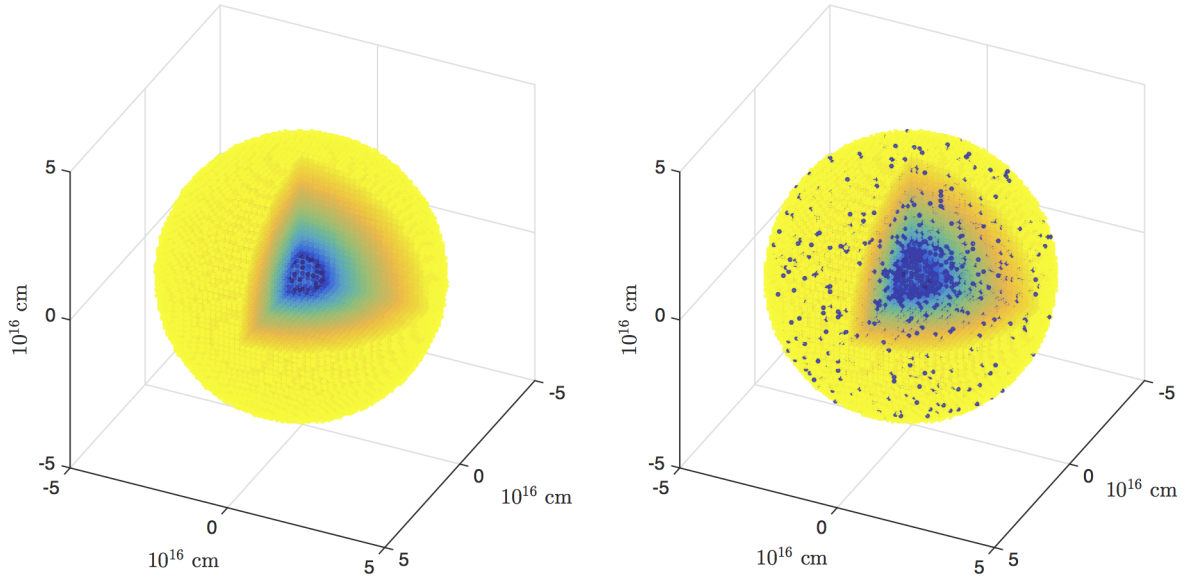


**Figure 2.2.** 3D representations of the grid generated by DAMOCLES. A smooth distribution is shown on the left and a clumped distribution on the right.

Ultimately, the overall scattering and absorption opacities in each grid cell must be known and so a weighted summation over  $Q_{abs}(\lambda, a)$  and  $Q_{sca}(\lambda, a)$  is performed. The number density in each cell must first be calculated as

$$n_d = \rho/m_{av} \quad (2.7)$$

where  $m_{av}$  is the average mass of a grain:

$$m_{av} = \sum_i \sum_a \frac{4}{3} \pi a_i^3 \rho_{g,i} w_i(a) x_{M,i} \quad (2.8)$$

$\rho_{g,i}$  is the density of the grain for species  $i$  (specified with the optical data),  $x_{M,i}$  is the relative abundance of species  $i$  by mass and  $w_i(a)$  represents the normalised weight of particles with grain radius  $a$ . For a given power-law distribution of grain radii  $n(a) \propto a^{-\alpha}$ ,  $w_i(a)$  is given by

$$w_i(a) = \frac{a^{-\alpha}}{\int_{a_{min}}^{a_{max}} a^{-\alpha} da} \quad (2.9)$$

The relative abundances of the different species are declared by the user in terms of cross-sectional area ( $x_{A,i}$ ). From this, the relative abundances by volume ( $x_{V,i}$ ) may be

calculated as

$$x_{V,i} = (1 + (x_{A,i} - 1)^{\frac{3}{2}})^{-1} \quad (2.10)$$

giving the relative abundance by mass  $x_{M,i}$  (used in Equation 2.8)

$$x_{M,i} = \frac{x_{V,i}\rho_{g,i}}{\sum x_{V,i}\rho_{g,i}} \quad (2.11)$$

For extinction, the total cross-section of interaction for extinction is then calculated as

$$C_{ext}(\lambda) = \sum_i \sum_a Q_{ext,i}(a, \lambda) w_i(a) \pi a_i^2 x_{A,i} \quad (2.12)$$

where the subscript  $i$  denotes species  $i$ ,  $x_{A,i}$  represents the relative abundance of species  $i$  by cross-sectional area and the summations are over species and grain radius. The calculation of the cross-section of interaction for scattering  $C_{sca}(\lambda)$  is performed in the same manner.

Using equations 2.7, 2.8 and 2.12, the dust opacity  $\kappa_{ext}$  can then be calculated using the relationship

$$n_d C_{ext} = \rho \kappa_{ext} \quad (2.13)$$

The values of  $C_{ext}(\lambda)$  and  $C_{sca}(\lambda)$  are calculated for the full wavelength range at the start of the simulation as are the number densities in each grid cell. As a packet passes through a grid cell, the optical depth  $\tau$  is determined from the above quantities according to the wavelength of the current packet (see Section 2.2.4 for further detail on this process). The above equations are discretised versions of continuous integral equations given in van de Hulst (1957) and Tielens (2005).

#### 2.2.4 Emission and Propagation

The initial radiation field is inherently tied to the distribution of gas throughout the supernova ejecta. The relationship between the emissivity and the gas density may vary under different regimes and therefore the emissivity distribution is also specified as a power-law with  $i(\rho) \propto \rho^q$ . In general, however, the emissivity distribution is assumed to be proportional to the square of the local gas density ( $i(r) \propto r^{-2\beta}$ ), i.e. proportional to

the product of the recombining ion and electron densities in the case of a recombination line or to the product of the atom and electron densities in the case of collisionally excited line emission.

The supernova ejecta is divided into shells between  $R_{in}$  and  $R_{out}$  and the number of packets to be emitted in each shell calculated according to the specified power-law emissivity distribution  $i(r) \propto r^{-q\beta}$ . For each packet a location within the appropriate shell must be determined and a propagation direction sampled. The initial propagation direction is sampled from an isotropic distribution as detailed in numerous publications (e.g. Wood et al. (2004a)). Three random numbers in the range [0, 1) are sampled and these are translated into spherical coordinates as

$$\phi = 2\pi\eta \quad (2.14)$$

$$\theta = \arccos(2\xi - 1) \quad (2.15)$$

where  $\eta$  and  $\xi$  are random numbers in the range [0, 1),  $\phi$  is the azimuthal angle and  $\cos\theta$  is the radial direction cosine. The initial packet trajectory in cartesian coordinates is then given by

$$n_x = \sin\theta \cos\phi \quad (2.16)$$

$$n_y = \sin\theta \sin\phi \quad (2.17)$$

$$n_z = \cos\theta \quad (2.18)$$

The process for sampling an initial position within the shell follows the same sampling process as described above but a radial position must be sampled in addition to the two angular coordinates. For a random number  $\zeta$ , the radial position  $r$  is calculated as

$$r = R_i + \zeta(R_{i+1} - R_i) \quad (2.19)$$

where  $R_i$  is the inner boundary of the  $i^{\text{th}}$  shell.

In total therefore five random numbers must be sampled in order to generate an initial position and trajectory for a packet. At every subsequent scattering event, the packet is propelled with a new direction vector which is sampled from an isotropic distribution in the rest-frame of the particle with two newly generated random numbers in the manner

described above.

Once a packet has been emitted into the nebula, it must be propagated through the grid until it escapes the outer bound of the ejecta  $R_{out}$  or is absorbed. In each cell that a packet passes through, a test must be performed in order to determine whether the packet passes through that cell and into the next or whether it is scattered or absorbed by a dust grain (i.e. an “event” occurs). The probability that a packet travels a distance  $l$  without interacting is

$$p(l) = e^{-n_d \sigma_\lambda l} = e^{-\tau_\lambda} \quad (2.20)$$

where  $n_d$  is the dust number density in the grid cell,  $\sigma_\lambda$  is the extinction cross-section of interaction at wavelength  $\lambda$  and

$$\tau_\lambda = n_d \sigma_\lambda l = \rho \kappa_\lambda l \quad (2.21)$$

for constant  $n_d$  and  $\sigma_\lambda$  (as in a grid cell). Note that  $\sigma_\lambda$  is used to denote the cross-section of interaction for a given grain radius. Where a grain radius distribution is adopted or multiple species are employed, the formula becomes  $\tau_\lambda = n C_{ext,\lambda} l$  as described in Section 2.2.3. The probability that a packet *does* interact within a distance  $l$  is therefore  $1 - e^{-\tau_\lambda}$ . The position at which the packet will be absorbed or scattered is then determined by comparing a randomly generated number in the interval  $[0,1)$  with this value. In practice however, it is easier to sample from the cumulative probability distribution and use the generated number to calculate an optical depth as

$$\xi = 1 - e^{-\tau_\lambda} \implies \tau_\lambda = -\log(1 - \xi) \quad (2.22)$$

where  $\xi \in [0, 1)$  is a sampled random number between 0 and 1. The properties of the cell as determined in Section 2.2.3 are then used to determine the distance that the packet travels:

$$l = \frac{\tau_\lambda}{n_d C_{ext,\lambda}} \quad (2.23)$$

If the distance to be travelled by the packet is greater than the distance from its position to the edge of the cell then the packet is moved along its current trajectory  $(n_x, n_y, n_z)$

to the cell boundary and the process is repeated. Alternatively, if the displacement is not sufficient for the packet to escape the cell then an event occurs. The packet is either scattered or absorbed with probability of scattering equal to the albedo of the cell

$$\omega = \frac{\sigma_{sca}}{\sigma_{sca} + \sigma_{abs}} \quad (2.24)$$

If the packet is absorbed (the case if a randomly generated number is greater than the albedo  $\omega$ ) then it is simply removed from the simulation as previously discussed. If this is not the case, then the packet is scattered and a new trajectory is sampled from an isotropic distribution in the comoving frame of the dust grain. The frequency of the packet is recalculated using Lorentz transforms as described in the next section and the process is repeated until the packet has either escaped the outer boundary of the supernova ejecta or been absorbed. If the packet does escape, its weighted energy is deposited in the appropriate frequency bin. Once all packets have escaped, the array of frequencies and fluxes produces the desired line profile.

### 2.2.5 The Velocity Field and Doppler shifting

At emission and at each scattering event the frequency of the packet is recalculated according to a radial velocity field

$$v(r) = v_{max} \frac{r^\alpha}{R_{out}^\alpha} \quad (2.25)$$

where the maximum velocity,  $v_{max}$ , at the outer edge of the ejecta and the exponent of the velocity profile,  $\alpha$ , are declared in the input file.

It is worth noting that if a constant mass loss rate is required, the exponent of the velocity profile and the exponent of the density profile are not independent. A constant mass loss rate implies that  $4\pi\rho v R^2 \propto k$ , where  $k$  is a constant, and thus for  $v \propto r^\alpha$  and  $\rho \propto r^{-\beta}$ , we require that  $\beta - \alpha = 2$ . However, it is possible that the supernova event may have induced a mass-flow rate that is not constant with radius and thus both exponents may be declared independently. It is also worth noting that for supernovae in their free expansion phase, as the majority are by the time of the onset of dust formation, the ejecta are expanding with a  $v \propto r$  Hubble law expansion.

The outflow velocities in supernovae can be extremely high, of the order of a few percent

of the speed of light. Escaping radiation is therefore subject to significant Doppler shifting. At emission and at each scattering event, the frequency of a packet must be recalculated according to the velocity of the scattering grain. When the packet is initially scattered, it has a frequency and a trajectory in the rest frame of the emitter. Both of these must be transformed to the observer's frame in order for the packet to be propagated through the grid. The new direction and frequency in the observer's frame may be simply found by transforming the momentum 4-vector  $\mathbf{P}$  which is defined as

$$\mathbf{P} = \begin{pmatrix} E \\ p_x \\ p_y \\ p_z \end{pmatrix} = \begin{pmatrix} h\nu \\ h\nu x \\ h\nu y \\ h\nu z \end{pmatrix} \quad (2.26)$$

We may then derive  $\mathbf{P}'$ , the momentum 4-vector in the observer's frame using the relation

$$\mathbf{P}' = \Lambda \mathbf{P} \quad (2.27)$$

where

$$\Lambda = \begin{pmatrix} \gamma & -\gamma\beta_x & -\gamma\beta_y & -\gamma\beta_z \\ -\gamma\beta_x & 1 + (\gamma - 1)\frac{\beta_x^2}{\beta^2} & (\gamma - 1)\frac{\beta_x\beta_y}{\beta^2} & (\gamma - 1)\frac{\beta_x\beta_z}{\beta^2} \\ -\gamma\beta_y & (\gamma - 1)\frac{\beta_y\beta_x}{\beta^2} & 1 + (\gamma - 1)\frac{\beta_y^2}{\beta^2} & (\gamma - 1)\frac{\beta_y\beta_z}{\beta^2} \\ -\gamma\beta_z & (\gamma - 1)\frac{\beta_z\beta_x}{\beta^2} & (\gamma - 1)\frac{\beta_z\beta_y}{\beta^2} & 1 + (\gamma - 1)\frac{\beta_z^2}{\beta^2} \end{pmatrix} \quad (2.28)$$

and  $\boldsymbol{\beta} = \frac{\mathbf{v}}{c} = (\beta_x, \beta_y, \beta_z)$ ,  $\beta = |\boldsymbol{\beta}|$  and  $\gamma = \frac{1}{\sqrt{1-\beta^2}}$ .

In practice, the velocities considered are low enough that it is unnecessary to consider

terms of order  $O(\frac{v^2}{c^2})$  and thus  $\Lambda$  may be reduced to

$$\Lambda = \begin{pmatrix} 1 & -\beta_x & -\beta_y & -\beta_z \\ -\beta_x & 1 & 0 & 0 \\ -\beta_y & 0 & 1 & 0 \\ -\beta_z & 0 & 0 & 1 \end{pmatrix} \quad (2.29)$$

The new direction of travel and frequency in the observer's frame are therefore given by

$$\nu' = \nu(1 - x\beta_x - y\beta_y - z\beta_z) \quad (2.30)$$

$$x' = \frac{\nu}{\nu'}(x - \beta_x)$$

$$y' = \frac{\nu}{\nu'}(x - \beta_y)$$

$$z' = \frac{\nu}{\nu'}(x - \beta_z)$$

For each scattering event, the packet must be transformed both into and out of the comoving frame. The reverse transform is applied by using the inverse Lorentz matrix  $\Lambda^{-1}$  which is obtained by reversing the sign of  $\mathbf{v}$ . Positive  $\mathbf{v}$  is defined for frames moving away from each other and thus  $\mathbf{v}$  is defined to be negative in the direction of the observer.

**Table 2.1.** Values of  $q_{H\alpha}(T)$  at three different temperatures as used by DAMOCLES.

	Temperature (K)		
	5,000	10,000	20,000
$q_{H\alpha}$ (erg cm <sup>3</sup> s <sup>-1</sup> )	$6.71 \times 10^{-25}$	$3.56 \times 10^{-25}$	$1.83 \times 10^{-24}$

### 2.2.6 Electron Scattering

As will be discussed in detail in chapter three, the effects of scattering on the shapes of line profiles can be quite pronounced and it is therefore important to consider the potential effects of electron scattering as well as those of dust scattering. A simple treatment of electron scattering calculates electron densities using an estimated average temperature of either 5,000K, 10,000K or 20,000K. An observed luminosity of  $H\alpha$  is then used to calculate

the optical depth to electrons. The overall optical depth within each cell is calculated as  $\tau = \tau_{dust} + \tau_e$ , with  $\tau_e = 0$  if electron scattering is not activated. The electron scattering optical depth,  $\tau_e$ , in a given cell (with constant properties therein) is calculated as

$$\tau_e = n_e \sigma_t l \quad (2.31)$$

where  $n_e$  is the electron density in that cell,  $\sigma_t$  is the Thomson cross-section of interaction for an electron and  $l$  is the distance travelled. In order to calculate this value, the electron density in each cell must be known. We assume that the electron density is the same as the ion density and that both are distributed according to the gas density distribution such that

$$n_e(r) = K r^{-\beta} \quad (2.32)$$

where  $K$  is a constant. The value of  $K$  must be determined from the total H $\alpha$  luminosity. We follow the formalism described by Osterbrock & Ferland (2006) in order to estimate the electron density from the total H $\alpha$  luminosity ( $L_{H\alpha}$ ).  $L_{H\alpha}$  is given by

$$L_{H\alpha} = \int_0^\infty n_p(r) n_e(r) E_{H\alpha} \alpha_{H\alpha}^{eff}(T) 4\pi r^2 dr \quad (2.33)$$

$$= \int_{R_{in}}^{R_{out}} n_p(r) n_e(r) q_{H\alpha}(T) 4\pi r^2 dr \quad (2.34)$$

where  $n_p(r)$  is the proton density at radius  $r$ ,  $n_e(r)$  is the electron density at radius  $r$ ,  $T$  is the temperature,  $\alpha_{H\alpha}^{eff}(T)$  is the temperature-dependent effective recombination coefficient for H $\alpha$ ,  $E_{H\alpha}$  is the energy of a single H $\alpha$  photon and

$$q_{H\alpha} = E_{H\alpha} \alpha_{H\alpha}^{eff} = \frac{4\pi j_{H\alpha}}{n_e n_p} \quad (2.35)$$

where  $j_{H\alpha}$  is the temperature-dependent emission coefficient for H $\alpha$  (i.e. the energy emitted per unit volume per unit time per unit solid angle). Substituting equation 2.32 into equation 2.34 gives the following

$$\frac{L_{H\alpha}}{4\pi q_{H\alpha}} = K^2 \int_{R_{in}}^{R_{out}} r^{2(1-\beta)} dr \quad (2.36)$$

which in the case  $\beta \neq \frac{3}{2}$  may be solved as

$$K = \sqrt{\frac{L_{H\alpha}}{4\pi q_{H\alpha}} \frac{3 - 2\beta}{R_{out}^{3-2\beta} - R_{in}^{3-2\beta}}} \quad (2.37)$$

and for  $\beta = \frac{3}{2}$  is

$$K = \sqrt{\frac{L_{H\alpha}}{4\pi q_{H\alpha}} \frac{1}{\ln(R_{out}/R_{in})}} \quad (2.38)$$

Substituting  $K$  back into equation 2.32 gives the electron density for each cell. In the code, only three gas temperatures may be specified and three corresponding values of  $q_{H\alpha}(T)$  are included, as per Table 2.1.

If, for a given packet, an event occurs, it is first calculated whether this is an electron scattering event or a dust event (either scattering or absorption) by considering the ratio of the optical depths to each. The process by which a packet is scattered by an electron is almost identical to the dust scattering process except for the adopted velocity of the scatterer. In the case of a dust grain, the velocity is simply the bulk velocity of the ejecta at that radius as determined from the specified velocity profile. For an electron, the assumed velocity must include a thermal component as well as the same bulk velocity as would be adopted for a dust grain at the same location. As in the electron scattering calculation of Hillier (1991), the components  $(v_x, v_y, v_z)$  of the thermal velocity  $\mathbf{v}_{therm}$  are assumed to follow a Maxwellian distribution with zero mean and standard deviation

$$\sigma = \sqrt{\frac{k_B T}{m_e}} \quad (2.39)$$

where  $k_B$  is Boltzman's constant and  $m_e$  is the mass of an electron. The components are then sampled from a normal distribution with specified mean and standard deviation using the Marsaglia polar method (Marsaglia & Bray 1964). This method generates two random numbers from a uniform distribution in the interval  $[0,1]$  and uses a number of transformations to convert them to random numbers as generated from a standard normal distribution with zero mean and unity variance. They may then be scaled to the appropriate normal distribution. Finally, the overall velocity of the electron is then

calculated as

$$\mathbf{v}_e = \mathbf{v}_{bulk} + \mathbf{v}_{therm} \quad (2.40)$$

and the Lorentz transforms are applied in the same manner as a dust scattering event.

In the majority of cases it seems that the electron densities are not high enough to discernibly affect the overall shape of the profile. However, there may be a few rare cases (the concept is discussed for SN 2010jl by Fransson et al. (2013)) where the electron densities are high enough to become significant in the observed profiles. Whilst the inclusion of electron scattering in the code is an approximation since it is not necessarily true that  $n_e = n_p$  and the exact gas temperature is unknown, it provides a good suggestion of the potential effects of electron scattering.

### 2.2.7 Doublets

One of the lines in supernovae emission spectra that is frequently seen to be blue shifted is the forbidden [OI] $\lambda 6300, 6363\text{\AA}$  doublet. DAMOCLES therefore has the capacity to treat doublets as well as single lines. When a doublet is specified, both the initial wavelengths and the initial intensity ratio must be declared. The code will create a wider frequency array than for a single line in order to accommodate both lines. It will then model each line independently, adding the final fluxes of the lines weighted by their intrinsic flux ratio to produce the desired doublet profile at the end of the modelling.

### 2.2.8 Comparing a Model with Observations

DAMOCLES includes the capacity to read in observed line profile data for direct comparison with a modelled line profile. Once all packets have been processed through the nebula and collected into bins, a flux is calculated at each of the wavelength bins in the observed data by interpolating between modelled wavelength bins. A mean squared error (MSE) calculation is then performed to compare the model with the data quantitatively, where the MSE is equal to

$$\frac{1}{N} \sum_i (f_{obs,i} - f_{mod,i})^2 \quad (2.41)$$

and  $f_{obs,i}$  is the observed flux in the  $i^{\text{th}}$  frequency bin,  $f_{mod,i}$  is the modelled flux in the

$i^{\text{th}}$  frequency bin, and  $N$  is the total number of frequency bins. Minimising the MSE minimises the error between the model and the observed line and therefore provides a quantitative measure of goodness of fit that may be used in addition to or instead of any qualitative assessment. Since the total inherent error on each observation is variable, the exact value of the MSE should not be compared between different line profile observations and only between different models and sets of parameters for a given line profile. A MSE calculation is preferred over a  $\chi^2$  calculation since for the vast majority of observed spectra I do not have information on the uncertainties associated with the spectral point and any error would therefore have to be estimated.

## 2.3 The Structure of DAMOCLES

DAMOCLES is written using Fortran 95. Since the major modernisation of Fortran 77 in 1990, the language includes a number of more modern elements that make it an ideal choice for this type of numerical computation. Firstly, a fast, high-level language is required that allows for dynamic memory allocation and deallocation. Whilst DAMOCLES could have been written in a number of other languages, this is a critical feature that is only available in a few languages. Very large numbers of packets are required to achieve reasonable resolutions in Monte Carlo codes of this nature and therefore large arrays of data are required. The ability to maintain careful control of memory allocation is very important.

Fortran 95 also has a number of other features that make it especially suitable for this sort of code. Derived types group a number of variables of different intrinsic or other derived types. This allows different properties of a particular item (for example a packet or grid cell) to be grouped together and accessed via that item. Though not a necessary feature, derived types make the code simpler, faster and more legible. They also make it easier to write and therefore help to minimise the risk of errors. Similarly, the modular structure that was introduced to Fortran in 1990 allows the programmer to distribute their code over a number of modules and ensures that variables that are declared within a particular module can be accessed by other modules if necessary (Ellis et al. 1994). This eliminates the need for common blocks of code and allows a large program to be segmented into logical divisions. This increases the speed, clarity and ease of maintenance and development in the future.

The obvious alternative programming language to Fortran 95 is C or C++. Both of

these languages have all of the features described above and are exceptionally fast. From a computation perspective, there is, arguably, little to separate them for this type of coding. I ultimately decided to write DAMOCLES in Fortran 95 because of its heritage in astrophysics. A very large number of astrophysical codes have been written using current or previous versions of Fortran and writing the code in Fortran 95 allowed for easy compatibility and the use of various astrophysics libraries and routines.

DAMOCLES is parallelised using OpenMP (see Section 2.3.2) which restricts its use to shared memory machines. It has been developed on and currently runs on a MacBook Pro 11.2 quad core with Intel Core i7 2.8GHz processors and 16GB of memory. A typical, medium resolution simulation using 125,000 grid cells and  $10^5$  packets takes approximately 15 seconds to run. The number of packets transported and the total dust optical depth are the most important factors in determining runtime.

### 2.3.1 Computational Architecture and Processes

DAMOCLES was written using a modular structure. The “parent” driver has numerous “children” in the form of subroutines and modules which are each responsible for a separate task or tasks. This architecture has a number of advantages. Firstly, it serves to clarify both the functionality and legibility of the code allowing for easier debugging and maintenance. It also allows for the implementation of features such as recursive subroutines which are ideally suited to a Monte Carlo methodology. Finally, it allows for the code to be developed further in the future simply by including additional modules and subroutines. A brief description of every module and subroutine in the code is presented in the following subsections. The descriptions are ordered according to the first time they or their contents are called by the driver (see Figure 2.1 for a flowchart of the order of the processes that take place in DAMOCLES and see Figure 2.3 for a flowchart of the modular hierarchy).

#### (a) The driver

The *driver* module is at the centre of DAMOCLES. It is from here that all subroutines are called. The calls to construct the grid and calculate dust opacities, to emit and propagate packets and to compare the results with observational data are all made from here. The parallelisation process is also controlled from here (see section 2.3.2 for more details on the parallel function of DAMOCLES). Having called the initialisation routines, the driver

is responsible for dividing the ejecta into shells and calculating how many packets are emitted within each shell. Each shell is looped over and each packet is looped over within each shell. Emission and propagation routines are called inside this loop. At the end of each packet’s lifetime, either once it has been absorbed or has escaped, the driver adds the weighted packet’s energy to the appropriate frequency bin and stores this information before looping back to emit and propagate the next packet. It is here that a line of sight is applied if so desired. This is achieved by collecting only packets that have escaped within a cone of vertical angle  $\pi/6$ . Once all packets have been processed, the driver writes the relevant information (the wavelengths, velocities and fluxes that describe the outputted line profile) to an output file and calls the model comparison module.

The driver is also the section of code responsible for processing doublets. The code treats doublets by processing two batches of packets with differing initial frequency through the same grid. Before they are collected in frequency bins, the flux ratio that is specified by the user is applied to one batch of the packets. All packets are then collected as per a single line.

Various statistics are also processed and output here including the fraction of packets that are absorbed and the estimated undepleted luminosity of the observed line.

### (b) The input module

The *input* module is where the primary input file is read into the code and all global variables are declared and assigned. A number of logicals are assigned based on values declared in the input file and some simple calculations are performed that determine the inner and outer radii based on the maximum velocity specified and the epoch of consideration ( $R_{out} = V_{max} \times t$ ). A number of physical constants that are used throughout the code are also declared here as “parameters”, meaning that their value cannot be changed at any point in the simulation.

### (c) The initialisation module

The *initialise* module acts as a driver to run all of the subroutines associated with initialising the program. A number of dynamically allocatable arrays are declared allowing for a grid of densities to be calculated, a frequency grid to be stored and optical properties to be read in. Arrays to store the emergent spectrum are also declared. The calculation of dust opacities, which calls the *grain\_sizes* subroutine and the *BHmie* subroutine, is

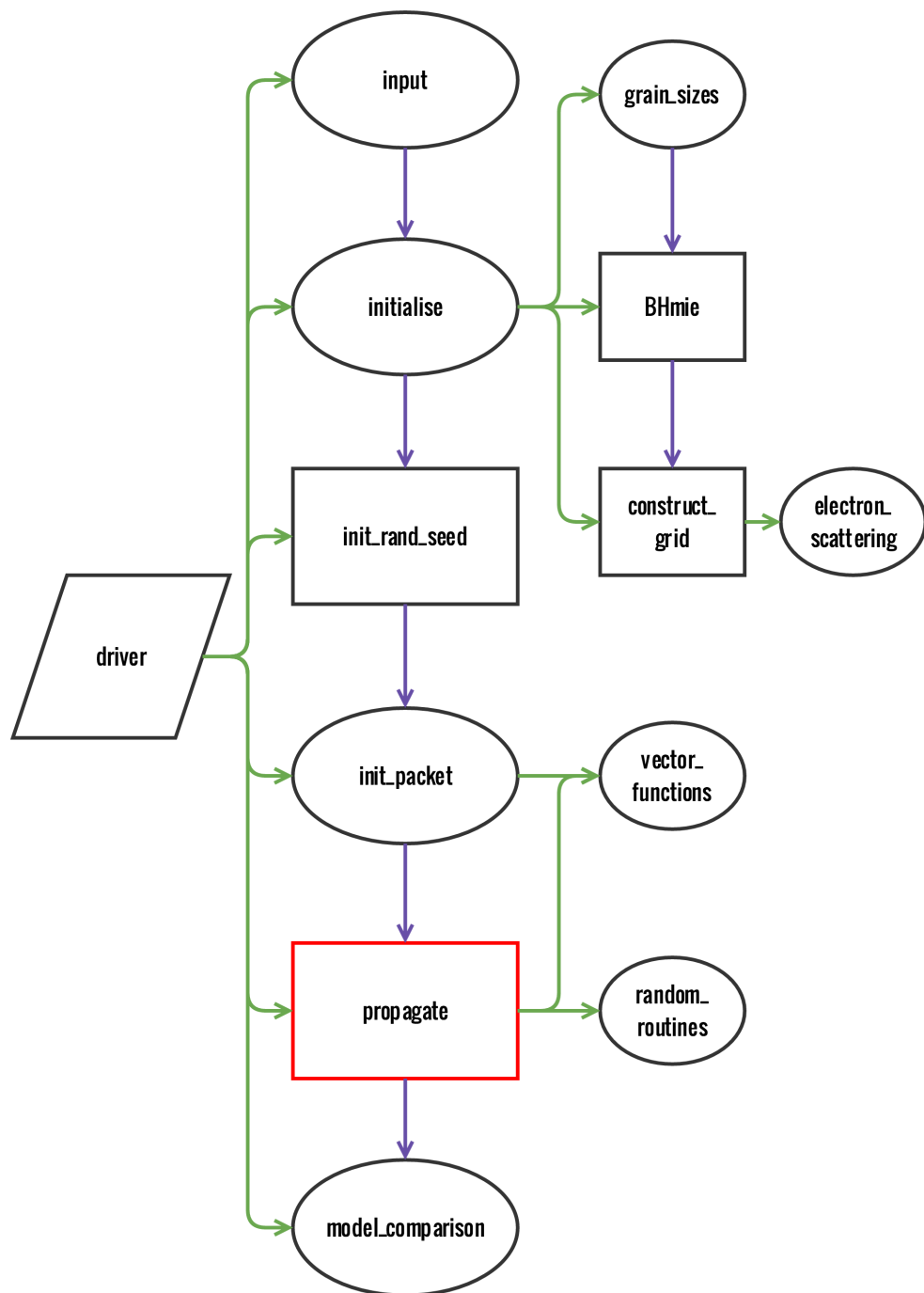


**Figure 2.3.** A flowchart representing the hierarchy of modules and subroutines in the DAMOCLES code. Ellipses represent modules and rectangles represent subroutines (the red rectangle is a recursive subroutine). Green arrows indicate the dependence of a module or subroutine on previous modules or subroutines. Purple arrows indicate the flow of the code.

performed here. For each species, the wavelength-dependent optical properties,  $n$  and  $k$ , are read in and the Mie routine applied to every pair of frequencies and grain radii. The resulting extinction and scattering efficiencies are summed over all grain radii for each wavelength, weighted appropriately, to calculate overall wavelength-dependent extinction and scattering opacities (see Section 2.2.3 for further detail). These data are stored in an array that is accessed as necessary when packets are propagated through the grid.

The command to construct the grid is called before some basic statistics about the grid are calculated. The average optical depth from  $R_{in}$  to  $R_{out}$  in both the V band and the rest-frame wavelength of the line being modelled are calculated and sent to stdout. The average number density of grains in each cell is also computed and output. Finally, the frequency array is constructed.

This module is also where the ‘gridcell’ derived type is declared. A ‘gridcell’ type was specified as it allowed for easy and clear access to any of a grid cell’s properties as a packet passed through it. The type consists of a number of arrays of real, integer and logical variables. The properties recorded for each cell include the physical bounds of the cell in each axis, the mass and number dust densities, the electron density, an identifying number (ID) and a logical clumped property.

#### (d) The grain size module

The *grain\_sizes* module reads in the file that specifies the list of species to be used. This file is a list of species detailing the name of the file containing the optical data for the species, the relative abundance of that species, the maximum and minimum grain radii and the exponent of the power law of the grain radius distribution. It also declares how fine the grid of grain radii should be. These properties are all read in by the *grain\_sizes* module and a relative weight for each grain radius for each species is calculated here.

The ‘species’ derived type is declared in this module. Similarly to the ‘gridcell’ type, using a derived type allowed for the easy storing and accessing of a large number of properties of each species. Many multi-dimensional arrays and scalars are stored for the ‘species’ type including properties relating to the grain radius distribution, the density of a dust grain, the extinction and scattering opacities and the relative abundance of the species amongst others. After the processing of the optical data for all species is completed, the calculated quantities are stored in arrays as components of the ‘species’ type.

**(e) The Mie approximation subroutine**

The *BHmie* subroutine is a standard routine that was obtained from an online library of routines (Press et al. 2007). It is a modified version of the Bohren & Huffman (1983) Mie scattering routine. The algorithm applies the mathematics described in Section 1.1.5 to determine the extinction and scattering efficiencies of a single size spherical grain at a specified wavelength given its complex refractive index  $n + ik$ .

**(f) The grid construction subroutine**

The *construct\_grid* subroutine is called from within the initialisation module. The purpose of this subroutine is to populate the grid, which is an array of derived type *gridcell* and size  $n_{cells}$  where  $n_{cells}$  is the number of cells in the grid. The bounds of the grid are initialised and the radii of all cells from the centre of the grid to the centre of the cell are calculated. The density of each cell is then calculated according to a smooth power-law density distribution and scaled so that the total dust mass is equal to that specified in the input file. If clumps are used then the total number of clumps is calculated and these are distributed throughout the grid stochastically according to the smooth density profile stipulated. This subroutine also calls the electron scattering subroutine contained within the *electron\_scattering* module so that the electron density of a cell may be stored at the same point as the dust density.

**(g) The electron scattering module**

The *electron\_scattering* subroutine is a simple subroutine that is used to calculate the value of  $K$  as described in equation 2.32. The total H $\alpha$  luminosity and the gas temperature are read in and the gas temperature used to determine the appropriate value of  $q_{H\alpha}$  from Table 2.1. These values are then used to calculate the value of  $K$  as described by equations 2.37 and 2.38. The variable is passed back to the *grid construction* subroutine where it is used to calculate the electron density in each cell. The electron densities will be used by the *propagate* subroutine to calculate the electron scattering optical depth in each cell.

**(h) The random seed subroutine**

The *init\_rand\_seed* is a short subroutine that calculates a seed for the standard Fortran pseudo-random number generator (*random\_number*). It uses the system clock to generate the random seed and thus varies with every implementation of the code. A seed is a number

that is used as a “starting point” for a pseudo-random number generator. Varying the random seed ensures that a different set of random numbers is generated every time the code is run, which can be useful to ensure that any peculiar or interesting features of the outputted line profiles are definitely a product of the physical processes involved and not a result of random fluctuations in the simulation. The more packets are used however, the more the Monte Carlo noise in the emergent line profile is reduced and the contribution from any anomalous packets should be insignificant.

#### (i) The packet initialisation module

The *init\_packet* module is responsible for the creation and emission of packets at the start of the simulation. It is called from the driver for each packet. By generating an array of five random numbers, the position and emission direction vectors in the rest frame of the emitter are calculated according to the formulae described in equations 2.14 to 2.19. The scalar velocity of the emitter is calculated based on its radial position and this converted into a velocity vector by normalising the position vector and multiplying by the scalar velocity. The velocity vector is passed to the Lorentz transforms subroutine contained in the *vector\_functions* module. The frequency of the packet is also passed to this subroutine. After the propagation direction vector and the frequency of the packet have been updated to the observer’s rest frame, the grid cell in which the packet starts its path is identified and the code passes back to the driver to propagate the packet through the nebula.

#### (j) The vector functions module

A number of vector functions are contained within the *vector\_functions* module and are accessed throughout the program. These include normalisation functions, conversions from spherical coordinates to cartesian and both forward and inverse Lorentz transforms. It is the latter of these that are most important for the physics of the code. The Lorentz functions are called for each packet at emission from the *driver* and at every subsequent scattering event from within the *propagate* routine. As well as performing the necessary frequency shift based on the velocity of the scatterer or emitter, they also transform into and out of the rest frame of the particle thus ensuring that the packet is propagated through the nebula with a direction in the rest frame of the observer but that its new direction is sampled from an isotropic distribution in the rest frame of the emitting or scattering dust grain.

The  $\beta$  and  $\gamma$  values are calculated based on the input velocity vector. The momentum 4-vector  $\mathbf{P}$  is then multiplied by the Lorentz matrix  $\mathbf{\Lambda}$  using the Fortran function *matmul* to produce a new frequency and a new direction vector in the appropriate frame of reference. If a scattering event has occurred then the weight of the packet is also updated here. The new direction vector, frequency and weight are then passed back to the propagate routine and the process repeated. At each scattering event the inverse Lorentz matrix must first be applied to move from the observer's rest frame to the particle's. A new direction vector must then be sampled from an isotropic distribution before applying the forward Lorentz transform to move back from the rest frame of the dust grain to the observer's frame. The next step in the packet's trajectory may then be calculated in the *propagate* subroutine.

#### (k) The *propagate* subroutine

The *propagate* subroutine is at the heart of the Monte Carlo simulation. It is here that the trajectories of all packets in the simulation are determined. The *propagate* subroutine is a subprogram called a recursive subroutine. This allows the subroutine to call itself, at which point it will loop back to the start of the subroutine. It will continue this process until a condition is reached that instructs it to return to the driver. In this case a number of conditions will arrest the circulation of the packet. If the packet has escaped the outer radius of the ejecta or has been absorbed then the routine will pass this information along with the frequency and weight of the packet back to the driver. The routine would also stop recurring if a packet has undergone a maximum number of scattering events (500 by default). At this point it is deemed that the weight of the packet is so small as to be negligible and it is classified as "inactive". This prevents the code from lagging by becoming stuck on a particular packet that has become trapped in a region of high density and albedo. It is noted that if this is the case for a large number of packets then a bias may be introduced - packets emitted in particularly high density regions may be discarded more frequently than those emitted in less dense regions. The number of packets that are deemed "inactive" is output as a percentage of the total number of packets employed at the start of the simulation as a check for the user. In practice, unless the albedo of the dusty medium is extremely high and the medium is very dense, this is rarely an issue (for an average simulation with  $10^7$  packets, normally only one or two are discarded for this reason).

There are a number of processes that take place in this module in order to propagate

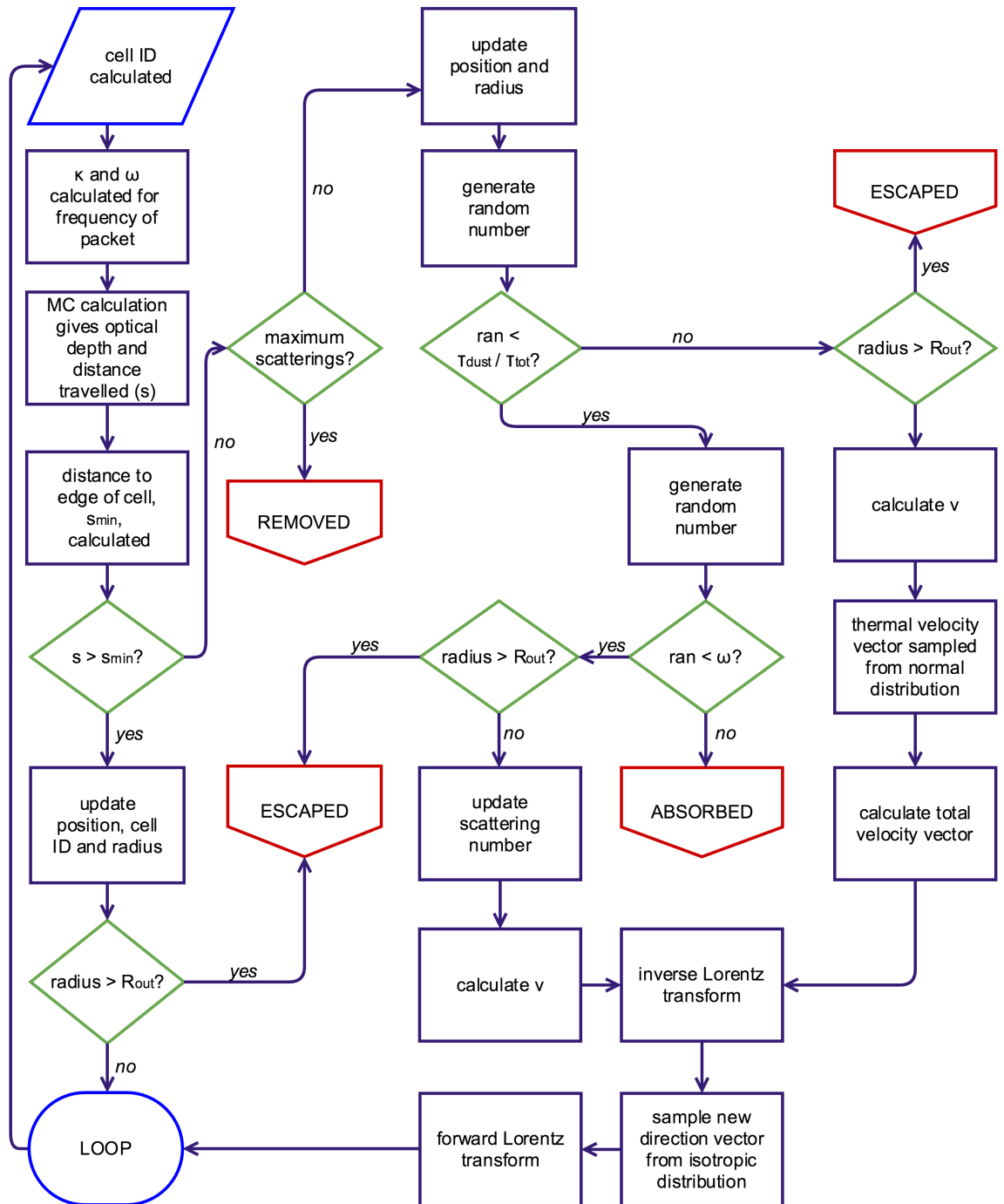


**Figure 2.4.** A flowchart representing the processes that occur in the *propagate* subroutine. The life of a packet passing through the grid may be determined by following the flowchart starting at the blue parallelogram (top left). Purple rectangles indicate a standard step in the evolution, green diamonds indicate that a determination must be made, red boxes mean that the packet's evolution has concluded as it has escaped, been absorbed or been removed and the blue oval indicates a return to the start of the routine.

a packet through the nebula accurately. A full pictorial representation of the procedures that are implemented in this module may be found in the flowchart in Figure 2.4. For each packet in each grid cell, the optical depth in that cell is calculated based on the dust density and the opacity at the wavelength of the current packet. These are obtained by interpolating between discrete opacities at points in the frequency array. At this stage, the Monte Carlo technique is applied in order to determine the distance travelled by the packet by sampling from the cumulative probability distribution. This displacement is then compared to the distance from the packet's current location to the edges of the grid cell in order to ascertain whether or not the packet escapes the cell. If it does escape then the packet advances to the bounds of the current grid cell and the process is repeated in the next cell. If it does not escape then an event occurs. In this case, random numbers are sampled in order to determine whether the packet experiences electron scattering, dust scattering or absorption. If the packet is absorbed then it is removed from the simulation, the *propagate* subroutine is arrested and the code returns to the driver to emit a new packet. If it is scattered then the velocity vector is calculated. In the case of electron scattering this involves considering the thermal velocity component as well as the bulk velocity at that radius. The Lorentz transforms are applied based on the velocity vector and the frequency and weight of the packet are updated. A new direction of propagation is sampled in the scatterer's rest frame from an isotropic distribution and is transformed into the observer's rest frame. The routine is recalled to start afresh with the new propagation direction.

### (I) The random routines module

The *random\_routines* module contains a single subroutine which is, like the *BHmie* routine, a standard routine obtained from an online library. It allows for a random velocity vector to be sampled from a normal distribution with specified mean and standard deviation. The standard deviation is calculated as per equation 2.39 and passed to the subroutine which samples a random 3-dimensional vector from the normal distribution with the specified standard distribution and zero mean. This is passed back to the *propagate* routine where it is added to the bulk velocity in order to determine the overall velocity of the scattering electron.

**(m) The model comparison module**

The *model\_comparison* module is responsible for post-processing the outputted line profile and comparing the model results with inputted observed data. The routine interpolates between two model frequency points to obtain a flux value at each frequency point of the observed line profile. Both profiles are then normalised such that the total flux is unity. A MSE calculation is then performed as per equation 2.41. The smaller the value of MSE, the better the fit is. It should be noted however that observational data with a poor signal-to-noise ratio will have an inherently larger MSE than data with a good signal-to-noise ratio.

### 2.3.2 OpenMP Parallelisation

Monte Carlo simulations are exceptionally well-suited to parallelisation. The path of each packet through the nebula is unaffected by the transport of any other packet. It is therefore possible to run multiple instances of the *propagate* module at once by using several threads. Since the vast majority of the processing power of the simulation is driven from this module, it is theoretically possible to achieve a nearly linear speed-up; i.e. if the number of cores is doubled, the run time should be approximately halved.

DAMOCLES was parallelised using OpenMP. OpenMP is an Application Program Interface (API) that allows for shared-memory parallel programming in Fortran and C/C++. OpenMP causes the code to be run serially on a single processor until a parallel region is reached. At this point the single master thread branches into multiple threads, and multiple instances of the same section of code are run on each. In DAMOCLES, this splitting occurs at the start of the loop which controls the emission and propagation of packets from each shell. If, for example,  $10^7$  packets are emitted and 5 threads are used, then approximately  $2 \times 10^6$  packets will be independently processed on each thread. Practically however, the OpenMP keyword *dynamic* is declared ensuring that, as soon as each thread has finished processing a packet, it immediately moves onto the next one. If the *static* keyword were specified instead then the number of packets to be processed would be equally divided between the threads at the start of the loop. In this case, if, by random chance, one thread happened to have significantly more absorbed packets than another, then potentially utilisable processing power would be lost as the core waited for the others to finish.

At the start of the parallel region variables accessed within the shared region are specified as shared or private. Private variables are not seen by other threads and allow the value of a single named variable, for example “frequency”, to have different values on different threads. Shared variables have the same value regardless of the thread number, for example, “grid cell density”. As each packet escapes, its weighted energy must be added to the final energy array. It is important that two threads do not attempt to alter the value of this shared array at the same time as data may be lost or corrupted. This section of code is therefore enclosed inside a *critical* region. This instruction ensures that code in this block is to be executed by only one thread at a time. Extensive testing was performed to ensure that outcomes were not affected by the implementation of a parallel environment.

For further information about the OpenMP API please refer to Chapman et al. (2007).

### 2.3.3 Input Variables

There are a significant number of parameters that may be varied in the code. Many of these are important variable parameters that will be the parameters of interest when modelling. However, there are also a significant number of variables that allow other properties of the model to be controlled. All parameters can, broadly, be divided into one of three categories: properties of the emitted rest-frame line or doublet, properties of the dust and gas in the ejecta and properties of the grid and code architecture. I list all the variables that are input in the primary input file in Table 2.2 and will here briefly describe the basic meaning and function of each one.

#### (a) Properties of the emitted rest-frame line or doublet

##### **lambda1\_0**

This is a real number that specifies the initial rest-frame monochromatic wavelength at which packets are emitted in nanometres. If a doublet is to be modelled then this represents the wavelength of one of the singlets.

**Table 2.2.** The input variables read in from the input file and example values

Input Variable	Example Value	Input Variable	Example Value
lambda1_0	636.3	MD_tot	1.0e-4
L_tot	0.003	l	1.0
L_Halpha	0.005	q	1.3
doublet	1	b	2.0
lambda2_0	630.0	gas_shell	1
L_ratio	3.1	v_max_gas	8000
ES	1	Rrat_gas	0.05
ES_temp	10000	l_gas	1.0
LS	0	q_gas	1.5
VelShift	1	b_gas	2.0
MF	0.5	ncells	50
FF	0.1	n_packets	1e8
dayno	680	n_bins	1000
v_max	5000	n_shells	100
Rrat	0.2	dustfile	“species_file.in”

### **L\_tot**

$L_{tot}$  is the total luminosity of the line in units of  $10^{40}$  ergs  $s^{-1}$ . The initial energy of each packet ( $E_0$ ) is therefore  $L_{tot}$  divided by the total number of packets used in the simulation (n\_packets). For lines which have flux calibrated observed spectra, this allows the flux of the line to be modelled in addition to the normalised shape. This variable is also used to estimate the undepleted luminosity of the observed line when it is initially emitted from the ejecta.

### **L\_Halpha**

Similar to  $L_{tot}$ ,  $L_{H\alpha}$  is the total luminosity of the  $H\alpha$  line. In the case of  $H\alpha$  modelling, this value should be the same at the value of  $L_{tot}$ . This variable is used in the calculation of the electron density and it is not necessary to specify it unless the electron

---

scattering environment is switched on (see section 2.2.6 for further details).

### **doublet**

This is an integer of value 1 or 0 that indicates the use or otherwise of the doublet environment. If set to 1 it triggers the doublet logical in the code to be initialised to *true*. The code will then read in the values of lambda2\_0 and L\_ratio in order to initialise packets with two different starting monochromatic wavelengths. Packets are processed through the nebula as normal before being collated in bins weighted according to both their history and the intrinsic flux ratio of their parent singlet.

### **lambda2\_0**

This is a real number that specifies the initial rest-frame monochromatic wavelength of packets emitted from the second line in a doublet environment. The wavelength is specified in nanometres.

### **L\_ratio**

This real number gives the ratio between the respective luminosities of the lines in a doublet environment. The ratio should be declared as the flux at lambda1\_0 divided by the flux at lambda2\_0. It is expected that the doublet environment will generally be used to model forbidden lines, for example the [OI] $\lambda 6300, 6363\text{\AA}$  doublet, where the intrinsic flux ratio between the singlets may be theoretically determined.

## (b) Properties of the dust and gas in the ejecta

### **ES**

This keyword is similar to the doublet keyword in that, by setting it equal to 1 or 0, it indicates the use or otherwise of the electron scattering environment. If it is set to 1 then it initialises the electron scattering logical in the code to *true*. If the electron scattering environment is switched on then this triggers the calculation of electron densities for every cell in the grid. This density contributes to the total optical depth of a cell and, as packets are propagated through each cell, they will experience an electron scattering event with probability  $1 - e^{\tau_e}$ , where  $\tau_e$  is the electron scattering optical depth.

**ES\_temp**

When the electron scattering environment is switched on, it is necessary to calculate the electron density of each cell in the grid. In order to do this an average gas temperature must be specified to allow for  $q_{H\alpha}$  to be determined. DAMOCLES will not accept any value for this input variable; only 5,000K, 10,000K and 20,000K will be accepted. These are thought to be a representative range of temperatures for the ejecta of supernovae at epochs where electron scattering still has the potential to influence observed line profiles. These specific values were selected since they are the values of  $q_{H\alpha}$  that are given in Osterbrock & Ferland (2006).

**MF**

If this keyword (short for mass fraction) is set to 0 then a smooth density distribution of both gas and dust will be constructed. If it is not however, then this will automatically initialise the clumping logical present in the code to *true*. The value specified should be between 0 and 1 and gives the total fraction of the dust mass that should be located in clumps. The remaining fraction will be smoothly distributed according to the power-law density profiles declared in the input file.

**FF**

If the clumping environment is switched on (using the **MF** keyword) then **FF** declares the total filling factor of the clumps. The filling factor is defined as the fraction of the total volume of the ejecta that is occupied by clumps. For a fixed clump size, this parameter effectively determines the number of clumps to be used. Once the number of clumps to be used has been determined, the mass fraction then determines the density of the clumps.

**dayno**

This keyword represents the epoch being modelled. In combination with the declared maximum velocity, it is used to consistently calculate an outer radius as

$$R_{out} = 8.64 \times 10^{-6} \left( \frac{t}{\text{days}} \right) \left( \frac{v_{max}}{\text{kms}^{-1}} \right) \quad (2.42)$$

where  $R_{out}$  is in units of  $10^{15}\text{cm}$ .

**v\_max**

This is the maximum velocity used in the code. It is assumed to be the velocity at the outer radius of the ejecta and is used to construct a velocity profile of the form

$$v(r) = v_{max} \left( \frac{r}{R_{out}} \right)^l \quad (2.43)$$

where  $l$  is also declared in the input file and  $R_{out}$  is calculated based on the epoch and the maximum velocity.

**Rrat**

This number is the ratio between the inner and outer radii. Once the outer radius has been calculated as per Equation 2.42, this ratio is used to calculate the value of the inner radius.

**MD\_tot**

This real number specifies the total dust mass to be distributed throughout the grid in solar masses ( $M_\odot$ ).

**l**

$l$  is the exponent of the radial velocity law in the code as per equation 2.43.

**q**

$q$  describes the relationship between the radial dust density distribution and the emissivity distribution. It is the exponent of the emissivity distribution as a function of density such that  $i(\rho) \propto \rho^q$  where  $i(\rho)$  is the emissivity at a given density. Though this parameter may take any real value, it is frequently fixed to be  $i(\rho) \propto \rho^2$ , i.e. proportional to the product of the recombining proton and electron densities in the case of H $\alpha$  and to the product of the neutral atom oxygen and electron densities in the case of collisionally excited emission (e.g. [O I], [O III]).

**b**

This parameter describes the value of the exponent of the dust density distribution in terms of radius such that  $\rho \propto r^{-b}$ .

**gas\_shell**

This flag may be set to 0 or 1 to indicate that dust and gas are coupled or decoupled respectively. If it is set to 1 then the “decoupled” logical in the code is set to *true* and the gas follows a density distribution that is independent of the density distribution followed by the dust. The following five parameters specify the geometry of the emitting gas. It is worth noting that in the case where gas and dust are coupled to each other, the gas follows the same distributions as specified for dust by the parameters described above.

**v\_max\_gas**

This is the gas analogue of the v\_max parameter described above.

**Rrat\_gas**

This is the gas analogue of the Rrat parameter described above.

**l\_gas**

This is the gas analogue of the parameter *l* described above.

**q\_gas**

This is the gas analogue of the parameter *q* described above.

**b\_gas**

This is the gas analogue of the parameter *b* described above.

**(c) Properties of the grid and code architecture****LS**

For an initially symmetric distribution of gas and dust, it is not necessary to specify a line of sight as all lines of sight will produce the same profile. It is therefore more efficient to collect all packets that escape regardless of their direction of flight. However, if an alternative, axisymmetrical or asymmetrical geometry is adopted then the ability to specify a line of sight is important. If this keyword is set to 1 then the “line of sight”

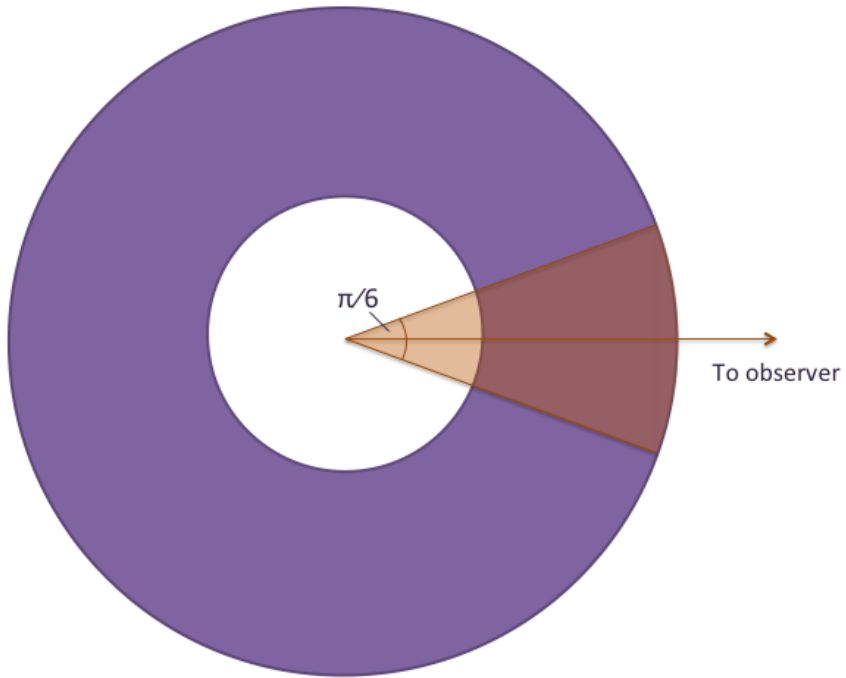


**Figure 2.5.** Schematic representing which packets are collected when the line of sight environment is switched on. Packets that contribute to the emergent line profile are those that escape the nebula within a cone with vertical angle  $\pi/6$ .

logical will be initialised as *true*. Only packets that escape within a cone of vertical angle  $\pi/6$  will be collected. Clearly, in practice, the angle would be very much smaller but it is prohibitively expensive to run enough packets through the simulation that enough are collected to achieve a reasonable resolution when a very small angle is adopted. A representation of this construction is presented in Figure 2.5.

### VelShift

This is another environment flag. As a packet is transported through the nebula it may experience repeated scattering events that shift its original frequency beyond that expected from the maximum theoretical velocity. It is discussed in depth in the next chapter how this process of “velocity shifting” may result in a profile that exhibits an extended red wing. It is useful for the purposes of comparison and investigation to be able to turn off this process of repeated scattering events so that the only frequency shift experienced by a packet is at the initial emission.

**ncells**

Each axis is split into this number of divisions. The total number of cells in the grid is therefore  $\text{ncells}^3$ .

**n\_packets**

This variable determines the number of packets to be emitted and processed through the grid. This parameter is particularly important for achieving a resolution that is high enough to give representative results. The larger the number of packets used, the less noise is present in the final profile. The Monte Carlo process introduces noise that can sometimes be construed as a result when it is in fact a numerical artefact. Using a large number of packets reduces this risk and improves the output of the model. In general, the more dense an environment, the more packets it is necessary to use. This is because any packets which are absorbed are removed from the simulation and therefore reduce the desired resolution. Since the vast majority of the total processing power is used to propagate packets through the grid, an increase in the number of packets results in a significant reduction in runtime. Optically thick simulations of dust with a very high or a very low albedo have a significantly longer runtime than optically thin scenarios. When choosing this parameter, a careful balance must be found between the total runtime and the desired resolution.

**n\_bins**

This value gives the total number of divisions in the frequency array and thus determines the overall frequency resolution of the output line profile. Since the resulting profile is in fact a histogram binned into a frequency array, it is important that these divisions are fine enough to provide a seemingly continuous line profile. Apparent jumps or discontinuities could be produced if too few bins are used.

**n\_shells**

This parameter controls the total number of shells the ejecta is divided into at the start. If a particularly steep radial profile is adopted for either the velocity profile or the density profile then the user may wish to increase the number of shells used to compensate. Increasing the number of shells will have an effect on the overall runtime, but this will be

insignificant in comparison to altering the number of packets.

#### **dustfile**

Finally, this string gives the name of the input file that itemises the list of dust species, their relative abundances and size distributions.

### **2.3.4 Output, Post-Processing and Visualisation**

The primary output file contains details of the emergent line profile. Three columns are written out to the file at the end of the simulation. These are the wavelength, velocity and flux of the modelled line profile. Another output file is also produced by the *model\_comparison* module. This file prints both the inputted observed line profile and the outputted emergent line profile to one file in the same velocity bins. This allows for easy plotting. The columns printed in this file are wavelength, modelled flux and observed flux. The total flux is normalised to unity for both line profiles. Both of these files may be represented graphically in a straightforward fashion using any plotting package. In addition to these output files, a number of useful quantities are also calculated by DAMOCLES and output to *stdout* throughout the course of the simulation. If desired, the user may direct the *stdout* to a file for a record of these quantities. A list of all quantities output by DAMOCLES is given in Table 2.3.

Throughout my modelling, I used standard and custom routines written with MATLAB to plot line profiles, both modelled and observed. I also use MATLAB to process some of the data. For example, where I have observations with accurate observed fluxes, I scale the modelled profile to the observed profile so that fluxes remain to scale. This is initially performed by a custom MATLAB routine which smooths the modelled data to reduce any Monte Carlo noise before identifying the maximum flux value. Identifying the peak flux of the observed line profile allows the modelled profile to be automatically scaled. Any inaccuracies in the scaling may then be easily adjusted manually. I also use MATLAB for any other illustrative graphs or plots, for example, the plots in Figure 2.2 were generated in MATLAB using its 3D-scatter plotting function.

**Table 2.3.** List of all outputs and example values produced by the DAMOCLES code.

Output	Example Value
Total number of cells	125000
Number of grid cells inside ejecta	65544
Total volume of supernova ejecta ( $10^{42}$ cm $^3$ )	304523264
Volume of a grid cell or volume of a clump ( $10^{42}$ cm $^3$ )	4668.52
Width of a grid cell (cm)	1.67e+15
Mass check (calculated as $\rho V$ )	6.03e-04
Average grain number density (cm $^{-3}$ )	1.96e-09
$C_{ext}$ at rest-frame wavelength	2.94e-08
$C_{sca}$ at rest-frame wavelength	1.63e-08
Albedo at rest-frame wavelength	0.554
Average optical depth to rest-frame wavelength	2.062
Average optical depth in V band	2.18
Average electron density (cm $^{-3}$ )	71509.1
Average electron scattering optical depth	1.31e-02
Total number of packets	100000
Number of active (propagated) packets	100000
Number of inactive packets	0
Number of absorbed packets	82949
Percentage of absorbed packets out of all active packets	82.95
Number of packets in line of sight	17050
Percentage of escaped packets in line of sight	100.0
Estimated undepleted line luminosity ( $10^{40}$ ergs s $^{-1}$ )	1.10e-05
Total (depleted) luminosity ( $10^{40}$ ergs s $^{-1}$ )	1.90e-06
Total energy absorbed ( $10^{40}$ ergs s $^{-1}$ )	1.57e-06
Energy per active packet ( $10^{40}$ ergs s $^{-1}$ )	1.90e-11
MSE	0.3557

## 2.4 Further Developments

The modular structure of DAMOCLES allows for easy implementation of additional functionality in the future. By simply adding extra modules, extra physics can be included in the code. There is potential for this code to be expanded in a number of directions. An immediately apparent development involves the dust itself. The treatment and understanding of the dust in the ejecta is crucial to understanding the shape of the line profile. The ability to place different species in different locations within the ejecta is not currently included. This would allow for stratified or asymmetrical distributions of dust species motivated by the potentially discrete locations of the parent elements. Similarly, streamlining the ability to model arbitrary density distributions and geometries would allow for more complex and accurate modelling of supernova ejecta. The ejecta of SN 1987A, for example, is known to have an asymmetric distribution which could potentially affect the contour of the line profile (e.g. Sinnott et al. (2013)).

As mentioned previously, dust grains are rarely perfectly spherical and can be far more complicated in shape. It might be of interest to include a module that treats a continuous distribution of ellipsoids (Bohren & Huffman 1983), as mentioned in Section 1.1.3, in order to more accurately model the effects of different dust grain shapes. Subsequent development of the code has allowed for the consideration of the effects of modelling forward scattering. By adopting the Henyey-Greenstein model, forward scattering was included for a fixed value of the anisotropy parameter  $g$  (Henyey & Greenstein 1941). Resultant line profiles were affected only slightly, with profiles exhibiting a reduced degree of both absorption and scattering due to a lower incidence of scattering events. However, because of the spherically symmetric geometry of the models and the original isotropic emission, the observed effects of including forward scattering were found not to be substantial even for an extremely high value value of  $g = 0.98$ . Further development of the code should allow for arbitrary phase functions to be implemented and the treatment of anisotropic scattering should be included by default where non-spherically symmetric geometries are modelled. In these cases, the effects of forward scattering may be more significant than in cases of spherically symmetric geometries. Anisotropic expansion of supernova ejecta can sometimes result in radiation that is polarised. By extending this development to include the capacity to model polarised radiation, we may be able to glean further information about the distribution and nature of dust forming within the ejecta.

It would also be theoretically possible to expand the code to become a fully self-consistent radiative transfer code or to include certain approximations (e.g. the Sobolev approximation) to allow for full spectral modelling of non-optically thin lines throughout the optical and infrared.

Aside from the development of the code directly, the current process of manual fitting can be laborious and has the potential miss potentially good fits due to the large number of variable parameters. I have completed some work over the course of this PhD wrapping DAMOCLES in a MCMC (nested sampling) routine that allows for a more thorough investigation of parameter space resulting in a full multivariate probability distribution. For reasons of time, the research presented in the following chapters was performed using manual fitting but further work finishing the implementation of this routine or a similar one would be invaluable in the future.

## Chapter 3

---

# Probing DAMOCLES: Testing and a Parameter Sensitivity Analysis

The introduction of any new piece of software into a field has the potential to yield exciting new results. The first step in this process should therefore be a thorough investigation into the reliability of the code and an assessment of the outputs from a theoretical standpoint. Before the modelling of real data takes place, it is important to understand why the variation of a given parameter affects results in a particular way. A comprehensive understanding of parameter space not only facilitates the modelling process but may also give rise to interesting results in and of itself.

To this end, this chapter describes the ways in which DAMOCLES was tested and the results of these tests. I then also present a parameter sensitivity analysis. I describe the changes that are seen in the shapes of line profiles and consider any distinctive features that arise as a result of varying the parameters of interest. I also consider the physical processes behind these effects.

### 3.1 Testing and benchmarking the code

The field of astronomy is highly reliant on the production of bespoke software to understand and interpret observations from telescopes and to develop and test new theories. As one of only a few sciences which do not have the ability to run experiments or to vali-

date results in a laboratory, progress is made via mathematical analyses or computational models based on observed data. Astrophysicists typically develop their own programs because a deep understanding of the topic to be modelled is required. Like any experiment, however, the “apparatus” should be checked and tested in order to establish its reliability.

Throughout the production of DAMOCLES, I sought, as far as was possible, to maintain best practices in scientific computing as detailed by Wilson et al. (2012). The code is carefully structured into modules and subroutines as described in the previous chapter. Each of these units was inspected for sense and accuracy as it was written, and at each update and addition the code as a whole was tested against basic logical checks, for example comparing outputs to manually calculated properties. I used GitHub for version control and uploaded new versions after any significant alterations. In addition to regular evaluations conducted throughout the program development, it was very important to establish that DAMOCLES produced standard results as expected.

There is a general lack of published models in the literature that consider dust-affected asymmetric line profiles. This is problematic since there are no published benchmark cases against which I could compare results. I therefore considered a number of analytic line profiles derived from first principles for the case of a dust-free spherically symmetric expanding medium. This process ensured the functionality of the grid and the initialisation and propagation of energy packets. Additionally, I also checked the absorption and scattering components of the code which are crucial to the modelling of a dusty medium. I considered some optically thick scenarios and qualitatively compared my results with those presented by Lucy et al. (1989). The profiles presented by Lucy et al. (1989) were produced both analytically and from numerical modelling and are of scenarios that are typical of those treated by DAMOCLES. They are also the only published numerical models of dust-affected asymmetric line profiles and as such it is important that DAMOCLES is capable of reproducing these results.

### 3.1.1 Theoretical line profiles from first principles

The simple nature of a spherically-symmetric expanding medium with a given velocity outflow law and emissivity distribution allows for analytical line profiles to be calculated from first principles in the dust-free case. Based on the methods of Gerasimovic (1933), I derive a set of three equations that describe the contours of theoretical line profiles under different starting conditions.

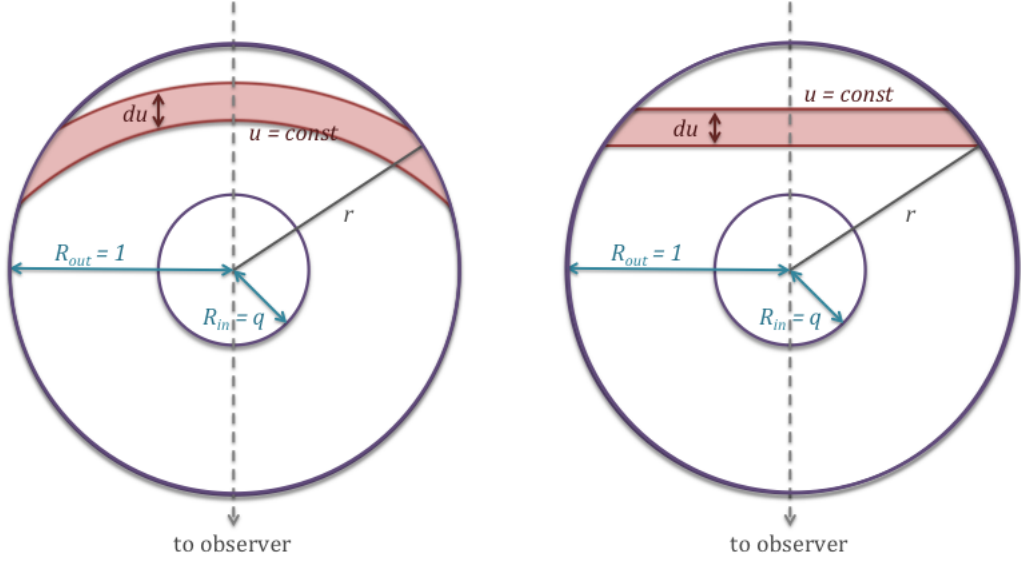


**Figure 3.1.** Diagrams illustrating the dust-free model and some of the relevant variables used in the derivation of the equations of analytical line profiles. On the left is the general case with curves of constant  $u$  labelled. On the right is the special case of an orthogonal  $(u, s)$  net when  $\alpha = 1$  and therefore  $v(r) \propto r$ .

Describing the fractional expansion velocity of the shell as  $v(r) \propto r^\alpha$  with  $\alpha \neq 0$  such that  $v(r) = \frac{V(r)}{V_{max}}$  where  $V(r)$  and  $V_{max}$  represent physical velocities and  $v_{max} = 1$ , the velocity along the line-of-sight to the observer is given by

$$u(r, \theta) = r^\alpha \cos \theta \quad (3.1)$$

where  $r = R/R_{max}$  is the fractional radius and  $R$  and  $R_{max}$  represent physical radii. For curves with constant line-of-sight velocity  $u = const$  we therefore have

$$dr = \frac{r}{\alpha} \tan \theta d\theta \quad (3.2)$$

For  $u = const$ , the line element  $ds$  is given by

$$ds^2 = r^2 d\theta^2 + dr^2 = r^2 \left( \frac{\tan^2 \theta}{\alpha^2} + 1 \right) d\theta^2 \quad (3.3)$$

and therefore, along curves of constant  $u$  we have

$$s = u^{\frac{1}{\alpha}} \int_{\theta_0}^{\theta_1} \frac{\sqrt{\frac{\tan^2 \theta}{\alpha^2} + 1}}{\cos^{\frac{1}{\alpha}} \theta} d\theta \quad (3.4)$$

The angle  $\psi$  between the tangent to a curve and the radial line is given by the formula (in polar coordinates)

$$\tan \psi = r \frac{d\theta}{dr} \quad (3.5)$$

which for curves of  $u = \text{const}$  gives

$$\tan \psi = \frac{\alpha}{\tan \theta} \quad (3.6)$$

Curves of constant line-of-sight velocity therefore intersect the line  $\theta = 0$  orthogonally, although the  $(u, s)$  net is only orthogonal if  $\alpha = 1$  (see Figure 3.2).

We can now construct a volume element between  $u$  and  $u + du$  by rotating a section of thickness  $du$  around the  $\theta = 0$  axis. Assuming that  $i(r)$  is the emission per unit volume (dependent only on radius), then the energy emitted by the nebula between  $u$  and  $u + du$  is proportional to

$$\int_{\mathcal{C}} i(r) r \sin \theta \, r \, d\theta \, dr = \int_{\mathcal{C}'} [i(r) r^2 \sin \theta] \frac{\partial(r, \theta)}{\partial(u, s)} \, ds \, du \quad (3.7)$$

where the integral is a line integral along curves  $\mathcal{C}$  of constant  $u$  and square brackets denote a change of variables.

We therefore compute the Jacobian from Equations 3.1 and 3.4 as

$$\frac{\partial(u, s)}{\partial(r, \theta)} = \alpha u \sqrt{\frac{\tan^2 \theta}{\alpha^2} + 1} \quad (3.8)$$

Assuming an initial emissivity distribution dependent on radius only, we put  $i(r) \propto r^{-2\beta}$  (i.e. appropriate for a gas density distribution  $\rho \propto r^{-\beta}$  with the emissivity proportional to the gas density squared). Substituting Equation 3.8 into Equation 3.3 and calculating the curvilinear integral along curves of constant  $u$  yields the following:

$$i(u) du \sim du \int_{\mathcal{C}} \frac{r^{2(1-\beta)} \sin \theta}{\alpha u \sqrt{\frac{\tan^2 \theta}{\alpha^2} + 1}} \, ds \quad (3.9)$$

Substituting in Equations 3.1 and 3.7 and transforming to an integral in  $\theta$  gives

$$\begin{aligned} i(u) du &\sim \frac{du}{\alpha u^{\frac{2\beta-3+\alpha}{\alpha}}} \int_{\theta_0}^{\theta_1} \cos^{\frac{2\beta-3}{\alpha}} \theta \sin \theta d\theta \\ &\sim \frac{du}{u^{\frac{2\beta-3+\alpha}{\alpha}}} \left[ \frac{\cos^{\frac{2\beta-3+\alpha}{\alpha}} \theta}{2\beta - 3 + \alpha} \right]_{\theta_0}^{\theta_1} \end{aligned} \quad (3.10)$$

for  $\frac{2\beta-3}{\alpha} \neq -1$  where  $i(u) du$  is the energy emitted in a volume element and  $\theta_0$  and  $\theta_1$  are the bounds of this element. The case  $\frac{2\beta-3}{\alpha} = -1$  results in a logarithmic relationship.

In the case of a “filled” nebula, i.e. one where the inner radius is vanishingly small in comparison to the outer radius the above result may be evaluated between  $\theta_0 = 0$  and  $\theta_1 = \arccos u$  and the equation of the line profile is

$$i(u) du \sim \pm \frac{du}{(2\beta - 3 + \alpha) u^{\frac{2\beta-1+\alpha}{\alpha}}} \left( 1 - u^{\frac{2\beta-3+\alpha}{\alpha}} \right) \quad (3.11)$$

If the nebula is not “filled”, that is to say, the inner radius is some fraction of the outer radius and the remnant is a detached shell with inner radius  $R_{in} = q$  and outer radius  $R_{out} = 1$  such that  $q = \frac{R_{in}}{R_{out}}$ , the above formula is only valid from some critical value  $u' = q^\alpha$  to  $u = 1$ . For  $u < u'$ , we obtain

$$i(u) du \sim \pm \frac{du}{(2\beta - 3 + \alpha)} \left( \frac{1}{q^\alpha} - 1 \right) \quad (3.12)$$

and therefore the top of the line is flat while the sides are sloping.

Crucially, the width of the flat section is determined by

$$u' = q^\alpha \quad (3.13)$$

or simply  $u' = q$  in the case where  $v \propto r$ , whilst the shape of the profile outside of the flat-topped region is described by Equation 3.11.

Profiles with a variety of shapes may be derived from these formulae depending on the relative values of  $\alpha$  and  $\beta$ . Here we consider three main families of curves:

1.  $i(u) \sim u^{-\gamma} - 1 \quad (\alpha > 0, 2\beta - 3 + \alpha > 0)$
2.  $i(u) \sim 1 - u^\gamma \quad (\alpha > 0, 2\beta - 3 + \alpha < 0)$
3.  $i(u) \sim -\log u \quad (\alpha > 0, 2\beta - 3 + \alpha = 0)$

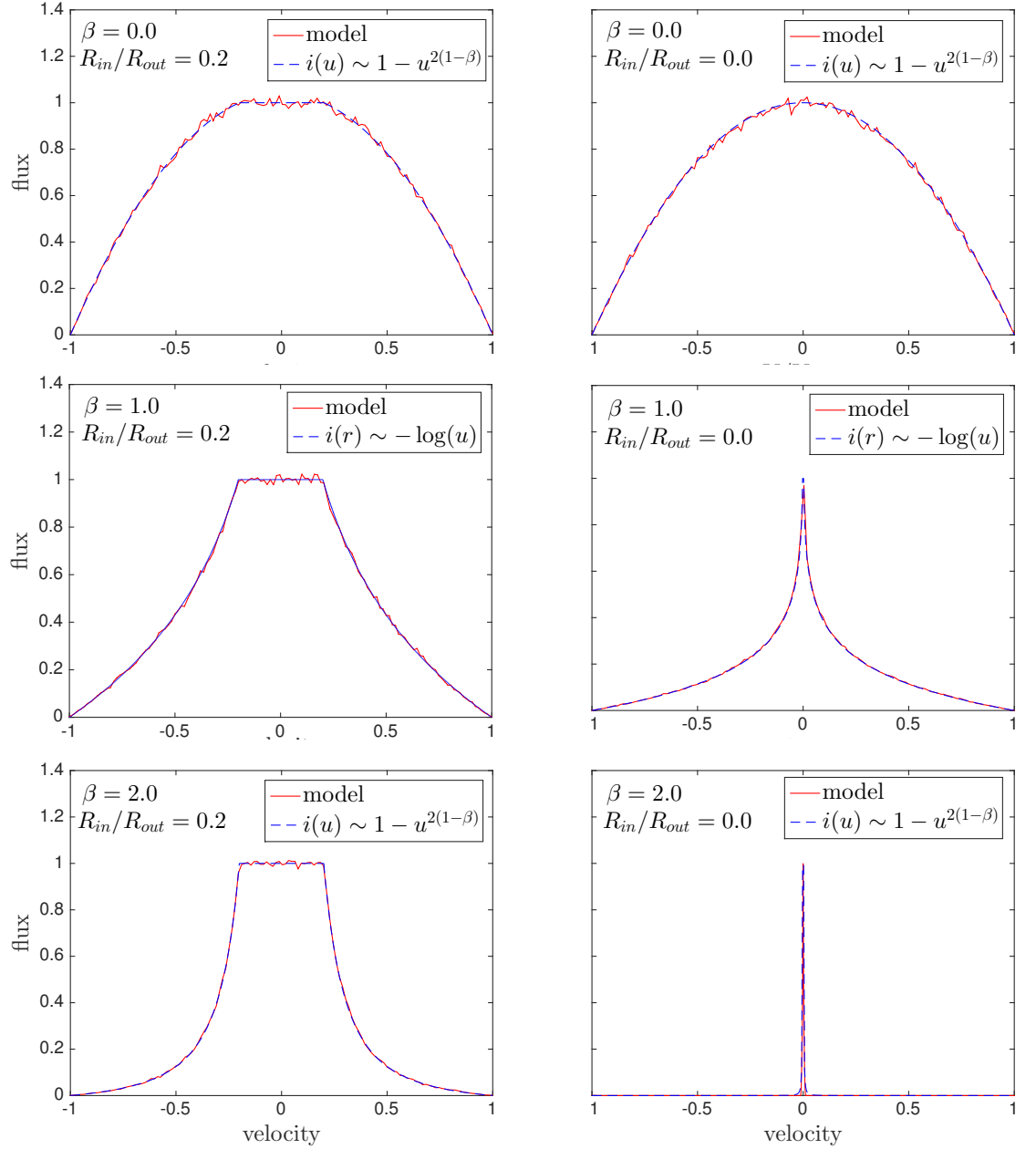


**Figure 3.2.** *Red:* Benchmark models for optically thin ( $\tau = 0$ ) line profiles with fractional velocity  $v(r) \propto r$ . Top to bottom: initial emissivity profiles  $i(r) \propto r^{-2\beta}$  with  $\beta = 0.0$ ,  $\beta = 1.0$  and  $\beta = 2.0$ . Cases with  $R_{in}/R_{out} = 0.2$  are on the left and  $R_{in}/R_{out} = 0.0$  on the right. The presence of a plateau in the upper plots is due to the finite inner radius (detached shell). *Blue:* The analytical case with  $i(u) \sim 1 - u^{2(1-\beta)}$  except in the case of  $\beta = 1$  where  $i(u) \sim -\log u$ .

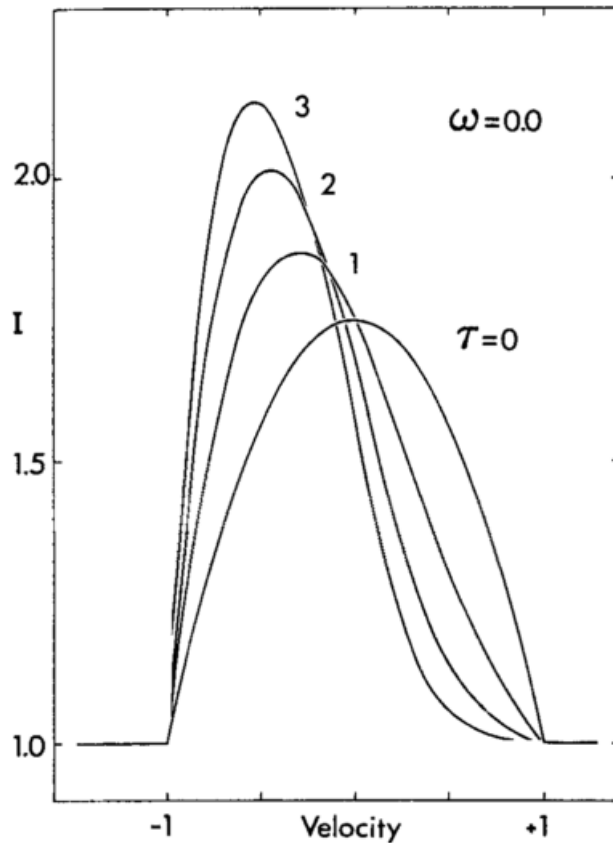


**Figure 3.3.** The analytically derived line profiles of Lucy et al. (1989) corresponding to their Model II scenario with zero albedo dust, for a variety of total dust optical depths.

where  $\gamma$  is defined as  $\gamma = |\frac{2\beta-3+\alpha}{\alpha}|$ .

Models are presented for each of these cases, both for a filled nebula and for a shell structure with  $R_{in}/R_{out} = 0.2$ . A velocity profile  $v \propto r$  appropriate for supernova ejecta in the free expansion phase is used throughout (Li & McCray 1992; Xu et al. 1992; McCray 1996; Baron et al. 2005). Values of  $\beta = 0, 1$  and  $2$  are adopted. Figure 3.2 illustrates the excellent agreement between the analytical case and the models. All fluxes are scaled to unity at the peak.

I conclude from this testing that all aspects of the code that are associated with initialising the packets into the grid are functioning correctly since an error at this stage would result in disagreement with the above theory.

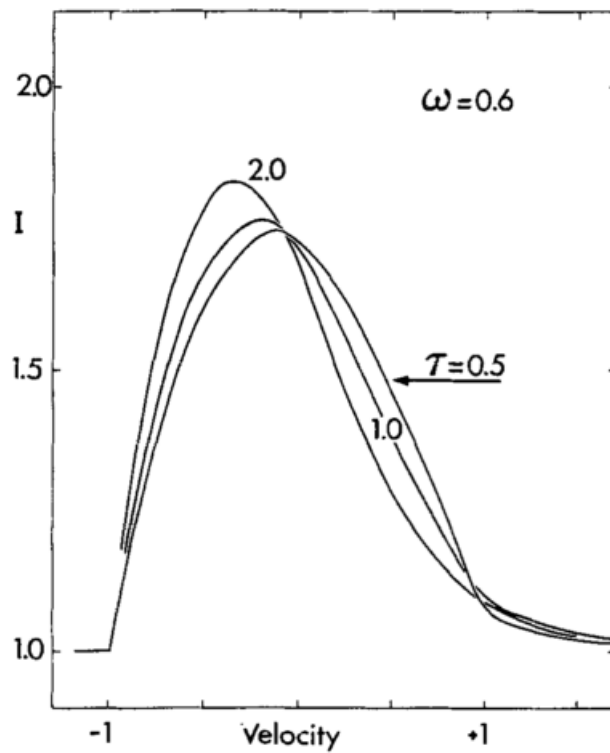


**Figure 3.4.** The numerically modelled line profiles of Lucy et al. (1989) corresponding to their Model III scenario with dust of albedo  $\omega = 0.6$ , for a variety of total dust optical depths.

### 3.1.2 Benchmarking against numerical models

In addition to the tests for the optically thin line profiles detailed above, I also compared my outputs to those derived by Lucy et al. (1989) in order to assess the accuracy of the scattering and absorption aspects of the code. I considered two similar cases, equivalent to Models II and III of Lucy et al. (1989) (see Figures 3.3 and 3.4 respectively). In the first case, dust with zero albedo (pure absorption) was uniformly distributed throughout a filled nebula with a velocity profile  $v \propto r$ . In the second case, the same scenario was considered but in a medium of dust with albedo  $\omega = 0.6$ .

In the first case, the profile may once again be derived analytically from the basic geometry using the fact that radiation will be attenuated by a factor  $e^{-2\tau_\nu v}$  between points with line-of-sight fractional velocities  $-v$  and  $+v$  where  $\tau_\nu$  is the optical depth at frequency  $\nu$  from the centre to the outer edge of the ejecta. The line profile is therefore

given by

$$\frac{I(v)}{I(-v)} = \exp(-2\tau_\nu v) \quad (3.14)$$

Lucy et al. (1989) presented several examples for both the analytical case of the perfect absorber and a Monte Carlo model for grains with albedo  $\omega = 0.6$ . I include their profiles here for comparison in Figures 3.3 and 3.4. I present line profiles in Figure 3.5 that were generated by DAMOCLES using the same model parameters as described by Lucy et al. (1989). I note that the resulting profiles exhibit the same features and shape. The peaks of all profiles are shifted further to the blue with increasing optical depth and all profiles are also flux-biased towards the blue. Of particular interest is the scattering wing that appears beyond the maximum velocity ( $v_{max} = 1$ ) on the red side of the profiles in the partial scatterer case as a result of the packets doing work on the expanding sphere. This was noted by Lucy et al. (1989) as a potential diagnostic for the presence of dust in the ejecta of a supernova and I will discuss this further in the next section.

## 3.2 A Parameter Sensitivity Analysis

It is of general interest to establish potential diagnostic signatures in the line profiles of supernovae and their remnants in order to trace dust formation more effectively. The capacity to specify a number of parameters is included in DAMOCLES. The variation of each parameter potentially affects the contour of the resulting line profile in a different way. By investigating each parameter separately over a range of values whilst keeping the other parameters fixed, it may be possible to identify certain characteristics of dust-affected line profiles that may be associated with a particular property of the dusty medium. This insight could help to explain unusual or interesting features of observed line profiles where dust is suspected to be an influential factor. In this chapter, I investigate and discuss the effects of the main parameters of interest, namely:

- the maximum velocity,  $V_{max}$
- the ejecta radius ratio,  $R_{in}/R_{out}$
- the dust optical depth,  $\tau$

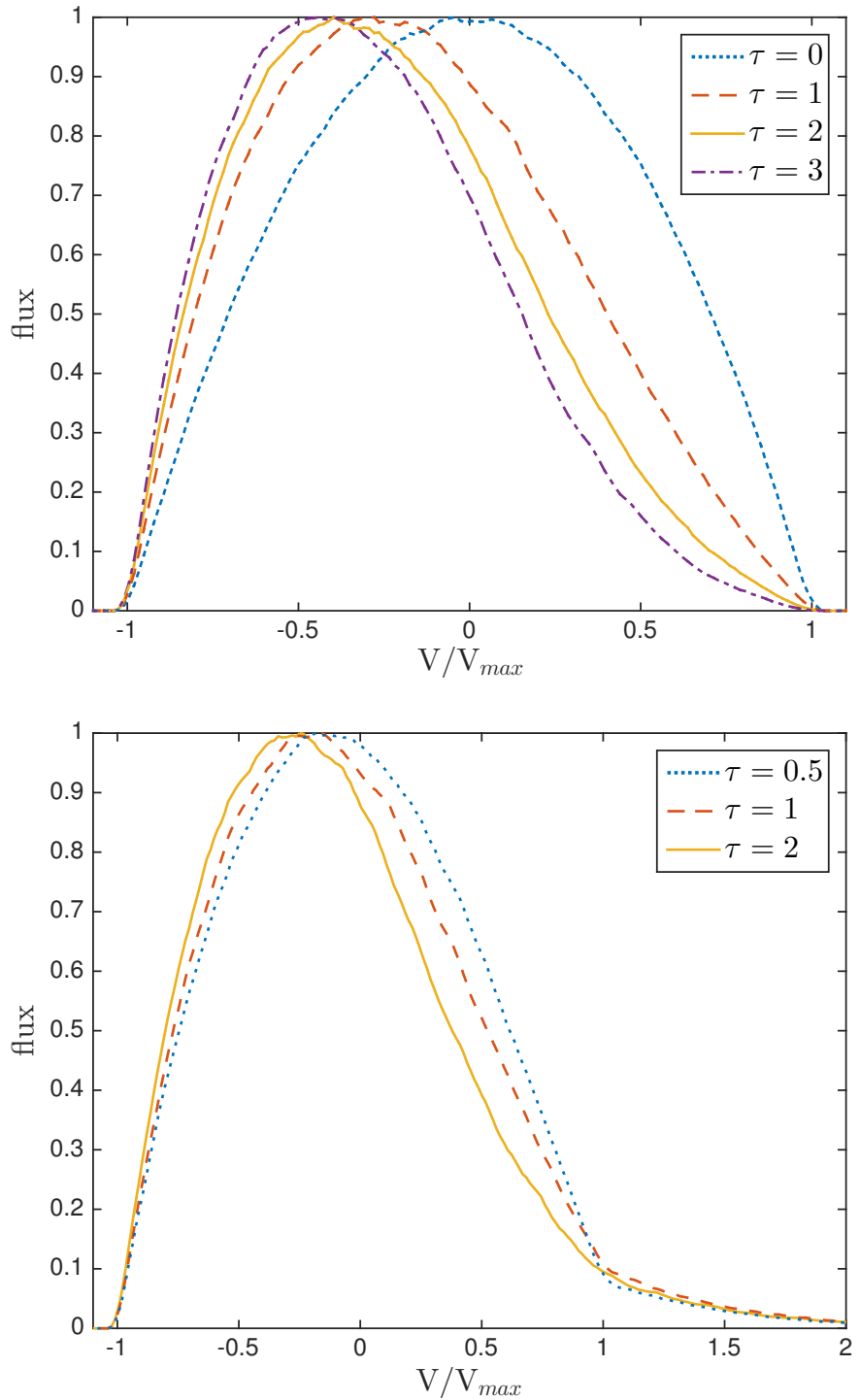


**Figure 3.5.** Benchmark models for line profiles with  $v \propto r$ ,  $i(r) \propto \text{constant}$  and a filled sphere with  $R_{in}/R_{out} = 0$ . Pure dust absorption models ( $\omega = 0$ ) are presented in the top plot, whilst partially scattering models are presented at the bottom ( $\omega = 0.6$ ) as per Lucy et al. (1989) Models II and III. All resulting profiles have been scaled to unity flux at their peaks.

- the dust albedo,  $\omega$
- the dust density profile exponent,  $\beta$ , where  $\rho \propto r^{-\beta}$

I also investigate the capacity of this type of model to infer properties of the dust itself, specifically the dust grain radius range and distribution, and the variety and relative abundances of different grain species present in the dusty medium.

### 3.2.1 The maximum line velocity, $V_{max}$

The maximum velocity is defined as the velocity at the outer edges of the line emitting region for a given line. The maximum velocity may vary between different spectral lines or doublets due to different locations of species having differing ionization thresholds. Clearly, the larger the maximum velocity used the wider the profile becomes. To some extent therefore the steepness of the density profile and the maximum velocity can act to counter each other since a steeper density distribution narrows the profile (see Section 3.2.5). The shape of the wings of the profiles, however, generally precludes much degeneracy in this aspect - the overall shape of the line profile can be used to determine the exponent of the density distribution to within a relatively small range.

More important is the effect that the maximum velocity has on the overall optical depth. Since the outer radius is calculated directly from the maximum velocity (as  $R_{out} = V_{max} \times t$  where  $V_{max}$  is determined from the blue side of the observed line profile), the overall volume of the ejecta is determined solely by this value and the ratio of the inner and outer radii. The total dust optical depth to which the radiation is exposed can therefore be greatly affected by even a relatively small change in the maximum velocity for fixed values of the other parameters. Practically, however, the maximum velocity can usually be fairly well determined from the observations (identified as the point where the flux vanishes on the blue side) and may be further constrained through modelling.

### 3.2.2 The ejecta radius ratio, $R_{in}/R_{out}$

As already discussed in Section 3.1.1, the width of the flat top is determined by the ratio of the inner and outer radii, the exponent of the velocity profile and the maximum velocity. I assume that the supernova is in free expansion from just a few months after the explosion and therefore  $r = vt$  such that within the ejecta the velocity profile takes the form  $v \propto r$

at a fixed time i.e. the supernova expands self-similarly (Li & McCray 1992; Xu et al. 1992; Kozma & Fransson 1998b). For this case,  $R_{in}/R_{out}$  is given by

$$\frac{R_{in}}{R_{out}} = \frac{V_{min}}{V_{max}} \quad (3.15)$$

where it is often possible to constrain  $V_{min}$  and  $V_{max}$  to a relatively narrow range simply from the observed line profile.

The majority of spectral lines emitted from supernovae and supernova remnants are expected to have a flat top before dust attenuation effects since it is rare for these objects to form a completely filled nebula. However, even a very small amount of dust attenuation may result in the line profile appearing to be smoothed at its peak.

The effects of absorption by dust on a line profile for a filled nebula with  $R_{in}/R_{out} = 0$ , as opposed to a detached shell, are shown in Figure 3.5. All profiles have been scaled to unit flux at their peaks.

### 3.2.3 The dust optical depth, $\tau$

As expected, greater attenuation of the original line profile is seen on the red side (see Figures 3.6 and 3.7). The profiles are most revealing at lower dust optical depths since the effects of the asymmetric absorption can be seen in different sections of the profiles and the profiles therefore tend to exhibit more features. The region of the profile that is most clearly affected by dust absorption is the flat-topped region. A small amount of absorption in this region results in a skewed profile, with a fraction of the flat-topped section removed. The peak becomes blue-shifted as a result, but only to the original value of  $-V_{min}$ , the minimum velocity corresponding to  $R_{in}$ . In addition to the attenuation in this region, the red wing of the profile is also somewhat reduced, and the blue wing somewhat increased relative to their original symmetric positions. The result is a relatively “jagged” looking profile, often with sharp changes at  $\pm V_{min}$ . The profile is generally asymmetric, although the degree of absorption in the flat-topped region may sometimes make it seem as though the profile is in fact symmetric and uniformly blue-shifted (see Section 3.2.7 for further discussion). Observationally, these sharp features might become smoothed due to insufficient spectral resolution.

At high dust optical depths or when the ratio of the inner and outer radii is small,

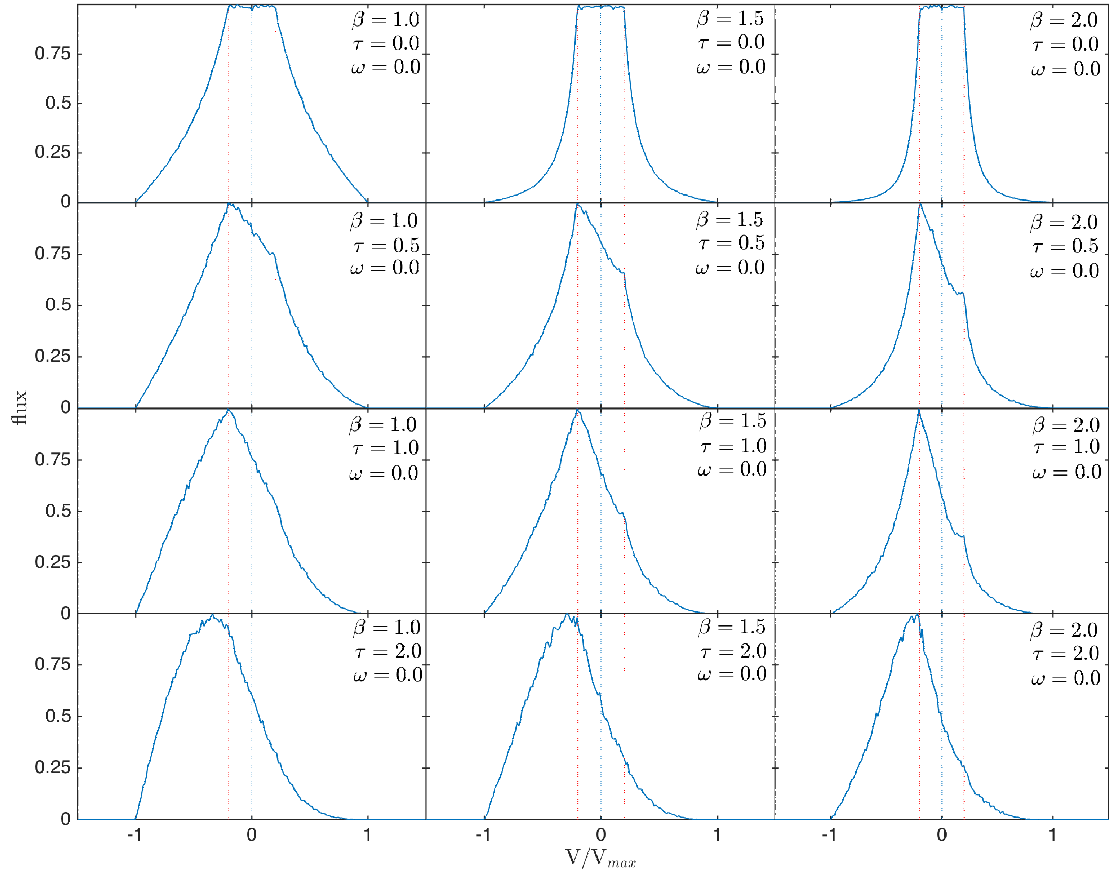


**Figure 3.6.** Set of models with  $i(r) \propto r^{-2\beta}$  for  $\beta = 1.0$  (left),  $\beta = 1.5$  (middle) or  $\beta = 2.0$  (right),  $\omega = 0$ ,  $R_{in}/R_{out} = 0.2$ ,  $v(r) \propto r$  and  $v_{max} = 1$  illustrating the effects of varying  $\tau$ . Peak fluxes are scaled to unity.

the entire profile is shifted to the blue and the peak moves beyond  $-V_{min}$  further into the blue. The profiles also tend to become more smooth and featureless. A set of models showing the effects of varying optical depths for different density profiles and dust albedos are presented in Figures 3.6 and 3.7 with  $R_{in}/R_{out} = 0.2$ .

#### The completely filled nebula case

To reproduce similar characteristic dust-affected line profiles where the peak of the profile is shifted beyond  $-V_{min}$  into the blue is “easier” for smaller values of  $V_{min}$ . The completely filled nebula is therefore effectively analogous to cases of higher optical depths for a detached shell and the same effects that are illustrated in Figures 3.6 and 3.7 apply.

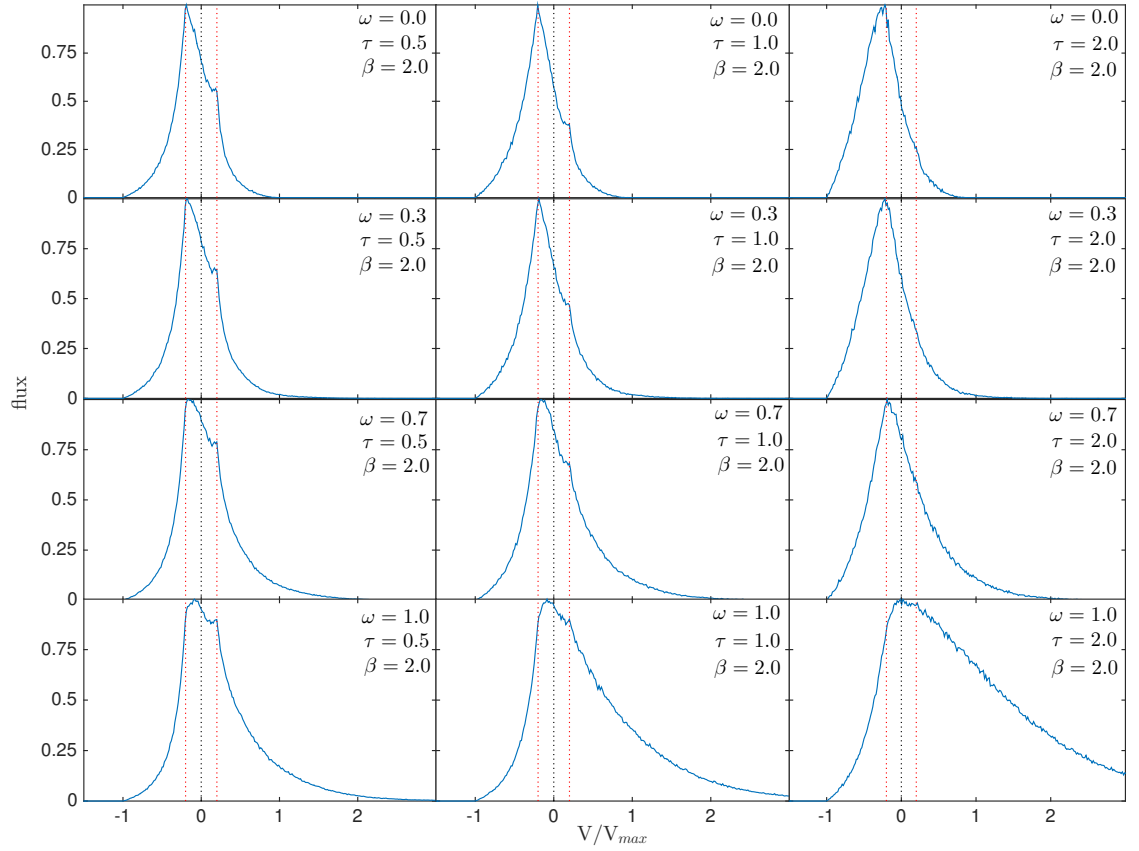


**Figure 3.7.** Set of models with  $i(r) \propto r^{-4}$  (i.e.  $\beta = 2.0$ ),  $R_{in}/R_{out} = 0.2$ ,  $v(r) \propto r$  and  $v_{max} = 1$  illustrating the effects of varying  $\tau$  and  $\omega$ . Peak fluxes are scaled to unity.

### 3.2.4 The dust albedo, $\omega$

In the past, there has often been a focus on the effects of absorption by dust on the shapes of line profiles and less attention has been paid to the potential effects of scattering by dust. In fact, line profiles can be significantly affected by scattering of radiation. The greater attenuation of radiation received from the receding portion of the ejecta results in an asymmetry of the line profile whereby the majority of the observed emission is located bluewards of the peak. However, the effects of repeated dust scattering events within the ejecta can substantially alter the shape of a line profile and potentially can act to counter the blue-shifted asymmetry.

Not only does repeated scattering of photons increase the number of potential opportunities for a given photon to be absorbed but it also results in continuous shifting of the frequency of the photon to the red. The photon must do work on the expanding shell of dust in order to escape and thus many of the photons are reprocessed beyond the theoret-

ical maximum velocity on the red side of the profile. Even in the case of dust grains with a relatively low albedo, a surprisingly persistent wing on the red side of the profile is seen, generally beyond the maximum theoretical velocity of the emitting region. In the case of strong dust scattering and high dust optical depths, this can actively result in a shift in the overall asymmetry of the profile, with the majority of the emission being emitted redwards of the peak. The peak however, remains blue-shifted (for example the bottom left panel of Figure 3.7) or central (for example the bottom right panel of Figure 3.7). For the line profile to exhibit this effect requires the dust to be a nearly perfect scatterer; of the albedos plotted in Figure 3.9 only the nearly-transparent MgSiO<sub>3</sub> sample of Jäger et al. (2003) exhibits such a behaviour.

The combination of relatively low dust optical depths, initially flat-topped profiles, greater attenuation on the blue side along with increased flux on the red side due to scattering can result in a profile that sometimes ends up appearing almost symmetrical, particularly if contaminants, such as narrow lines or blending with other broad lines, are present or if the resolution of the data is low. The potential for apparently symmetrical profiles that appear to have been uniformly blue-shifted should be noted (see Figures 3.6 and 3.7 for examples of this).

### 3.2.5 The dust density profile, $\rho \propto r^{-2\beta}$

Whilst the density profile of the dust may have some effect on the resulting profiles, it is the initial emissivity profile (dependent on the gas density profile) that has the greatest effect on the shape of the line profile. In general, the steeper the emissivity distribution, the narrower the line profile becomes. The sides of the line profile may become almost vertical for a very steep distribution since the majority of the emission then comes from a very narrow velocity range (see Figure 3.2). For a flat-topped profile of fixed width this approximates the square profile produced in the case of an emitting shell with constant velocity.

The dependence of the shape of the line profile on the emissivity distribution is described analytically in Section 3.1.1 for the case of very optically thin dust. However, for even fairly low dust optical depths, the density profile plays a significant role in determining the shape of the line profile where it is affected by dust absorption. As previously discussed, at relatively small optical depths for reasonable  $R_{in}/R_{out}$ , a section of the flat-topped region is removed resulting in a peak at  $-V_{min}$ . The shape of the profile in this

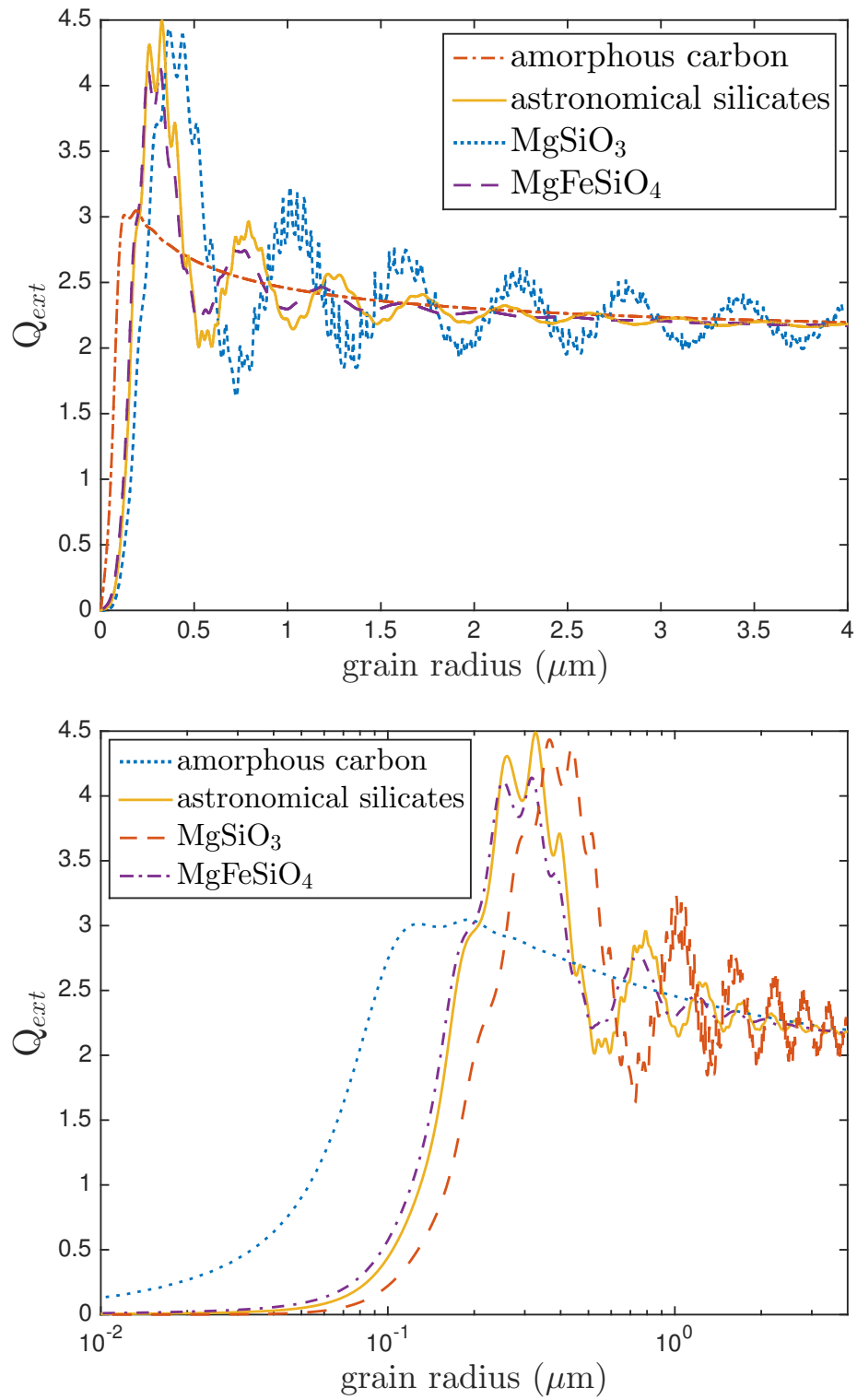


**Figure 3.8.** The variation of extinction efficiency ( $Q_{ext}$ ) with grain radius at  $\lambda = 656$  nm for Zubko et al. (1996) BE amorphous carbon, Draine & Lee (1984) astronomical silicate and the  $\text{MgSiO}_3$  and  $\text{MgFeSiO}_4$  samples of Jäger et al. (2003) and Dorschner et al. (1995) respectively. A linear scale is presented on the top and a log scale on the bottom.

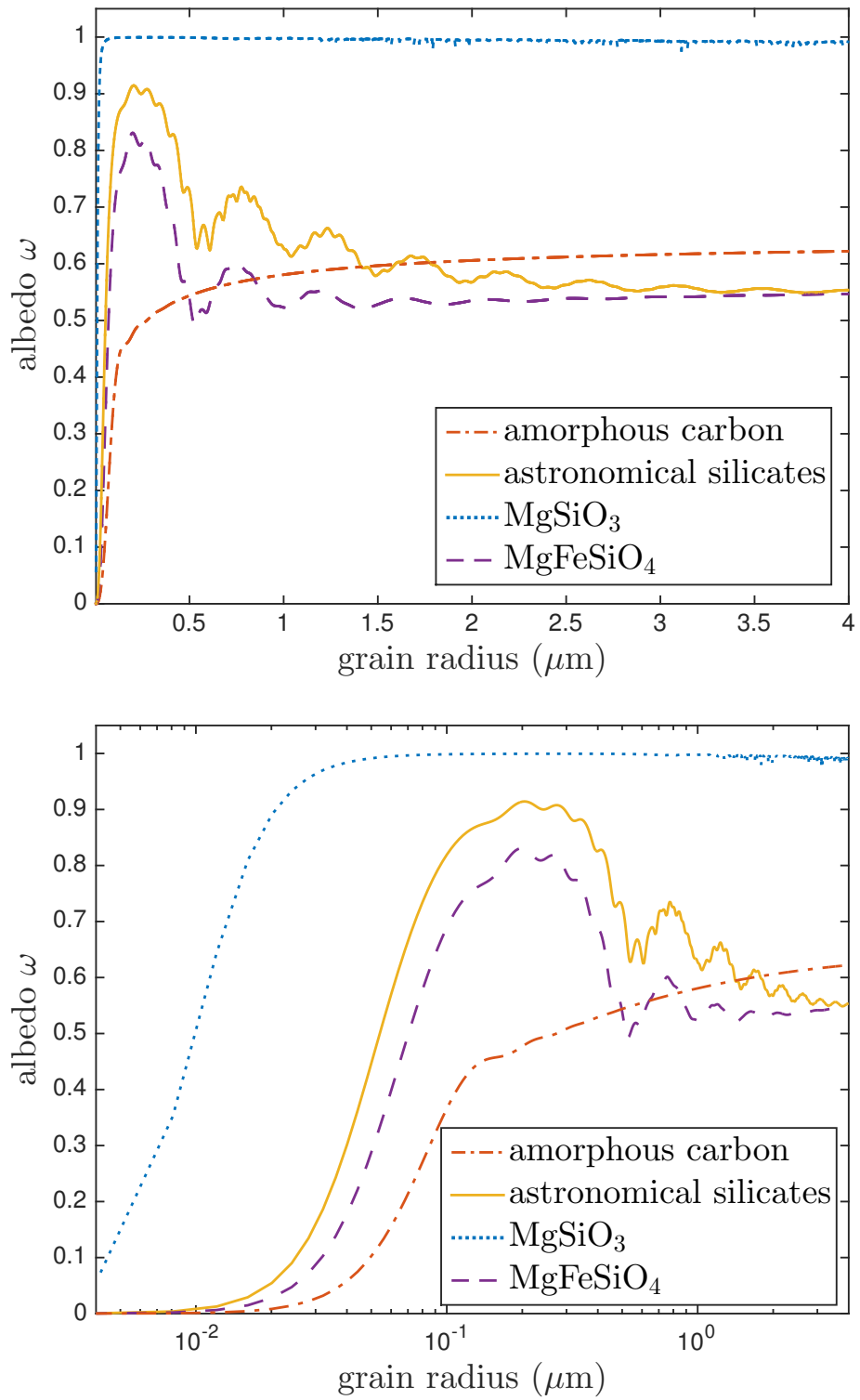


**Figure 3.9.** The variation of albedo with grain radius at  $\lambda = 656 \text{ nm}$  for Zubko et al. (1996) BE amorphous carbon, Draine & Lee (1984) astronomical silicate and the MgSiO<sub>3</sub> and MgFeSiO<sub>4</sub> samples of Jäger et al. (2003) and Dorschner et al. (1995) respectively. A linear scale is presented on the top and a log scale on the bottom.

region is significantly affected by the density profile. Shallow density profiles (low  $\beta$ ) produce a virtually linear variation in flux between  $-V_{min}$  and  $+V_{min}$  (for example the profiles in the left column of Figure 3.6). For a fixed dust optical depth, the steeper the distribution becomes, the more concave the profile becomes between  $-V_{min}$  and  $+V_{min}$ , ultimately resulting in a clear shoulder to the profile at  $+V_{min}$  (for example the profiles in the right column of Figure 3.6). For extremely steep density distributions this can result in a double peaked profile with a trough to the red of  $V = 0$ . An illustration of the effects on the line profiles of varying  $\beta$  and  $\tau$  is shown in Figure 3.6. As previously noted, these features may not be apparent in observed line profiles with poor spectral resolution.

### 3.2.6 Inferring properties of the dust from the models

The presence of an extended red wing at large positive velocities in combination with increased extinction on the red side at smaller positive velocities can allow the values of  $\tau$  and  $\omega$  to be well constrained. Where this occurs it is possible to translate these values into a dust mass and grain radius for a given species or combination of species using grain optical properties and Mie theory (see Figures 3.8 and 3.9).

For amorphous carbon, the albedo generally increases with grain radius. The presence and extent of any scattering wing on the red side of the observed profile can therefore help to place limits on the grain radius. However, the greater the grain radius used the smaller the available cross-section for interaction per unit dust mass. Larger masses of dust are therefore required to fit the same degree of absorption if a larger grain radius is used. This is in contrast to SED radiative transfer modelling where larger grain radii generally result in less dust being required to fit the IR portion of the SED (W15). These two techniques in tandem may therefore provide limits on grain radii for different species or combinations thereof.

It is known that the use of different optical properties may substantially alter dust masses derived using SED fitting for a given species of specific grain radius (e.g. Owen & Barlow (2015)). However, the use of different sets of grain optical constants in our models seems to have only a minor effect on the required dust masses, except for cases where the albedo is close to unity (pure scattering grains).

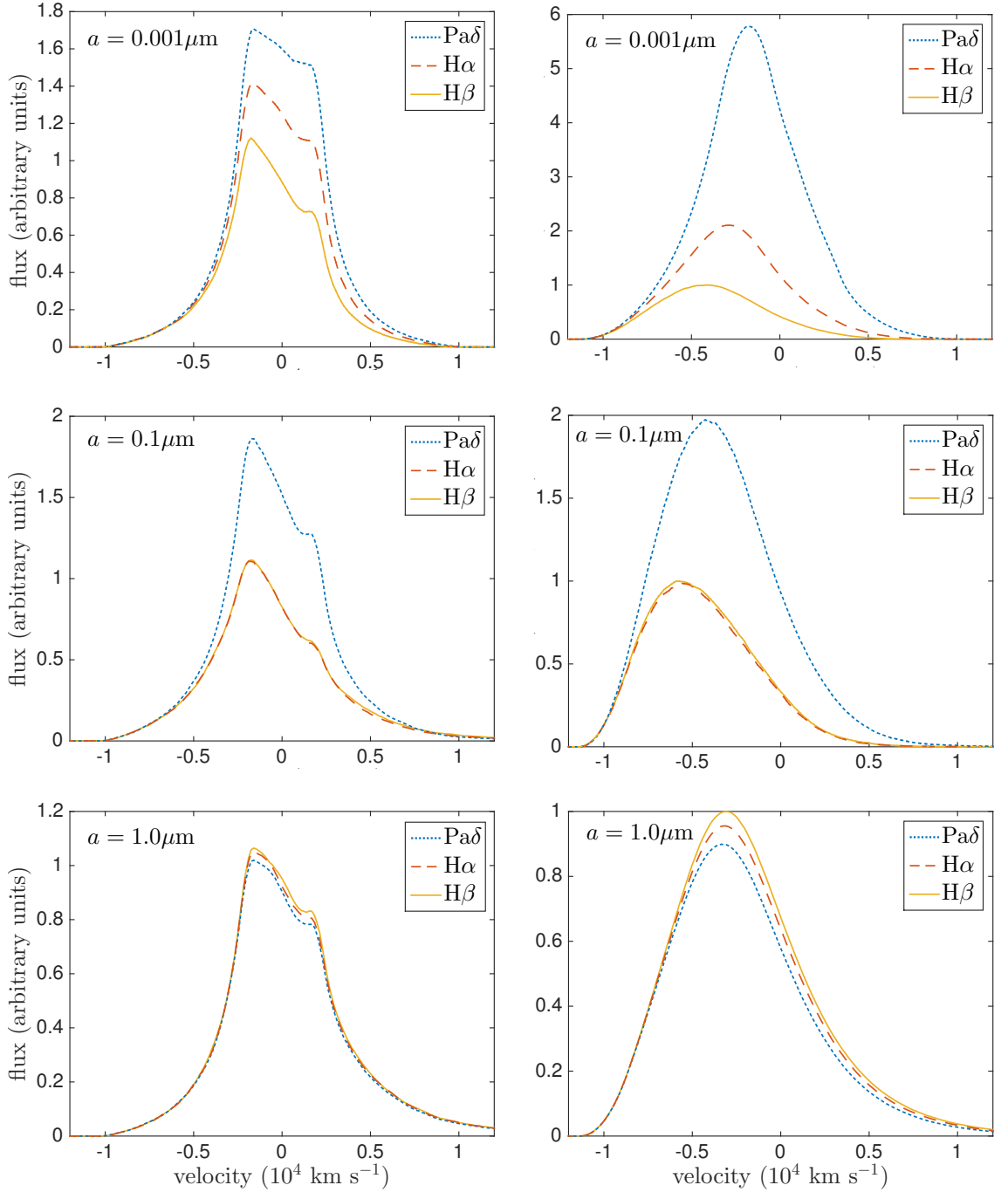


**Figure 3.10.** Model line profiles for H $\alpha$  (6563Å in red), H $\beta$  (4861Å in yellow) and Pa $\delta$  (10049Å in blue) for optically thin and optically thick cases on the left-hand side and right-hand side respectively. All models adopted density profile  $\rho(r) \propto r^{-4}$  (i.e.  $\beta = 2$ ), velocity profiles  $v(r) \propto r$  and radii ratio  $R_{in}/R_{out} = 0.2$ . The grain radii used were  $a = 0.001 \mu\text{m}$  (top),  $a = 0.1 \mu\text{m}$  (middle) and  $a = 1.0 \mu\text{m}$  (bottom). All the above models used amorphous carbon.

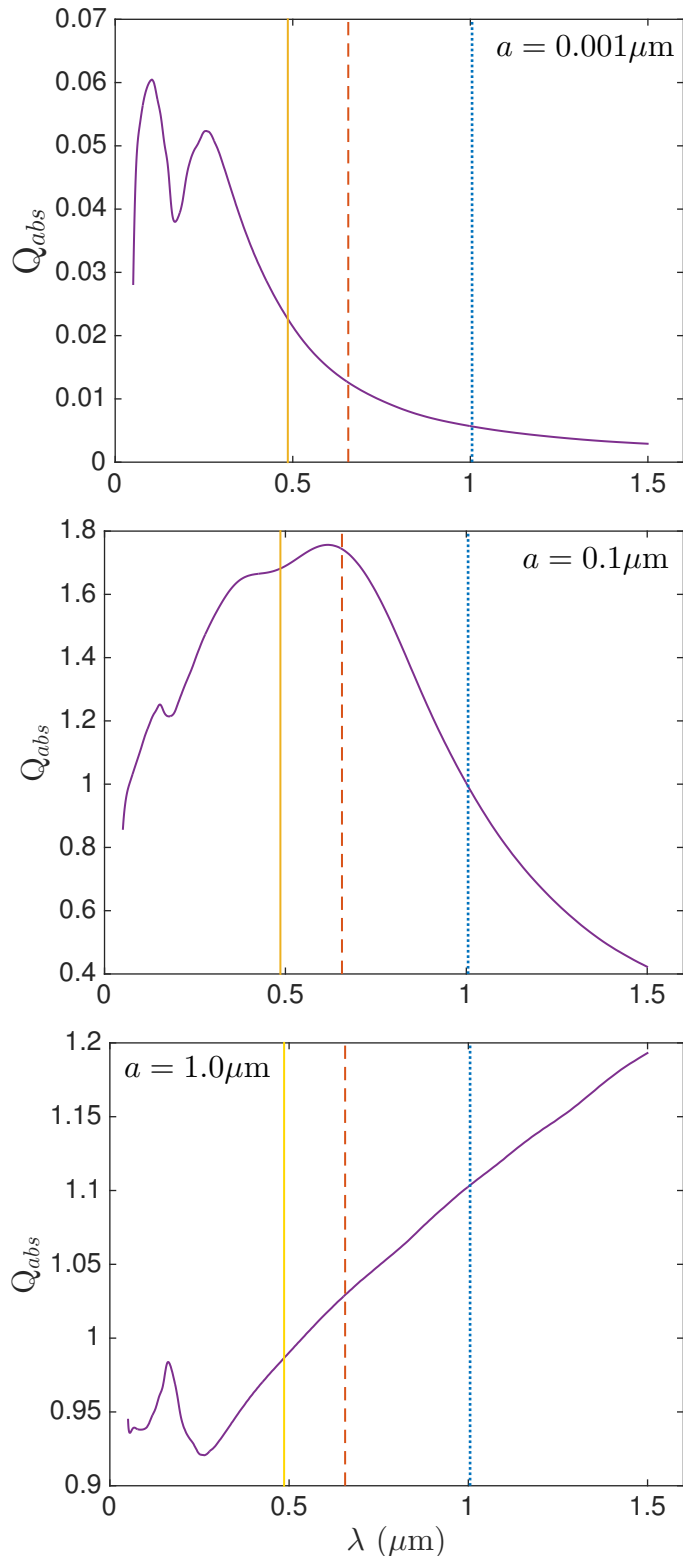


**Figure 3.11.** The variation of amorphous carbon dust absorption efficiency with grain radius. The grain radii plotted are  $a = 0.001 \mu\text{m}$  (top),  $a = 0.1 \mu\text{m}$  (middle) and  $a = 1.0 \mu\text{m}$  (bottom). The vertical lines mark the wavelengths of H $\alpha$  (6563Å in red), H $\beta$  (4861Å in yellow) and Pa $\delta$  (10049Å in blue).

### 3.2.7 The wavelength dependence of dust absorption

The greater the dust optical depth, the more attenuation of the line there will be. As expected, the red side of the profile suffers a greater degree of absorption than the blue side. The resulting asymmetry is somewhat more complex than perhaps previously thought. Dust has repeatedly been cited as the agent responsible for the apparent blue-shifting of supernova line profiles in the manner of the profiles presented in Figure 3.5; that is, relatively high optical depths result in an overall shift of the entire profile towards the blue. The relationship between the blueshifting of the peaks of profiles and their wavelength has been discussed by several authors in relation to dust formation (Smith et al. 2012; Fransson et al. 2014; Gall et al. 2014).

In practice a relatively large dust optical depth is required to actively shift the peak of the profile bluewards of its natural  $-V_{min}$  position (corresponding to the velocity at the inner radius of the shell) unless this value is very small in comparison to  $V_{max}$  i.e. the profile originally had a very narrow flat top. In many cases it seems likely that the dust may not be optically thick and the blue-shifting of the peak of the profile is just a result of attenuation in the flat-topped section (close to  $R_{in}$ ). The peak would then tend to be located at  $-V_{min}$ .

Since dust absorption is wavelength dependent for  $2\pi a < \lambda$ , one might expect the position of the peak line flux to be dependent on the wavelength of the line being considered. I note here that whilst variations of the peak velocity of a line as a function of line wavelength may occur in cases of high dust optical depths or small  $R_{in}/R_{out}$ , this may not be the case for many supernova lines emitted from ejecta with low dust optical depths. The wavelength-dependence of dust absorption instead can result in differing degrees of extinction in the flat-topped region of each profile but still leave the peak at its blue-shifted position of  $-V_{min}$ . If this is the case then there would be no reason to expect a variation in the position of the peaks of profiles to be correlated with the wavelength dependence of dust absorption. Instead one would expect it potentially to trace the location of different ions within the ejecta, possibly with different  $V_{min}$  values observed for different species.

For lines from the same ion, for example the Balmer and Paschen lines of HI, we might expect to see peaks at the same position but differing degrees of absorption. At high spectral resolutions, it might be possible to detect differences in the shapes of the line profiles, particularly between  $-V_{min}$  and  $+V_{min}$  where the steepness of the incline

traces the degree of dust absorption. This can be seen in Figure 3.10 where I illustrate the effects of the wavelength dependence of dust absorption for three lines, H $\alpha$  (6563Å), H $\beta$  (4861Å) and Pa $\delta$  (10049Å). All lines were modelled using three different grain radii and for both optically thin and thick dust cases. I also show in Figure 3.11 the variation of the absorption efficiency with wavelength for three different amorphous carbon grain radii.

### 3.2.8 The effect of a grain radius distribution

It is important to consider the potential effect on the dust mass of modelling a grain radius distribution instead of a single grain radius. For a grain radius distribution the overall extinction cross section,  $C_{ext}$ , at a given wavelength is calculated as

$$C_{ext} = \int_{a_{min}}^{a_{max}} Q_{ext}(a)n(a)\pi a^2 da \quad (3.16)$$

where  $Q_{ext}(a)$  is the extinction efficiency for a grain radius  $a$  and  $n(a)$  is the number of grains with size  $a$ . The overall extinction efficiency is then

$$Q_{ext} = \frac{C_{ext}}{\int_{a_{min}}^{a_{max}} n(a)\pi a^2 da} \quad (3.17)$$

The scattering cross-section  $Q_{sca}$  is similarly calculated. As a result of these calculations, there is rarely a single grain radius that has the same albedo and extinction efficiency as a size distribution. Modelling a size distribution instead of a single grain radius may therefore alter the deduced dust mass. Since models are only sensitive to the optical depth and the albedo, however, it is not possible to deduce the grain radius range or distribution and only single grain radii are investigated in the models that are presented in the following chapters.

Whilst this apparently limits the scope of these results, it is important to consider the extent to which considering grain radius distributions would alter the derived dust masses. For each model that I construct, I derive a dust mass for a given species at a single grain radius. By considering the equation that determines the optical depth for both a single grain radius and a grain radius distribution, I can approximately calculate the required dust mass for a distribution of grain radii from the properties of a single-size model by equating the optical depths. The optical depth for a single grain radius is proportional to

$$\tau_\nu \propto Q_{ext,\nu}(a)\sigma(a)n_d \quad (3.18)$$

where  $n_d$  is the number density of dust grains,  $\sigma(a)$  is the cross-sectional area of a grain of radius  $a$  and  $Q_{ext,\nu}(a)$  is the extinction efficiency for a grain of radius  $a$  at frequency  $\nu$ . On average, this gives

$$\tau_\nu \propto \frac{Q_{ext,\nu}(a)M\pi a^2}{\frac{4}{3}\pi a^3\rho V} \propto \frac{Q_{ext,\nu}(a)M}{\frac{4}{3}a\rho V} \quad (3.19)$$

for a total dust mass  $M$ , total volume of the ejecta  $V$  and density of a dust grain  $\rho$ .

By equating the equations for the total dust optical depth for a single grain radius and a distribution of grain radii, we obtain (at a specific frequency)

$$M_d = \frac{M_s Q_{ext,s}(a_s)}{a_s} \times \frac{\int_{a_{min}}^{a_{max}} n(a)a^3 da}{\int_{a_{min}}^{a_{max}} Q_{ext}(a)n(a)a^2 da} \quad (3.20)$$

where the subscript  $s$  represents the single grain radius quantities and the subscript  $d$  represents quantities for the grain radius distribution. This is only calculable for a specific wavelength and is therefore only an approximate conversion when performed at the rest-frame wavelength of the line in question. However, practically, the variation of extinction efficiency and albedo over the narrow wavelength ranges modelled within the code is not significant and so this method produces relatively accurate dust masses (corroborated by running models with the new parameters).

### 3.2.9 The effect of different species

In the majority of the modelling that follows, a single species, amorphous carbon, is considered. A single species is used since the parameters that affect the quantity of dust required in the model are the albedo and the optical depth. There are therefore likely many possible combinations of species that may result in a good fit to the data. The choice of amorphous carbon is partly motivated by evidence that, for SN 1987A (which, as an very well-observed, local core-collapse supernova, is an excellent test case) the fraction of silicates present in the dusty ejecta is limited to approximately 15% (Ercolano et al. 2007; Wesson et al. 2015). It is also motivated by previously published SED models which generally employ amorphous carbon. This is because SED models frequently require far

larger masses of silicate dust than more absorbing amorphous carbon dust in order to produce similar levels of infrared flux and therefore amorphous carbon models are likely to produce the more conservative dust mass estimates. By modelling with amorphous carbon I may compare directly to these SED models where possible.

I consider the change in dust mass when an alternative dust medium is used instead of amorphous carbon. I use a generic silicate dust medium as an illustrative example. In a similar manner to the approach detailed in Section 4.3.6, I may calculate the mass of silicates that is equivalent to an amorphous carbon mass for a single grain radius. I consider the albedo at the original grain radius, calculate the equivalent grain radius for silicates that results in the same albedo and then calculate the new dust mass by considering the change in the extinction efficiency as

$$M_{sil} = M_{amc} \left( \frac{Q_{amc}}{Q_{sil}} \right) \left( \frac{a_{sil}}{a_{amc}} \right) \left( \frac{\rho_{sil}}{\rho_{amC}} \right) \quad (3.21)$$

I will make use of the above “conversion” equations in the next chapter when I consider various models of SN 1987A and discuss the effects of varying both species and grain radius.

### 3.2.10 The velocity distribution

I do not thoroughly investigate the effects of varying the steepness of the velocity distribution since the influence of this parameter is thoroughly detailed from a mathematical perspective in Section 3.1.1. Simply, the steeper the velocity distribution, the steeper the slope of the sides of the output line profile. In this sense, there is some degeneracy with the exponent of the density profile. The steepness of the velocity distribution also affects the width of the flat-topped region of the profile via Equation 3.13. One of the primary reasons that this variable is not investigated in more depth is that all models of late-time line profiles from the ejecta of supernovae adopt a free expansion velocity law  $v \propto r$  until the remnant reaches a much later stage of its evolution. However, by this point the remnant will likely no longer be visible in the optical or IR.

## 3.3 Conclusions

Throughout this chapter, I have discussed the various ways in which I tested DAMOCLES against both theoretical line profiles derived from first principles and previously published

---

models, and have presented example profiles illustrating the excellent agreement between them. For each parameter of interest, I have described the manner in which its variation affects different aspects of the emergent line profile. I have also discussed the effects of altering the properties of the dust itself and have calculated the degeneracies relating to grain radius distributions and composition. This allows for any model with a given set of dust properties to be easily compared to a model with the same intrinsic geometry but with a different dusty medium.

This investigation of parameter space resulted in some very interesting insights that may prove important when considering dust formation in the ejecta of CCSNe in the future. Historically, a line profile that was flux-biased towards the blue with a blue-shifted peak was considered to be potentially indicative of dust formation. Whilst this is undeniably the case, it seems likely that a number of other features may also point towards the formation of dust in the ejecta. I have discussed the presence of an extended red-scattering wing and the lack of a need for asymmetry. I have also mentioned the possibility of symptomatically jagged profiles, often with sharp inflection points around the value of the minimum velocity ( $\pm V_{min}$ ). The presence of any or all of these features in the line profiles of the spectra of CCSNe may suggest the presence of newly-formed dust. In addition to these results, the process of exploring parameter space greatly aided me in modelling SN 1987A and the several other supernova remnants taht are presented in the following chapters.

## Chapter 4

---

# The Evolution of Dust Formation in SN 1987A

On 23 February 1987, a star died in an explosion that would inform our understanding of core-collapse supernovae for decades to come. SN 1987A is uniquely important to the study of supernovae. At only 50 kpc away in the Large Magellanic Cloud (LMC) and as the brightest supernova to be observed since SN 1604 (Kepler), it has provided an unprecedented opportunity for studying every aspect of supernovae. Since its discovery by Ian Shelton and Oscar Duhalde at Las Campanas, Chile (Kunkel et al. 1987), SN 1987A has been continuously observed across the entire wavelength range, providing astronomers with a wealth of data and discoveries.

SN 1987A was the first supernova to be detected via the emission of neutrinos. Hours before the visible light from SN 1987A reached Earth, 19 neutrinos were simultaneously detected in various locations across the globe confirming the core-collapse theory of supernovae (Bionta et al. 1987; Hirata et al. 1987). However, the neutron star that is expected to have resulted from this collapse has yet to be detected. Various theories exist for this non-detection such as the possibility that a black hole formed instead of a neutron star or that dust is obscuring our view.

The detection of neutrinos in combination with the presence of hydrogen lines in the early spectra resulted in the classification of SN 1987A as a Type II supernova. However, SN 1987A was unusually dim at peak magnitude compared to other Type II SNe and



**Figure 4.1.** SN 1987A in the Large Magellanic Cloud. The three-colour image is composed of several pictures of the region taken with the Wide Field and Planetary Cameras on the Hubble Space Telescope between September 1994 and July 1997. Image courtesy of NASA, ESA, and The Hubble Heritage Team (STScI/AURA).

brightened very quickly, its magnitude increasing by a factor of 100 in just three hours compared to a normal timeframe of several days. SN 1987A exhibited a number of other somewhat unusual features. Broad lines detected in the very early spectra indicated expansion velocities of up to  $30,000 \text{ km s}^{-1}$ , much faster than the typical  $15,000 \text{ km s}^{-1}$ . The colour evolution of the object was also faster than expected. These atypical properties suggested that the progenitor star was more compact than the red supergiants that are believed to normally give rise to Type II SNe. In fact, four days after the initial detection of SN 1987A, the progenitor star was identified as having been the blue supergiant Sanduleak -69° 202 confirming this theory (Sonneborn et al. 1987). These distinctive features, in combination with a plateauing light curve, led to the final classification of SN 1987A as a peculiar Type II-P supernova.

After the initial flash of ionising radiation in the first few hours (Ensmann & Burrows

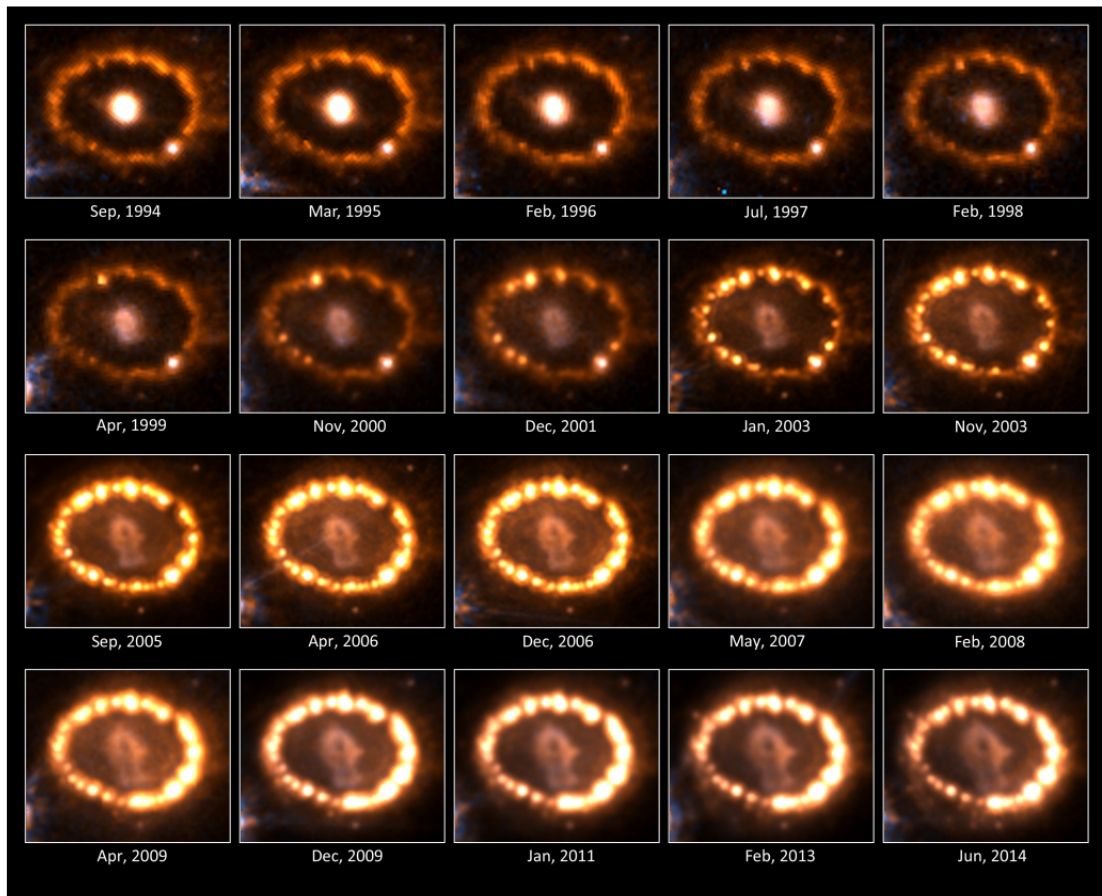


**Figure 4.2.** Evolution of the ring collision from 1994 to 2014 from a combination of HST B- and R- band images. The brightness of the ring has been reduced by a factor of 20 by applying a mask to the images making it possible to see the morphology of the ring at the same time as the faint ejecta. The image is taken from (Fransson et al. 2015).

1992), the expanding debris of SN 1987A cooled rapidly, dropping from 14,000 K to 6,000 K between the first and tenth days after outburst (Kirshner et al. 1987) before eventually stabilising at around 5,500 K. By just four months after outburst, the debris were transparent in the optical and IR (McCray 1993). The ejecta spectrum was dominated by emission lines, often exhibiting P-Cygni profiles, arising from a blackbody-like continuum. Numerous hydrogen, calcium and sodium lines could be seen in the optical as well as a rich spectrum of IR emission lines from other heavy elements.

The forward shock continued to propagate through the ejecta and by the mid 1990s reached the innermost of the beautiful and complex system of rings that are observed around SN 1987A (see Figures 4.1 and 4.2). The rings were most likely caused by an ejection of mass following a binary merger some 20,000 years before SN 1987A exploded

(Morris & Podsiadlowski 2005; Fitzpatrick et al. 2013). This merger also likely explains the surprising blue colour of the progenitor star. A series of images of the equatorial ring (ER) taken using the Hubble Space Telescope (HST) clearly show the appearance of “hot spots” as the dense material is shock-ionised on impact with the forward shock (see Figure 4.2). The interaction of the forward shock with the ER has precipitated a strong reverse shock that is now travelling back through the ejected material (Fransson et al. 2013). The illumination of the outer parts of the ejecta by the reverse shock is visible in spectra taken at later epochs as faster regions became more dominant in line profiles making them appear broader. It has been suggested that this point in SN 1987A’s evolution marks its transition to a remnant (McCray 2003).

The ionisation and heating of the ejecta of the supernova is caused by gamma rays that result from the decay of  $^{56}\text{Co}$ ,  $^{57}\text{Co}$  and  $^{44}\text{Ti}$  (with half lives of 77.3 days, 272 days and 59 years respectively (Ahmad et al. 2002)). The gamma rays Compton scatter off electrons that are often bound causing the production of fast, primary photoelectrons. These primary electrons go on to impact atoms causing further ionisations and excitations. A population of secondary electrons is thus produced. Recombinations and de-excitations result in the emission of monochromatic photons. These emission lines are then broadened thermally and via the large bulk velocity of the emitting medium. I present models of these optical and IR emission line profiles from SN 1987A throughout this chapter. The ionisation state of the ejecta of SN 1987A is thought to reach a period of stability known as the “freeze-out” when a balance is reached between the recombination and ionisation rates (Danziger et al. 1991b; Kozma & Fransson 1998a; Fransson et al. 2013). This is discussed in further detail later in this chapter as it has relevance to the evolution of the shapes of the line profiles.

A full review of SN 1987A in all its glory would likely extend to many dozen of pages and so in the following paragraphs I will focus only on those facets of the history of SN 1987A that relate to the formation of dust in its ejecta. For extensive reviews covering the progenitor, the explosion mechanism, the dynamics and geometry, the light curves and spectral evolution, the thermodynamics, the chemistry and the circumstellar ring system I refer the reader to the reviews by Arnett et al. (1989), McCray (1993) and McCray (2003). A comprehensive review of SN 1987A by Richard McCray encompassing its later evolution is due to be published next year (McCray & Fransson 2016).

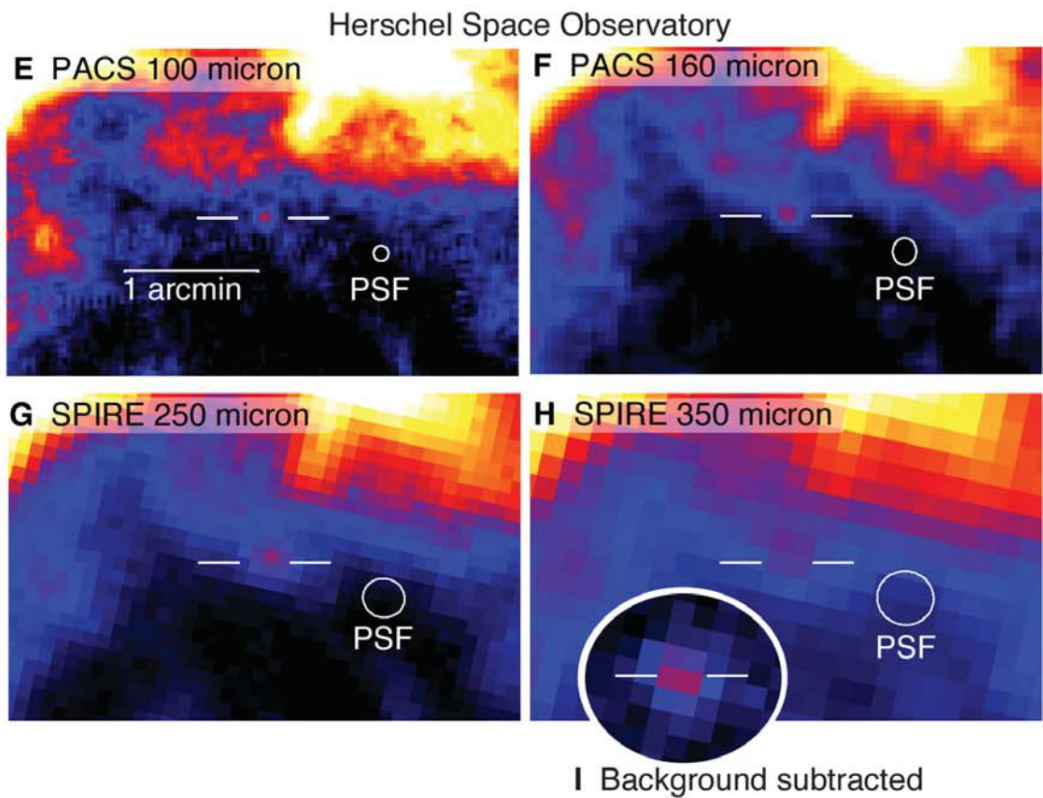


**Figure 4.3.** *Herschel* images of SN 1987A. Image taken from Matsuura et al. (2011).

## 4.1 10,000 Days of Dust

SN 1987A is the first and only supernova to have had the formation of dust in its ejecta traced via all three observable signatures described in Section 1.2.6 (Bouchet & Danziger 2014). Before dust was observed, its formation in the ejecta of SN 1987A was predicted. Gehrz & Ney (1987) recognized that conditions in the cooling ejecta would eventually reach temperatures and densities appropriate for dust formation to occur. They predicted that the onset of dust formation would occur at around days 240-300. This idea was expanded upon by Dwek (1988) who estimated that dust would begin to form slightly later at around day 400 and might even cause an optical black-out of the supernova.

The first indications of dust in the ejecta of SN 1987A appeared at around day 350 with the emergence of continuum radiation in the IR longward of  $5\mu\text{m}$  (Meikle et al. 1993). This had become prominent by day 550 (Roche et al. 1993; Wooden et al. 1993). It was suggested by some that this excess IR emission was the result of a light echo reflecting off the circumstellar material (Roche et al. 1989). However, at around day 530, the optical

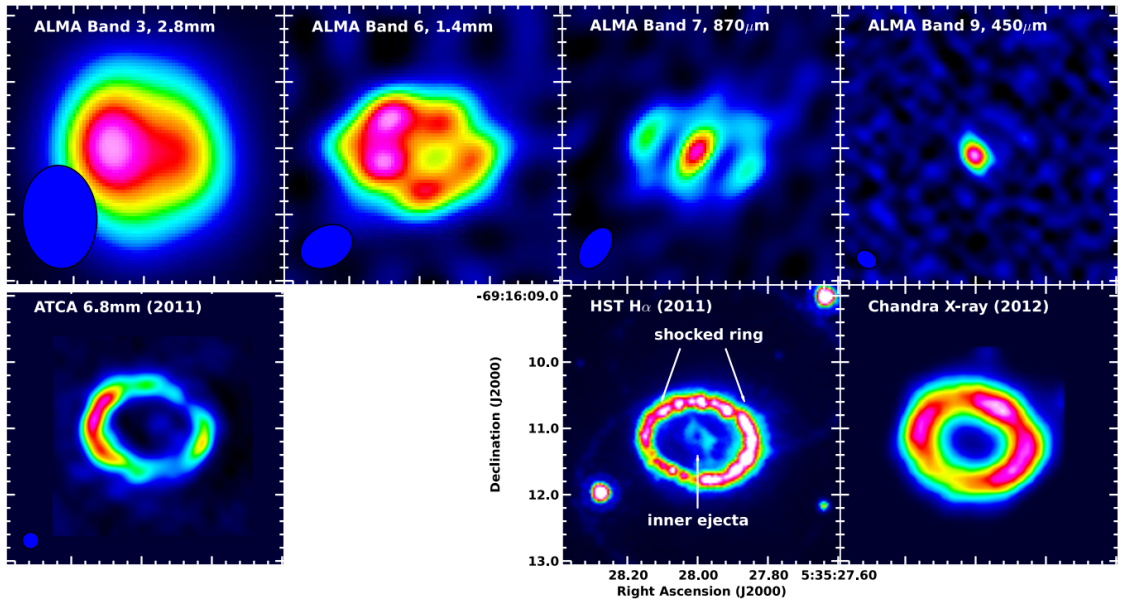


**Figure 4.4.** ALMA, ATCA, HST and Chandra images of SN 1987A showing the location of the dust in the inner ejecta at 450 $\mu$ m. The image is taken from (Indebetouw et al. 2014). Inset HST image courtesy of R. Kirshner and the SAINTS collaboration (also see Larsson et al. (2013)) and the inset Chandra X-ray image is from Helder et al. (2013).

luminosity suddenly started dropping more rapidly than it had done previously. The IR luminosity started to increase, compensating for the drop in the optical and ensuring that the bolometric light curve continued to follow the same trajectory (Suntzeff et al. 1991; Whitelock et al. 1991). At the same time it was observed that the peaks of several emission lines in the optical and IR had become shifted towards the blue indicating that the dust was indeed within the supernova envelope itself (Lucy et al. 1989; Danziger et al. 1991a,b; Meikle et al. 1991, 1993; Suntzeff et al. 1991; Hanuschik et al. 1993). It was Leon Lucy and collaborators who first suggested that the presence of blue-shifted line profiles may indicate dust formation in the ejecta of supernovae and they even went as far as producing some models to illustrate the effects. They used this method to estimate for the first time the dust mass in the ejecta of SN 1987A ( $10^{-6}M_{\odot} - 10^{-4}M_{\odot}$ ) (Lucy et al. 1989, 1991).

After this intensive monitoring of SN 1987A in the MIR, there was something of a gap in observations. By the mid 1990s SN 1987A had faded and could no longer be detected in the MIR with current instruments. It was not until 2004 that new instruments at the Gemini South telescope and at the Very Large Telescope allowed for the resumption of observations of SN 1987A at these wavelengths. The first resolved detection of the central ejecta was reported by Bouchet et al. (2004) who observed the object at 10 $\mu$ m

and  $20\mu\text{m}$ . They estimated a mass of  $10^{-4}M_{\odot} - 2 \times 10^{-3}M_{\odot}$  for the dust in the ejecta, with an estimated temperature of  $90K < T < 100K$ . They concluded that CCSNe could potentially be a significant source of dust in the Universe but could not solely account for the masses seen at high redshifts (see Chapter 1). Subsequent observations continued to detect this faint MIR emission right up to the present day (Dwek et al. 2010; Bouchet & Danziger 2014) whilst radiative transfer models of the SEDs continued to find dust masses of the order of  $10^{-4} - 10^{-3}M_{\odot}$  during the first 1000 days (Ercolano et al. 2007).

For many years it was assumed that only a small mass of dust, possibly as much as a few  $\times 10^{-3}M_{\odot}$ , had formed in the ejecta of SN 1987A within the first 1000 days. It was not until the first *Herschel* observations of SN 1987A that the picture suddenly changed. SN 1987A had not been chosen as a target for the *Herschel* mission as it was believed that it would not be detectable at far-IR and sub-mm wavelengths. However, in 2010, whilst *Herschel* was performing a survey of the LMC as a part of the HERITAGE survey (Meixner et al. 2013), an unexpectedly strong signal was detected in the same region as SN 1987A. In 2011, Matsuura et al. (2011) published the first detections of the SN 1987A system at long wavelengths (100, 160, 250 and  $350\mu\text{m}$  presented in Figure 4.3). These observations revealed the presence of a massive reservoir ( $0.4 - 0.7 M_{\odot}$ ) of cold dust ( $17K < T < 23K$ ) that they argued was located in the ejecta. *Herschel* did not have the angular resolution to determine the location of the emitting dust and as a result there was much contention over this assertion with many claiming that the detection was of pre-existing dust located in the circumstellar material (Bouchet & Danziger 2014). However, follow-up observations of SN 1987A with the Atacama Large Millimetre Array (ALMA) published by Indebetouw et al. (2014) resolved the SN-ring system and revealed the location of the dust to be entirely within the ejecta (see Figure 4.4). Further pointed *Herschel* observations corroborated the large estimated dust masses (Matsuura et al. 2015). These dust mass estimates were all based on fitting dust spectral energy distributions (SEDs) that peaked at far-IR wavelengths.

The majority of the dust in the ejecta of SN 1987A is located centrally and as such has not yet encountered the reverse shock that is propagating back towards it. Whilst it is now clear that very large masses of dust have indeed formed in the ejecta of SN 1987A, it remains unclear whether the dust will survive the passage of the reverse shock. The composition of the dust and the size of the grains are crucial to understanding how much of the dust that has formed will actually be deposited into the ISM in the future. Further ob-

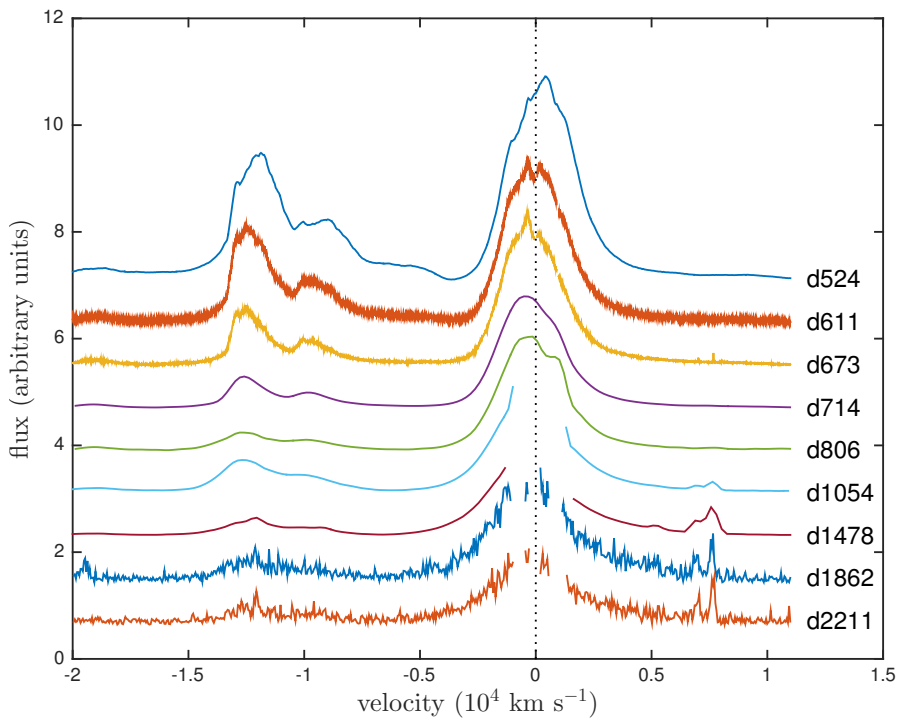


**Figure 4.5.** Archival data showing the evolution of the H $\alpha$  and [O I] line profiles from SN 1987A at the earlier of the epochs considered. The spectral gaps at the last two epochs correspond to where narrow line emission from the equatorial ring has been removed. The spectra have been continuum-subtracted and offsets have been applied for display purposes.

servations and analyses of the dust mass present in the ejecta are crucial to understanding how much dust is actually contributed to the ISM from CCSNe.

The *Herschel* mission ended in 2013 and there is now likely to be a long wait for far-IR facilities with comparable or better sensitivities than *Herschel* to become available. The method of SED fitting is therefore unhelpful until other telescopes come into operation. This provides a strong incentive to make use of alternative methods to estimate the dust masses that form in supernova ejecta. Following the work of Lucy et al. (1989), no further analysis of the shapes of the line profiles in SN 1987A has been performed. With such a large database of spectral observations available, SN 1987A provides the perfect opportunity to assess the evolution of the formation of dust in the ejecta of CCSNe.

In this chapter, I present a number of models of line profiles of SN 1987A. I have collated optical spectra from the archives of four different telescopes in order to study the effects of dust formation on the H $\alpha$  line and on the [O I]  $\lambda 6300, 6363$  Å doublet. I have modelled epochs spanning a range of approximately 8 years, from the first indications

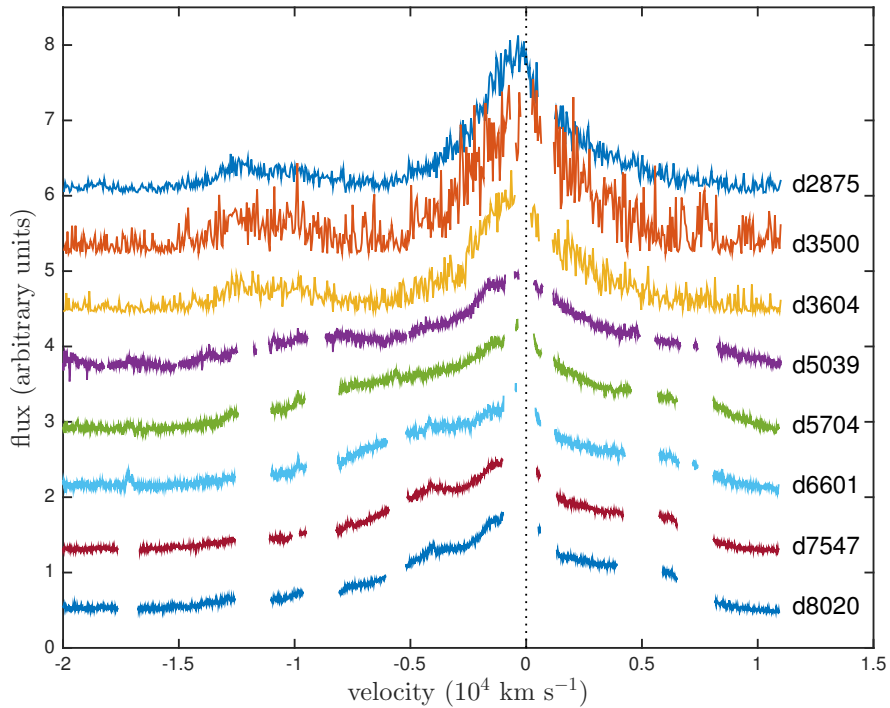


**Figure 4.6.** Archival data showing the evolution of the H $\alpha$  line profile from SN 1987A at the later epochs. The spectral gaps correspond to where narrow line emission from the ER has been removed. The spectra have been continuum-subtracted and offsets applied for display purposes.

of blue-shifting in the H $\alpha$  line between days 600-700, using both smooth and clumped geometries. I compare my derived dust masses to those obtained by Wesson et al. (2015) (hereafter W15) and Dwek & Arendt (2015) (hereafter DA15) and consider the implied dust formation rate.

In Section 4.2, I detail the observed spectra that I used for my modelling and I present my modelling of the H $\alpha$  and [O I]  $\lambda\lambda 6300, 6363$  Å lines in Section 4.3. Finally, I discuss my findings in Section 4.4.

## 4.2 Spectral Observations of SN 1987A

SN 1987A has been the most intensively observed supernova in history, with an abundance of both spectral and photometric data available to model. From the archives of a number of different telescopes I have collated optical spectra acquired over a wide range of epochs. At the earlier epochs I use spectra obtained by the Anglo-Australian Telescope (AAT) and the Cerro Tololo Inter-American Observatory (CTIO) and at later epochs I use spectra

**Table 4.1.** Details of the archival data for SN 1987A.

Date	Age (days)	Telescope	Inst	$\lambda_{min}$ (Å)	$\lambda_{max}$ (Å)	Res. (Å)	Res. Power	Reference
31 Jul 1988	524	AAT	FORS	5500	10190	20		Spyromilio et al. (1991)
26 Oct 1988	611	AAT	UCLES	6011	7336	30000		Hanuschik et al. (1993; Spyromilio et al. (1993))
27 Dec 1988	673	AAT	UCLES	5702	10190	30000		Hanuschik et al. (1993; Spyromilio et al. (1993))
06 Feb 1989	714	CTIO-1.5m	Cass.	6420	10380	16		Phillips et al. (1990)
09 May 1989	806	CTIO-1.5m	Cass.	6430	10330	16		Phillips et al. (1990)
12 Jan 1990	1054	CTIO-4m	RC	3565	10000	11		Suntzeff et al. (1991)
12 Mar 1991	1478	CTIO-4m	RC	3245	9175	11		
30 Mar 1992	1862	HST	STIS	4569	6818	4.4		Wang et al. (1996)
14 Mar 1993	2211	HST	STIS	4569	6818	4.4		Wang et al. (1996)
07 Jan 1995	2875	HST	STIS	4569	6818	4.4		Chugai et al. (1997)
23 Sep 1996	3500	HST	STIS	4569	6818	4.4		
05 Jan 1997	3604	HST	STIS	4569	6818	4.4		
10 Dec 2000	5039	VLT	UVES	4760	6840	50000		Grönigsson et al. (2006, 2007)
06 Oct 2002	5704	VLT	UVES	4760	6840	50000		Grönigsson et al. (2006, 2007, 2008)
21 Mar 2005	6601	VLT	UVES	4760	6840	50000		Grönigsson et al. (2006, 2007)
23 Oct 2007	7547	VLT	UVES	4760	6840	50000		Grönigsson et al. (2007)
07 Feb 2009	8020	VLT	UVES	4800	6800	50000		Tziampatzis et al. (2010)

from the archives of the Hubble Space Telescope (HST) and the Very Large Telescope (VLT). An explosion date of 23 February 1987 is adopted throughout and epochs are measured relative to this date. Full details of all observations may be found in Table 4.1. The spectral resolutions of the grating spectrograph observations are listed in column 7, while column 8 lists the spectral resolving powers of the echelle spectrograph observations.

Wavelength ranges encompassing the H $\alpha$  line and [O I]  $\lambda\lambda 6300, 6363$  Å doublet were selected in order to trace their evolution from day 524, near the time of the first indications of dust formation (Wooden et al. 1993), to day 8020, near the current era. Optical spectroscopy obtained at the AAT using the Faint Object Red Spectrograph (FORS) during the first two years after outburst was kindly supplied by Dr Raylee Stathakis (Spyromilio et al. 1991, 1993; Hanuschik et al. 1993) and optical spectra from the CTIO were donated by Dr Mark Phillips (Suntzeff et al. 1991).

The evolution of the H $\alpha$  and [O I] line profiles is presented in Figures 4.5 and 4.6. At later epochs, the broad H $\alpha$  profile emitted by the ejecta becomes contaminated by narrow line emission from the ER. These lines have been removed for the purposes of modelling the broad line. A continuum fit has been subtracted from each spectrum and a velocity correction has been applied for a recession velocity of 287 km s $^{-1}$  (Gröningsson et al. 2008).

#### 4.2.1 Contamination of the H $\alpha$ profiles

The H $\alpha$  profile at day 714 exhibits a very slight inflection visible at  $V \approx +900$  km s $^{-1}$ . By day 806, this slight inflection has developed into a noticeable shoulder in the line profile of H $\alpha$  (see Figure 4.9).

Although these features are similar in nature to features produced by dust absorption in the flat-topped region (as discussed in Section 3.2.5), I conclude that this shoulder is an early appearance of the unresolved [N II]  $\lambda 6583$  Å line from the ER (Kozma & Fransson 1998b). Unresolved nebular [N II] lines at  $\lambda = 6583$  Å and  $\lambda = 6548$  Å either side of the H $\alpha$  rest frame velocity at 6563 Å are certainly seen by day 1054 and have to be removed in order to consider the evolution of the broad H $\alpha$  profile (see Figure 4.5). I do not remove this potential contaminant at earlier epochs but try to fit the broad line profiles around it.

By day 1054, all three of the narrow nebular lines (H $\alpha$  and N[II]) are strong. They remain unresolved in the low spectral resolution CTIO data at days 1054 and 1478 and

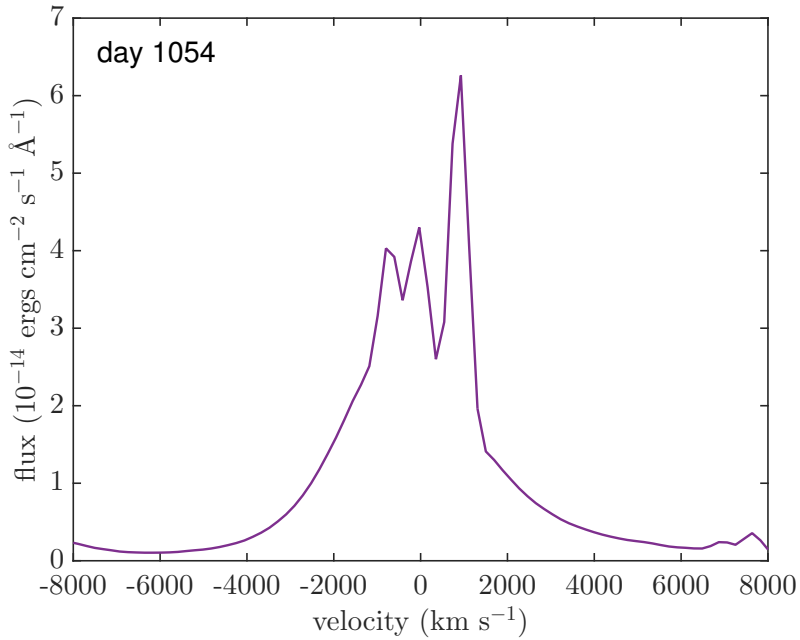


**Figure 4.7.** The low resolution H $\alpha$  line profile from SN 1987A observed at the CTIO on day 1054. The unresolved narrow nebular [N II] lines at  $\lambda = 6583 \text{ \AA}$  and  $\lambda = 6548 \text{ \AA}$  and the narrow nebular H $\alpha$  line at  $\lambda = 6563 \text{ \AA}$  can be clearly seen.

therefore contaminate the entire central region of the H $\alpha$  line profile (see Figure 4.7). Their presence renders two CTIO H $\alpha$  profiles from days 1054 and 1478 unusable for modelling purposes. The HST and VLT H $\alpha$  profiles at later epochs ( $\geq 1862$  days) have a higher spectral resolution and it was therefore easier to remove the narrower [N II] and H $\alpha$  lines from the broad H $\alpha$  profiles (for example Figures 4.5 and 4.6). Although this does remove a potentially informative section of the profile ( $+500 \text{ km s}^{-1} < v < +1500 \text{ km s}^{-1}$ ), I achieve good fits to the overall line profiles at these epochs.

#### 4.2.2 The evolution of the maximum and minimum velocities

For a freely expanding medium, the velocity of any fractional radial element should not change with time. The maximum velocity of any line-emitting region is therefore expected to be constant. However, at the epochs I consider here, it appears that the maximum velocities of the H $\alpha$  line, as determined by the velocity at zero intensity on the blue side, generally increase over time (see Table 4.2). I attribute this to the start of the freeze-out phase in the outer regions of the ejecta, while the hydrogen neutral fraction is still increasing in the denser inner regions (Danziger et al. 1991b; Fransson & Kozma 1993).

**Table 4.2.** H $\alpha$  full-width half-maxima (FWHM) and the half-width zero intensities (HWZI) in km s $^{-1}$  determined by the zero intensity velocity on the blue side of the line. The tabulated line widths have been corrected for the relevant instrumental resolution.

day	FWHM (km s $^{-1}$ )	HWZI (km s $^{-1}$ )
524	3200	3600
611	2700	3400
673	1600	3700
714	3100	4500
806	3200	5500
1054	2100	5600
1478	1400	6600
1862	1600	6800
2211	1400	6700
2875	2700	6700
3500	3500	7000
3604	2100	7000

The onset of a fixed ionization structure in the ejecta causes the rate of H $\alpha$  flux decline to slow. Since the outer, faster moving regions reach this state at earlier times than the inner, slower moving regions, the relative flux contribution of the outer regions is increased. At early epochs ( $t < 900$  days) the flux contribution from hydrogen in the core dominates the overall H $\alpha$  flux, whereas at later epochs ( $t > 900$  days) the flux from the envelope dominates (Fransson & Kozma 1993; Kozma & Fransson 1998a). This shift likely explains apparent broadening of the line with the higher velocity material becoming increasingly noticeable in the line profiles. This may also explain the increase in half-width zero intensity (HWZI) velocities at these epochs with the relative flux from the very densest regions dropping more rapidly relative to the outer line-emitting region. The full-width half maximum (FWHM) remains relatively steady (see Table 4.2). However, the FWHM values presented in Table 4.2 were difficult to determine accurately since the peak of the broad line profile is contaminated by narrow line emission from the ER.

### 4.3 Modelling SN 1987A

I have modelled the H $\alpha$  line of SN 1987A at days 714, 806, 1862, 2211, 2875, 3500 and 3604, and the [O I]  $\lambda\lambda 6300, 6363$  Å doublet at days 714, 806, 1054 and 1478. After day 3604 the H $\alpha$  profile begins to become dominated by emission from the reverse shock and the structure of the emitting region may no longer be approximated by a single shell model

**Table 4.3.** Observed luminosities of the H $\alpha$  line and estimated electron scattering optical depths from  $R_{in}$  to  $R_{out}$  for the radii detailed in Tables 4.4 to 4.5 based on an assumed gas temperature of 10,000 K.

day	H $\alpha$		[O I]		
	$L_{obs}$ ( $10^{37}$ erg s $^{-1}$ )	$L_{undep}/L_{obs}$	$L_{obs}$ ( $10^{37}$ erg s $^{-1}$ )	$L_{undep}/L_{obs}$	$\tau_e$ ( $10^{-2}$ )
714	1.36	1.65	0.313	3.57	1.44
806	0.57	1.77	0.0942	3.57	0.840
1054			0.0242	3.23	
1478			0.00185	2.70	
1862	0.0063	2.06			0.159
2211	0.0041	2.07			0.0378
2875	0.0019	2.84			0.0219
3500	0.00079	3.16			0.0125
3604	0.00098	3.27			0.0149

as I do here (Fransson et al. 2013). The [O I]  $\lambda 6300, 6363$  Å doublet becomes too weak to model after day 1478 (see Figure 4.5). I continue to adopt a velocity profile  $V(r) = \frac{V_{max}}{R_{max}} r$  and treat the variable parameters listed at the start of Section 3.2. Whilst the albedo and optical depth are not varied directly, they are altered by adjusting the dust mass,  $M_{dust}$ , and the grain radius,  $a$ , which together determine the albedo and optical depth via Mie theory and the optical properties of the dust.

In all models, the ejecta occupies a shell with inner radius  $R_{in}$  and outer radius  $R_{out}$ . Packets are emitted according to a smooth density profile assuming recombination or collisional excitation such that  $i(r) \propto \rho(r)^2 \propto r^{-2\beta}$ . Initially the dust is considered to have a smooth density distribution and is assumed to be coupled to the gas so as to follow the same radial profile. A clumped distribution of dust is considered later (see Section 4.3.2).

Assuming an electron temperature of 10,000 K, I estimated the total electron scattering optical depths between  $R_{in}$  and  $R_{out}$  based on the observed fluxes of the H $\alpha$  recombination line. A temperature of 10,000 K for the recombining material is likely too high at the epochs considered but I adopt it in order not to underestimate electron scattering optical depths. The values I calculate from the observed H $\alpha$  luminosities are listed in Table 4.3. Since the electron scattering optical depths at these epochs are negligibly small I therefore do not include electron scattering in the models.

There is rarely a unique set of parameters that provide the best fit to the data. However, the majority of the parameters of interest can be well constrained from my modelling

by considering different elements of the shape of the profile. In particular, by constructing fits to the data using minimum and maximum limits for the grain radius, credible lower and upper bounds on the dust mass formed within the ejecta may be derived. I present here fits to the data obtained using both small and large values of the grain radius  $a$  since it is the grain radius which has the most significant effect on the overall dust mass required to reproduce the line profile (see Section 3.2).

All of my models are of a dusty medium composed solely of amorphous carbon grains. I use the optical constants from the BE sample presented by Zubko et al. (1996). Although previous SED modelling of SN 1987A limited the fraction of silicates present in the dusty ejecta to a maximum of 15% (Ercolano et al. (2007), W15), the recent work of Dwek & Arendt (2015) has suggested that a large mass of mostly silicate dust may have formed at early epochs ( $\sim 615$  days). It is therefore useful to consider the effects on my models of using silicate dust. I discuss this in detail in Sections 4.3.7 and 4.3.8.

For each profile, the maximum velocity is initially identified from the data as the point where the emission vanishes on the blue side and is then varied throughout the modelling in order to produce the best fit. The equivalent point on the red side is indeterminate from observations due to the effects of dust scattering. I determine the approximate value of  $V_{min}$  by examining the width of the profile near its peak. Using the features and shapes presented in Figures 3.6 and 3.7 as a guide, I first examined the observed profile for any obvious points of inflection or abrupt changes in the steepness of the profile. If these were observed then they were compared to similar changes in theoretical profiles which allowed me to estimate the value of  $V_{min}$ . If none were observed, then a model setting  $V_{min}$  to be the velocity of the profile peak was considered. Where neither of these approaches yielded a good model (this was rare) I iterated over a range of values of  $V_{min}$  as with other variable parameters such as the dust mass. On the red side the theoretical minimum velocity often falls at a similar velocity to the narrow nebular [N II] 6583Å line so any dust-induced features near this wavelength that would allow a more accurate determination of  $V_{min}$  can be overwhelmed by the nebular line. Having determined the minimum and maximum velocities, the ratio of the inner and outer radii of the supernova ejecta can be determined since  $R_{in}/R_{out} = V_{min}/V_{max}$ . The outer radius is calculated from the epoch and the maximum velocity.

The only parameters that remain to be determined are the exponent of the density profile  $\beta$ , the mean grain radius and the total dust mass. The shape of the blue wing is

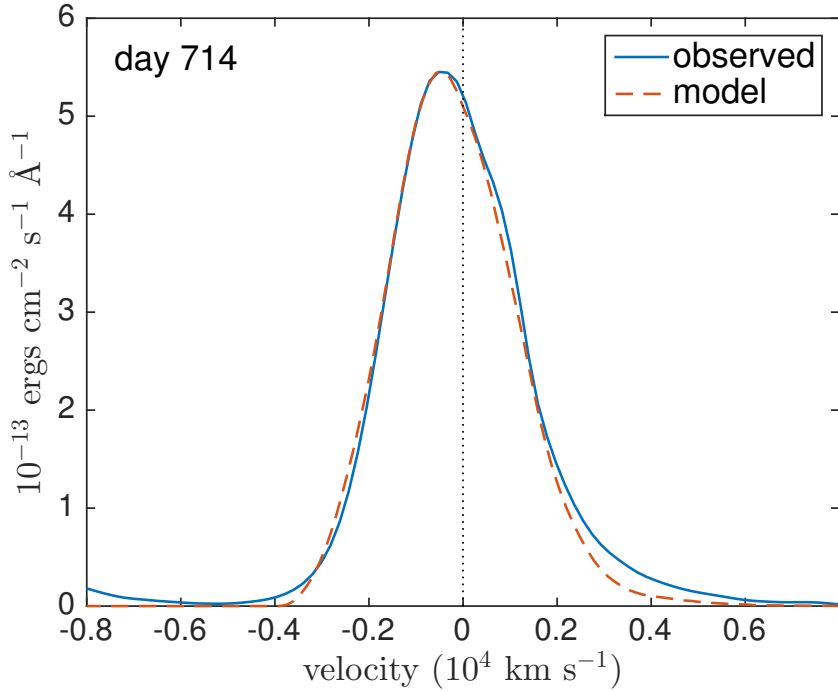


**Figure 4.8.** Amorphous carbon smooth dust fit to the day 714 H $\alpha$  line of SN 1987A using an MRN size distribution, illustrating the underestimation of the red scattering wing for small grain radii. Model parameters are the same as the smooth dust fit for day 714 (Table 4.4) except for the grain radius distribution and dust mass:  $M_{dust} = 8.0 \times 10^{-6} M_{\odot}$ ,  $a_{min} = 0.005 \mu\text{m}$ ,  $a_{max} = 0.25 \mu\text{m}$  and  $n(a) \propto a^{-3.5}$ .

solely a product of the density profile and the dust mass; the height and shape of the red wing is a product of these and also of the scattering efficiency of the grains (the albedo  $\omega$ ); the extent and shape of the asymmetry in the flat-topped portion of the profile is a function of only the total dust optical depth determined by the dust mass and the grain radius. By iterating over these three parameters, an excellent fit to the data can usually be obtained.

Models are produced in the same manner for the [O I]  $\lambda 6300, 6363 \text{ \AA}$  doublet as for the single H $\alpha$  line, with each component of the doublet being modelled independently and the resulting profiles added according to a specified ratio. Although the theoretical intrinsic flux ratio is 3.1 for optically thin emission (Storey & Zeippen 2000), the actual ratio between the two components can be affected by self-absorption (Li & McCray 1992) and I therefore left it as a free parameter. The deduced doublet ratios are listed in Tables 4.4, 4.5 and 4.6.

For all lines, though particularly at very late epochs, even small fluctuations in the

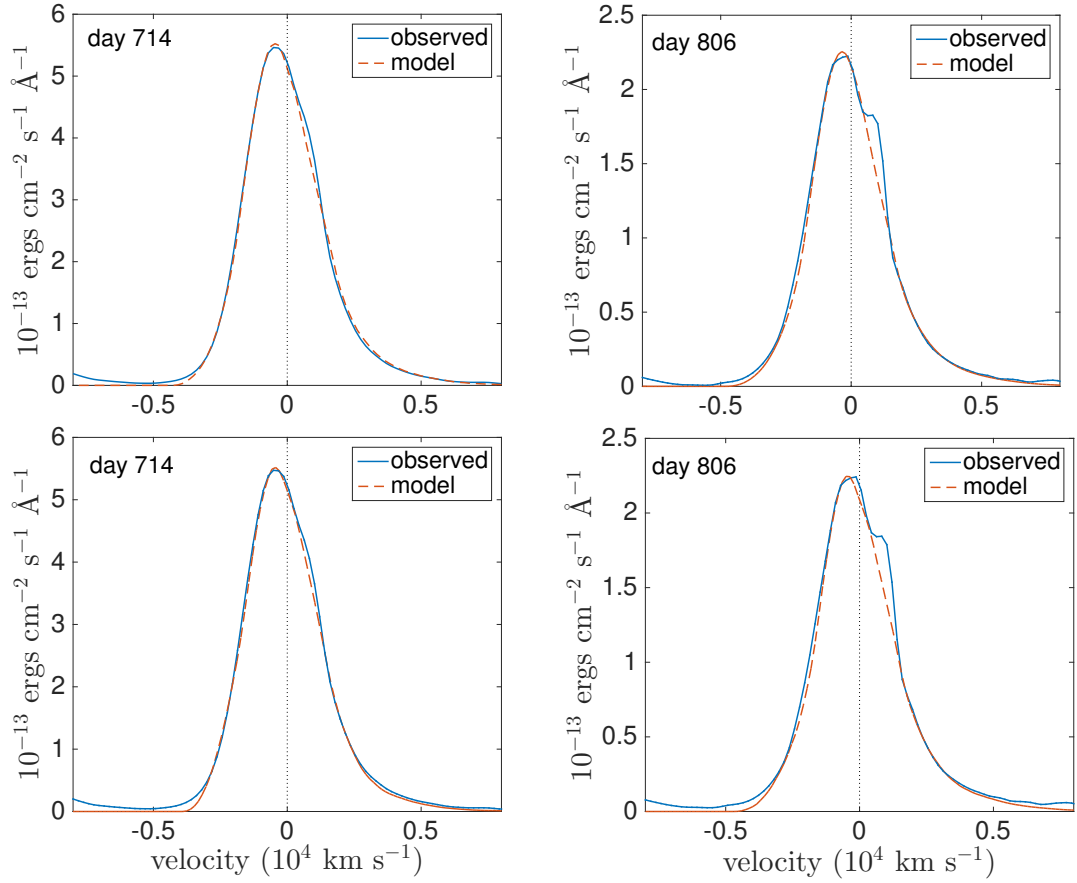


**Figure 4.9.** Best model fits to the SN 1987A H $\alpha$  line at day 714 and day 806 for the parameters detailed in Tables 4.4 and 4.5. The two fits on the top are smooth dust models using amorphous carbon grains of radius  $a = 0.35 \mu\text{m}$  and the two fits on the bottom are clumped dust models using amorphous carbon grains of radius  $a = 0.6 \mu\text{m}$ .

adopted value of the continuum level can have a substantial effect on the fit to the resulting profile. Since it is not feasible to establish the level of the continuum so precisely, the value of the continuum has been left as a free parameter that may be adjusted (to within sensible margins) in order to allow for the widest possible dust mass range to be determined. I generally find it is necessary to assume a continuum level that is slightly lower where the dust mass is higher. The [O I] $\lambda\lambda 6300, 6363 \text{ \AA}$  doublets at days 1054 and 1478 are weak relative to the continuum and are also blended with the wings of other lines making it difficult to fit their wings accurately. I aim to fit the lines between approximately  $-3000 \text{ km s}^{-1}$  and  $+5000 \text{ km s}^{-1}$  but present a wider velocity range for context (for example see Figure 4.11).

Fits to the H $\alpha$  line profile at days 2211 and 3500 are omitted for the sake of space

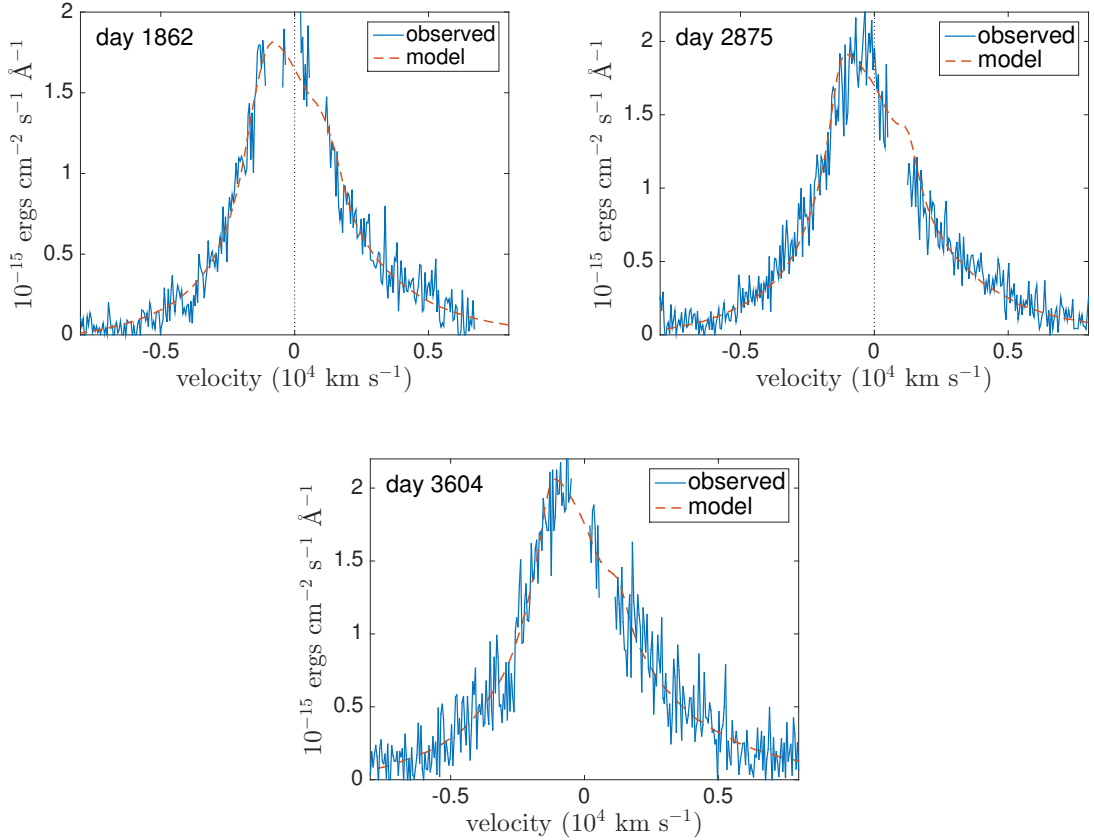


**Figure 4.10.** Best model fits to the SN 1987A H $\alpha$  line at days 1862, 2875 and 3604 for the parameters detailed in Tables 4.4. Smooth model fits with amorphous carbon grains of radius  $a = 0.35 \mu\text{m}$  are presented.

but are very similar to those of days 1862 to 3604. All profiles have been smoothed to approximately the same resolution as the observed profiles using a moving-average procedure. Parameters for the models at all epochs including days 2211 and 3500 are detailed in Tables 4.4 to 4.6.

#### 4.3.1 Smooth Density Models for SN 1987A

Even at the earliest epochs there is a substantial wing on the red side of the H $\alpha$  line profile that cannot be fitted by scattering from moving grains with a low albedo. The minimum required albedo is approximately  $\omega \approx 0.5$  implying relatively large grain radii. As previously discussed, the larger the grain radius the larger the mass of dust required to reproduce the same optical depth. Figure 4.8 illustrates the fit for the day 714 H $\alpha$  profile for the case where a classic MRN (Mathis et al. 1977) grain radius distribution is adopted, with  $a_{min} = 0.005 \mu\text{m}$ ,  $a_{max} = 0.25 \mu\text{m}$  and  $n(a) \propto a^{-3.5}$ . It can be seen clearly

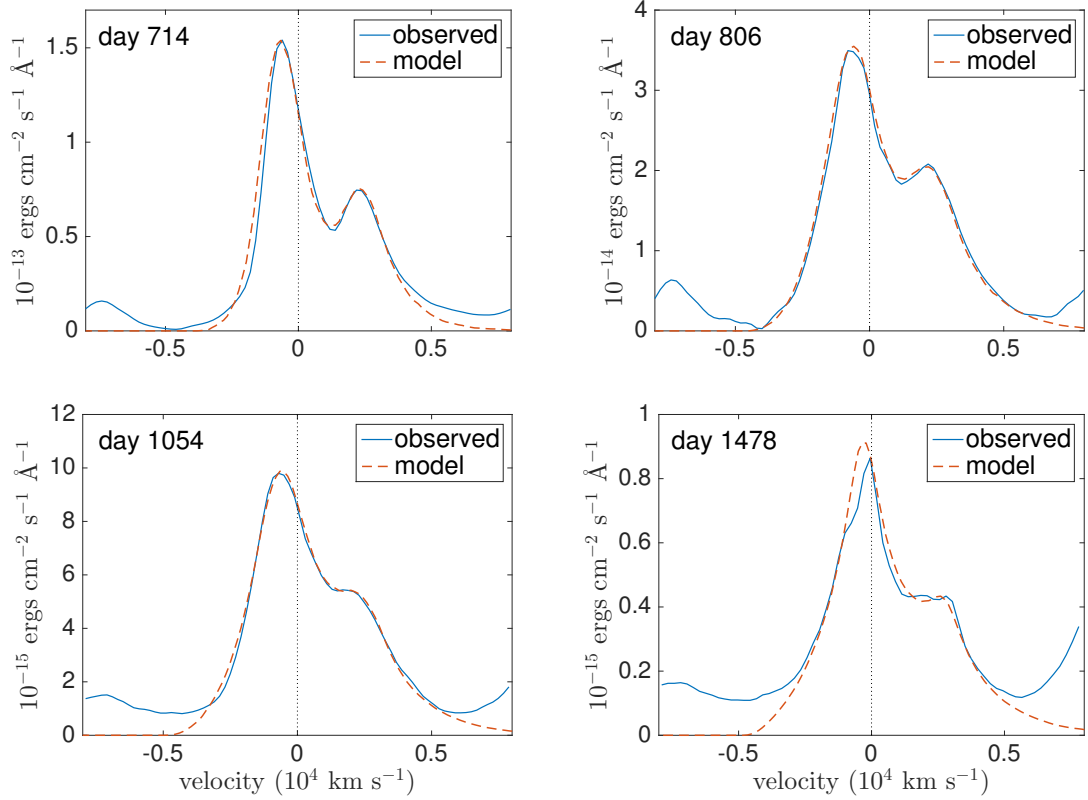


**Figure 4.11.** Best smooth dust fits to the SN 1987A [O I]  $\lambda\lambda 6300, 6363$  Å doublet at days 714, 806, 1054 and 1478 for the parameters detailed in Tables 4.4. Smooth dust fits with amorphous carbon grains of radius  $a = 0.35\mu\text{m}$  are presented.

that the extended red wing is significantly underestimated. Since the albedo of amorphous carbon grains varies significantly with grain radius (see Figure 3.9) I can establish a strong lower bound to the mean dust grain radius, which I estimate to be  $a \geq 0.35\mu\text{m}$ . This is the smallest grain radius that is still capable of reproducing the red scattering wing at all epochs and I therefore use this lower limit value throughout my smooth density modelling.

The inner and outer radii of the ejecta are calculated at each epoch from the maximum velocity used, the day number and the specified ratio  $R_{in}/R_{out}$ . The radii generated are consistent with those used in previous models of SN 1987A (Ercolano et al. (2007), W15) and the minimum velocities for both the [O I] and H $\alpha$  line emitting regions are relatively consistent with those obtained by Kozma & Fransson (1998b) who estimate that hydrogen extends into the core to a depth of  $\lesssim 700\text{ km s}^{-1}$  and the oxygen reaches down to  $\sim 400\text{ km s}^{-1}$ . They are also consistent with predictions from 3D explosion models at the time of shock-breakout that predict the oxygen to reach to a depth of  $\sim 200\text{ km s}^{-1}$  (Hammer et al. 2010; Wongwathanarat et al. 2015). Figures 4.9 to 4.11 show the best fits

**Table 4.4.** The parameters used for the best fitting smooth models of SN 1987A with amorphous carbon grains of radius  $a = 0.35 \mu\text{m}$ . Optical depths are given from  $R_{in}$  to  $R_{out}$  at  $\lambda = 6563 \text{ \AA}$  for H $\alpha$  and  $\lambda = 6300 \text{ \AA}$  for [O I]. Values of  $\tau_V$  are very close to the quoted values of  $\tau_{H\alpha}$ .

	day	$V_{max}$ (km s $^{-1}$ )	$V_{min}$ (km s $^{-1}$ )	$R_{in}/R_{out}$	$\beta$	$M_{dust}$ ( $M_\odot$ )	$R_{out}$ (cm)	$R_{in}$ (cm)	[O I] ratio	$\tau_\lambda$
[O I]	714	3250	228	0.07	2.9	$9.65 \times 10^{-5}$	$2.00 \times 10^{16}$	$1.40 \times 10^{15}$	2.6	3.60
[O I]	806	4000	240	0.06	2.4	$1.50 \times 10^{-4}$	$2.79 \times 10^{16}$	$1.67 \times 10^{15}$	2.3	2.86
[O I]	1054	4300	215	0.05	2.1	$2.35 \times 10^{-4}$	$3.92 \times 10^{16}$	$1.96 \times 10^{15}$	2.7	2.23
[O I]	1478	4500	180	0.04	1.7	$2.95 \times 10^{-4}$	$5.75 \times 10^{16}$	$2.30 \times 10^{15}$	3.0	1.30
H $\alpha$	714	3250	813	0.25	1.2	$2.10 \times 10^{-5}$	$2.00 \times 10^{16}$	$5.01 \times 10^{15}$	0.61	
H $\alpha$	806	4000	880	0.22	1.9	$3.80 \times 10^{-5}$	$2.79 \times 10^{16}$	$6.13 \times 10^{15}$	0.59	
H $\alpha$	1862	8500	1275	0.15	1.9	$5.00 \times 10^{-4}$	$1.37 \times 10^{17}$	$2.05 \times 10^{16}$	0.35	
H $\alpha$	2211	9000	1260	0.14	1.9	$9.25 \times 10^{-4}$	$1.72 \times 10^{17}$	$2.41 \times 10^{16}$	0.42	
H $\alpha$	2875	9500	1330	0.14	1.9	$1.50 \times 10^{-3}$	$2.36 \times 10^{17}$	$3.30 \times 10^{16}$	0.36	
H $\alpha$	3500	10000	1400	0.14	1.9	$3.35 \times 10^{-3}$	$3.02 \times 10^{17}$	$4.23 \times 10^{16}$	0.49	
H $\alpha$	3604	10250	1333	0.13	1.9	$4.20 \times 10^{-3}$	$3.19 \times 10^{17}$	$4.15 \times 10^{16}$	0.55	

**Table 4.5.** The parameters used for the best fitting clumped models of SN 1987A with amorphous carbon grains of radius  $a = 0.6 \mu\text{m}$ . Optical depths are given from  $R_{in}$  to  $R_{out}$  at  $\lambda = 6563 \text{ \AA}$  for H $\alpha$  and  $\lambda = 6300 \text{ \AA}$  for [O I]. Values of  $\tau_V$  are very close to the quoted values of  $\tau_{H\alpha}$ .

	day	$V_{max}$ (km s $^{-1}$ )	$V_{min}$ (km s $^{-1}$ )	$R_{in}/R_{out}$	$\beta$	$M_{dust}$ ( $M_\odot$ )	$R_{out}$ (cm)	$R_{in}$ (cm)	[O I] ratio	$\tau_\lambda$
[O I]	714	3250	228	0.07	2.7	$2.00 \times 10^{-4}$	$2.00 \times 10^{16}$	$1.40 \times 10^{15}$	2.3	3.84
[O I]	806	4000	240	0.06	2.3	$4.00 \times 10^{-4}$	$2.79 \times 10^{16}$	$1.67 \times 10^{15}$	2.0	4.02
[O I]	1054	4300	215	0.05	2.3	$7.50 \times 10^{-4}$	$3.92 \times 10^{16}$	$1.96 \times 10^{15}$	2.3	3.85
[O I]	1478	4500	180	0.04	2.0	$1.10 \times 10^{-3}$	$5.75 \times 10^{16}$	$2.30 \times 10^{15}$	2.8	2.65
H $\alpha$	714	3250	813	0.25	1.4	$5.50 \times 10^{-5}$	$2.00 \times 10^{16}$	$5.01 \times 10^{15}$	0.87	
H $\alpha$	806	4000	880	0.22	1.8	$9.00 \times 10^{-5}$	$2.79 \times 10^{16}$	$6.13 \times 10^{15}$	0.76	
H $\alpha$	1862	8500	1190	0.14	1.9	$1.20 \times 10^{-3}$	$1.37 \times 10^{17}$	$1.91 \times 10^{16}$	0.46	
H $\alpha$	2211	9000	1260	0.14	1.9	$3.00 \times 10^{-3}$	$1.72 \times 10^{17}$	$2.41 \times 10^{16}$	0.73	
H $\alpha$	2875	9500	1140	0.12	2	$8.00 \times 10^{-3}$	$2.36 \times 10^{17}$	$2.83 \times 10^{16}$	1.05	
H $\alpha$	3500	10000	1200	0.12	2	$1.35 \times 10^{-2}$	$3.02 \times 10^{17}$	$3.63 \times 10^{16}$	1.08	
H $\alpha$	3604	10250	1230	0.12	2	$1.70 \times 10^{-2}$	$3.19 \times 10^{17}$	$3.83 \times 10^{16}$	1.22	

**Table 4.6.** The parameters used for the best fitting clumped models of SN 1987A with amorphous carbon grains of radius  $a = 3.5 \mu\text{m}$ . Optical depths are given from  $R_{in}$  to  $R_{out}$  at  $\lambda = 6563 \text{ \AA}$  for H $\alpha$  and  $\lambda = 6300 \text{ \AA}$  for [O I]. Values of  $\tau_V$  are very close to the quoted values of  $\tau_{H\alpha}$ .

	day	$V_{max}$ (km s $^{-1}$ )	$V_{min}$ (km s $^{-1}$ )	$R_{in}/R_{out}$	$\beta$	$M_{dust}$ ( $M_\odot$ )	$R_{out}$ (cm)	$R_{in}$ (cm)	[O I] ratio	$\tau_\lambda$
[O I]	714	3250	228	0.07	2.9	$1.50 \times 10^{-3}$	$2.00 \times 10^{16}$	$1.40 \times 10^{15}$	2.3	4.20
[O I]	806	4000	240	0.06	2.3	$2.70 \times 10^{-3}$	$2.79 \times 10^{16}$	$1.67 \times 10^{15}$	2.1	3.95
[O I]	1054	4300	215	0.05	2.3	$5.50 \times 10^{-3}$	$3.92 \times 10^{16}$	$1.96 \times 10^{15}$	2.5	4.12
[O I]	1478	4500	180	0.04	1.9	$8.00 \times 10^{-3}$	$5.75 \times 10^{16}$	$2.30 \times 10^{15}$	2.8	2.81
H $\alpha$	1862	8500	1190	0.14	1.9	$1.00 \times 10^{-2}$	$1.37 \times 10^{17}$	$1.91 \times 10^{16}$	0.55	
H $\alpha$	2211	9000	1260	0.14	1.9	$2.40 \times 10^{-2}$	$1.72 \times 10^{17}$	$2.41 \times 10^{16}$	0.85	
H $\alpha$	2875	9500	1140	0.12	2	$6.00 \times 10^{-2}$	$2.36 \times 10^{17}$	$2.83 \times 10^{16}$	1.15	
H $\alpha$	3500	10000	1200	0.12	2	$1.15 \times 10^{-1}$	$3.02 \times 10^{17}$	$3.63 \times 10^{16}$	1.34	
H $\alpha$	3604	10250	1230	0.12	2	$1.25 \times 10^{-1}$	$3.19 \times 10^{17}$	$3.83 \times 10^{16}$	1.31	

to the data for days 714 to 3604 whilst Table 4.4 details the parameters used.

It can be seen from Tables 4.4 to 4.6 that, in order to reproduce the blueshifts seen in the [O I]  $\lambda 6300, 6363$  Å doublet, considerably larger dust masses are required than to fit the H $\alpha$  line at the same epoch. Although the same maximum velocities and therefore outer radii are used in my [O I] and H $\alpha$  models, the inner radii for the [O I] models are significantly smaller and the density distribution much steeper. This implies that [O I] is concentrated towards the centre of the ejecta whereas H $\alpha$  is more diffuse. This is broadly in agreement with 3D explosion dynamics models that suggest that a few hours after the explosion the heavier elements will, in comparison to hydrogen, be located more centrally in the ejecta with “bullets” of heavier material reaching the outer edges (Hammer et al. 2010). If dust is forming in the inner regions of the ejecta then the majority of the [O I] emission must travel through the newly formed dust whereas the more diffuse H $\alpha$  emission has a greater chance of escaping unaffected. This may explain the difference between the dust masses needed for the [O I] and H $\alpha$  models.

### 4.3.2 Clumped Dust Models for SN 1987A

A number of investigators have presented arguments for the material in the ejecta of SN 1987A being clumped (Lucy et al. 1991; Li & McCray 1992; Kozma & Fransson 1998b) and so I consider clumped models for the ejecta dust to be more realistic than smoothly distributed dust models. It has been shown through the modelling of optical-IR SEDs that when dust is assumed to have a clumped distribution then the derived dust masses can be significantly larger than for the case of dust that is distributed smoothly between the inner and outer radii (e.g. Ercolano et al. (2007); Owen & Barlow (2015)). I present in Figure 4.12 two sets of fits to the line profile based on the clumped dust modelling of W15, one set with a minimum grain radius and one set with a maximum grain radius. Each fit is based on the best fitting smooth model such that the photon packets are emitted assuming a smooth radial density profile. However, the dust is no longer coupled to the gas but instead is located entirely in clumps of size  $R_{out}/25$ . The clumps are distributed stochastically between  $R_{in}$  and  $R_{out}$  with the probability of a given grid cell being a clump proportional to  $r^{-\beta}$  where  $i(r) \propto r^{-2\beta}$ . The number of clumps used is determined by the clump filling factor  $f$  which is kept constant at  $f = 0.1$ . All properties are fixed from the smooth models with the exception of the grain radius, density profile exponent ( $\beta$ ) and the total dust mass.

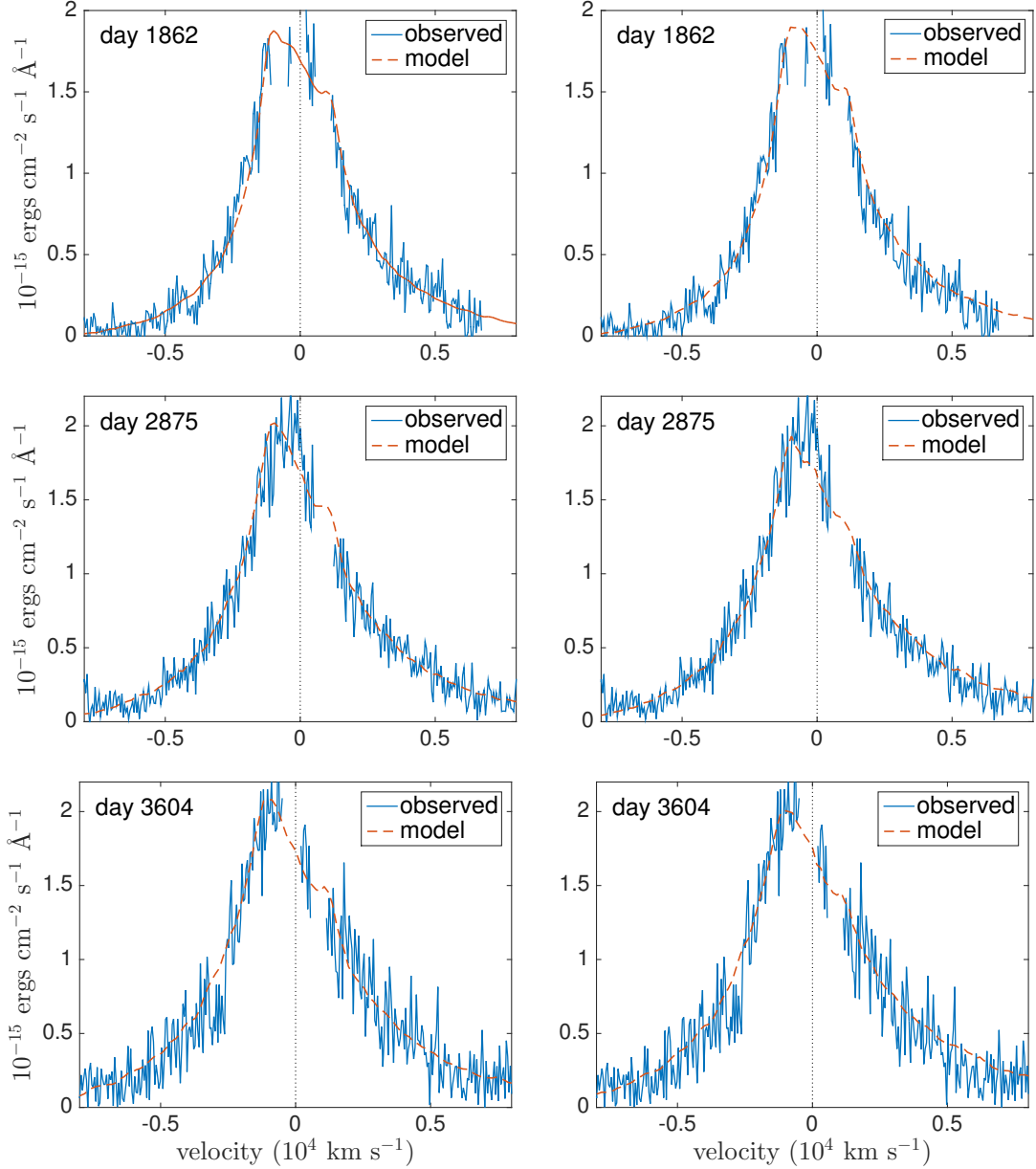


**Figure 4.12.** Best model fits to the SN 1987A H $\alpha$  line at days 1862, 2875 and 3604 for the parameters detailed in Tables 4.5 and 4.6. On the left are clumped model fits with amorphous carbon grains of radius  $a = 0.6 \mu\text{m}$  and on the right are clumped model fits with amorphous carbon grains of radius  $a = 3.5 \mu\text{m}$ .

Models were again constructed using the smallest possible grain radius ( $a=0.6\text{ }\mu\text{m}$  in the clumped case) in order to derive minimum dust masses for clumped distributions. By considering the extent of the red scattering wing, upper limits to the grain radius were also derived with the purpose of limiting the maximum dust mass at each epoch. By steadily reducing the grain radius from an initial value of  $5\text{ }\mu\text{m}$  (motivated by the maximum possible grain radius derived by W15 for their day 8515 model), I produced a set of models with a maximum grain radius of  $a = 3.5\text{ }\mu\text{m}$ .

The increase in grain radius from the smooth case to the clumped case is necessary in order to have a slightly larger albedo. Grains of radius  $a = 0.35\text{ }\mu\text{m}$  do not reproduce the red side of the profiles well for a clumped medium. This is because when the dust is located in clumps the radiation is subject to less scattering as well as to less absorption. The reduction in scattering appears not to be compensated for by the increased dust mass and a larger grain radius is therefore required, particularly at day 714.

For all but the  $\text{H}\alpha$  line at days 714 and 806 a similar fit could be obtained with either a grain radius of  $a = 0.6\text{ }\mu\text{m}$  or  $a = 3.5\text{ }\mu\text{m}$  (see Figures 4.9 and 4.12). However, for  $\text{H}\alpha$  at days 714 and 806 even a small change to the grain radius from  $0.6\text{ }\mu\text{m}$  resulted in a significantly poorer fit, either over- or under-estimating the red wing. I therefore conclude that the dust mass estimates produced for the  $\text{H}\alpha$  lines at days 714 and 806 for a grain radius of  $a = 0.6\text{ }\mu\text{m}$  are the best  $\text{H}\alpha$ -based estimates of the dust mass at this epoch.

In my subsequent analyses, I adopt the values derived from my clumped models. Details of the parameters used are presented in Tables 4.5 and 4.6 and the fits are presented in Figures 4.9 and 4.12.

### 4.3.3 Goodness of fit

I detailed at the start of Section 4.3 the process by which parameters were constrained in order to obtain good fits to the data. These fits were judged both by eye and by minimising the mean square error between the model and the observed data for each line profile. The sensitivity of the fits to various parameters may be of interest and so, in Tables 4.7 and 4.8, I detail the mean square error (MSE) for the  $\text{H}\alpha$  profile at days 714 and 2875 for a range of dust masses and density profile exponents. All other parameters were kept fixed at their best-fitting values for the clumped models of  $\text{H}\alpha$  with a grain radius  $a = 0.6\mu\text{m}$  as in Table 4.5. The line profiles for these models are presented in Figures 4.14 to 4.17.

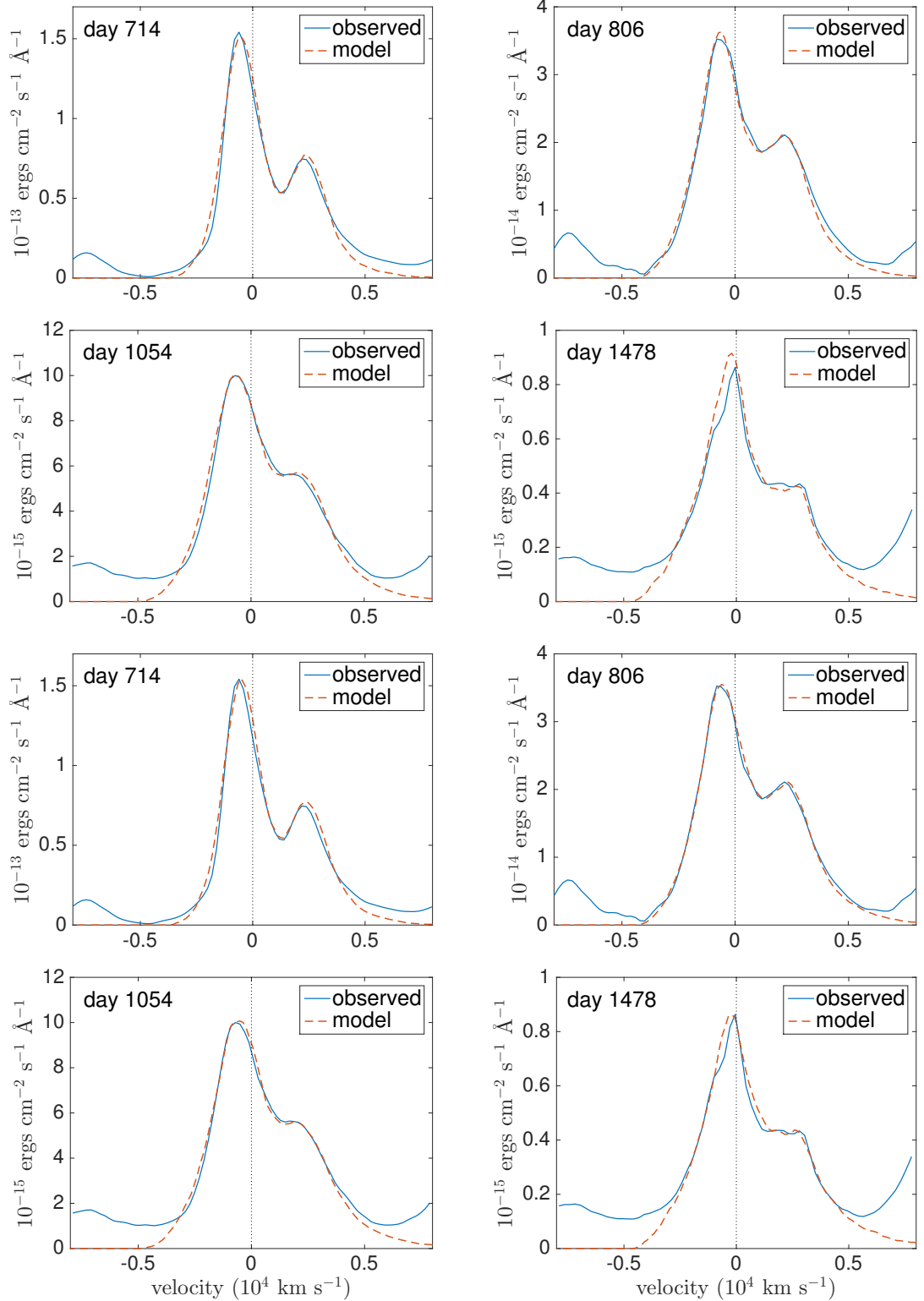


**Figure 4.13.** Best clumped model fits to the SN 1987A [O I]  $\lambda 6300, 6363 \text{ \AA}$  doublet at days 714, 806, 1054 and 1478 for the parameters detailed in Tables 4.5 and 4.6. On the left are clumped dust fits with amorphous carbon grains of radius  $a = 0.6 \mu\text{m}$  and on the right are clumped dust fits with amorphous carbon grains of radius  $a = 3.5 \mu\text{m}$ .

**Table 4.7.** Mean square errors illustrating the variation in goodness of fit for the H $\alpha$  line profile for a range of dust masses with other parameters fixed at their best-fitting values for the clumped model with  $a = 0.6\mu\text{m}$  as detailed in Table 4.5. The MSE is calculated between  $-5000 \text{ km s}^{-1}$  and  $+7000 \text{ km s}^{-1}$  for the day 714 H $\alpha$  profile and between  $-8000 \text{ km s}^{-1}$  and  $+8000 \text{ km s}^{-1}$  for the day 2875 H $\alpha$  profile. A factor of zero represents the dust-free model. The best-fitting model is italicised.

	<i>multiple of best-fit mass</i>				
	0	0.1	0.5	1.0	2.0
Day 714 MSE ( $10^{-13} \text{ ergs cm}^{-2} \text{ s}^{-1}$ )	0.167	0.133	0.043	<i>0.005</i>	0.115
Day 2875 MSE ( $10^{-15} \text{ ergs cm}^{-2} \text{ s}^{-1}$ )	0.0791	0.0604	0.0258	<i>0.0182</i>	0.0563

**Table 4.8.** Mean square errors illustrating the variation in goodness of fit for the H $\alpha$  line profile for a range of density profiles with other parameters fixed at their best-fitting values for the clumped model with  $a = 0.6\mu\text{m}$  as detailed in Table 4.5. The MSE is calculated between  $-5000 \text{ km s}^{-1}$  and  $+7000 \text{ km s}^{-1}$  for the day 714 H $\alpha$  profile and between  $-8000 \text{ km s}^{-1}$  and  $+8000 \text{ km s}^{-1}$  for the day 2875 H $\alpha$  profile. The best-fitting model is italicised.

	<i>density profile exponent (<math>\beta</math>)</i>				
	1.0	1.2	1.4	1.6	1.8
Day 714 MSE ( $10^{-13} \text{ ergs cm}^{-2} \text{ s}^{-1}$ )	0.0328	0.0117	<i>0.005</i>	0.0184	0.0410
Day 2875 MSE ( $10^{-15} \text{ ergs cm}^{-2} \text{ s}^{-1}$ )	0.0282	0.0205	<i>0.0182</i>	0.0193	0.0255

The MSE is calculated as

$$\frac{1}{N} \sum_i (f_{obs,i} - f_{mod,i})^2 \quad (4.1)$$

where  $N$  is the number of data points,  $f_{obs,i}$  is the observed flux at the  $i^{th}$  data point and  $f_{mod,i}$  is the modelled flux at the  $i^{th}$  data point. The MSEs were calculated between  $-5000 \text{ km s}^{-1}$  and  $+7000 \text{ km s}^{-1}$  for the day 714 H $\alpha$  profile and between  $-8000 \text{ km s}^{-1}$  and  $+8000 \text{ km s}^{-1}$  for the day 2875 H $\alpha$  profile. Note that the MSEs should only be compared between models for a given observed line profile and not between different line profiles since each observation is associated with a different inherent error.

For day 714, I find that increasing or decreasing the total dust mass by a factor of two with all other parameters fixed causes a substantial increase in the mean square error (by factors of 23 and 8.6 respectively) effectively ruling out these values. For day 2875 a similar variation is seen but with the MSE varying by factors of 1.4 and 3.0 for each case. The narrower range of MSEs at day 2875 compared to day 714 is due to a noisier profile which results in a greater allowed range of good fits. The sensitivity of the goodness of fit to the dust mass and density profile is similar for the other modelled epochs.

#### 4.3.4 The effects of clumping

As in the case of SED radiative transfer models, the dust masses required to reproduce the observations in the clumped scenario are considerably higher than for the smooth scenario. The dust masses differ between my smooth models for  $a = 0.35 \mu\text{m}$  and clumped models for  $a = 0.6 \mu\text{m}$  by a factor of approximately 3. The dust mass estimates are even larger when comparing clumped  $a = 0.6 \mu\text{m}$  models to clumped  $a = 3.5 \mu\text{m}$  models at later epochs. This does not take into account the increase in grain radius between the two cases however. This increase accounts for a reasonable fraction of this difference. I estimate the effects of clumping alone to increase the required dust mass by a factor of approximately 1.5-2.0 from the smooth case.

#### 4.3.5 More complex models

Where blue-shifted lines are observed in the spectra of CCSNe it is often the case that the Balmer lines of HI are less affected than the [O I] lines (Milisavljevic et al. 2012).

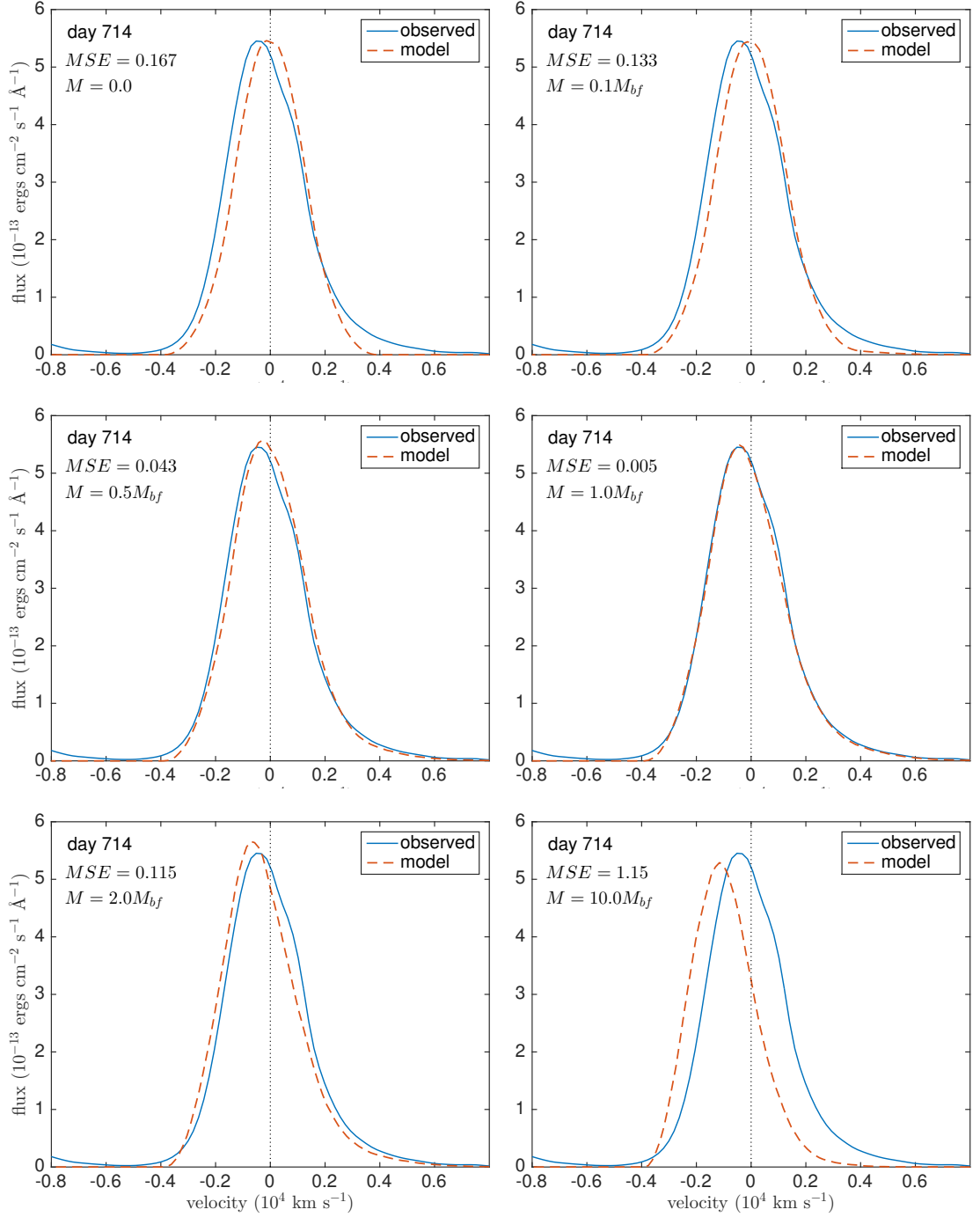


**Figure 4.14.** Fits to the H $\alpha$  line profile for day 714 for a variety of dust masses. All other parameters are given as per Table 4.5. Dust masses are given as a multiple of the best fitting dust mass ( $M_{bf}$ ) and the mean squared error is presented for each plot.

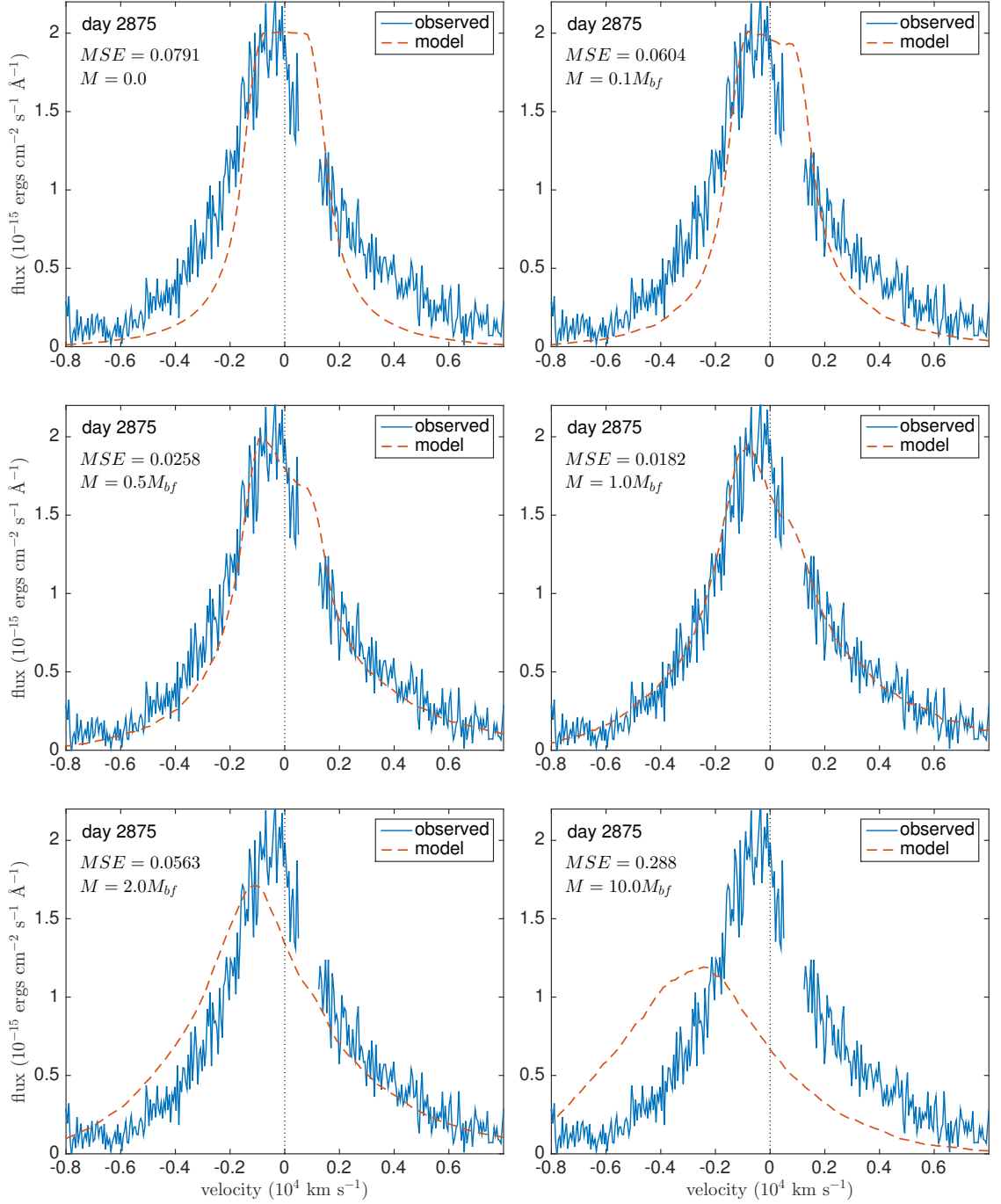


**Figure 4.15.** Fits to the H $\alpha$  line profile for day 2875 for a variety of dust masses. All other parameters are given as per Table 4.5. Dust masses are given as a multiple of the best fitting dust mass ( $M_{bf}$ ) and the mean squared error is presented for each plot.

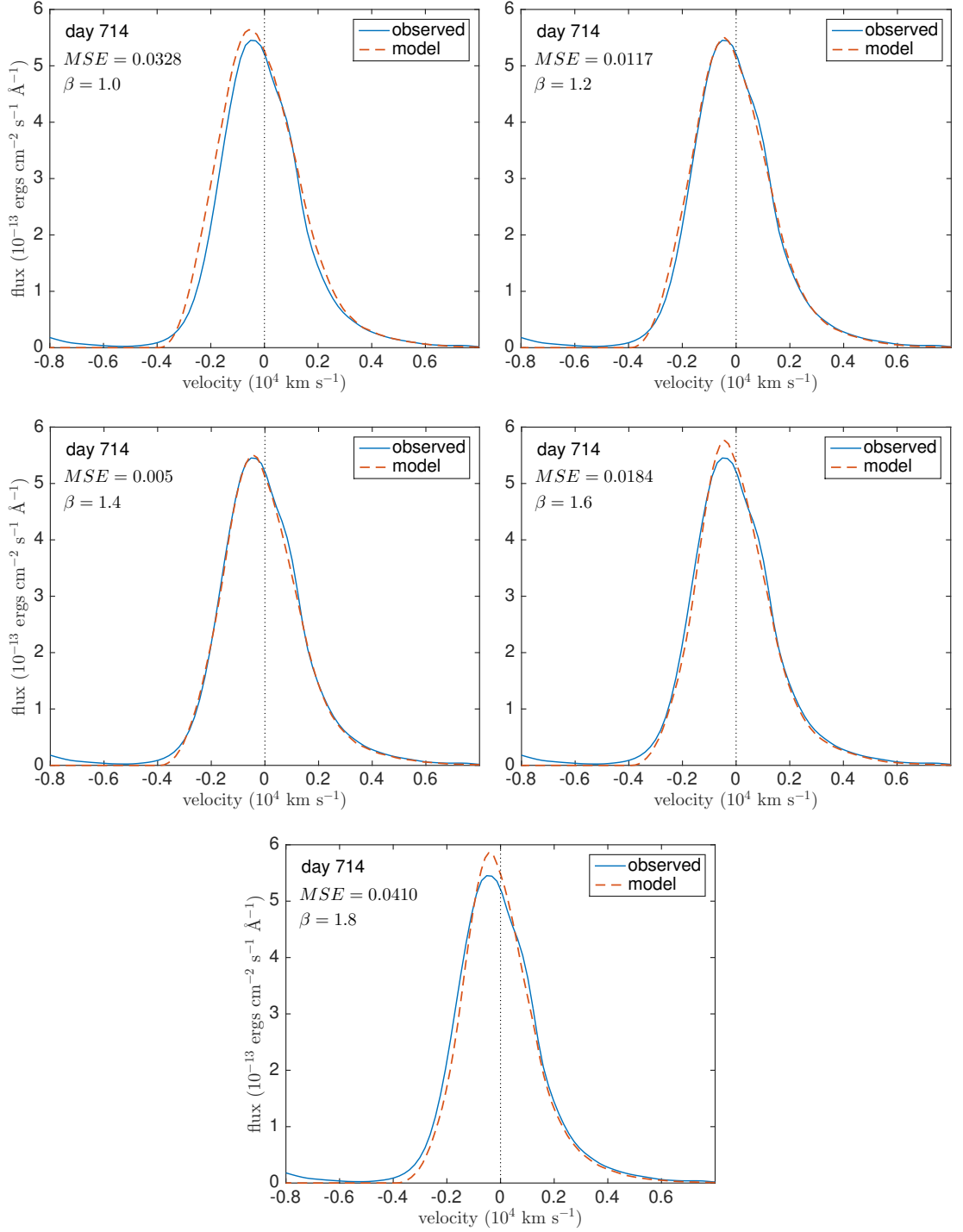


**Figure 4.16.** Fits to the H $\alpha$  line profile for day 714 for a variety of density distributions with the  $\beta = 1.4$  case representing the best fit. All other parameters are given as per Table 4.5. The mean squared error is presented for each plot.

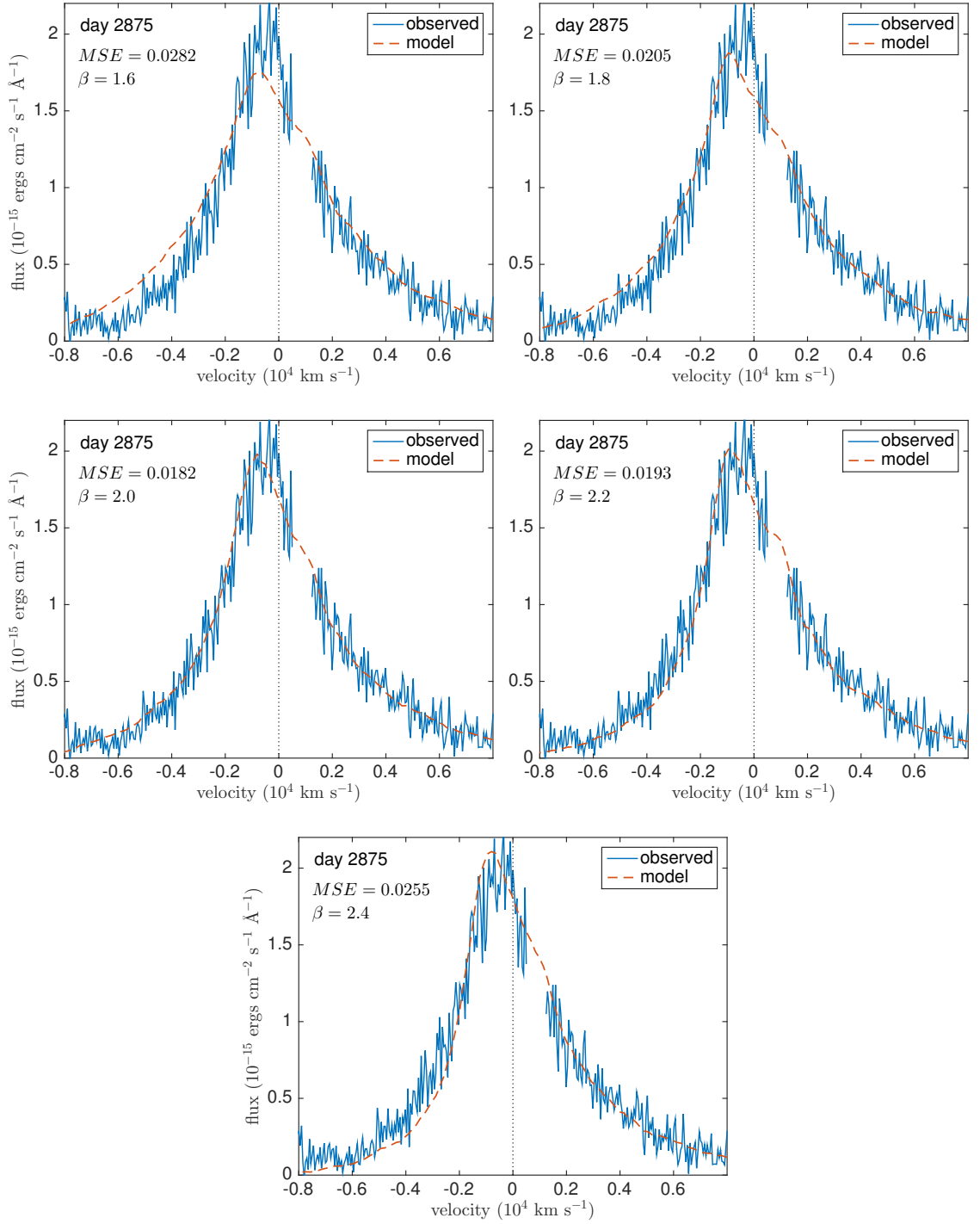


**Figure 4.17.** Fits to the H $\alpha$  line profile for day 2875 for a variety of density distributions with the  $\beta = 2.0$  case representing the best fit. All other parameters are given as per Table 4.5. The mean squared error is presented for each plot.

This may be due to a difference in the location or distribution of the emitting elements; if the neutral hydrogen was diffusely distributed throughout the envelope but the oxygen was co-located with the dust in the core and in clumps then this could result in [O I] emission undergoing greater attenuation than H $\alpha$ . This geometry would be in line with previous models of SN 1987A that suggested that the dust-forming regions are likely to include those which are oxygen-rich (Kozma & Fransson 1998a). Clearly, any model of dust formation in the ejecta of a CCSN must consistently reproduce all of the line profiles at a given epoch. The models presented in this paper thus far have coupled the gas and dust distributions for a fixed clump volume filling factor and clump size. The H $\alpha$  and [O I] models therefore require different dust masses with the [O I] models usually requiring a dust mass  $\sim 4$  times larger than the H $\alpha$  models.

I now present a model that reconciles this difference by additionally varying the clump filling factor, clump size and emissivity distribution. I assume that neutral hydrogen is likely diffuse throughout the ejecta and so maintains a smoothly distributed power-law emissivity distribution between  $R_{in}$  and  $R_{out}$  for H $\alpha$ . However, I now assume that dust mostly forms in dense regions of high metallicity and so restrict the [O I] $\lambda 6300, 6363$  Å emission to originate entirely from the dusty clumps. As previously discussed, the greater the covering factor of the dust the greater the albedo required in order to reproduce the H $\alpha$  red scattering wing. In order to obtain both the strong blue-shifting of the [O I] line and the extended red scattering wing observed in H $\alpha$  a small number of dense clumps were required along with a small mass of diffusely distributed highly scattering dust in the inter-clump medium.

In order to fit both line profiles simultaneously I required a very high albedo ( $\omega > 0.8$ ) that demanded the inclusion of some fraction of silicate dust. Amorphous carbon grains alone are incapable of producing this level of scattering for any grain radius. I adopted a grain radius of  $a = 0.6\mu\text{m}$ , the same as that used in my initial clumped models and I varied the relative proportions of amorphous carbon and MgSiO<sub>3</sub> in order to achieve the necessary albedo. The adopted grain densities were  $\rho_c = 1.85 \text{ g cm}^{-3}$  for amorphous carbon grains and  $\rho_s = 2.71 \text{ g cm}^{-3}$  for MgSiO<sub>3</sub>. The resulting dust model for day 714 used 75% MgSiO<sub>3</sub> and 25% amorphous carbon by cross-sectional area with a volume filing factor  $f_V = 0.1$  and a clump size  $R_{out}/5$ . 90% of the dust mass was located in clumps with the remaining 10% distributed smoothly between  $R_{in}$  and  $R_{out}$  according to a power law  $\rho \propto r$ . Clumps were distributed stochastically with probability  $\propto r^{-8}$  compared to  $r^{-2.7}$

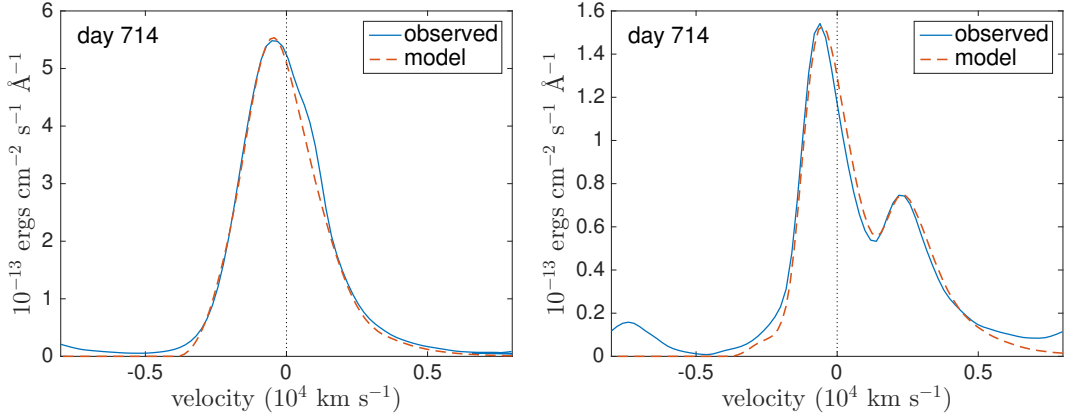


**Figure 4.18.** Fits to the H $\alpha$  and [O I] $\lambda\lambda 6300,6363$  Å lines at day 714 using the more complex dust model described in Section 4.3.5 with a dust mass of  $2.3 \times 10^{-4} M_{\odot}$ .

in my standard models discussed earlier. Equal numbers of [O I] packets were emitted from each clump. The increased steepness of the density profile is required to compensate for the clumped packet emission relative to the previous smooth distribution. Since the clumps are distributed stochastically according to the density profile, less flux is emitted from the central regions in a clumped emission model than in a smooth distribution model (since there are gaps between the clumps). In order to obtain a sufficiently steeply rising line profile, the density profile must therefore be steepened in clumped emission models. The adopted value of  $\beta$  does not significantly affect the best-fitting values of the other parameters of interest however. H $\alpha$  emission was distributed smoothly according to an emitting density power law  $\rho(r) \propto r^{-1.3}$ .  $R_{out}$  was the same for all components (i.e. clumped dust, diffuse dust, [O I] emission and H $\alpha$  emission) and was calculated using a maximum velocity of  $3250 \text{ km s}^{-1}$ . The inner radius was  $R_{in} = 0.07R_{out}$  for all components except the smooth H $\alpha$  emission which was emitted between  $R_{in} = 0.25R_{out}$  and  $R_{out}$ .

The total dust mass used was  $M_{dust} = 2.3 \times 10^{-4} M_{\odot}$ . This dust mass is very similar to that derived from my original clumped models of [O I] using amorphous carbon grains of radius  $a = 0.6 \mu\text{m}$ . The slight increase over my amorphous carbon dust mass of  $1.5 \times 10^{-4} M_{\odot}$  is largely due to the higher grain density of MgSiO<sub>3</sub>. At this grain radius amorphous carbon and MgSiO<sub>3</sub> have similar extinction efficiencies and so the change in species and geometry does not substantially alter the dust mass. I therefore adopt the [O I] dust masses in my further analyses and consider the differences in my derived dust masses between H $\alpha$  and [O I] to be the result of the clumped emission of [O I].

Fits to both the [O I] $\lambda$ 6300,6363 Å and H $\alpha$  lines for day 714 using these parameters are presented in Figure 4.18.

#### 4.3.6 The effect of a grain radius distribution

All of the models heretofore have been based on a single grain radius. As previously discussed in Chapter 3, it is important to consider the possible effects of a dust grain radius distribution. This is more likely to be the case in reality and potentially has a significant effect on the derived dust mass.

As discussed in Section 4.3.1, for a classical MRN power law ( $n(a) \propto a^{-3.5}$ ) with a wide grain radius range ( $a_{min} = 0.001 \mu\text{m}$  to  $a_{max} = 4.0 \mu\text{m}$ ) the derived albedo is much too small to reproduce the required wing seen at early epochs. I therefore adopt an approach whereby, for a number of grain radius ranges, I adjust the exponent of the distribution until the overall albedo is the same as that seen for the best fitting single grain radius for the clumped distributions. Using Equation 3.20 from Chapter 3, I calculate the required dust masses for the clumped H $\alpha$  model on day 714 for a selection of distributions with varying  $a_{min}$ . These are presented in Table 4.9.

It can be seen that in all cases, a larger dust mass is required for grain radius distributions in order to reproduce the same profile as a single grain radius. The conversion factors presented in the table are valid for any model with grain radius  $a = 0.6 \mu\text{m}$  and may therefore also be applied to the models for day 806. I repeated the process for  $a = 3.5 \mu\text{m}$  but found that, in order to reproduce the required albedo, the distribution had to be heavily weighted towards the larger grains and that the value of  $a_{min}$  had no effect on the required dust mass. Increasing the value of  $a_{min}$  to larger values ( $> 2 \mu\text{m}$ ) does not have a significant effect either. This is because both extinction efficiency and albedo tend to a constant value with increasing grain radius and the adoption of different grain radius ranges and distributions above a certain threshold results in only insignificant variations in these quantities.

I conclude that if a distribution of grain radii is indeed present, the deduced single size dust masses are likely to under-estimate the true mass of newly formed dust.

#### 4.3.7 The effect of different grain species

In my analyses so far I have mostly focussed on amorphous carbon as the species of interest. This was motivated by previously published early epoch optical and IR SED

**Table 4.9.** Dust masses for day 714 clumped models of the H $\alpha$  line using different grain radius distributions and 100% amorphous carbon. The final column shows the factor of increase over the dust mass for the single size model ( $M = 7 \times 10^{-5} M_{\odot}$  with  $a = 0.6 \mu\text{m}$ ) and  $p$  is the exponent of the grain radius distribution  $n(a) \propto a^{-p}$ .

$a_{min}$ ( $\mu\text{m}$ )	$a_{max}$ ( $\mu\text{m}$ )	$p$	$M$ ( $M_{\odot}$ )	$M/M_{0.6}$
0.001	4.0	2.45	$1.93 \times 10^{-4}$	2.76
0.01	4.0	2.45	$1.93 \times 10^{-4}$	2.76
0.05	4.0	2.52	$1.84 \times 10^{-4}$	2.62
0.1	4.0	2.72	$1.61 \times 10^{-4}$	2.3
0.5	4.0	8.20	$7.23 \times 10^{-5}$	1.03

analyses that found that the silicate mass fraction must be limited to  $\leq 15\%$  (Ercolano et al. (2007), W15). The recent suggestion by Dwek & Arendt (2015) that large masses of the glassy silicate MgSiO<sub>3</sub> may have formed at early epochs is discussed further in the next subsection. As previously discussed in Chapter 3, the parameters that affect the quantity of dust required by my models are the mean albedo and optical depth of the dust and there could therefore be multiple combinations of grain species and sizes that result in a good fit to the data.

In Chapter 3, I evaluated the required change in dust mass when a medium of 100% silicates was used instead of amorphous carbon (see Equation 3.21).

Because of the nature of the variation of albedo with grain radius for the Draine & Lee (1984) astronomical silicate (see Figure 3.9), there is often more than one silicate grain radius that will give rise to the same albedo at a given wavelength. Some of the possibilities and the resulting mass conversion factors between media composed of 100% Zubko BE amorphous carbon and 100% Draine & Lee silicates derived using Equation 3.21 in Chapter 3 are given in Table 4.10. For my best fitting amorphous carbon models with  $a = 0.6 \mu\text{m}$  (the first two entries in Table 4.10), using any fraction of silicates with either  $a = 0.6 \mu\text{m}$  or  $a = 3.5 \mu\text{m}$  would increase the dust mass. However, for the case of an amorphous carbon grain radius of  $a = 3.5 \mu\text{m}$  (the last three entries), using silicate dust would reduce the dust mass by a factor of between 0.49 - 0.65 relative to my amorphous carbon values.

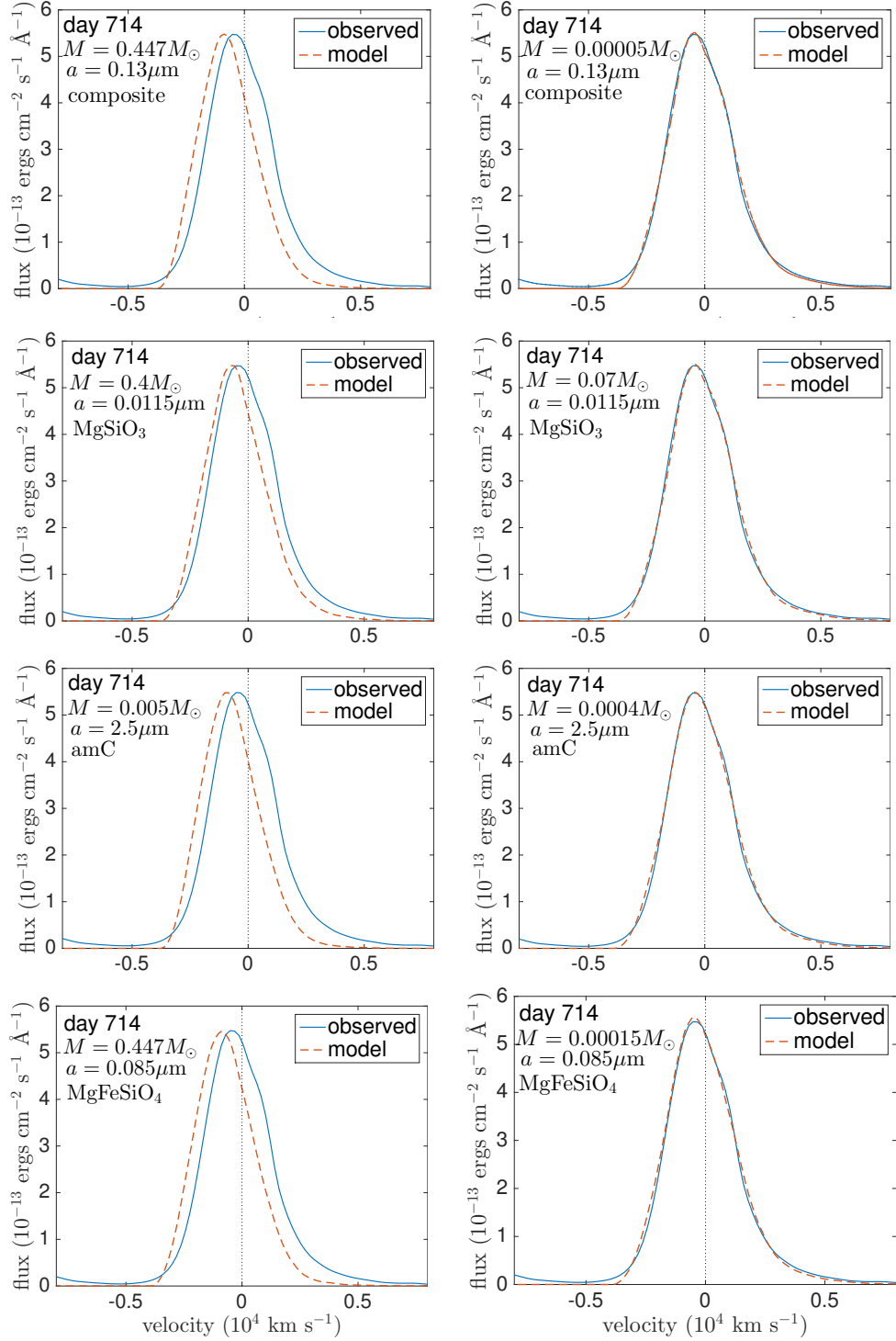


**Figure 4.19.** H $\alpha$  models using different grain species and dust masses. Models for the dust masses presented by Dwek & Arendt (2015) are on the top and models using my minimum required dust masses are on the bottom. From left to right the dust species are composite grains (82% MgSiO<sub>3</sub> and 18% amorphous carbon by volume), pure MgSiO<sub>3</sub>, pure amorphous carbon and pure MgFeSiO<sub>4</sub>. A density distribution with  $\beta = 2.3$  was adopted with a filling factor  $f = 0.09$  and an effective clump radius  $R_{\text{eff}}/R_{\text{out}} = 0.044$ . All other parameters are the same as in Table 4.5.

**Table 4.10.** Dust mass conversion factors for single size models using grains of 100% Zubko BE amorphous carbon or 100% Draine & Lee silicate at  $\lambda \sim 656$  nm.  $f$  is the factor by which the dust mass changes on going from amorphous carbon to silicates.

carbon			silicates				$M_{sil}/M_{amc}$
$a$ ( $\mu\text{m}$ )	$\omega$	$Q_{ext}$	$a$ ( $\mu\text{m}$ )	$\omega$	$Q_{ext}$		
0.6	0.56	2.61	0.0583	0.58	0.08	5.37	
0.6	0.56	2.61	4.00	0.56	2.18	13.0	
3.5	0.62	2.21	0.0641	0.64	0.10	0.65	
3.5	0.62	2.21	1.020	0.63	2.15	0.49	
3.5	0.62	2.21	1.376	0.62	2.35	0.61	

### 4.3.8 Modelling large masses of dust at early epochs: comparison with the results of Dwek & Arendt (2015)

In a recent analysis of infrared SED data, Dwek & Arendt (2015) (hereafter DA15) suggested that it may be possible for a large mass ( $0.4 M_\odot$ ) of  $\text{MgSiO}_3$  silicate dust to have been present in SN 1987A even at relatively early epochs ( $t \sim 615$  days), since that species has very low IR emissivities. Up to this point I have constructed models using Zubko et al. (1996) BE amorphous carbon dust but in the previous section I discussed the effect on derived dust masses of instead using Draine & Lee (1984) astronomical silicate, which has higher optical and IR emissivities than the glassy  $\text{MgSiO}_3$  species considered by DA15.

I now consider models for day 714 based on the grain types used by DA15. I adopt a clumped structure equivalent to the preferred model of DA15 who considered 1000 clumps with a filling factor of 0.09 and a negligible dust mass in the inter-clump medium. I calculate the effective spherical radius of my clumps by equating the volume of my cubic clumps to a sphere of radius  $R_{eff}$ . Clumps of width  $R_{out}/14$  generate the desired  $R_{eff}/R_{out} = 0.044$  equivalent to that of DA15. In my code, using a filling factor of 0.09 then generates 1034 clumps, similar to the number used by DA15. I ran a series of models (presented in Figures 4.19 and 4.20) for both the  $\text{H}\alpha$  and  $[\text{O I}]\lambda 6300, 6363 \text{ \AA}$  line profiles. In each case I modelled the lines using a dust grain mixture as described by DA15 such that the medium comprised 18% amorphous carbon and 82%  $\text{MgSiO}_3$  by volume. I adopted the same optical constants as used in their work (i.e. Jäger et al. (2003) for  $\text{MgSiO}_3$  grains and Zubko et al. (1996) for amorphous carbon) and the same grain mass densities as DA15,  $\rho_s = 3.2 \text{ g cm}^{-3}$  and  $\rho_c = 1.8 \text{ g cm}^{-3}$ . In addition to modelling their composite grain

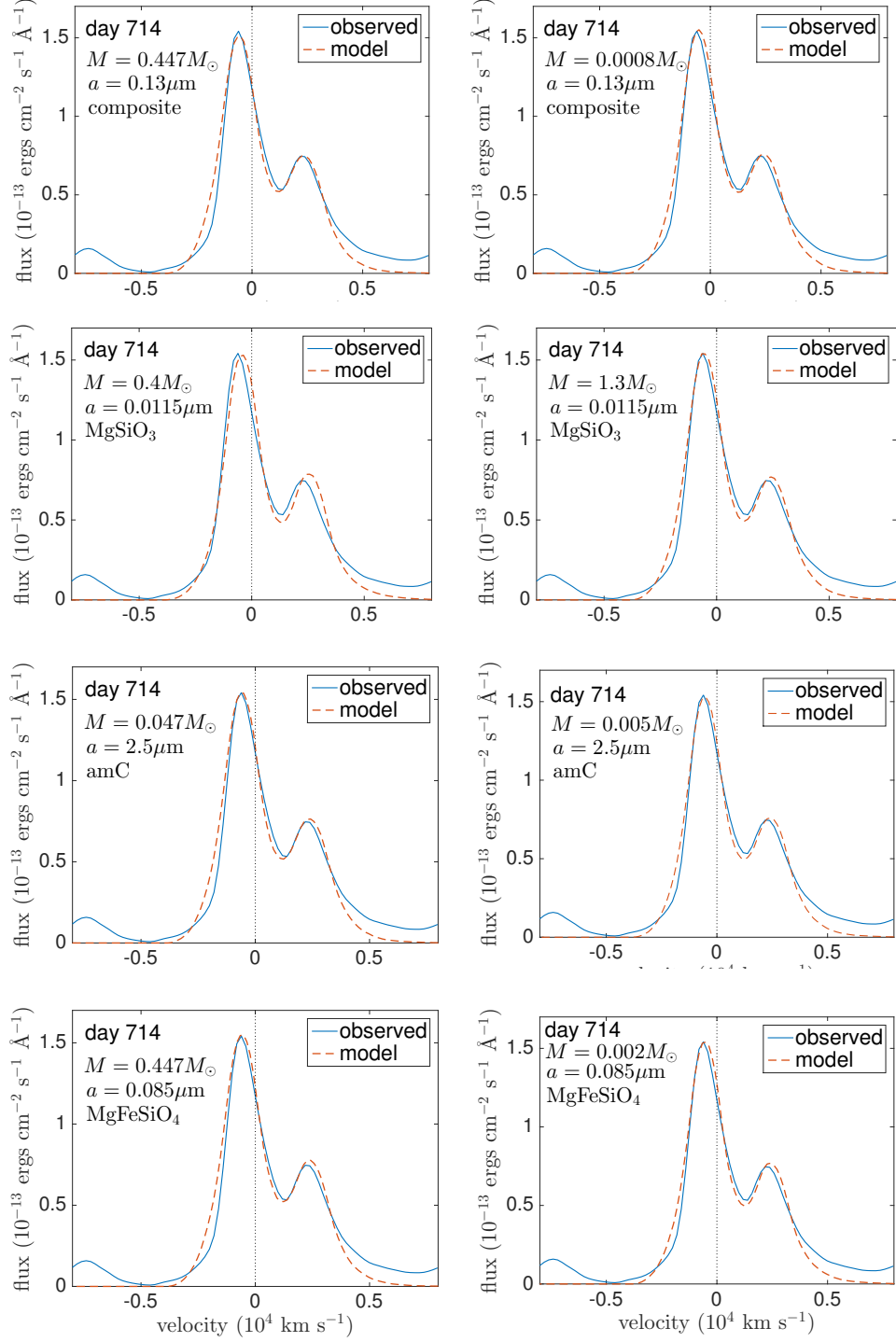


**Figure 4.20.** [O I] $\lambda 6300,6363$  Å models using different grain species and dust masses. Models using the dust masses presented by DA15 are on the top and models using my minimum required dust masses are on the bottom. From left to right the species are composite grains (82% MgSiO<sub>3</sub> and 18% amorphous carbon by volume), pure MgSiO<sub>3</sub>, pure amorphous carbon and pure MgFeSiO<sub>4</sub>. A density distribution with  $\beta = 1.3$  was adopted with a filling factor  $f = 0.09$  and an effective clump radius  $R_{eff}/R_{out} = 0.044$ . The ratio between the doublet components was 2.2. All other parameters are the same as in Table 4.5.

case, I also considered three single species models, using Zubko BE amorphous carbon,  $\text{MgSiO}_3$ , and  $\text{MgFeSiO}_4$  (in the latter two cases the optical constants were taken from Jäger et al. (1994) and Dorschner et al. (1995)). For each species I adopted the smallest single grain radius that has an albedo of  $\omega \approx 0.6$ . The ejecta parameters were as listed in Table 4.5, with the exception of the density distribution which I took to be  $\rho(r) \propto r^{-1.3}$  for  $\text{H}\alpha$  and  $\rho(r) \propto r^{-2.3}$  for [O I] in order to optimise the best fits.

For each species, two models are presented. The first adopts the minimum possible dust mass that provides a reasonable fit to the observed line profiles and the second uses the dust mass derived by DA15 for that specific species ( $M = 0.4 M_\odot$  for  $\text{MgSiO}_3$  and  $M = 0.047 M_\odot$  for amorphous carbon giving a total composite dust mass of  $M = 0.447 M_\odot$ ). I treated  $\text{MgFeSiO}_4$  as I do the composite grains and adopted a dust mass of  $M = 0.447 M_\odot$  for it. Results from the models are presented in Figures 4.19 and 4.20.

The [O I] models can display similar profiles for substantially different dust masses. This is a result of the relatively high optical depths within the clumps themselves. If a clump is optically thick then the majority of radiation that hits it will be absorbed and the profile becomes insensitive to how much dust is actually contained within the clump. For my [O I] minimum dust mass models, the optical depths within a clump over an effective clump radius  $R_{eff}$  at 6300Å are around  $\tau_{clump} \approx 0.4$ . Over the entire nebula optical depths are very high and  $\sim 72\%$  of the total flux is absorbed. Increasing the total dust mass therefore has only a small effect on the emergent line profile and once  $\tau_{clump} > 1$  then the line profile remains unchanged for increasingly large dust masses. It is because of this fact that I present only the smallest dust mass capable of reproducing the [O I] profiles seen in Figure 4.20. The insensitivity of the [O I] profiles to dust mass is not the case for the  $\text{H}\alpha$  profile models (where  $\tau_{clump} < 0.05$  for all of my models) and the  $\text{H}\alpha$ -fit dust masses presented in Figure 4.19 therefore represent the most sensitive diagnostic of the dust mass for each grain type. All of my models discussed in previous sections have significantly smaller clump optical depths ( $\tau_{clump} < 0.1$ ), making them sensitive to dust mass variations.

For all the [O I] line profile models, except for those using pure  $\text{MgSiO}_3$  or pure  $\text{Mg}_2\text{SiO}_4$  dust, the required dust masses are significantly less than those proposed by DA15. The [O I] profile obtained using DA15's very large  $\text{MgSiO}_3$  dust mass of  $0.4 M_\odot$  provides a reasonable fit, but the same dust mass significantly overestimates the blueshifting of the  $\text{H}\alpha$  line (Figure 4.19). I can place an upper limit on the mass of pure  $\text{MgSiO}_3$  on day 714

of  $0.07 M_{\odot}$ , as this is the highest mass for which a fit to the observed H $\alpha$  profile can be obtained (Figure 4.20).

Pure MgSiO<sub>3</sub> is extremely glassy, with very high albedos in the optical for a wide range of grain radii. At grain radii small enough to reduce the albedo to  $\omega \approx 0.6$ , in order to fit the observed line profiles, the extinction efficiency in the optical becomes extremely low (see Figure 3.9), with large masses of dust therefore required in order to produce even a small amount of line absorption. However, for a given albedo, the extinction efficiencies increase by large factors if either carbon or iron is included in the grain. In the composite grain model the amorphous carbon component dominates the overall extinction due to its much larger extinction efficiency at small grain radii. Similarly, for MgFeSiO<sub>4</sub> (or Mg<sub>0.5</sub>Fe<sub>0.5</sub>SiO<sub>3</sub>) grains the iron component leads to much larger optical and IR extinction efficiencies and much lower dust mass upper limits. If the dust that formed at early epochs contained some fraction of elements such as carbon, iron or aluminium, yielding ‘dirtier’ silicate grains or composite grains, then fits to the observed blue-shifted line profiles imply low dust masses. I conclude that for dust masses as large as  $0.07 M_{\odot}$  to have been present in SN 1987A’s ejecta as early as days 600-1000 then the dust would have to have been formed of glassy pure magnesium silicates.

In order to be certain that there was no set of parameters for which a dust mass of  $M = 0.447 M_{\odot}$  comprising 82% MgSiO<sub>3</sub> and 18% amorphous carbon by volume could result in a good fit, a thorough investigation of the variable parameters was performed. Having fixed the clump size, filling factor, dust mass and composition as per the values detailed above and in DA15, I varied the density profile ( $\beta$ ) and grain radius  $a$ . Varying the maximum velocity and the ratio of the inner and outer radii was found to have little effect on the goodness of fit. The MSE for the H $\alpha$  profile presented in the upper left panel of Figure 4.19 was 0.599 (in units of  $10^{-13}$  ergs cm $^{-2}$  s $^{-1}$ ). This was improved to 0.246 by increasing the grain radius to  $a = 0.6 \mu\text{m}$  and the density profile exponent to  $\beta = 1.5$ , which represents the best fit that I could achieve using the values described by DA15 and a dust mass of  $M = 0.447 M_{\odot}$ . However, the overall best fit I obtain for this scenario (see the lower left panel of 4.19) used a much lower dust mass of  $M = 5 \times 10^{-4} M_{\odot}$  giving an MSE=0.0058, substantially improving the fit.

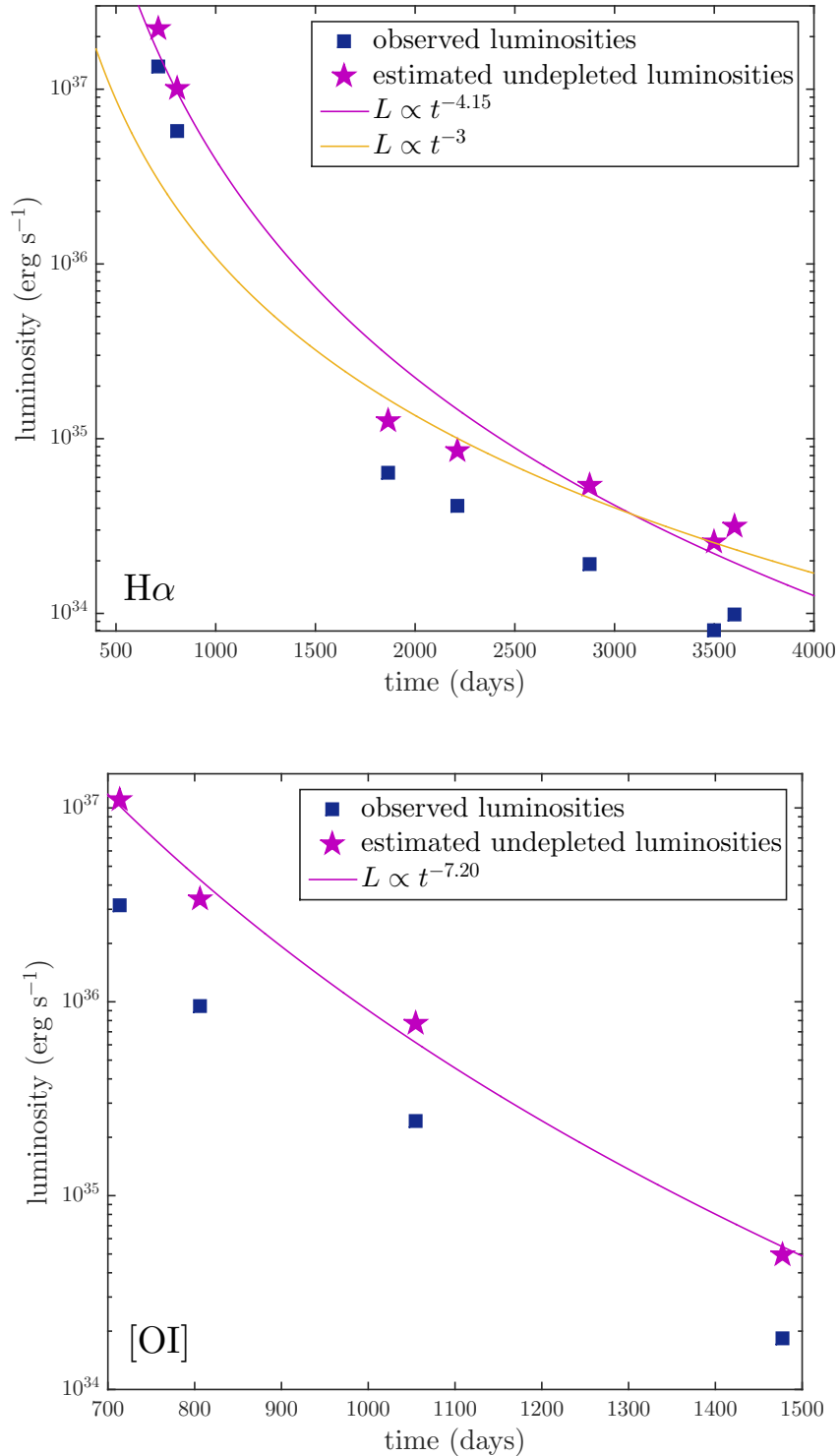


**Figure 4.21.** Predicted undepleted luminosities for the H $\alpha$  line (*above*) and [O I] $\lambda\lambda 6300, 6363$  Å doublet (*below*) presented with the best power-law fit to the data.

### 4.3.9 Unattenuated line fluxes

The evolution of the SN 1987A H $\alpha$  and [O I] $\lambda\lambda 6300, 6363$  Å line fluxes over time has been discussed previously by, for example, Li & McCray (1992), Xu et al. (1992) and Kozma & Fransson (1998b). I may use my clumped models to predict the unattenuated emitted line fluxes and consider their evolution through time. For each model, the fraction of the total line energy absorbed by the dust was predicted. I determined the total flux for each observed line profile and used the absorbed fraction from my clumped models for  $a = 3.5\mu\text{m}$  to predict the undepleted flux of the line before attenuation by the dust. Gaps in the observed data due to contamination by narrow line emission were interpolated over in order to estimate the flux of the broad line component. The observed H $\alpha$  luminosities and predicted undepleted luminosities are given in Table 4.3 along with the energy fraction absorbed by the dust in each model. No correction has been made for interstellar extinction along the sightline to SN 1987A. There is very little change in these values if I adopt the models with  $a = 0.6\mu\text{m}$  instead of  $a = 3.5\mu\text{m}$ . Plots of the observed and undepleted line luminosities are given for all modelled epochs of H $\alpha$  and [O I] in Figure 4.21.

I also present power-law fits to the time evolution of the unattenuated H $\alpha$  and [O I] line fluxes. For H $\alpha$ , I find that  $L_{H\alpha}(t) \propto t^{-4.15}$  between days 714 and 3604. I can compare this value to the theoretical time dependence of the flux of a recombination line based on the dynamics of the ejecta for an environment in a Hubble-type flow  $r = vt$ . For a frozen-in ionization structure, the mean intensity of a recombination or collisionally-excited line per unit volume is locally proportional to the product of the densities of the recombining species i.e.  $J_{H\alpha} \propto n_e n_p \propto n_e^2$ . The total luminosity of the line is therefore dependent on the volume  $V$  as  $L_{H\alpha} \propto 1/V$ . Assuming a constant maximum expansion velocity, the luminosity should vary with time as  $L_{H\alpha}(t) \propto t^{-3}$ .

This relationship is only true for a constant ionization fraction. This “freeze-out” phase is estimated to have begun at  $\sim 800$  days and first sets in at lower density high velocity regions, gradually moving inwards with time (Danziger et al. 1991b; Fransson & Kozma 1993). Since my modelling begins at day 714, the ionization fraction in the inner higher density regions is likely still decreasing due to recombination during my first two epochs. This presumably accounts for the slightly steeper  $L_{H\alpha}(t) \propto t^{-4.15}$  that I find across all epochs. Kozma & Fransson (1998b) estimate that H $\alpha$  emission from the outer regions begins to dominate over H $\alpha$  emission from core regions for  $t > 900$  days. If earlier

epochs are ignored, the last five epochs ( $t \geq 1862$  days) plotted in (Figure 4.21) exhibit a shallower trend that is in good agreement with the expected  $L_{H\alpha}(t) \propto t^{-3}$  evolution.

The  $[O\ I]\lambda 6300, 6363$  Å doublet exhibits a much steeper evolution,  $L_{[OI]}(t) \propto t^{-7.2}$ , than the  $H\alpha$  line (Figure 4.21). These collisionally excited lines are very sensitive to the gas temperature, with emissivities that fall to low values for temperatures below  $\sim 3000$  K. The models of Li & McCray (1992); Kozma & Fransson (1998a) predict that the gas temperature in the relevant  $[O\ I]$  emitting regions should have fallen below 1000 K after day  $\sim 1000$ .

## 4.4 Discussion

Using Monte Carlo models that consider both the absorbing and scattering effects of dust, I have modelled the evolution of the  $H\alpha$  and  $[O\ I]\lambda 6300, 6363$  Å line profiles over time, enabling me to place constraints on the evolution of newly formed dust in the ejecta of SN 1987A.

As can be seen in Figure 4.12, even a small degree of asymmetry in observed supernova line profiles can be indicative of dust formation within the ejecta. In addition to this, a line profile that is consistently asymmetric through time requires increasingly large dust masses to account for a similar degree of blue-shifting since the expansion of the ejecta would otherwise cause the dust optical depth to the edge of the ejecta to be reduced.

In Section 4.3.8 I compared my results with those of Dwek & Arendt (2015) and concluded that large dust masses can only have been present at early epochs if the grains were formed purely of glassy magnesium silicates that contained no iron or carbon component and that even for pure magnesium silicates no more than  $0.07 M_\odot$  of dust can have been present. I now compare my results with those of Lucy et al. (1989) and W15.

Lucy et al. (1989) analysed the  $[O\ I]\lambda 6300, 6363$  Å doublet for SN 1987A and estimated dust optical depths for a number of epochs. They translated these into dust masses for day 775 only. From my smooth flow modelling of the  $[O\ I]$  doublets I obtain  $\tau_V \approx 3.60$  at day 714 and  $\tau_V \approx 2.86$  at day 806. These values are higher than the values given by Lucy et al. (1989) who derived  $\tau_V = 1.19$  at day 725 and  $\tau_V = 1.25$  at day 775. The value of the assumed albedo accounts for the majority of this discrepancy. Lucy et al. (1989) considered line profiles before and after dust condensation and concluded that any evidence of an extended red scattering wing was unconvincing. Accordingly, they adopted

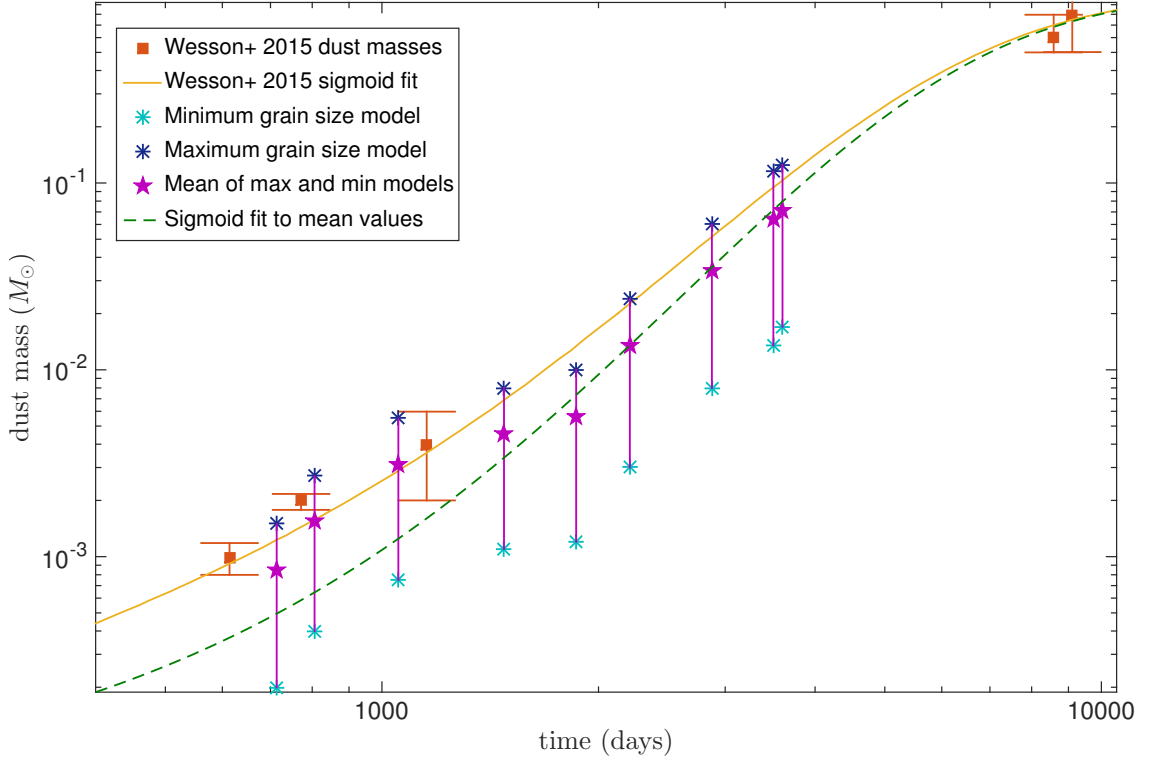


**Figure 4.22.** Derived dust masses for SN 1987A as a function of epoch. Red squares - dust masses derived by W15 from their photometric SED modelling of SN 1987A. Yellow line - W15's sigmoid fit to their values. Dark and light blue asterisks - maximum ( $a = 3.5 \mu\text{m}$ ) and minimum ( $a = 0.6 \mu\text{m}$ ) dust masses respectively for the [O I] models for  $t \leq 1478$  days and for the H $\alpha$  models for  $t \geq 1862$  days. Purple stars - predicted dust masses calculated as the mean of the maximum and minimum dust masses. Green line - sigmoid fit to my predicted dust masses.

a model with perfectly absorbing dust ( $\omega = 0$ ). For my amorphous carbon models for the [O I]  $\lambda 6300, 6363 \text{ \AA}$  profile using a grain radius  $a = 0.35 \mu\text{m}$ , I obtain an albedo of approximately  $\omega = 0.5$  at  $\lambda = 6300 \text{ \AA}$ .

The dust masses derived by Lucy et al. (1989) at day 775 (e.g.  $M_{dust} = 4.4 \times 10^{-6} M_\odot$  for amorphous carbon) are different to those obtained from my smooth dust modelling of the [O I]  $\lambda 6300, 6363 \text{ \AA}$  doublet at day 806 ( $M_{dust} = 1.5 \times 10^{-4} M_\odot$  for amorphous carbon). There are three main reasons for the discrepancy. Firstly, the albedo is significantly larger in my modelling as already discussed. A larger dust mass is therefore required to produce the same amount of absorption. Secondly, to match the extended red wing my required grain radius is considerably larger than the small grains ( $a < 0.1 \mu\text{m}$ ) adopted by Lucy et al. (1989). Larger grain radii reduce the total cross-section of interaction and so a

greater dust mass must be present to compensate for this. Finally, the adopted maximum velocity ( $4000 \text{ km s}^{-1}$ ) in my model is larger than the value adopted by Lucy et al. (1989) ( $1870 \text{ km s}^{-1}$ ). The larger value of  $V_{max}$  increases the total volume of the ejecta significantly and therefore significantly more dust is required to produce the same optical depth.

Lucy et al. (1989) also noted that the dust optical depth increased rapidly after day 580 and that the rate of increase of the dust optical depth appeared to slow between day 670 and day 775, the latest day that they considered. My results, for both clumped and smooth models, suggest that the dust optical depth actually drops between day 714 and day 806 before starting to increase again at later epochs. This is consistent with the results of Lucy et al. (1989) where the slowing rate of increase of dust optical depth could be consistent with a turning point subsequent to day 775.

I can also compare my dust masses with the mass estimates derived from SED-fitting by W15 (see Figure 4.22). W15 used a sigmoid fit to their dust mass evolution, of the form

$$M_d(t) = ae^{be^{ct}} \quad (4.2)$$

where  $a = 1.0M_\odot$  (representing the limiting dust mass),  $b = -8.53$  and  $c = -0.0004$ . Both their dust masses and this sigmoid fit are shown in Figure 4.22. It exhibits an initial period of slow growth in mass followed by an intermediate period of accelerating growth followed by another slowing until a plateau is ultimately reached. In this sense it may be representative of the process of dust formation whereby initial conditions appropriate for grain growth gradually develop until optimal conditions are reached at an intermediate epoch when grain growth is at its fastest before conditions once again deteriorate and the rate slows again (as discussed by W15). Performing a least-squares regression to this function using just my own derived clumped dust masses, I obtain a sigmoid fit with coefficients  $a = 1.0M_\odot$ ,  $b = -10.0$  and  $c = -0.0004$ . These values are remarkably similar to those derived by W15. This sigmoid fit is also plotted in Figure 4.22.

I find that at all epochs the dust masses derived by W15 are entirely within the dust mass ranges determined by my models.

My sigmoid fit to the mean of the maximum and minimum dust masses does not take into account any systematic effects of grain growth. At earlier epochs, whilst grains are

still small relative to later epochs, the lower bound to the dust mass estimates may be more representative than the upper end; the reverse would be true at later epochs. This is in contrast to the sigmoid fit of W15, whose fits to their early epoch SEDs used an MRN distribution with grain radii between  $0.005 \mu\text{m}$  and  $0.25 \mu\text{m}$ , whilst their fits to their last two epochs required grain radii between  $3.005 \mu\text{m}$  and  $3.25 \mu\text{m}$ . The dust masses used for their sigmoid fit thus accounted for the effects of grain growth between the earlier and later epochs. As mentioned, I could not fit the extended red wings of the profiles at early epochs using an MRN distribution. W15 found that at their earlier epochs they could not obtain SED fits with grain radii as large as  $\sim 1.0 \mu\text{m}$ . However, they did not consider radii in between these size ranges, such as the grains with  $a \approx 0.6 \mu\text{m}$  that I require at earlier epochs. For SED modelling it is generally the case that the larger the grain radius used, the less dust is required to produce the same level of flux. This may account for the differences between W15's earlier epoch dust masses and my own minimum dust mass estimates at similar epochs. The models of W15 used 15% silicate dust, in contrast to my models which used 100% amorphous carbon dust. This could also contribute to the differences at early epochs, as could the use of different sets of optical constants - I used the BE amorphous carbon optical constants of Zubko et al. (1996) whereas W15 used AC constants from Hanner (1988). W15 found that in order to fit early epoch SEDs epochs (e.g. day 615) with Zubko ACH2 constants, smaller inner and outer ejecta radii were needed, with half as much dust ( $5.0 \times 10^{-4} M_{\odot}$ ) compared to the Hanner AC results.

W15 derived a maximum possible grain radius at late epochs, concluding that the grains could not be larger than  $\sim 5 \mu\text{m}$  by day 8515. This is consistent with the maximum grain radii that I derive at my latest epochs. I find that grain radii most likely cannot have exceeded  $\sim 3.5 \mu\text{m}$  at day 3604 - the dust mass that I obtain using this grain radius is similar to the value predicted by W15's sigmoid fit at that epoch.

The relationship between ejecta dust grain radii and post-explosion time is important for understanding the likelihood of dust surviving the passage of a reverse shock propagating back through the ejecta. By the time the effects of a reverse shock begin to appear in the line profiles (around day 5000), my models imply that the grains could already be as large as several microns in radius and are likely to be larger than  $\sim 0.6 \mu\text{m}$ . Grains as large as this are more likely to survive destruction by sputtering in supernova reverse shocks and in interstellar shocks (Silvia et al. 2010, 2012; Slavin et al. 2015). It has been suggested that very large grains (radii up to  $4.2 \mu\text{m}$ ) formed in the ejecta of SN 2010jl

within a few hundred days after the explosion Gall et al. (2014). The grain radii that W15 and I obtain for SN 1987A at very late epochs are nearly as large as found by Gall et al. (2014) for SN 2010jl, with both results suggesting that grains large enough to survive the destructive force of a reverse shock have formed by a few hundred days post-explosion.

The dust masses obtained from my modelling of SN 1987A’s line profiles support the conclusion of W15 that even after  $\sim 3000$  days the dust mass was still only a fraction of its current value. This contrasts with the results of Sarangi & Cherchneff (2015) whose grain chemistry models predict that ejecta dust masses should plateau by around 5 years after the explosion. My results show that SN 1987A’s dust mass had reached the order of  $0.1M_{\odot}$  by day 3604. Since its present dust mass is several times larger than this (Matsuura et al. (2015), W15), a substantial fraction of the current dust mass must have condensed after this epoch, in agreement with the conclusions of W15.

Ideally, my models would cover the entire evolution of SN 1987A’s H $\alpha$  line profiles up to the present day. However, the excitation of gas in the outer edges of the ejecta by the reverse shock after  $\sim$  day 5000 results in significant broad and asymmetric emission that dominates the original line profile (Fransson et al. 2013). In addition to this, the narrow lines from the ER start to become so strong relative to the declining broad H $\alpha$  profile that, post-removal, not enough of the broad profile remained to be able to reliably infer information from the profile structure. These factors may be common to some other CCSNe that have interactions with surrounding circumstellar material. Care should also be taken to ensure that any observed late-time line profiles being modelled are not in fact the product of a light echo reflecting the spectrum from near maximum light. Nonetheless, detailed line modelling of asymmetric line profiles has proved effective in determining dust masses in the ejecta of SN 1987A at multiple epochs during the first ten years after outburst. The method clearly has wider application to other supernovae as demonstrated in Chapter 5.

## 4.5 Conclusions

I have modelled the H $\alpha$  and [O I]  $\lambda 6300, 6363$  Å line profiles from SN 1987A over a range of epochs and have obtained dust masses of the order of  $0.1M_{\odot}$  by day 3604. I derive a sigmoid fit to my dust mass data that predicts a current dust mass of  $0.68M_{\odot}$ , in line with current SED-based dust mass estimates for SN 1987A. I find that large grains are

necessary in order to reproduce both the extended red scattering wings and the asymmetry seen in several of the lines and that grains larger than  $0.6 \mu\text{m}$  have formed by day 714, while by day 3604 grain radii of  $\sim 3.5 \mu\text{m}$  are needed. I find from fits to the H $\alpha$  profile that dust masses cannot have exceeded a few  $\times 10^{-3} M_{\odot}$  on day 714 for all the grain types investigated, apart from glassy pure magnesium silicate grains, for which up to  $0.07 M_{\odot}$  can be fitted.

The observed red-blue line asymmetries persist right through to day 3604 and beyond - if no further dust had formed after day  $\sim 800$  then the expansion of the ejecta dust shell would cause dust optical depths to drop rapidly with time thereafter, leading to the disappearance of red-blue asymmetries. Just to maintain the observed degree of red-blue asymmetry seen at the earlier epochs therefore requires that dust must have continued to form beyond those epochs.

# Chapter 5

---

## Dust Masses in Other Supernova Remnants

### 5.1 Introduction

SN 1987A has provided a rare opportunity to follow the evolution of a CCSNe in close detail. It is now well established that there is a significant mass of dust forming in the ejecta. However, the question of the dust mass budget problem in the early universe cannot be solved by considering SN 1987A alone. If CCSNe are indeed the primary source of the dust seen at high redshifts, it is necessary to establish that the majority of CCSNe do indeed produce sizeable quantities of dust. This motivates the study of other CCSN remnants with the aim of determining the masses of dust that have formed in their ejecta.

Blue-shifted line emission is a common and long-lasting feature of the late-time spectra of CCSNe. In particular the emission lines of oxygen and hydrogen are often visible and often exhibit asymmetries and significant substructure. If these lines can be modelled then it may be possible to determine the dust masses in SNRs at later times.

There are only a few objects that lend themselves to this sort of modelling however. The primary obstacle to assessing a large number of late-time spectra from CCSNe is that the majority fade rapidly, with their brightness decreasing by eight magnitudes after maximum light within the first two years (Kirshner 1990). They are also frequently further than  $\sim 10$  Mpc from us and detections are relatively infrequent in the first place. As a

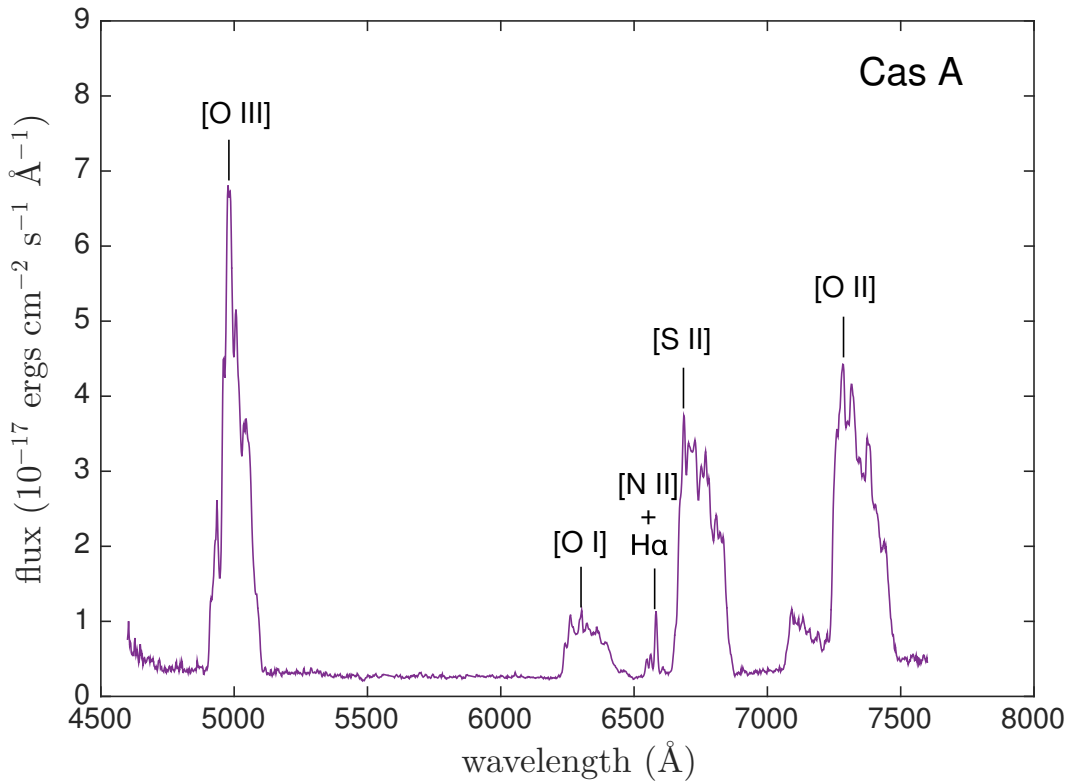


**Figure 5.1.** The integrated spectrum of Cas A (Milisavljevic & Fesen 2013).

result, the optical spectra are rarely visible after approximately 700 days (Milisavljevic et al. 2012).

However, there are a few unusual objects that, for various reasons, we may still be able to see many years or even decades after maximum light. This could be because they are unusually close, like SN 1987A, or more usually because some late-time energy source is illuminating the ejecta. The most obvious of these energy sources is the interaction between the forward shock and the surrounding circumstellar material. This interaction is known to emit across a wide range of wavelengths from radio to X-rays and causes a reverse shock to propagate inwards through the ejecta heating and ionising the material it passes through. Other postulated energy sources include interaction between a central pulsar or magnetar and the expanding debris (Woosley 2010), or accretion onto a black hole (Patnaude et al. 2001).

Recent work by (Milisavljevic et al. 2012) identified a number of CCSNe that were still visible in the optical despite being more than 20 years old. These included SN 1957D, SN 1970G, SN 1979C, SN 1980K, SN 1986E, SN 1986J, SN 1987A, SN 1993J and SN 1996cr.

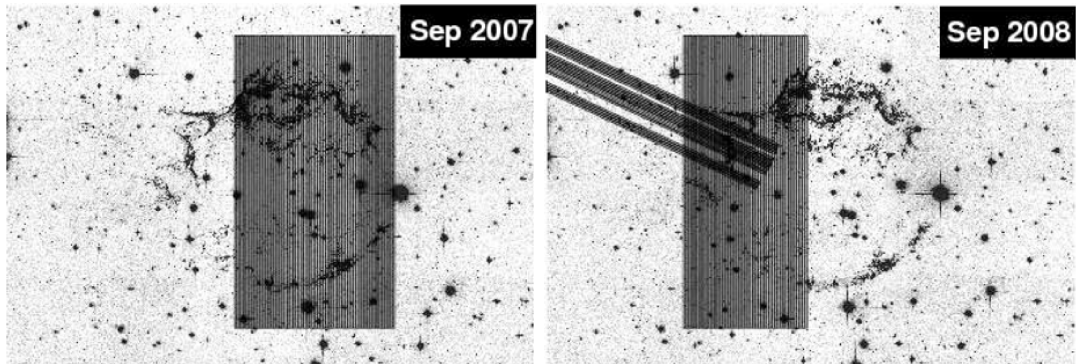


**Figure 5.2.** Finding charts of the long-slit positions used to compose the integrated spectrum of the main shell of Cas A. The background image is a mosaic created from 2004 HST/ACS observations (Fesen et al. 2006). Image is taken from Milisavljevic & Fesen (2013).

Many of these SNe exhibited strong asymmetries and blue-shifting in their profiles in the optical, particularly in the oxygen and hydrogen lines. In this chapter I present models of two of these objects, namely SN 1980K and SN 1993J. I select these as both exhibit at least two blue-shifted line profiles and the lines of interest are largely uncontaminated by other lines with wings that do not overlap with other lines.

In addition to these SNRs, I also present models of the oxygen lines of Cassiopeia A (Cas A). Cas A is a very well studied object and at  $\sim 300$  years old is easily the oldest observable remnant to have detectable line emission in the optical. I will discuss why this is possible along with some other interesting facts about Cas A at the start of the Section 5.2.

By modelling these three objects, and from my models of SN 1987A presented in the previous chapter, I hope to be able to determine the order of magnitude of the mass of dust that forms in the ejecta of CCSNe.

## 5.2 Cassiopeia A

### 5.2.1 Integrated Spectrum of Cas A

The integrated spectrum presented in Figure 5.1 is from Milisavljevic & Fesen (2013). It is composed of observations from a series of observing runs between September 2007 and November 2010 that were conducted in order to obtain low-dispersions optical spectra across the remnant. The majority of observations were carried out at the MDM Observatory

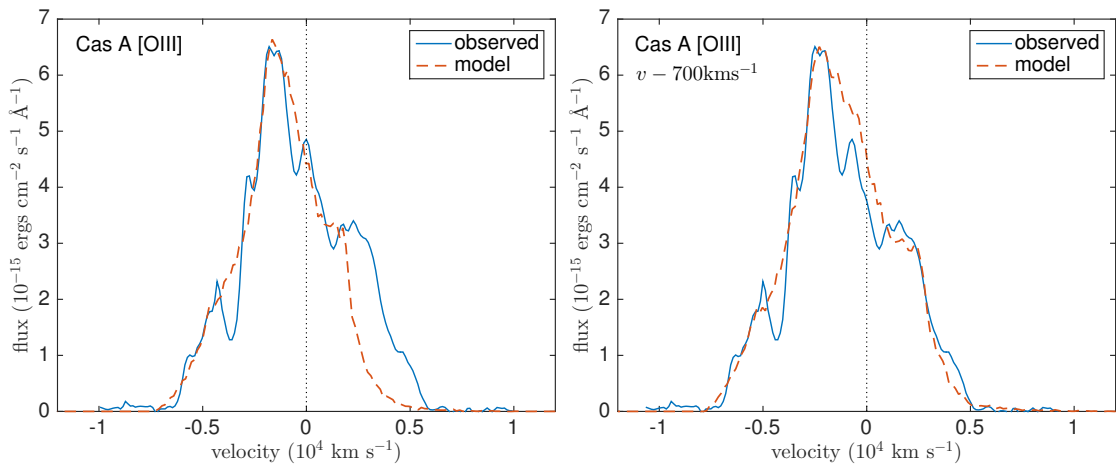


**Figure 5.3.** smooth fits to Cas A OIII shifted and unshifted

at Kitt Peak, Arizona using the 2.4m Hiltner telescope and the Mayall 4m telescope. The MDM Modular Spectrograph was used with an ‘Echelle’ detector. A long slit of dimensions  $2'' \times 5'$  was used oriented North-South. Exposure times were generally  $2 \times 500$ s. The wavelength range covered was  $4500\text{-}7000\text{\AA}$  with a spectral resolution of  $6\text{\AA}$ .

The integrated spectrum was ultimately composed of 80 long slit spectra spaced  $3''$  apart across the entire main shell which is approximately  $4'$  in diameter. The slit positions are shown in Figure 5.2.

### 5.2.2 Smooth Models

My modelling of the Cas A spectrum was initially focussed on the [O III] line, which exhibits a pronounced asymmetry. I managed to produce a reasonable fit to the data using the parameters listed in the first row of Table 5.2. The profile is presented in the left pane of Figure 5.3. As can be seen, the modelled line profile generally fits the observed line profile quite well, although it fails to fit the red side of the profile adequately. A thorough, manual investigation of parameter space resulted in the conclusion that the profile was much better fitted if the entire observed profile was shifted to the blue by  $-700 \text{ km s}^{-1}$ . This might well be a reasonable assumption. The integrated spectrum does not sample the entire ejecta. Additionally, Cas A is known to be significantly asymmetrical (Rest et al. 2011). The integrated profile may well sample regions with different line-of-sight velocities, the sum of which could result in a net line-of-sight velocity shift. This was also found to be the case with the [O II] and [O I] lines. Throughout the remainder of my modelling I therefore allowed the profiles to be shifted in velocity space to better fit the

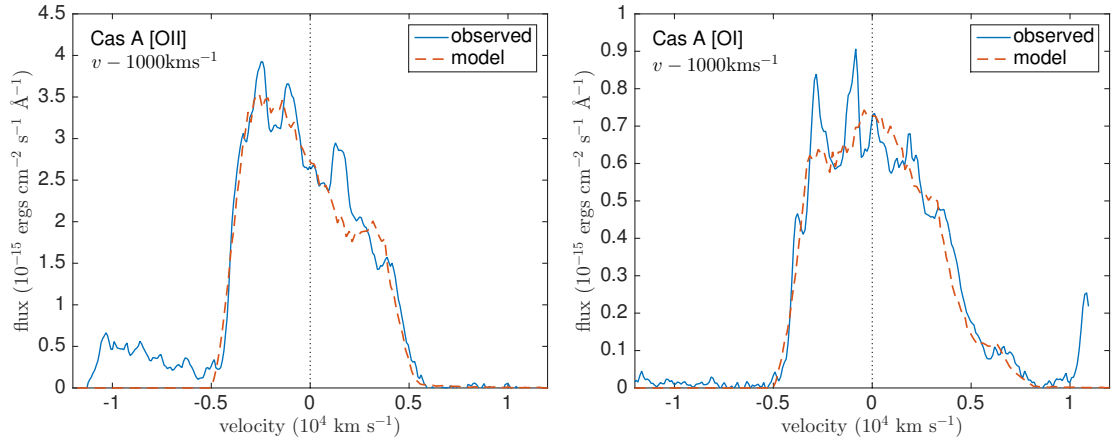
data based on the possibility that the sampled emitting regions had an overall net velocity towards the observer. Fits to the line profiles were significantly improved following this translation (see Figures 5.3 to 5.5).

A model of the shifted [O III] line is presented in Figure 5.3 and the parameters used for this model are presented in the second row of Table 5.2. The line profile was shifted by  $-700 \text{ km s}^{-1}$ . A total dust optical depth of  $\tau = 0.49$  at  $5007\text{\AA}$  between  $R_{in}$  and  $R_{out}$  was found to best fit the profile. An albedo of  $\omega \approx 0.15$  at  $5007\text{\AA}$  was also necessary.

The composition of the dust has a significant effect on the overall dust mass for this optical depth and albedo. A line profile model of the [O III] line profile from Cas A could not be found using 100% astronomical silicate dust (Draine & Lee 1984). There is little to no scattering wing seen, hence the relatively low value of  $\omega$ , and therefore relatively small silicate grains are required to reproduce the red side of the profile. Silicate grains of this size have extremely low absorption efficiencies and therefore the best-fitting optical depth of  $\tau = 0.49$  corresponds to an implausibly large mass of dust ( $> 20M_\odot$ ) if it is composed entirely of astronomical silicates.

The chemical composition of the dust in the ejecta of Cas A is known to be extremely complex (Arendt et al. 2014). There are many different species of dust grain present in the ejecta, and it is known that silicate dust is present based on emission features observed in the IR region of the spectrum. However, the presence of a variety of other species is also predicted. I therefore investigate the dust masses required to fit the profile for varying fractions of silicate and amorphous carbon dust. In Table 5.1, I detail the dust masses required to fit the [O III] line profile for different fractions of silicates and amorphous carbon grains for a single grain size. For each composition I determine the grain radius based on the albedo necessary to fit the profile ( $\omega \approx 0.15$ ) and then vary the dust mass to achieve the required optical depth. The calculated dust masses cover a wide range of values between  $0.65 - 6.5M_\odot$ . All of the line profile models listed above adopted intrinsic doublet strengths from the theory as detailed by Zeippen (1987) and Storey & Zeippen (2000).

It might be possible to approximately determine the composition based on the relative optical depths necessary to fit different blue-shifted lines in the spectrum and the wavelength dependence of dust absorption for different compositions. I therefore considered fitting the blue-shifted [O II] and [O I] lines from Cas A. Sadly, at the small grain sizes required, there is not significant variation in the absorption efficiencies of either amor-

**Figure 5.4.** Cas A OI and OII**Table 5.1.** The variation in dust mass for a fixed optical depth  $\tau_{5007\text{\AA}} = 0.49$  for the parameters listed in Table 5.2.

% silicate grains	% amorphous carbon grains	grain radius $a$ ( $\mu\text{m}$ )	$M_{dust}$ ( $\text{M}_\odot$ )
90	10	0.035	6.5
75	25	0.04	2.5
50	50	0.045	1.1
25	75	0.048	0.6
0	100	0.05	0.37

**Table 5.2.** The parameters used for the smooth models of Cas A with a medium composed of 50% amorphous carbon and 50% silicate grains of radius  $a = 0.05 \mu\text{m}$ . Optical depths are given from  $R_{in}$  to  $R_{out}$  at  $\lambda = 5007 \text{ \AA}$  for [O III],  $\lambda = 7319 \text{ \AA}$  for [O II] and  $\lambda = 6300 \text{ \AA}$  for [O I]. The doublet ratio is always the ratio of the stronger line to the weaker line. The asterisk indicates that the parameters listed describe the gas density distribution. The dust density distribution is the same in all cases (as detailed for the shifted [O II] doublet in the second row).

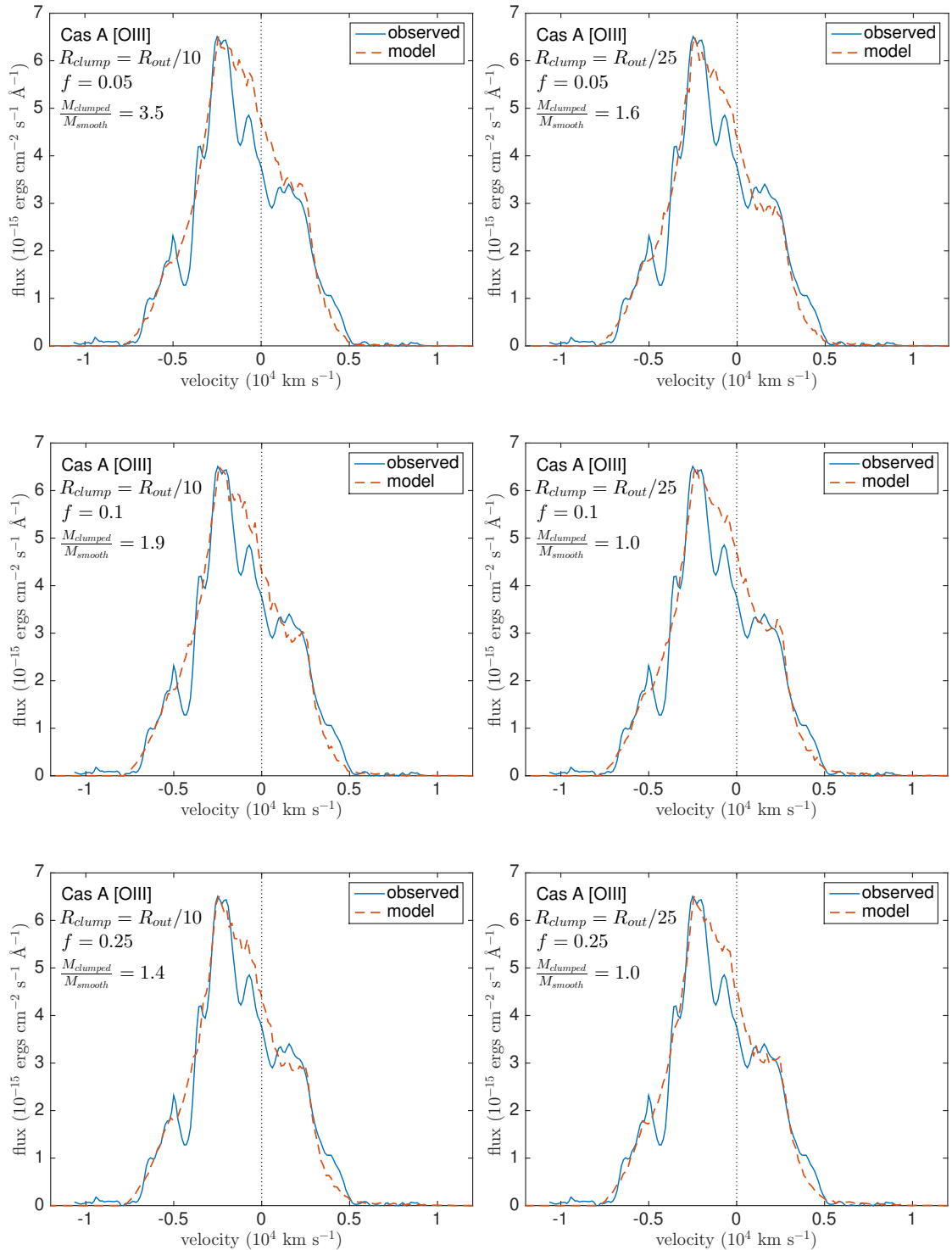
	$v$ shift (km s $^{-1}$ )	$V_{max}$ (km s $^{-1}$ )	$V_{min}$ (km s $^{-1}$ )	$R_{in}/R_{out}$	$\beta$	$M_{dust}$ ( $M_{\odot}$ )	$R_{out}$ (10 $^{18}$ cm)	$R_{in}$ (10 $^{18}$ cm)	doublet ratio	$\tau_{\lambda}$
[O III]	0	4500	1800	0.4	2.0	1.1	4.7	1.9	2.9	0.53
[O III]	-700	5000	2500	0.5	2.0	1.1	5.2	2.6	2.9	0.49
[O II]*	-1000	5000	3250	0.65	2.0	1.1	5.2	3.4	1.23	0.21
[O I]*	-1000	5000	3250	0.65	2.0	1.1	5.2	3.4	3.1	0.30

phous carbon or astronomical silicates between 5007Å and 7319Å and I cannot therefore determine the composition via this approach. Additionally, the [O II] and [O I] lines are much less sensitive to variations in both distribution and dust mass, partly due to the high frequency of bumpy features observed in these lines which contaminate the intrinsic broad profile. The best-fitting models for these lines were therefore quite degenerate i.e. there were multiple sets of parameters that resulted in reasonable fits.

However, it was possible to use these lines to determine the feasibility of the best-fitting model for the [O III] line profile. I adopted the dust distribution that I determined using the [O III] line and investigated models for the [O II] and [O I] line profiles to see if this dust distribution were capable of fitting these lines as well. I adopted an emissivity distribution that was slightly different to the [O III] line (see Table 5.2) and shifted the observed line profiles by  $-1000 \text{ km s}^{-1}$ . These emissivity distributions were modelled with the dust distribution and mass for the best-fitting smooth [O III] model. The resultant [O II] and [O I] line profiles are very good fits (see Figure 5.4). This suggests that the models are consistent and, if the relative abundance of species can be determined, that the dust masses can be well-constrained.

### 5.2.3 Clumped Models of Cas A

The ejecta of Cas A is highly clumped. Recently, models by Biscaro & Cherchneff (2014) have suggested that dust cannot in fact form in the gas phase in the ejecta of Cas A unless extremely dense knots of material are present. It is therefore important, as with SN 1897A, to consider the effects of clumping on the line profiles. I continue to focus on the [O III] line profile from Cas A and consider the effects of clumping. Clearly, the ejecta has a complex geometry with many clumps of different sizes and likely different ionisation states and dust species within each and therefore the models we present here only aim to provide some indication of the effects of clumping within the ejecta. To this end I present a number of models of the [O III] line profile based on the smooth fits that I presented in the previous section. I consider two different clump sizes, ones with width  $R_{out}/25$  and ones with width  $R_{out}/10$ . I also consider three different clump volume filling factors  $f = 0.05$ ,  $f = 0.1$  and  $f = 0.25$ . For each combination of clump size and filling factor I re-evaluate the required increase or decrease in the dust mass over the smooth model. All other parameters were kept fixed such that the emission was emitted smoothly according to the distribution and geometry described by the parameters listed in Table 5.2.

**Figure 5.5.** Cas A clumped

**Table 5.3.** The fraction of increase in dust mass over the smooth model with parameters as given in Table 5.2 for clumped models with different clump widths and different clump volume filling factors. The other parameters in the models were fixed at the values given in Table 5.2.

	$f = 0.05$	$f = 0.1$	$f = 0.25$
$R_{out}/10$	3.5	1.9	1.4
$R_{out}/25$	1.6	1.0	1.0

The change in the required dust mass is listed as a fraction of the smooth dust mass (e.g.  $M_{dust} = 1.1M_{\odot}$  for a medium of 50% astronomical silicates and 50% amorphous carbon - see Table 5.1 for other dust masses with different dust compositions) is given in Table 5.3. Whilst clumping can be seen to increase the required dust mass in all cases, in the most extreme it is still only by a factor of 3.5. The fits for each of these cases are presented in Figure 5.5.

#### 5.2.4 The Geometry of Cas A

Consider section 2 of conclusions of DAN and FESEN - talk about overall velocity of optical emitting regions being towards us

#### 5.2.5 The Chemistry of Cas A

Compare to the biscaro paper and the other species paper

#### 5.2.6 The Dust Mass in Cas A

Mike's paper and others. Need a reason why my estimate is higher.

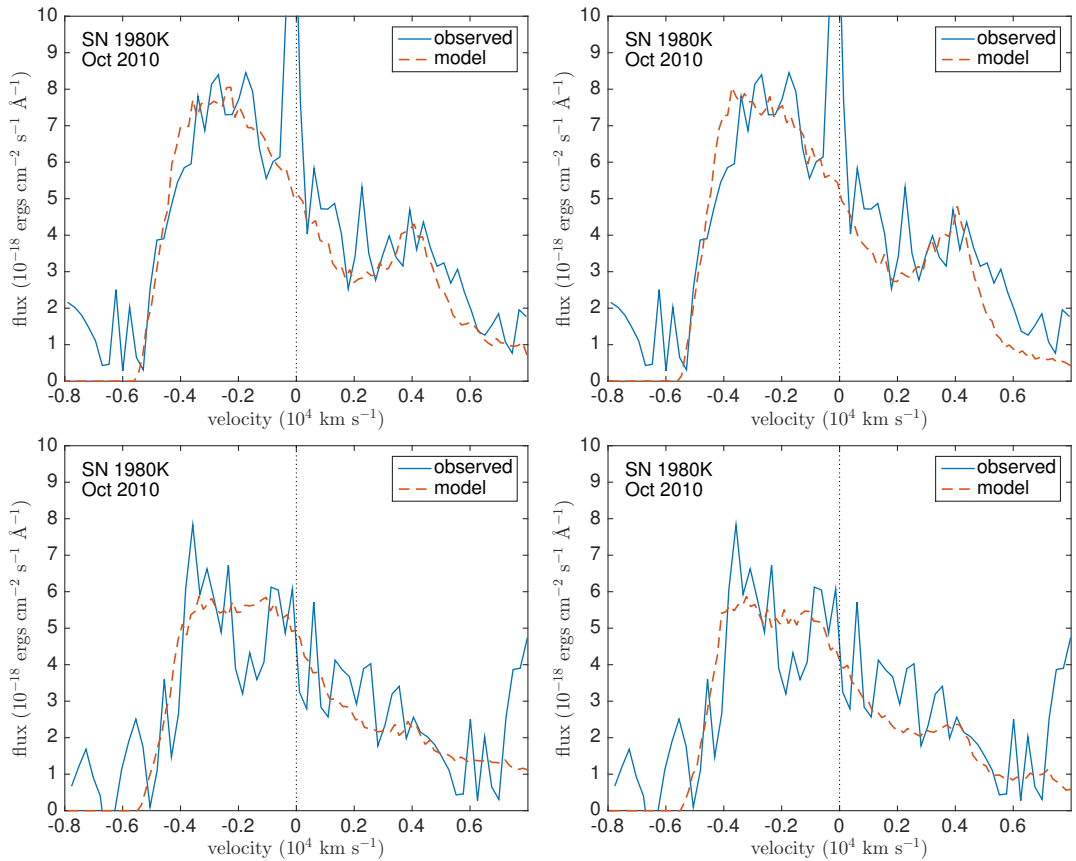


**Figure 5.6.** Smooth fits to SN 1980K

## 5.3 SN 1980K

### 5.3.1 Smooth Models

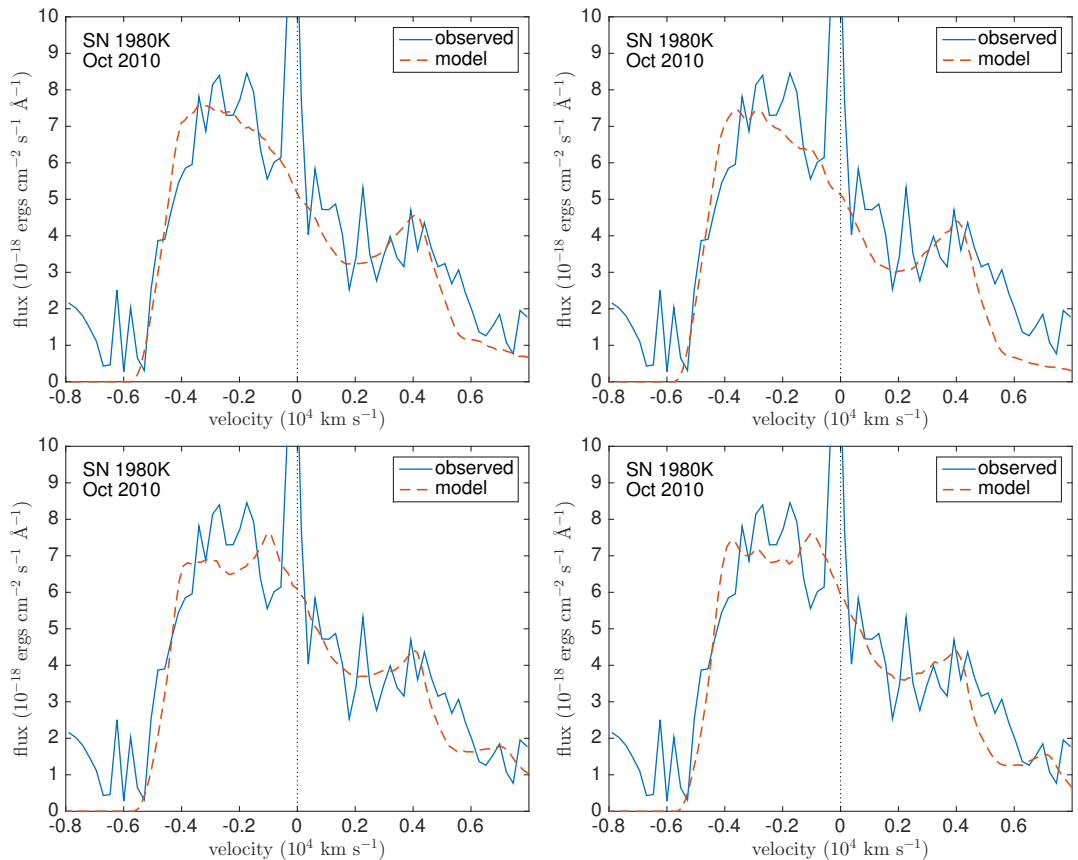


**Figure 5.7.** clumped fits to SN 1980K

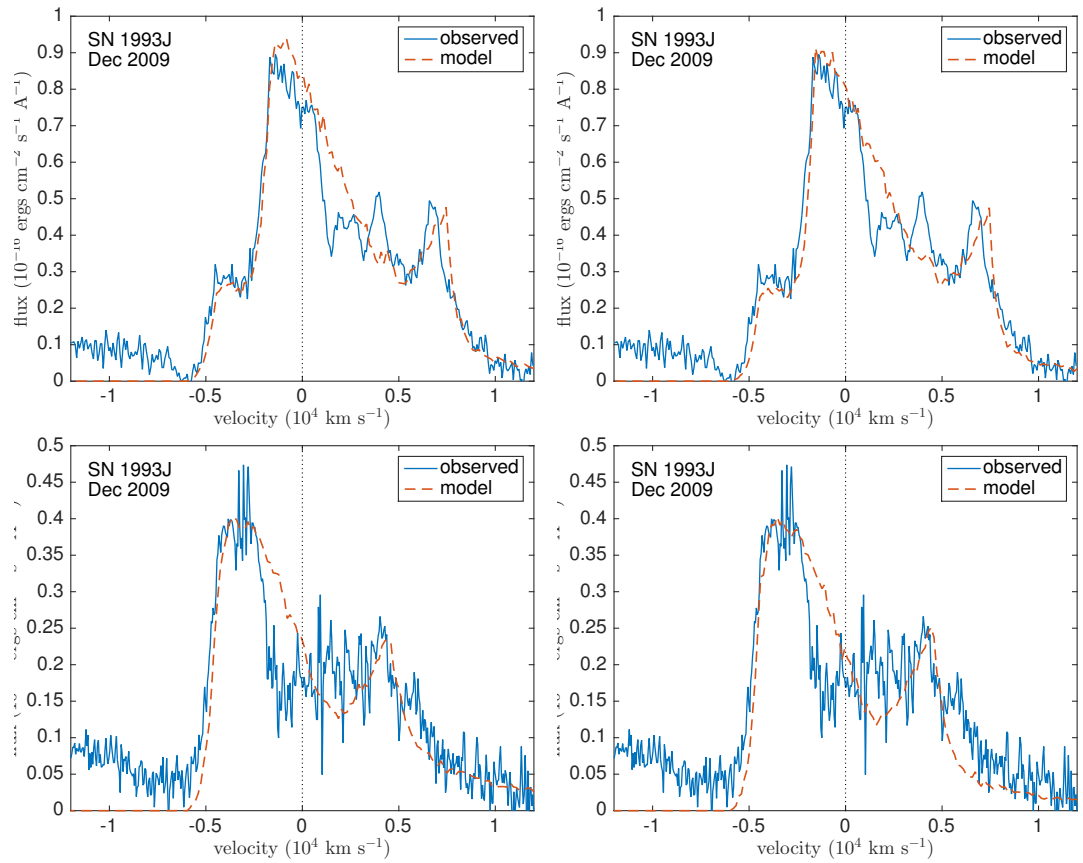


**Figure 5.8.** smooth fits to SN 1993J

## 5.4 SN 1993J

## 5.5 Discussion

## 5.6 Conclusions

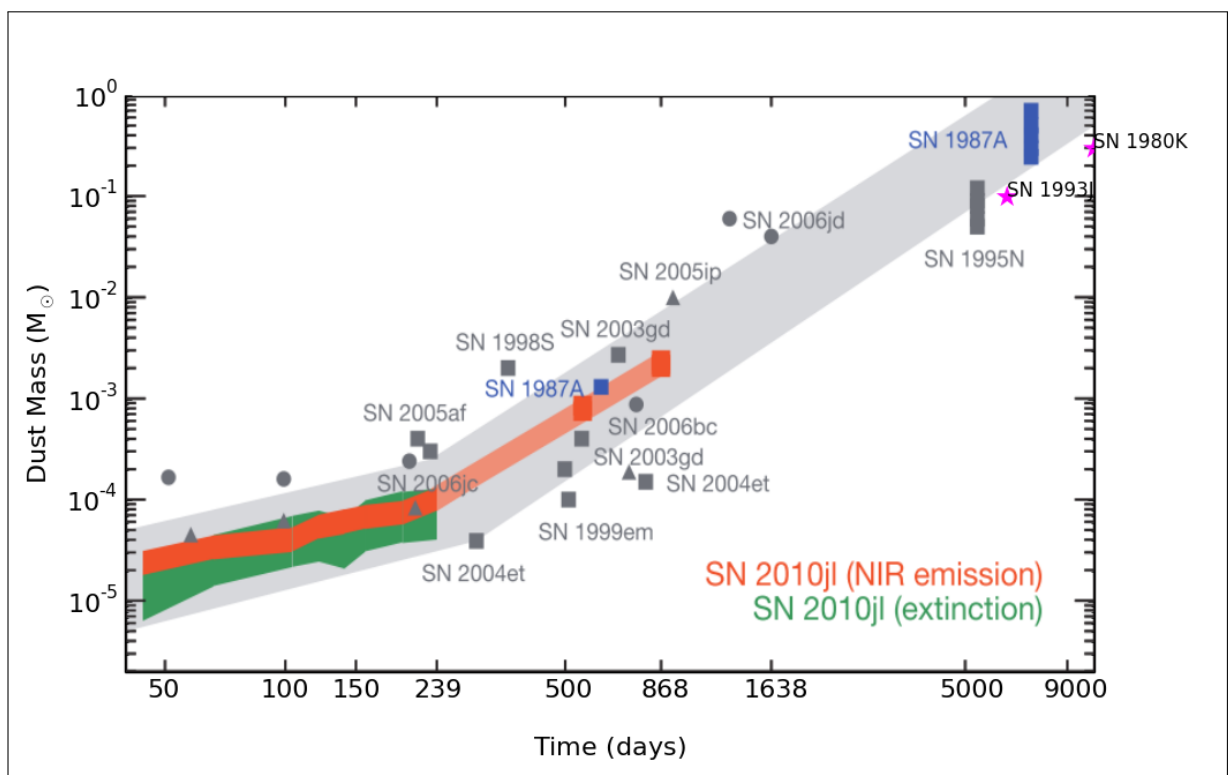


**Figure 5.9.** dust masses

## Chapter 6

---

### Conclusions and Future Work

*QUOTE GOES HERE*

AUTHOR

FIRST PARAGRAPH

INCLUDE HERE THE PLOT OF DUST MASS EVOL FROM GALL WITH ALL  
THE MODELLED SUPERNOVAE

# Appendix A

---

## Mie Theory

The aim is to understand the nature of the scattered electromagnetic field given a field incident on a single spherical particle. In order to calculate this, Maxwell's equations must be solved inside and outside of the sphere, using boundary conditions at the surface to determine the amount and angular distribution of the scattered wave. Beginning with Maxwell's equations, I will formulate the problem, derive the vector wave equation, illustrate its reduction to the scalar wave equation and solve this to produce the scattering coefficients that may be used to calculate the desired scattering and extinction cross-sections of interaction.

The derivation given here follows the theory as described by Bohren & Huffman (1983).

### A.1 Formulating the Problem

Consider a spherical particle with complex refractive index  $m$  and radius  $a$  that is illuminated by a monochromatic electromagnetic plane wave of wavelength  $\lambda$ . We must determine the electromagnetic field at all points within the particle and in the homogeneous medium in which it is embedded.

The field inside the particle is defined by  $(\mathbf{E}_1, \mathbf{H}_1)$  and the field outside of the particle in the surrounding medium by  $(\mathbf{E}_2, \mathbf{H}_2)$ . Similarly the incident field is defined by  $(\mathbf{E}_i, \mathbf{H}_i)$  and the scattered field by  $(\mathbf{E}_s, \mathbf{H}_s)$ . The field outside of the particle is a superposition of

the incident and scattered fields and we therefore have the relation

$$\mathbf{E}_2 = \mathbf{E}_i + \mathbf{E}_s, \quad \mathbf{H}_2 = \mathbf{H}_i + \mathbf{H}_s \quad (\text{A.1})$$

For a plane wave we may set

$$\mathbf{E}_i = \mathbf{E}_0 \exp(i\mathbf{k} \cdot \mathbf{x} - i\omega t), \quad \mathbf{H}_i = \mathbf{H}_0 \exp(i\mathbf{k} \cdot \mathbf{x} - i\omega t) \quad (\text{A.2})$$

where  $\omega$  is the frequency of the incident wave and  $\mathbf{k}$  is the wave vector appropriate to the surrounding medium. The fields defined above must satisfy Maxwell's equations:

$$\nabla \cdot \mathbf{E} = 0 \quad \nabla \cdot \mathbf{H} = 0 \quad (\text{A.3})$$

and

$$\nabla \times \mathbf{E} = i\omega\mu\mathbf{H}, \quad \nabla \times \mathbf{H} = -i\omega\epsilon\mathbf{E} \quad (\text{A.4})$$

Taking the curl of Equation A.4 gives the vector wave equation

$$\nabla^2 \mathbf{E} + k^2 \mathbf{E} = 0, \quad \nabla^2 \mathbf{H} + k^2 \mathbf{H} = 0 \quad (\text{A.5})$$

where  $k^2 = \omega^2\epsilon\mu$  and  $\epsilon$  is the complex permittivity of the medium and  $\mu$  the permeability. Note that the use of  $k$  throughout this derivation refers to the wave number as just defined rather than the imaginary part of the complex refractive index (which we will introduce later).

## A.2 Solving the Vector Wave Equations

It transpires that the easiest wave to solve the vector wave equations is to define a vector

$$\mathbf{M} = \nabla \times (\mathbf{c}\psi) \quad (\text{A.6})$$

where  $\psi$  is a scalar function and  $\mathbf{c}$  is an arbitrary constant vector. Since  $\mathbf{M}$  is the curl of a vector, the divergence of  $\mathbf{M}$  is zero ( $\nabla \cdot \mathbf{M} = 0$ ). By applying some vector identities to

$\mathbf{M}$  we derive

$$\nabla^2 \mathbf{M} + k^2 \mathbf{M} = \nabla \times [\mathbf{c}(\nabla^2 \psi + k^2 \psi)] \quad (\text{A.7})$$

$\mathbf{M}$  therefore satisfies the vector wave equation (Equation A.5) if  $\psi$  satisfies the scalar wave equation:

$$\nabla^2 \psi + k^2 \psi = 0 \quad (\text{A.8})$$

We will use  $\mathbf{M}$  to construct another vector which we define as

$$\mathbf{N} = \frac{\nabla \times \mathbf{M}}{k} \quad (\text{A.9})$$

$\mathbf{N}$  also has zero divergence and satisfies the vectore wave equation ( $\nabla^2 \mathbf{N} + k^2 \mathbf{N} = 0$ ). We also have  $\nabla \times \mathbf{N} = k\mathbf{M}$  ensuring that  $\mathbf{M}$  and  $\mathbf{N}$  have all of the required properties of an electromagnetic field (i.e. they satisfy Equations A.3 and A.4). If we can now find solutions to the scalar wave equation (Equation A.8) then we have solutions to the vector wave equation (Equation A.5) via Equations A.6 and A.9. Since we are interested in scattering by a sphere, we work in spherical polar coordinates and set  $\mathbf{c} = \mathbf{r}$ , where  $\mathbf{r}$  is the radius vector.

The scalar wave equation may be expanded in spherical polar coordinates as

$$\frac{1}{r^2} \frac{\partial}{\partial r} \left( r^2 \frac{\partial \psi}{\partial r} \right) + \frac{1}{r^2 \sin \theta} \frac{\partial}{\partial \theta} \left( \sin \theta \frac{\partial \psi}{\partial \theta} \right) + \frac{1}{r^2 \sin^2 \theta} \frac{\partial^2 \psi}{\partial \phi^2} + k^2 \psi = 0 \quad (\text{A.10})$$

Solutions of the form  $\psi(r, \theta, \phi) = R(r)\Theta(\theta)\Phi(\phi)$  are sought such that Equation A.10 divides into three separate equations. Each of these equations may then be solved to derive a complete solution for  $\psi(r, \theta, \phi)$ . These solutions are standard solutions to the spherical wave equation in spherical polar coordinates and so I will not go into detail here. Solving each of the three equations yields the final result

$$\psi_{emn} = \cos m\phi P_n^m(\cos \theta) z_n(kr) \quad (\text{A.11})$$

$$\psi_{omn} = \sin m\phi P_n^m(\cos \theta) z_n(kr) \quad (\text{A.12})$$

$m$  and  $n$  are constants that are introduced that relate the three equations. Requiring  $\psi$  to be a single-valued function determines that  $m$  and  $n$  are integers where  $m \geq 0$ .

$P_n^m(\cos \theta)$  are the Legendre functions of the first kind of degree  $n$  and order  $m$  where  $n = m, m+1, \dots$ .  $z_n$  represents any of the four Bessel functions  $j_n$ ,  $y_n$ ,  $h_n^{(1)}$  or  $h_n^{(2)}$ . Definitions of these functions and their derivation from the scalar wave equation may be found in any number of textbooks (for example see Riley et al. (2006)). The subscripts  $e$  and  $o$  simply differentiate between the odd and even solutions. The nature of the above solutions is such that any solution to the scalar wave equation in spherical polar coordinates may be expanded as an infinite series in Equations A.11 and A.12.

The solutions for the desired vector fields  $\mathbf{M}$  and  $\mathbf{N}$  are therefore given by

$$\mathbf{M}_{emn} = \nabla \times (\mathbf{r}\psi_{emn}), \quad \mathbf{M}_{omn} = \nabla \times (\mathbf{r}\psi_{omn}) \quad (\text{A.13})$$

$$\mathbf{N}_{emn} = \frac{\nabla \times \mathbf{M}_{emn}}{k}, \quad \mathbf{N}_{omn} = \frac{\nabla \times \mathbf{M}_{omn}}{k} \quad (\text{A.14})$$

These functions are known as the “vector spherical harmonics”. They may be expanded as an infinite series to solve the vector wave equation (Equation A.5), which is now our task.

### A.3 Calculating the Incident and Scattered Fields

The issue is now to consider the scattering of an incident plane wave  $\mathbf{E}_i$ . Based on the above,  $\mathbf{E}_i$  may be expanded as an infinite series sum of the four vector spherical harmonics described by Equations A.13 and A.14,

$$\mathbf{E}_i = \sum_{m=0}^{\infty} \sum_{n=m}^{\infty} (B_{emn} \mathbf{M}_{emn} + B_{omn} \mathbf{M}_{omn} + A_{emn} \mathbf{N}_{emn} + A_{omn} \mathbf{N}_{omn}) \quad (\text{A.15})$$

with coefficients  $A_{emn}$ ,  $A_{omn}$ ,  $B_{emn}$  and  $B_{omn}$  that must be determined. The above expansion can be simplified by considering various orthogonality properties of the vector harmonics. It can be shown (though I omit the proofs here for reasons of brevity) that all of the vector spherical harmonics are orthogonal. This determines the form of each of the four coefficients and, in combination with the orthogonality of sine and cosine, we find that  $B_{emn} = A_{omn} = 0$  for all  $m$  and  $n$  (see Bohren & Huffman (1983)). Similarly, we find that all the remaining coefficients vanish unless  $m = 1$ . In this case, we may also adopt the Bessel function  $z_n = j_n$  based on the requirement that the field must be finite at the origin (the other functions misbehave at the origin under these circumstances). I adopt the superscript (1) to illustrate that the radial dependence of the solution is specific by

$j_n$ . Equation A.15 therefore reduces to

$$\mathbf{E}_i = \sum_{n=1}^{\infty} (B_{o1n} \mathbf{M}_{o1n}^{(1)} + A_{e1n} \mathbf{N}_{e1n}^{(1)}) \quad (\text{A.16})$$

Evaluating the forms of  $A_{e1n}$  and  $B_{o1n}$  via some rather unpleasant integrals and a lot of algebraic manipulation yields

$$\mathbf{E}_i = E_0 \sum_{n=1}^{\infty} i^n \frac{2n+1}{n(n+1)} (\mathbf{M}_{o1n}^{(1)} - \mathbf{N}_{e1n}^{(1)}) \quad (\text{A.17})$$

The corresponding magnetic field may be calculated via the curl of Equation A.17 and is found to be

$$\mathbf{H}_i = \frac{-k}{\omega\mu} E_0 \sum_{n=1}^{\infty} i^n \frac{2n+1}{n(n+1)} (\mathbf{M}_{e1n}^{(1)} - \mathbf{N}_{o1n}^{(1)}) \quad (\text{A.18})$$

Finally, all that remains is to determine the scattered electromagnetic field  $(\mathbf{E}_s, \mathbf{H}_s)$ . This may be done by imposing the boundary condition that the tangential component of the fields must be continuous across the boundary of the two materials, i.e.

$$(\mathbf{E}_i + \mathbf{E}_s - \mathbf{E}_1) \times \hat{\mathbf{e}}_r = (\mathbf{H}_i + \mathbf{H}_s - \mathbf{H}_1) \times \hat{\mathbf{e}}_r = 0 \quad (\text{A.19})$$

Applying this boundary condition and once again applying various orthogonality relationships and the condition of finiteness at the origin gives the expansions of the field inside the sphere and the scattered field as:

$$\mathbf{E}_1 = \sum_{n=1}^{\infty} E_n (c_n \mathbf{M}_{o1n}^{(1)} - id_n \mathbf{N}_{e1n}^{(1)}), \quad \mathbf{H}_1 = \frac{-k_1}{\omega\mu_1} \sum_{n=1}^{\infty} E_n (d_n \mathbf{M}_{e1n}^{(1)} - ic_n \mathbf{N}_{o1n}^{(1)}) \quad (\text{A.20})$$

$$\mathbf{E}_s = \sum_{n=1}^{\infty} E_n (-b_n \mathbf{M}_{o1n}^{(3)} + ia_n \mathbf{N}_{e1n}^{(3)}), \quad \mathbf{H}_s = \frac{k}{\omega\mu} \sum_{n=1}^{\infty} E_n (a_n \mathbf{M}_{e1n}^{(3)} + ib_n \mathbf{N}_{o1n}^{(3)}) \quad (\text{A.21})$$

where  $E_n = i^n E_0 \frac{2n+1}{n(n+1)}$  and the superscript (3) denotes radial dependence on the Bessel function  $h_n^{(1)}$  for unknown coefficients  $a_n$ ,  $b_n$ ,  $c_n$  and  $d_n$ .

## A.4 Determining the Scattering Coefficients

The formal theory is lengthy and still has yet to yield any real physical insight. At this point we may now turn our attention to actually deriving the scattering coefficients  $a_n$  and

$b_n$  that we will then use to determine the scattering efficiencies. We consider a spherical particle of radius  $a$  and consider the boundary conditions at the surface where  $r = a$ . In component form these are

$$E_{i\theta} + E_{s\theta} = E_{1\theta}, \quad E_{i\phi} + E_{s\phi} = E_{1\phi} \quad (\text{A.22})$$

$$H_{i\theta} + H_{s\theta} = H_{1\theta}, \quad H_{i\phi} + H_{s\phi} = H_{1\phi} \quad (\text{A.23})$$

Substituting in all relevant equations (boundary conditions, orthogonality relations, and the expansions of Equations A.17, A.18, A.20 and A.21) eventually gives

$$j_n(mx)c_n + h_n^{(1)}(x)b_n = j_n(x) \quad (\text{A.24})$$

$$\mu[mxj_n(mx)]'c_n + \mu_1[xh_n^{(1)}(x)]'b_n = \mu_1[xj_n(x)]' \quad (\text{A.25})$$

$$\mu m j_n(mx)d_n + \mu_1 h_n^{(1)}(x)a_n = \mu_1 j_n(x) \quad (\text{A.26})$$

$$[mxj_n(mx)]'d_n + m[xh_n^{(1)}(x)]'a_n = m[xj_n(x)]' \quad (\text{A.27})$$

where the prime denotes differentiation with respect to the argument in parentheses,  $x = ka = \frac{2\pi Na}{\lambda}$  is the size parameter and  $m = \frac{k_1}{k} = \frac{N_1}{N}$  is the relative complex refractive index of the two materials with  $N_1$  the refractive index of the particles and  $N$  the refractive index of the medium. Solving the above system of equations, assuming that the permeability of the particle and the surrounding medium are the same, and substituting in the Riccati-Bessel functions  $\psi_n(\rho) = \rho j_n(\rho)$  and  $\xi_n(\rho) = \rho h_n^{(1)}(\rho)$  finally gives the scattering coefficients:

$$a_n = \frac{m\psi_n(mx)\psi'_n(x) - \psi_n(x)\psi'_n(mx)}{m\psi_n(mx)\xi'_n(x) - \xi_n(x)\psi'_n(mx)} \quad (\text{A.28})$$

$$b_n = \frac{\psi_n(mx)\psi'_n(x) - m\psi_n(x)\psi'_n(mx)}{\psi_n(mx)\xi'_n(x) - m\xi_n(x)\psi'_n(mx)} \quad (\text{A.29})$$

## A.5 The Scattering and Extinction Cross-Sections

And last but not least, we must use these scattering coefficients to calculate the scattering cross-section of the particle. We define  $W_a$  to be the net rate at which electromagnetic energy cross the surface A of the particle and  $W_s$  to be the rate at which energy is scattered across the surface A. For a beam of incident irradiance  $I_i$ , we write  $W_{ext} = W_a + W_s$  and

define the extinction, absorption and scattering cross-sections to be

$$C_{ext} = \frac{W_{ext}}{I_i}, \quad C_{abs} = \frac{W_{abs}}{I_i}, \quad C_{sca} = \frac{W_{sca}}{I_i} \quad (\text{A.30})$$

and note that we therefore also have  $C_{ext} = C_{sca} + C_{abs}$ .

$W_{ext}$  and  $W_s$  may be expressed in terms of the components of the scattered and incident fields defined above in Equations A.17, A.18 and A.21. Doing so and manipulating the algebra at length eventually yields the desired relationship between the scalar wave function and the scattering cross-section via the scattering coefficients:

$$C_{sca} = \frac{2\pi}{k^2} \sum_{n=1}^{\infty} (2n+1)(|a_n|^2 + |b_n|^2) \quad (\text{A.31})$$

$$C_{ext} = \frac{2\pi}{k^2} \sum_{n=1}^{\infty} (2n+1)\text{Re}\{a_n + b_n\}. \quad (\text{A.32})$$

# Bibliography

- Ahmad I., Greene J., Kutschera W., Paul M., 2002, in Manuel O., ed., , Origin of Elements in the Solar System. Springer US, pp 203–210, doi:10.1007/0-306-46927-8\_17
- Andrews J. E., et al., 2010, ApJ, 715, 541
- Arendt R. G., Dwek E., Kober G., Rho J., Hwang U., 2014, ApJ, 786, 55
- Arnett W. D., Bahcall J. N., Kirshner R. P., Woosley S. E., 1989, Ann. Rev. Astr. Astrophys., 27, 629
- Auer L. H., van Blerkom D., 1972, ApJ, 178, 175
- Baes M., et al., 2003, MNRAS, 343, 1081
- Barlow M. J., Silk J., 1977, ApJL, 211, L83
- Barlow M. J., et al., 2010, A&A, 518, L138
- Baron E., Nugent P. E., Branch D., Hauschildt P. H., 2005, in Turrato M., Benetti S., Zampieri L., Shea W., eds, Vol. 342, 1604-2004: Supernovae as Cosmological Light-houses, Astronomical Society of the Pacific Conference Series. p. 351
- Beelen A., Cox P., Benford D. J., Dowell C. D., Kovács A., Bertoldi F., Omont A., Carilli C. L., 2006, ApJ, 642, 694
- Bertoldi F., Cox P., 2002, A&A, 384, L11
- Bertoldi F., Carilli C. L., Cox P., Fan X., Strauss M. a., Beelen A., Omont A., Zylka R., 2003, A&A, 406, L55
- Bianchi S., Ferrara A., Davies J. I., Alton P. B., 2000, MNRAS, 311, 601

- Bionta R. M., Blewitt G., Bratton C. B., Casper D., Ciocio A., 1987, Physical Review Letters, 58, 1494
- Biscaro C., Cherchneff I., 2014, A&A, 564, A25
- Bless R. C., Savage B. D., 1972, ApJ, 171, 293
- Bohren C. F., Huffman D., 1983, Absorption and scattering of light by small particles. Wiley science paperback series, Wiley
- Bouchet P., Danziger J., 2014, in Ray A., McCray R. A., eds, IAU Symposium Vol. 296, IAU Symposium. pp 9–14, doi:10.1017/S1743921313009162
- Bouchet P., Danziger I. J., Lucy L. B., 1991, AJ, 102, 1135
- Bouchet P., De Buizer J. M., Suntzeff N. B., Danziger I. J., Hayward T. L., Telesco C. M., Packham C., 2004, ApJ, 611, 394
- Boyer M. L., et al., 2011, AJ, 142, 103
- Boyer M. L., et al., 2012, ApJ, 748, 40
- Brinch C., Hogerheijde M. R., 2010, A&A, 523, A25
- Buslenko N. P., Golenko D. I., Shreider Y. A., Sobol' I. M., Sragovich V. G., 1966, The Monte Carlo Method: The Method of Statistical Trials. International Series of Monographs in Pure and Applied Mathematics Vol. 87, Pergamon Press
- Cardelli J. A., Clayton G. C., Mathis J. S., 1989, ApJ, 345, 245
- Carilli C. L., et al., 2001, ApJ, 555, 625
- Cernuschi F., Marsicano F., Codina S., 1967, Annales d'Astrophysique, 30, 1039
- Chapman B., Jost G., Pas R. v. d., 2007, Using OpenMP: Portable Shared Memory Parallel Programming (Scientific and Engineering Computation). The MIT Press
- Cherchneff I., 2000, in Wing R. F., ed., IAU Symposium Vol. 177, The Carbon Star Phenomenon. p. 331
- Cherchneff I., Dwek E., 2009, ApJ, 703, 642
- Cherchneff I., Dwek E., 2010, ApJ, 713, 1

- Chugai N. N., Chevalier R. a., Kirshner R. P., Challis P. M., 1997, ApJ, 483, 925
- Danziger I. J., Lucy L. B., Bouchet P., Gouiffes C., 1991a, in Woosley S. E., ed., Supernovae. p. 69
- Danziger I. J., Bouchet P., Gouiffes C., Lucy L. B., 1991b, in Danziger I. J., Kjaer K., eds, European Southern Observatory Conference and Workshop Proceedings Vol. 37, European Southern Observatory Conference and Workshop Proceedings. p. 217
- Dorschner J., Begemann B., Henning T., Jaeger C., Mutschke H., 1995, A&A, 300, 503
- Draine B. T., 2003, Ann. Rev. Astr. Astrophys., 41, 241
- Draine B. T., Flatau P. J., 2004, ArXiv Astrophysics e-prints,
- Draine B. T., Lee H. M., 1984, ApJ, 285, 89
- Dunne L., Eales S., Ivison R., Morgan H., Edmunds M., 2003, Nature, 424, 285
- Dunne L., et al., 2009, MNRAS, 394, 1307
- Dwek E., 1988, ApJ, 329, 814
- Dwek E., Arendt R. G., 2015, ApJ, 810, 75
- Dwek E., Galliano F., Jones A. P., 2007, ApJ, 662, 927
- Dwek E., et al., 2010, ApJ, 722, 425
- Ellis T. M. R., Phillips I. R., Lahey T. M., 1994, Fortran 90 Programming. Addison-Wesley
- Ensman L., Burrows A., 1992, ApJ, 393, 742
- Ercolano B., Barlow M. J., Storey P. J., Liu X.-W., 2003, MNRAS, 340, 1136
- Ercolano B., Barlow M. J., Storey P. J., 2005, MNRAS, 362, 1038
- Ercolano B., Barlow M. J., Sugerman B. E. K., 2007, MNRAS, 375, 753
- Fabbri J., et al., 2011, MNRAS, 418, 1285
- Ferland G. J., et al., 2013, Revista Mexicana de Astronomia y Astrofisica, 49, 137
- Ferrarotti A. S., Gail H.-P., 2005, A&A, 430, 959

- Ferrarotti A. S., Gail H.-P., 2006, *A&A*, 447, 553
- Fesen R. A., Pavlov G. G., Sanwal D., 2006, *ApJ*, 636, 848
- Fitzpatrick B., Morris T., Podsiadlowski P., 2013, in Supernova Environmental Impacts. pp 328–329, doi:10.1017/S1743921313009666
- Fransson C., Kozma C., 1993, *ApJ*, 408, L25
- Fransson C., et al., 2013, *ApJ*, 768, 88
- Fransson C., et al., 2014, *ApJ*, 797, 118
- Fransson C., et al., 2015, *ApJL*, 806, L19
- Gail H.-P., Sedlmayr E., 1999, *A&A*, 347, 594
- Gall C., et al., 2014, *Nature*, 511, 326
- Gehrz R. D., Ney E. P., 1987, *Proceedings of the National Academy of Science*, 84, 6961
- Gerasimovic B., 1933, *Zeitschrift für Astrophysik*, 7, 335
- Gilks W. R., Richardson S., Spiegelhalter D. J., 1996, *Markov chain Monte-Carlo in practice*. London: Chapman and Hall
- Gomez H., 2013, in Andersen A., Baes M., Gomez H., Kemper C., Watson D., eds, *Proceedings of The Life Cycle of Dust in the Universe: Observations, Theory, and Laboratory Experiments*. p. 146
- Gomez H. L., et al., 2012, *ApJ*, 760, 96
- Gotthelf E. V., Koralesky B., Rudnick L., Jones T. W., Hwang U., Petre R., 2001, *ApJL*, 552, L39
- Greif T. H., Bromm V., 2006, *MNRAS*, 373, 128
- Grönningsson P., Fransson C., Lundqvist P., Nymark T., Lundqvist N., Chevalier R., Leibundgut B., Spyromilio J., 2006, *A&A*, 5325, 11
- Grönningsson P., et al., 2007, *A&A*, 491, 19
- Grönningsson P., et al., 2008, *A&A*, 479, 761

- Hammer N. J., Janka H.-T., Müller E., 2010, ApJ, 714, 1371
- Hanner M. S., 1988, NASA Conf. Publ., 3004, 22, NASA, Washington DC
- Hanuschik R. W., Spyromilio J., Stathakis R., Kimeswenger S., Gohermann J., Seidensticker K. J., Meurer G., 1993, MNRAS, 261, 909
- Harries T. J., 2000, MNRAS, 315, 722
- Hastings W., 1970, Biometrika, 57, 97
- Helder E. A., et al., 2013, ApJ, 764, 11
- Henyey L. G., Greenstein J. L., 1941, ApJ, 93, 70
- Hildebrand R. H., 1983, Quarterly Journal of the Royal Astronomical Society, 24, 267
- Hillier D. J., 1991, A&A, 247, 455
- Hirata K., Kajita T., Koshiba M., Nakahata M., Oyama Y., 1987, Physical Review Letters, 58, 1490
- Hogerheijde M. R., van der Tak F. F. S., 2000, A&A, 362, 697
- Hoyle F., Wickramasinghe N. C., 1970, Nature, 226, 62
- Indebetouw R., et al., 2014, ApJ, 782, L2
- Jäger C., Mutschke H., Begemann B., Dorshner J., Henning T., 1994, A&A, 292, 641
- Jäger C., Dorshner J., Mutschke H., Posch T., Henning T., 2003, A&A, 408, 193
- Kirshner R. P., 1990, in Petschek A. G., ed., Supernovae. pp 59–75
- Kirshner R. P., Sonneborn G., Crenshaw D. M., Nassiopoulos G. E., 1987, ApJ, 320, 602
- Kotak R., et al., 2009, ApJ, 704, 306
- Kozasa T., Hasegawa H., Nomoto K., 1989, ApJ, 344, 325
- Kozasa T., Hasegawa H., Nomoto K., 1991, A&A, 249, 474
- Kozma C., Fransson C., 1998a, ApJ, 496, 946
- Kozma C., Fransson C., 1998b, ApJ, 497, 431

- Krause O., Birkmann S. M., Rieke G. H., Lemke D., Klaas U., Hines D. C., Gordon K. D., 2004, *Nature*, 432, 596
- Krause O., Birkmann S. M., Usuda T., Hattori T., Goto M., Rieke G. H., Misselt K. A., 2008, *Science*, 320, 1195
- Kromer M., Sim S. A., 2009, *MNRAS*, 398, 1809
- Kunkel W., et al., 1987, *IAU Circ.*, 4316, 1
- Landau L., Lifshitz E., 1959, *Fluid Mechanics*, 2 edn. Course of Theoretical Physics Vol. 6, Pergamon Press
- Larsson J., et al., 2013, *ApJ*, 768, 89
- Li A., Greenberg J. M., 2003, in Pirronello V., Krelowski J., Manicò G., eds, *Solid State Astrochemistry*. pp 37–84 ([arXiv:astro-ph/0204392](https://arxiv.org/abs/astro-ph/0204392))
- Li H., McCray R., 1992, *ApJ*, 387, 309
- Lucy L. B., 1987, in Danziger I. J., ed., European Southern Observatory Conference and Workshop Proceedings Vol. 26, European Southern Observatory Conference and Workshop Proceedings. pp 417–431
- Lucy L. B., 1999, *A&A*, 345, 211
- Lucy L. B., 2002, *A&A*, 384, 725
- Lucy L. B., 2003, *A&A*, 403, 261
- Lucy L., 2005a, *A&A*, 429, 19
- Lucy L. B., 2005b, *A&A*, 429, 31
- Lucy L., Danziger I., Gouiffes C., Bouchet P., 1989, in Tenorio-Tagle G., Moles M., Melnick J., eds, *IAU Colloq. 120: Structure and Dynamics of the Interstellar Medium*, Lecture Notes in Physics. No. 350. Berlin Springer Verlag, p. 164, doi:10.1007/BFb0114861
- Lucy L., Danziger I. J., Gouiffes C., Bouchet P., 1991, in Woosley S. E., ed., *Supernovae*. Springer-Verlag, New York, p. 82
- Marsaglia G., Bray T. A., 1964, *SIAM Review*, 6, 260

- Mathis J. S., Rumpl W., Nordsieck K. H., 1977, ApJ, 217, 425
- Matsuura M., et al., 2009, MNRAS, 396, 918
- Matsuura M., et al., 2011, Science, 333, 1258
- Matsuura M., Woods P. M., Owen P. J., 2013, MNRAS, 429, 2527
- Matsuura M., et al., 2015, ApJ, 800, 50
- Mauerhan J., Smith N., 2012, MNRAS, 424, 2659
- McCray R., 1993, Ann. Rev. Astr. Astrophys., 31, 175
- McCray R., 1996, in Kuhn T. S., ed., IAU Colloq. 145: Supernovae and Supernova Remnants. p. 223
- McCray R., 2003, in Li X. D., Trimble V., Wang Z. R., eds, IAU Symposium Vol. 214, High Energy Processes and Phenomena in Astrophysics. p. 121
- McCray R., Fransson C., 2016, Annual Review of Astronomy and Astrophysics, 54, null
- Meikle W. P. S., Allen D. A., Spyromilio J., Varani G., 1991, in Woosley S. E., ed., Supernovae. p. 102
- Meikle W. P. S., Spyromilio J., Allen D. A., Varani G.-F., Cumming R. J., 1993, MNRAS, 261, 535
- Meikle W. P. S., et al., 2007, ApJ, 665, 608
- Meixner M., et al., 2006, AJ, 132, 2268
- Meixner M., et al., 2013, AJ, 146, 62
- Metropolis N., Ulam S., 1949, Journal of the American Statistical Association, 44, 335
- Metropolis N., Rosenbluth A. W., Rosenbluth M. N., Teller A. H., Teller E., 1953, Journal of Chemical Physics, 21, 1087
- Michałowski M. J., 2015, A&A, 577, A80
- Mie G., 1908, Annalen der Physik, 330, 377
- Milisavljevic D., Fesen R. A., 2013, The Astrophysical Journal, 772, 134

- Milisavljevic D., Fesen R. A., Chevalier R. A., Kirshner R. P., Challis P., Turatto M., 2012, ApJ, 751, 25
- Mishchenko M., Travis L., Lacis A., 2002, Scattering, Absorption, and Emission of Light by Small Particles. Cambridge University Press
- Morgan H. L., Edmunds M. G., 2003, MNRAS, 343, 427
- Morris T., Podsiadlowski P., 2005, in Turatto M., Benetti S., Zampieri L., Shea W., eds, Astronomical Society of the Pacific Conference Series Vol. 342, 1604-2004: Supernovae as Cosmological Lighthouses. p. 194
- Nozawa T., Kozasa T., Umeda H., Maeda K., Nomoto K., 2003, ApJ, 598, 785
- Omont A., Cox P., Bertoldi F., McMahon R. G., Carilli C., Isaak K. G., 2001, A&A, 374, 371
- Osterbrock D., Ferland G., 2006, Astrophysics of Gaseous Nebulae and Active Galactic Nuclei, 2 edn. University Science Books
- Ostriker J. P., McKee C. F., 1988, Reviews of Modern Physics, 60, 1
- Owen P. J., Barlow M. J., 2015, ApJ, 801, 141
- Patnaude D. J., Fesen R. A., Raymond J. C., Levenson N. A., Graham J. R., 2001, in American Astronomical Society Meeting Abstracts. p. 126
- Phillips M. M., Hamuy M., Heathcote S. R., Suntzeff N. B., Kirhakos S., 1990, AJ, 99, 1133
- Press W. H., Teukolsky S. A., Vetterlin W. T., Flannery B. P., 2007, Numerical Recipes: The Art of Scientific Computing, 3 edn. Cambridge University Press
- Rest A., et al., 2011, ApJ, 732, 3
- Rho J., et al., 2008, ApJ, 673, 271
- Riebel D., Srinivasan S., Sargent B., Meixner M., 2012, ApJ, 753, 71
- Rieke G. H., Lebofsky M. J., 1985, ApJ, 288, 618
- Riley K., Hobson M., Bence S., 2006, Mathematical Methods for Physics and Engineering: A Comprehensive Guide. Cambridge University Press

- Robitaille T. P., 2011, A&A, 536, A79
- Robson I., Priddey R. S., Isaak K. G., McMahon R. G., 2004, MNRAS, 351, L29
- Roche P. F., Aitken D. K., Smith C. H., James S. D., 1989, Nature, 337, 533
- Roche P. F., Aitken D. K., Smith C. H., 1993, MNRAS, 261, 522
- Salaris M., Weiss A., Cassarà L. P., Piovan L., Chiosi C., 2014, A&A, 565, A9
- Sarangi A., Cherchneff I., 2013, ApJ, 776, 107
- Sarangi A., Cherchneff I., 2015, A&A, 575, A95
- Schneider R., Ferrara A., Salvaterra R., 2004, MNRAS, 351, 1379
- Silvia D. W., Smith B. D., Michael Shull J., 2010, ApJ, 715, 1575
- Silvia D. W., Smith B. D., Shull J. M., 2012, ApJ, 748, 12
- Sinnott B., Welch D. L., Rest A., Sutherland P. G., Bergmann M., 2013, The Astrophysical Journal, 767, 45
- Slavin J. D., Dwek E., Jones A. P., 2015, ApJ, 803, 7
- Sloan G. C., et al., 2009, Science, 323, 353
- Smith N., Silverman J. M., Filippenko A. V., Cooper M. C., Matheson T., Bian F., Weiner B. J., Comerford J. M., 2012, AJ, 17, 6
- Sobolev V. V., 1957, Soviet Astronomy, 1, 678
- Sonneborn G., Altner B., Kirshner R. P., 1987, ApJL, 323, L35
- Spyromilio J., Stathakis R., Cannon R., Waterman L., Couch W., Dopita M., 1991, MNRAS, 248, 465
- Spyromilio J., Stathakis R. a., Meurer G. R., 1993, MNRAS, 263, 530
- Storey P. J., Zeippen C. J., 2000, MNRAS, 312, 813
- Sugerman B. E. K., Croots A. P. S., Kunkel W. E., Heathcote S. R., Lawrence S. S., 2005, ApJSS, 159, 60

- Sugerman B. E. K., et al., 2006, *Science*, 313, 196
- Suntzeff N. B., Phillips M. M., Depoy D. L., Elias J. H., Walker A. R., 1991, *AJ*, 102, 1118
- Takiwaki T., Kotake K., Suwa Y., 2014, *ApJ*, 786, 83
- Temim T., Dwek E., 2013, *ApJ*, 774, 8
- Temim T., Sonneborn G., Dwek E., Arendt R. G., Gehrz R. D., Slane P., Roellig T. L., 2012, *ApJ*, 753, 72
- Thomas R. C., Baron E., Branch D., 2003, in Hubeny I., Mihalas D., Werner K., eds, Astronomical Society of the Pacific Conference Series Vol. 288, Stellar Atmosphere Modeling. p. 453 ([arXiv:astro-ph/0207089](https://arxiv.org/abs/astro-ph/0207089))
- Tielens A., 2005, The Physics and Chemistry of the Interstellar Medium. Cambridge University Press
- Todini P., Ferrara A., 2001, *MNRAS*, 325, 726
- Trumpler R. J., 1930, *PASP*, 42, 214
- Tziampzis a., Lundqvist P., Groningsson P., Nasoudi-Shoar S., 2010, *A&A*, 53, 15
- Wang B., Han Z., 2012, *New Astronomy Reviews*, 56, 122
- Wang L., et al., 1996, *ApJ*, 466, 998
- Watson D., Christensen L., Knudsen K. K., Richard J., Gallazzi A., Michaowski M. J., 2015, *Nature*, 519, 327
- Wesson R., Barlow M. J., Matsuura M., Ercolano B., 2015, *MNRAS*, 446, 2089 (W15)
- Whitelock P., Menzies J., Caldwell J. A. R., 1991, *Proceedings of the Astronomical Society of Australia*, 9, 105
- Wilson G., et al., 2012, preprint, ([arXiv:1210.0530](https://arxiv.org/abs/1210.0530))
- Wongwathanarat A., Müller E., Janka H.-T., 2015, *A&A*, 577, A48
- Wood K., Mathis J. S., Ercolano B., 2004a, *MNRAS*, 348, 1337

- Wood P. R., Olivier E. A., Kawaler S. D., 2004b, ApJ, 604, 800
- Wooden D. H., Rank D. M., Bregman J. D., Witteborn F. C., Tielens A. G. G. M., Cohen M., Pinto P. A., Axelrod T. S., 1993, ApJSS, 88, 477
- Woosley S. E., 2010, ApJL, 719, L204
- Xu Y., McCray R., Oliva E., Randich S., 1992, ApJ, 386, 181
- Zeippen C. J., 1987, A&A, 173, 410
- Zubko V. G., Mennella V., Colangeli L., Bussoletti E., 1996, MNRAS, 282, L1321
- van de Hulst H., 1957, Light Scattering by Small Particles. Dover Books on Physics, Dover Publications

"KEEP LOOKING UP...  
THAT'S THE SECRET OF  
LIFE..."

- Snoopy

